Rheinland-Pfälzische
Technische Universität
Kaiserslautern
Landau

Elastohydrodynamic Interaction of Flowing Particles with Surfaces

Vom Fachbereich Maschinenbau und Verfahrenstechnik
der Rheinland-Pfälzischen Technischen Universität Kaiserslautern-Landau
zur Erlangung des akademischen Grades

Doktor-Ingenieur (Dr.-Ing.)

genehmigte

Dissertation

von

Dipl.-Ing. Isabell Noichl

aus Rodalben

Betreuerin der Dissertation:	Prof. Dr.-Ing. Clarissa Schönecker
Dekan:	Prof. Dr. rer. nat. Roland Ulber
Prüfungskommision	
Vorsitzende :	Prof. Dr.-Ing. Kristin de Payrebrune
1. Berichterstatter:	Prof. Dr.-Ing. Clarissa Schönecker
2. Berichterstatter:	Prof. Dr.-Ing. Sergiy Antonyuk
Eingereicht am:	01.08.2025
Tag der mündlichen Prüfung:	18.12.2025

Kaiserslautern 2026
D 386

Don´t be afraid of being slow. Be afraid of stagnation.

Wisdom from a fortune cookie found on New Year's Eve 2024/2025

Danksagung

Die vorliegende Dissertation entstand im Rahmen meiner Tätigkeit als wissenschaftliche Mitarbeiterin am Lehrstuhl für Mikrofluidmechanik im Fachbereich Maschinenbau und Verfahrenstechnik an der Rheinland-Pfälzischen Technischen Universität Kaiserslautern-Landau (RPTU). An dieser Stelle möchte ich allen einen Dank aussprechen, die, in welcher Art und Weise auch immer, an dieser Arbeit mitgewirkt haben. Und einigen davon ganz besonders.

Zunächst geht ein großer Dank an Clarissa Schönecker. Ich schätze mich glücklich, dass ich dich und deine Forschungsthemen im Rahmen deines Berufungsverfahrens vorab und quasi exklusiv kennenlernen durfte und ich dann nach meinem Diplom-Abschluss die Möglichkeit zur Mitarbeit an deinem neu gründeten Lehrstuhl bekommen habe. Das war sowohl zeitlich, als auch thematisch ein absoluter Jackpot für mich. Ich kann mir rückblickend nichts vorstellen, was in diesem Moment besser gepasst hätte. Es war nicht immer einfach, „Forschung bei Null zu starten“ und mich nebenbei mit den zahlreichen Hürden des öffentlichen Dienstes herumzuschlagen. Trotzdem habe ich dadurch aus vielerlei Hinsicht lernen können. Wahrscheinlich weitaus mehr, als wäre ich einfach „nur“ Doktorandin gewesen. Währenddessen hast du stets Geduld und Verständnis gezeigt. Vor allem, wenn Dinge einfach länger gedauert haben. Hierfür möchte ich einen großen Dank aussprechen Ich freue mich auf die weitere Zusammenarbeit und auf die Möglichkeit, nochmal ”zurück zum Anfang” zu gehen.

Als nächstes möchte ich mich gerne bei der Deutschen Forschungsgemeinschaft (DFG) für die Förderung des Projektes im Rahmen des Sonderforschungsbereiches 926 bedanken. Der Dank geht auch an alle Verantwortlichen und Mitwirkenden des SFB 926. Durch die Mitgliedschaft im SFB 926 haben sich zahlreiche zusätzliche Möglichkeiten ergeben, die nicht als selbstverständlich anzusehen sind. Hierzu zähle ich besonders die Möglichkeiten, sich weiterzubilden und sich, sowohl fachlich als auch persönlich, weiterzuentwickeln.

Der allergrößte Dank gebührt aber meinem besten Freund und Ehemann, Patrick. Es ist ein unbeschreibliches Glück, einen Partner zu haben, mit dem man sich nicht nur privat auf ganzer Linie versteht, sondern auch noch beruflich und fachlich. Es gibt niemanden, der mich besser versteht, wenn ich mal wieder

im wissenschaftlichen Wahnsinn schwelge. Und vor allem wäre diese Arbeit ohne deine Hilfe nicht zu dem geworden, was sie jetzt ist. Deine Fähigkeiten beim Programmieren haben einen ungemeinen Beitrag zur Auswertung der Messungen beigetragen. Und nicht zu vergessen, nur weil du Gleichberechtigung in der Erziehung tatsächlich ernst nimmst und wir uns die Erziehung unseres Sohnes von Anfang an gleich aufgeteilt haben, konnte ich ohne Unterbrechung weiterforschen und dieses Promotionsvorhaben zu Ende bringen. Ich kann dir hierfür nicht genug danken. Ich liebe dich und Till von ganzem Herzen.

Kaiserslautern, im August 2025

Isabell Noichl

Abstract

The influence of elasticity on the dynamics of nonheavy particles in creeping flows near rigid and elastic walls is investigated in this dissertation. These dynamics are central to processes like filtration and sedimentation of soft microparticles, including bioparticles and soft microplastics. To isolate elastic effects from microscale phenomena such as diffusion and electrostatics, centimeter-scale model experiments were performed using rigid and elastic spheres and rods in a highly viscous Newtonian fluid. The sedimentation of elastic spheres in the center of a large rectangular tank - initially similar to that of rigid ones - diverged beyond a characteristic distance from rest, where softer spheres experienced a second acceleration and reached terminal velocities up to 9% higher. Near-wall experiments revealed even more unexpected phenomena: *inertial wall attraction* during the transient mass acceleration phase at low Reynolds numbers ($Re_P \lessapprox 0.1$) and persistently unsteady, nonlinear kinematics even in the creeping-flow regime, where $Re_P \approx O(10^{-2})$. These behaviors are typically attributed to inertial forces in form of so-called memory forces. In the case of very soft spheres, the kinematics were superimposed by further nonlinearities, which indicates the presence of an *elastohydrodynamic memory effect*. Rods with small aspect ratios ($l/r \approx 5$) exhibited additional complexity. While axial sedimentation of rigid rods sedimenting at $Re_P \approx O(10^{-1})$ was in accordance with theoretical predictions, rods at lower Re_P showed kinematic *instabilities* and transitions from flipping to *drifting motion* near walls as deformability increased - reminiscent of the tank-treading motion of red blood cells in shear flows. Complementary CFD simulations visualized the transient flow fields and confirmed the importance of container boundaries and fluid inertia, even at low Re_P. The findings of this thesis challenge the widespread assumption that particle dynamics at $Re_P < 0.1$ are purely linear. Instead, they highlight the crucial role of fluid inertia and memory effects in the dynamics of soft particles near walls. A deeper understanding and accurate modeling of these overarching effects are essential for advancing the theory of elastohydrodynamics in confined, low-Reynolds-number flows.

Kurzfassung

In dieser Dissertation wird der Einfluss der Elastizität auf die Dynamik von Partikeln mit geringem Dichteunterschied zum umgebenden Fluid untersucht, welche bei niedrigen Reynolds Zahlen in der Nähe von starren und elastischen Wänden strömen. Diese Dynamik ist von zentraler Bedeutung für Prozesse, wie beispielsweise Filtration und Sedimentation von weichen Mikropartikeln, darunter Biopartikel und weiches Mikroplastik. Um elastische Effekte von mikroskaligen Phänomenen wie Diffusion und Elektrostatik isoliert zu betrachten, wurden Modellversuche mit starren und elastischen Kugeln und Stäbchen im Zentimetermaßstab in einer hochviskosen Newtonschen Flüssigkeit durchgeführt. Die Sedimentation elastischer Kugeln im Zentrum eines großen, rechteckigen Tanks verläuft anfangs ähnlich wie bei starren Kugeln. Nachdem elastische Kugeln eine charakteristische Strecke sedimentierten, zeigen diese eine zweite Beschleunigung und erreichen stationäre Geschwindigkeiten, die bis zu 9% höher als die von starren Kugeln sind. Experimente in Wandnähe zeigten noch weitere unerwartete Phänomene: während der transienten Massenbeschleunigungsphase bei niedrigen Reynolds-Zahlen ($Re_P \lessapprox 0.1$) zeigte sich eine Bewegung der Kugel zur Wand hin (*inertial wall attraction*). Desweiteren zeigten die Kugeln langanhaltend instationäre, nichtlineare Kinematiken selbst im Bereich sehr kleiner Reynolds Zahlen $Re_P \approx O(10^{-2})$. Diese Verhaltensweisen, werden typischerweise auf Trägheitskräfte in Form so genannter Memory Kräfte zurückgeführt. Bei sehr weichen Kugeln wird die Kinematik durch weitere Nichtlinearitäten überlagert, was auf das Vorhandensein eines *elastohydrodynamischen Memory-Effekts* hindeutet. Stäbchen mit kleinen Aspektverhältnissen ($l/r \approx 5$) zeigten zusätzliche Komplexitäten in der Kinematik. Während die Sedimentation von axial ausgerichteten, starren Stäbchen bei $Re_P \approx O(10^{-1})$ mit theoretischen Vorhersagen übereinstimmte, zeigten Stäbchen in der Nähe von Wänden bei niedrigeren Re_P kinematische *Instabilitäten* und, bei Zunahme der Verformbarkeit, den Übergang von Kipp-Drehbewegungen (Flipping) zu einer *driftenden Bewegung* entlang der Wand – ähnlich der "Tank-Treading"-Bewegung roter Blutkörperchen in Scherströmungen. Ergänzende CFD-Simulationen visualisierten die transienten Strömungsfelder und bestätigten die Bedeutung von Wänden und Fluidträgheit, selbst bei niedrigen Re_P. Die Ergebnisse dieser Arbeit stellen die weit verbreitete Annahme in Frage, dass die Partikeldynamik bei $Re_P < 0.1$ rein linear ist. Stattdessen unterstreichen sie die entscheidende Rolle der Flüssigkeitsträgheit und der Gedächtniskräfte in der Dynamik weicher Partikel in der Nähe von Wänden. Ein tieferes Verständnis und eine genaue Modellierung dieser übergeordneten Effekte sind für die Weiterentwicklung und Modellierung elastohydrodynamischer Kräfte im Bereich kleiner Reynolds-Zahlen unerlässlich.

Contents

Danksagung **III**

Abstract **IV**

Kurzfassung **VI**

List of Symbols **XIII**

1 Introduction **1**

1.1 Motivation 1

1.2 Simulation of particle-laden fluid flow over micro-structured surfaces 4

1.3 Objective and scope of the thesis 8

2 Dynamics of elastic, nonheavy spheres sedimenting in a rectangular duct **13**

2.1 Abstract 13

2.2 Introduction 14

2.3 Theoretical background 15

2.4 Methods 18

2.4.1 Experimental setup 18

2.4.2 Model particle fabrication 19

2.4.3 Material properties 20

2.5 Results and Discussion 22

2.5.1 Velocity measurements 22

2.5.2 Phase I and II: transient acceleration, rigid plateau and elastic time scale 25

2.5.3 Phase III: second acceleration 27

2.5.4 Phase IV: Second plateau - elastic terminal velocity 28

2.5.5 Influencing factors and future directions 31

2.6 Conclusion 32

2.7 Chapter Appendix 33

3 Inertial forces and elastohydrodynamic interaction of spherical particles in wall-bounded sedimentation experiments at low particle *Re* number 35

3.1 Abstract . . . 36

3.2 Introduction . . . 36

3.3 Theoretical background . . . 40

3.4 Methods . . . 44

3.4.1 Experimental setup and particle tracking velocimetry . . . 44

3.4.2 Fabrication of model particles and the soft layer . . . 45

3.5 Results and Discussion . . . 48

3.5.1 Sedimentation of rigid and elastic spheres near a plane, rigid wall . . . 48

3.5.2 Sedimentation of a rigid sphere near a plane, elastic wall . . . 63

3.6 Summary and Conclusions . . . 68

3.7 Chapter Appendix . . . 74

4 Computational fluid dynamics simulations of single particle sedimentation in a rectangular duct 85

4.1 Abstract . . . 85

4.2 Introduction . . . 86

4.3 Methods . . . 89

4.3.1 Parameter and numerical settings . . . 89

4.3.2 Geometry and Mesh . . . 91

4.4 Results . . . 94

4.4.1 Particle velocity and flow field . . . 95

4.4.2 Fluid stresses on the surface . . . 101

4.4.3 Traction forces, drag and lift . . . 105

4.5 Conclusions . . . 111

4.6 Chapter appendix . . . 115

5 Low *Re* kinematics of short, cylindrical rods accelerating axially aligned from rest in a rectangular duct 119

5.1 Abstract . . . 119

5.2 Introduction . . . 120

5.3 Theory . . . 125

5.4 Methods . . . 131

5.4.1 Experimental setup and definitions . . . 131

5.4.2 Data acquisition - Particle tracking velocimetry of cylindrical particles 134
5.4.3 Model particle fabrication and soft wall fabrication 136

5.5 Results and Disucssion 138
5.5.1 Kinematics of short, cylindrical rods falling near rigid, plane walls 138
5.5.2 Kinematics of short, cylindrical rods falling near a soft, plane wall 161
5.6 Conclusions and outlook 165
5.7 Chapter Appendix 170

Conclusions **175**

A Appendix **181**
A.1 Supplementary information 181
A.2 Programming and Codes 191
A.2.1 MATLAB object tracking application 191

Bibliography **207**

Declaration of authorship **218**

List of supervised theses **221**

Curriculum vitae **223**

List of Symbols

Latin Symbols

A	Area in m^2 or px^2
C	Wall correction factor; torque resistance coefficient
D	Depth in m
E	Young´s elastic modulus in Pa
F	Force in N
G	2. Lamé's constant, Shear modulus in Pa
H	Height in m or pixel
I	Unity matrix; Moment of inertia in $kg \cdot m^{-2}$
K_i	Specific elastic constant
L	Length in m
R	Radius in m
S	Surface; Area in m^2
T	Transient time scale; Torque in N·m
U	Translational velocity in $m \cdot s^{-1}$
V	Volume in m^3
W	Width in m or pixel
X	Position of particle center
d	Distance in m
$\mathbf{e}$	Unity vector
f	Force density in $N \cdot m^{-2}$
g	Gravitational acceleration in $m \cdot s^{-2}$
h	Immersion depth in m
l	Half-length of a cylinder in m
m	Mass in kg
$\mathbf{n}$	Normal vector
r	Radial position in m; Radius in m
t	Time in s
u, v, w	Velocity (in x, y, z direction)
x, y, z	Spatial directions; covered distances

Greek Symbols

α	Perturbation parameter
γ	Particle-to-fluid density ratio
η	Dynamic viscosity in Pa·s
θ	Orientation angle in the xy-plane in ˚
$\dot{\theta}$	Angular velocity in s^{-1}
$\ddot{\theta}$	Angular acceleration in s^{-2}
κ	Scaling variable
λ	1. Lamé's constant
ν	Kinematic viscosity in $m^2 \cdot s^{-1}$
ν	Poisson´s ratio
ρ	Mass density in $kg \cdot m^{-3}$
σ	Viscous stress in Pa
τ	Shear stress in Pa; Dummy time variable
ϕ	Angle of attack in ˚
φ	Orientation angle in the xz-plane in ˚
χ	Inertial correction of the wall factor

Abbreviations

ALE	Arbitrary Lagrangian-Eulerian
BBO	Basset-Boussinesq-Oseen
CFD	Computational Fluid Dynamics
CFL	Courant-Friedrichs-Lewy number
DEM	Discrete Element Methods
DSLR	Digital Single-Lense Reflex
EHD	Elastohydrodynamic
FEM	Finite element method
FSI	Fluid - Structural Mechanics - Interaction
fps	frames per second
GB	Gigabyte
GUI	Graphical User Interface
h	Hours
ML	Machine Learning
MR	Maxey - Riley
ODE	Ordinary differential equation
PDMS	Polydimethylsiloxane

PIV	Particle Image Velocimetry
PTV	Particle Tracking Velocimetry
PS	Polystyrene
RBCs	Red blood cells
RAM	Random access memory
Re	Reynolds number

Subscripts and Superscripts

AM	Added mass
B	Basset
D	Drag
F	Faxén
FO	Faxén-Oseen
H	Hydrodynamic
I	Inertia
L	Lift
M	Murata
MIX	mixture
P	Particle
St	Stokes
SYL	Sylgard
corr	corrected
el	elastic
exp	experimental
ext	external
f	fluid
g	gravitational
im	immersion
i	numerical iteration step
ini	initial
max	maximum
mig	migration
min	minimum
px	Pixel
s	solid
sim	simulation
term	terminal

th	theoretical
ub	unbounded
vid	video
wb	wall-bounded
wi	wall-induced
x, y, z	spatial direction

1 Introduction

Contents

1.1 Motivation 1
1.2 Simulation of particle-laden fluid flow over micro-structured surfaces 4
1.3 Objective and scope of the thesis 8

1.1 Motivation

This dissertation was written as part of Project A10 of the Collaborative Research Center (CRC) 926, funded by the German Research Foundation (DFG). The project focused on the interactions between surface morphology and elastic particles moving over such surfaces. These interactions can significantly influence particle dynamics and adhesion and are therefore relevant to a wide range of applications, such as filtration and sedimentation processes. However, this project specifically aimed to examine the effects of surface interactions in the context of bioparticles. A defining characteristic of many biotechnological systems is the elasticity of at least one interaction partner - both bioparticles and, for example, biofilms on surfaces are deformable. Even in the absence of direct contact, the deformation of the elastic body and the surrounding flow are nonlinearly coupled, giving rise to elastohydrodynamic forces that affect particle motion. As a result, particle dynamics under elastohydrodynamic conditions differ fundamentally from those in conventional, rigid-body flows. It is therefore assumed that such effects play a critical role in determining flow behavior and particle accumulation in biological systems. At the same time, many elastohydrodynamic interactions between particles and surfaces remain poorly understood - especially under flow conditions relevant to bioparticle systems, *i.e.*, in the creeping flow regime where particle Reynolds numbers satisfy $Re_P \lessapprox 0.1$. For biological particles near a surface, it is insufficient to assume that *"wall effects are negligible and Stokes' equations for a sphere apply"*. This project therefore aimed to investigate the fundamental characteristics

of such interactions. In particular, it focused on studying and modeling the influence of biosystem-relevant parameters on the elastohydrodynamic interaction, such as particle shape - specifically, spherical and rod-like geometries. The resulting models were intended as additional boundary conditions for simulations at a larger scale, where direct resolution of such small-scale interactions becomes computationally infeasible.

As a first step, numerical simulations of fluid flow over microstructured surfaces were conducted to characterize the flow fields and evaluate how particle transport occurs over such surfaces. Since particle adhesion requires that particles are first transported to the surface by the flow, the project initially focused explicitly on this transport process. The inherent complexity of the real-life system at the micro-scale - arising from surface geometry and multiple interacting forces - was to be systematically decomposed into its individual components. Accordingly, the flow over a microstructured surface must be treated as a multi-scale problem to address the question of how particles that are significantly smaller than the characteristic size of the surface topography can adhere to it. The multi-scale nature of the problem can be divided into several levels, as illustrated in Fig. 1.1.

Fig. 1.1 (top) represents the application scale, showing the global flow through the system (*e.g.*, an upright pipe with microstructured inner surfaces). At this level, the effect of surface morphology manifests as an averaged influence of the underlying multi-level processes, often represented as an effective boundary condition. Fig. 1.1 (center) schematically illustrates the microstructure scale. At this level, the microstructural geometry directly affects particle transport toward the surface. Beneath that is the particle interaction level. Here, local flow strongly interacts with individual particles and the surface, such as in the case of a soft particle near a rigid wall (bottom left in Fig. 1.1) or a particle interacting with a soft wall, *e.g.*, with a biofilm (bottom right in Fig. 1.1). This scale determines whether the particle ultimately makes contact and adheres to the surface. For bioparticles, additional processes may follow - such as docking, spreading, and biofilm growth. [1]

The microstructure and particle interaction levels are particularly critical for understanding particle deposition. The flow on the microstructure level is shaped by the surface topography, which can serve multiple functions: directing flow or particle motion, providing surface area for trapping particles, or generating vortices and dead zones where, for example, flow-sensitive biological particles preferentially accumulate. Trapping refers to a scenario in which a particle, carried by the flow, contacts the surface due to geometrical effects. The behavior of the flow at the microstructure scale - and whether particles can be trapped by artificial microstructures or obstacles - will be revisited in the following section using results from numerical fluid flow simulations.

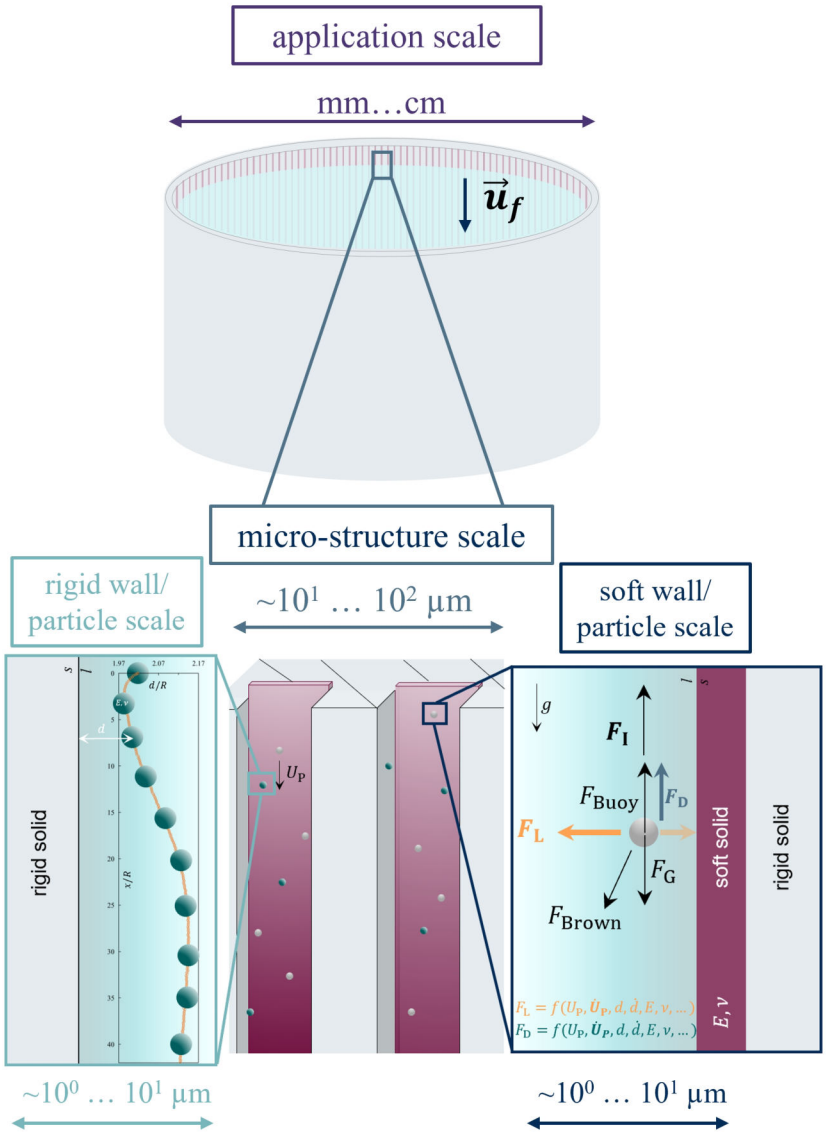


Figure 1.1: The multi-scale problem of particle-laden fluid flows. Top: application scale (*e.g.* upright cylindrical tube with micro-structure inside). Bottom center: micro-structure scale (*e.g.* rectangular grooves). Bottom left: rigid wall/particle scale - exemplary trajectory of a soft, spherical particle near a rigid wall, *cf.*, Chapter 3. Bottom right: soft wall/particle scale - exemplary force balance around a spherical micro-particle sedimenting near a soft wall.

1.2 Simulations of particle-laden fluid flow over micro-structured surfaces: Why µm-sized obstacles do not work as a trapping method for nonheavy micro-particles

The title of this section already suggests the answer to the previous question. In earlier phases of the CRC 926, the hypothesis was that particle adhesion or biofilm growth - and thus the productivity of these systems - could be enhanced by surface morphology, specifically surface topography. To investigate this, the bottom of a flow chamber was structured with microfeatures, and the chamber was filled and continuously flowed through with a solution (feed) containing biological cells. [1] For example, the flow chamber was equipped with surfaces containing grooves created by micromilling or 3D microstructures fabricated by direct laser writing.

Figure1.2 *(a)* shows a schematic of such a flow chamber. It essentially consists of two flat plates separated by a gap of height H_{ch}. A sample (*e.g.*, a glass slide or metal plate) with microstructure on it was embedded in the lower plate. In the example shown in Fig.1.2 *(a)*, the microstructure is a periodic groove pattern, where each groove has a length of $L_{\mathrm{gr}} = 300$ µm.

As part of Sebastian Zimmermann's master's thesis (*Numerical Investigation of Particle-Loaded Fluid Flow Over Microstructured Surfaces, 2019*), a model of periodic microstructures within a fluid domain was developed in COMSOL Multiphysics® to compute the flow field at the microstructure scale within such a flow chamber. The Stokes equations governing the fluid flow were solved, with shear stress applied as a boundary condition. This shear stress was estimated based on the wall shear stress or the shear stress at a defined height above the simulation domain, using the approximate solution for flow between two parallel plates (see Eq.1.1). [2]

$$\tau \approx \frac{6\eta\overline{u}_{\mathrm{f}}}{H} - \frac{12\eta\overline{u}_{\mathrm{f}}H_{\mathrm{D}}}{H^2} \tag{1.1}$$

In Eq. 1.1, η is the dynamic viscosity, $\overline{u}_{\mathrm{f}} = \dot{V}/A$ is the average fluid velocity through the chamber with cross section $A = H \cdot W$, H is the chamber height, W the chamber width and H_{D} is the height of the simulation domain. Simulations were carried out for various topographies, for example periodic transverse grooves or longitudinal grooves, nub-like hemisphere structures or so-called "shelters" (see Fig. 1.3).

In Fig 1.2, representative results from CFD simulations of fluid flow over longitudinal grooves are shown. Fig 1.2 *(c)* shows simulated viscous stresses on the surface, which were generated by the flow over longitudinal grooves of different groove width (w) and groove height (h). Fig 1.2 *(d)* shows streamline plots of the fluid flow longitudinally over the periodic grooves with a length of $L_{\mathrm{gr}} = 300$ µm and a height of $h = 15$ µm and varying width of the grooves.

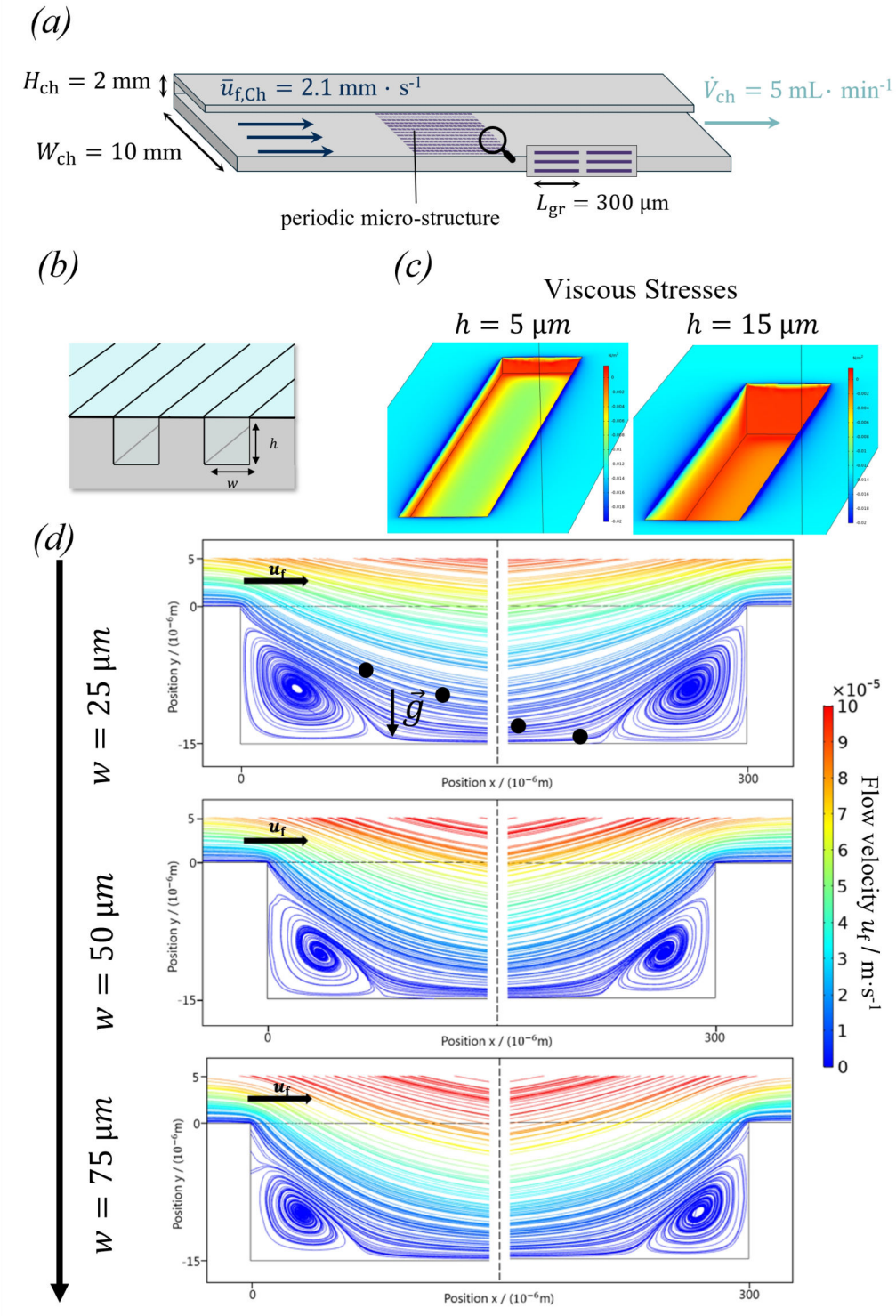


Figure 1.2: *(a)* Schematic of channel flow between two plates. *(b)* Definitions on the micro-structure scale (groove size). *(c)* Viscous stresses at the surface of grooves with various groove heights (note: smallest stress magnitude in red). *(d)* Streamlines of longitudinal fluid flow over 300 µm long grooves with various width (h = 15 µm; w_1 = 25 µm, w_2 = 50 µm, w_3 = 75 µm.

In the fluid flow simulation shown in Fig 1.2 *(c)* (fluid only, without particles), it can be observed that corner vortices - so-called Moffatt eddies - form within the longitudinal grooves. The narrower the groove, the deeper these eddies extend into it. As the groove becomes wider, higher flow velocities develop within the groove, causing the eddies to shrink (see streamline plot of the groove with width $w = 75$ µm). When non-diffusive particles particles ($d_P > 1$ µm) with a density similar to water (*e.g.*, $\rho_P \approx 1110$ kg·m^{-3}) are dispersed and transported by the fluid through these grooves, they predominantly follow the streamlines in the regions of higher velocity. Over time, these particles begin to sediment in the groove, as indicated in the upper streamline plot of Fig 1.2 *(d)* ($w = 25$ µm). Contrary to what might be expected, however, the particles do not accumulate in the rear corners, *i.e.*, they are not carried into and trapped by the eddies. This inhibits the formation of these stable, stationary corner eddies.

A similar phenomenon can be observed in the so-called "shelter" structure, which was designed to function as a type of baffle. Fig. 1.3 shows simulations conducted in COMSOL Multiphysics®, in which particle transport was modeled using the COMSOL Multiphysics® Particle Tracing Module. Fig. 1.3 *(a)* shows the trajectories from a 2D unidirectional simulation of particles ($\rho_P = 1100$ kg·m^{-3}; $d_P = 1$ µm) dispersed in a fluid and flowing in shear flow (boundary condition: $\tau = 12.6$ mPa) over a microstructure obstacle ("shelter"). *Unidirectional* means that the presence of the particles does not affect the surrounding fluid; that is, the flow field is solved independently, and the forces acting on the particles are derived from this fixed field.

In contrast, *bidirectional coupling* (see Fig. 1.3 *(b)* and *(c)*) allows the particles to influence the flow field, meaning they can locally alter the fluid dynamics. In these simulations, particles with diameter $d_P = 1$ µm were again introduced into a shear flow over the shelter structure, but with bidirectional coupling and with Brownian motion (diffusion) included. The random walk of a diffusing particle is illustrated schematically in the rear eddy in Fig. 1.3 *(d)*.

Fig. 1.3 *(a)* clearly illustrates what was already implied in the title of this section. From the outset, a particle was positioned very close to the surface. Its trajectory shows that it was simply carried over the obstacle by the flow, rather than becoming trapped beneath the "roof" of the microstructure. In the 2D simulations conducted during S. Zimmermann's master's thesis - specifically under the conditions exemplified in Fig. 1.3 *(a)* (unidirectional flow, no diffusion, $d_P = 1$ µm) - almost no contacts between particles and walls were observed. The gravitational force acting on these particles is too weak, resulting in minimal sedimentation.

Subsequently, a 3D simulation with bidirectional coupling and inclusion of Brownian motion was performed. These simulations were highly computationally intensive. They demonstrated that $d_P = 1$ µm particles can "jump" off the fluid's streamlines purely due to the random walk of the particle, *i.e.*, Brownian motion. This jumping occurs preferentially within the rear eddy of an obstacle. The principle of rear eddy trapping is shown in Fig. 1.4.

It can therefore be concluded that, at the microstructure level, particles cannot simply be trapped by

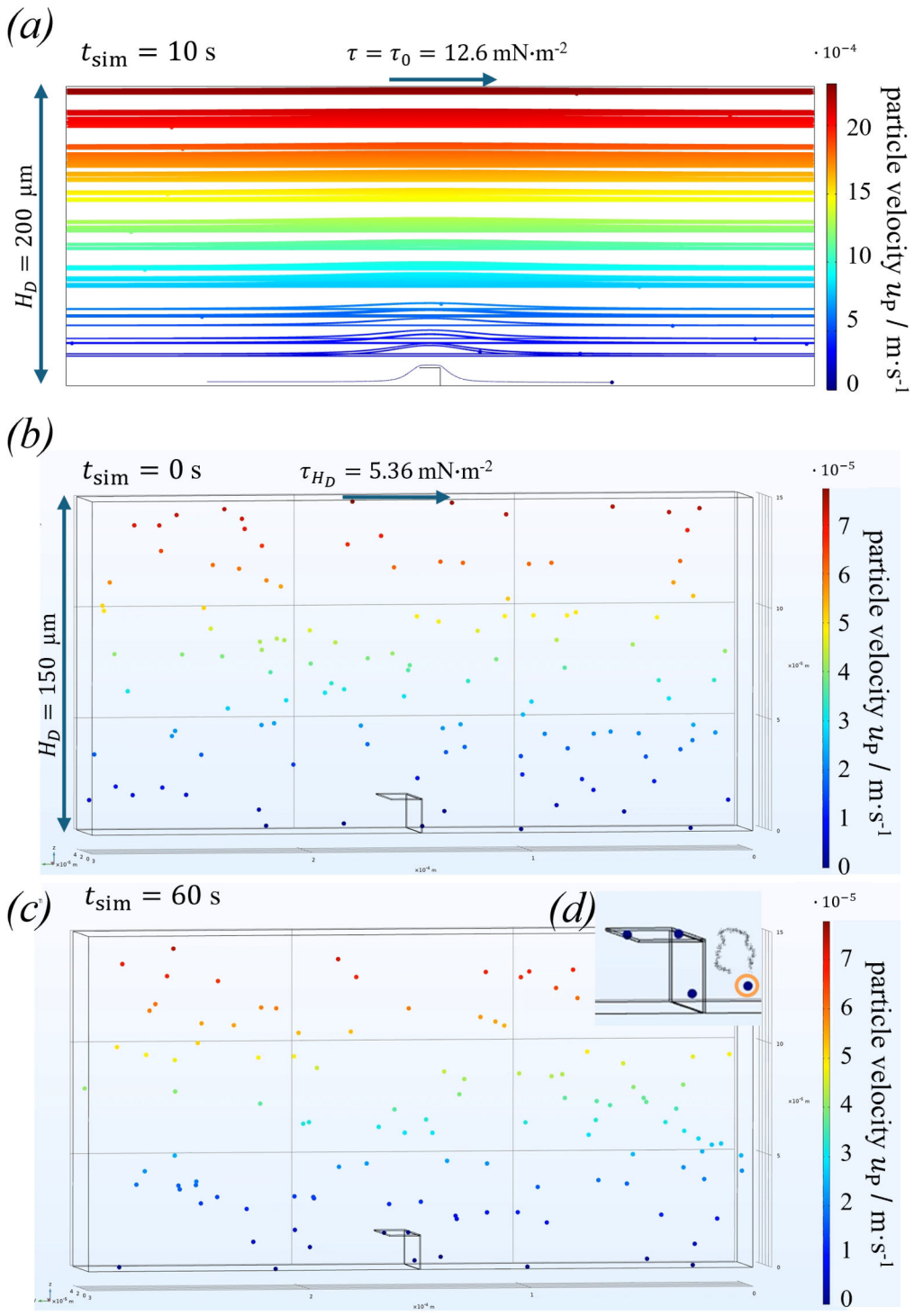


Figure 1.3: *(a)* 2D unidirectional simulation of particles (ρ_P = 1100 kg·m^{-3}; d_P = 1 µm) in a shear flow over a microstructure obstacle (”shelter”) after a simulation time of t_{sim} = 10 s; 3D bidirectionally coupled simulation of diffusive particles (ρ_P = 1100 kg·m^{-3}; d_P = 1 µm) in a shear flow over a shelter at t_{sim} = 0 s *(b)* and t_{sim} = 60 s *(c)*; *(d)* Schematic of the random walk of a diffusing particle in the backward eddy.

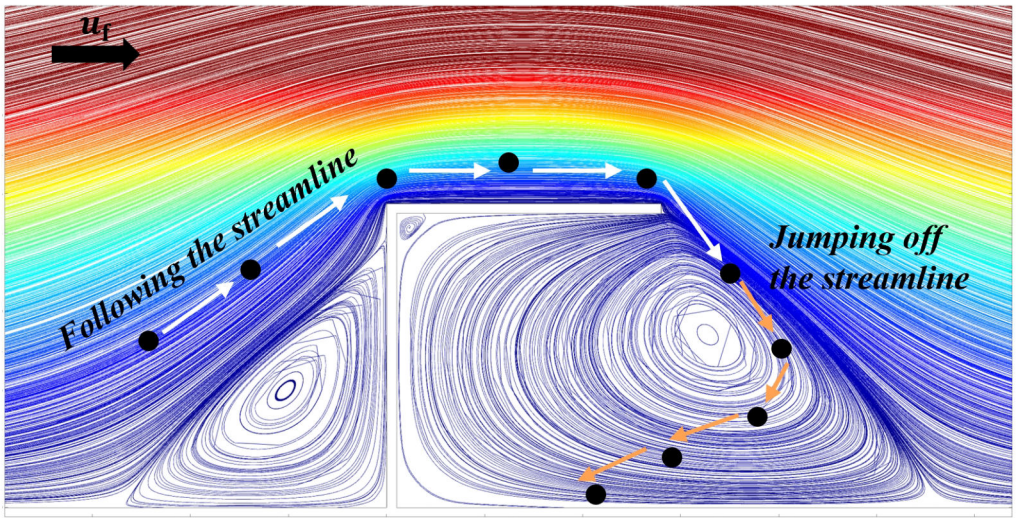


Figure 1.4: Exemplary eddy formation in the wake of a shelter obstacle, and an example of a particle trajectory becoming trapped in the rear eddy after jumping off the streamline.

obstacles, nor can they be forced into specific corners by surface topography alone. Instead, microparticles tend to reach flow-calmed regions through mechanisms such as diffusion or sedimentation, or they gradually deposit on flat surfaces in the wake of microstructures. This highlights the importance of understanding the underlying mechanisms in quiescent fluids, as deposition processes predominantly occur under such conditions.

1.3 Objective and scope of the thesis

COMSOL Multiphysics®'s Particle Tracing Module typically uses standard force models for rigid, non-deformable spheres, such as the Saffman lift force in shear flows. Forces that differ due to particle shape or deformation must be implemented via user-defined inputs in a Newtonian formulation of the particle equations of motion. Specifically for elastohydrodynamic lift forces, no general analytical expression exists for elastic particles at moderate wall distances. To date, most analytical solutions apply only in the lubrication limit - that is, at very small wall distances.

The aim of this project was therefore to determine and model elastohydrodynamic forces by performing experiments in which the kinematics of elastic particles near walls were optically recorded and analyzed. To simplify data acquisition and eliminate confounding microscale effects such as diffusion or electrostatics, the experiments were performed at a macroscopic scale using centimeter-sized elastic model particles. A highly viscous Newtonian fluid (silicone oil) was used to replicate the same low Reynolds number regime

encountered by microscopic particles in aqueous environments. Additionally, sedimentation was chosen as the mode of motion, *i.e.*, gravity alone initiated particle movement without the need of external mechanisms such as pumping. This approach helped to decompose individual force contributions. In shear flows over surfaces, sedimentation and shear-induced forces (*e.g.*, Saffman lift) act simultaneously. To specifically study wall-related interactions, it is therefore useful to eliminate shear-induced lateral force effects. In that case, only sedimentation-related forces - such as gravity, buoyancy, and wall-induced forces like Faxén´s lift (see Chapter 3) - must be computed and subtracted from the measured net force. Moreover, the sedimentation processes along vertical walls are relevant in systems of biological or neutrally buoyant particles, as illustrated in the previous simulations.

Even though it might be assumed that everything worth knowing about sedimentation has long since been covered in textbooks - take, for example, the outstanding compilation of particle phenomena in *Low Reynolds Number Hydrodynamics* by Happel and Brenner - it quickly becomes evident how much remains unknown even about the supposedly "simple" sedimentation of solid bodies. Over the course of this project, it became clear that in addition to elasticity, another characteristic of biological particles plays an even more decisive role in the dynamics of soft particles: the small density difference between the particle and the surrounding fluid. Biological particles are primarily composed of water or other liquids, meaning their density is nearly equal to that of the surrounding medium, *i.e.*, the density ratio is close to 1. When such particles sediment, forces come into play that are often neglected (or perhaps conveniently ignored) in the literature: inertial forces.

At this point, some readers might ask: *"Why inertial forces? We're dealing with creeping flow conditions and Reynolds numbers close to zero. Inertia doesn't matter there - surely we can use Stokes' equations to describe the motion..."*

Let us be clear: Sir George Gabriel Stokes' equations to describe fluid flow at small Reynolds numbers or the drag force on a sphere are by no means incorrect. However, they are only valid under the conditions on which they are based. These include the assumption of steady flow - no acceleration of either the surrounding fluid or the particle - and the absence of nearby boundaries (such as walls or other particles). And by "absence" we mean *absolutely* no walls anywhere near the particle. The real paradox of inertia in low Reynolds number flows (a paradox that Sir G.G. Stokes himself was aware of, by the way - not to be confused with the classical Stokes' paradox concerning flow over an infinitely long cylinder) becomes apparent in the creeping flow regime: the slower a particle moves, the *longer* it can "feel" a nearby wall - or, put differently, the *farther* a wall can be while still influencing the particle. This realization caused considerable confusion and frustration during the early phases of the project, as we initially lacked sensitivity to such effects. For instance, terms like *history forces* or *long-time persistent memory* were unfamiliar to me.

In much of the existing literature, the creeping flow regime is typically defined as encompassing Reynolds

numbers up to $Re = 0.1$. The widespread assumption seems to be that anything below this threshold is "completely linear and simple." This perspective likely stems from the increasing reliance on abstract mathematical models or numerical simulations in the field. Most studies halt at $Re = 0.1$, a point where there is just enough inertia for motion to be noticeable, yet still sufficiently low to justify neglecting the nonlinear inertial terms in the Navier-Stokes equations. Thus, $Re = 0.1$ is often treated as synonymous with the creeping flow regime.

Our initial lack of awareness regarding inertial effects in creeping flows is evident in the publication presented in Chapter 2 of this dissertation. In that study, the sedimentation dynamics of elastic, nonheavy spheres in the center of a rectangular duct were investigated. The kinematics of spheres with varying Young´s elastic modulus sedimenting in the center of a large tank with square cross-section filled with silicone oil were recorded and analyzed. It was was shown that rigid spheres sedimenting at $Re_P = O(10^{-1})$ in the center of the tank exhibit the expected behavior, and the results were deemed valid. However, as the spheres became softer (and the Reynolds number decreased slightly), the soft spheres accelerated more than rigid ones did. At the time, we attempted to explain the variations in kinematics and dynamics primarily through elasticity, as the most prominent difference among the spheres was their varying degrees of softness. Differences in density and Reynolds number appeared so minor that we did not expect them to influence the dynamics significantly over the relatively long time scales involved - although we did acknowledge the possibility of other contributing factors beyond elasticity. In retrospect, I would no longer attribute the effects so exclusively to elasticity. While elasticity certainly influences the sedimentation behavior of particles in the center of the container, the insights gained from the near-wall investigations in Chapter 3 support a broader interpretation.[1]

In Chapter 3, the sedimentation of spheres with varying Young's moduli and densities was investigated at various distances from both rigid and soft walls inside the rectangular duct. The peculiarities in the kinematics of both rigid and soft spheres sedimenting at $Re_P \approx O(10^{-2})$ near plane walls revealed that the primary cause of the observed instationarities is inertial forces, while elastic interactions introduce superimposed effects, such as additional nonlinearities in the particle kinematics.

In Chapter 4, the experimental setup was modeled using CFD simulations. These simulations provided detailed insights into the flow field inside the container during the sedimentation of spherical objects. The results showed that the commonly made assumption of a quiescent fluid in a confined geometry - such as a closed rectangular container - is not valid even at very low Reynolds numbers. Instead, large-scale vortical structures, or potential flows, develop within the container. These flow disturbances can significantly influence particle dynamics and may account for certain phenomena observed in the experiments that were previously attributed to inertial forces.

[1] Reading Chapter 3 may also change the reader's perspective on the results in Chapter 2. For example, today, I would likely interpret the diagram in Fig. 2.7 as showing a dependency not only on Poisson's ratio but also on the particle Reynolds number Re_P.

In Chapter 5, experiments were carried out with rods, in analogy to the sphere experiments in Chapter 3. The rods were released from rest in an axially aligned orientation at various distances from the wall. For rigid rods sedimenting at $Re_P = O(10^{-1})$, a semi-empirical equation for drag force and settling velocity was derived, which matched the experimental results well. Rods sedimenting at lower Reynolds numbers ($Re_P = O(10^{-2})$) exhibited instabilities and increasingly nonlinear behavior with increasing deformability. Through the use of specialized sorting and characterization methods, elastohydrodynamic features such as wall-induced, elastohydrodynamic drifting of rod-shaped particles near walls were identified.

Finally, the Conclusions compile the central findings of this dissertation. The significant differences in particle behavior near walls at $Re_P = O(10^{-1})$ versus $Re_P = O(10^{-2})$ are highlighted. This work contributes to a deeper and more nuanced understanding of sedimentation in the creeping flow regime and it illustrates how additional effects, such as elastohydrodynamic interactions, manifest in this context.

2 Dynamics of elastic, nonheavy spheres sedimenting in a rectangular duct

Contents

2.1 Abstract . . . 13
2.2 Introduction . . . 14
2.3 Theoretical background . . . 15
2.4 Methods . . . 18
2.4.1 Experimental setup . . . 18
2.4.2 Model particle fabrication . . . 19
2.4.3 Material properties . . . 20
2.5 Results and Discussion . . . 22
2.5.1 Velocity measurements . . . 22
2.5.2 Phase I and II: transient acceleration, rigid plateau and elastic time scale . . . 25
2.5.3 Phase III: second acceleration . . . 27
2.5.4 Phase IV: Second plateau - elastic terminal velocity . . . 28
2.5.5 Influencing factors and future directions . . . 31
2.6 Conclusion . . . 32
2.7 Chapter Appendix . . . 33

Chapter 2 presents an updated reprint of the following publication: Isabell Noichl and Clarissa Schönecker, Dynamics of elastic, nonheavy spheres sedimenting in a rectangular duct, *Soft Matter*, 2022, **18**, 2462, DOI: 10.1039/d1sm01789f.

2.1 Abstract

Understanding of sedimentation dynamics of particles in bounded fluids is of crucial importance for a wide variety of processes. While there is a profound knowledge base regarding the sedimentation of rigid solid particles, the fundamental principles of sedimentation dynamics of elastic spheres in bounded fluids are not

well understood. This especially applies to nonheavy spheres, whose density is close to that of the surrounding medium and which therefore show extended inertial effects upon acceleration. Here, we present model experiments of the sedimentation dynamics of deformable, nonheavy spheres in the presence of walls. Despite the deformations of the particles being small, the particle dynamics of elastic spheres differed fundamentally from that of rigid spheres. Initially, the sedimentation of elastic spheres is comparable with the sedimentation of rigid spheres. From a characteristic onset position of about $10R$, deformability effects kick in and a second acceleration appears. Finally, the deformable spheres reach a terminal sedimentation velocity. The softer the spheres are (in terms of Young's elastic modulus), the higher the terminal velocity is. In the present setup, a terminal velocity up to 9 % higher than the velocity for comparable rigid spheres was reached. By analyzing the obtained data, insights into the dynamics are given that could serve as basic approaches for modelling the dynamics of elastic spheres in bounded fluids.

2.2 Introduction

Solid sedimentation in liquids due to gravity is a widely used process in civil and environmental engineering. In a variety of applications, like in wastewater treatment or in food industry, sedimentation is used specifically as for example separation method. [3] In other applications, such as in the ink and paint industry, sedimentation of solid pigments is an undesirable effect that must be avoided. Profound knowledge and modelling of fluid-particle dynamics of sedimentation is therefore essential and it is the basis for the design of these processes. The calculation and design of such processes is mostly based on the assumption of spherical, heavy and rigid particles. However, both in nature and in applications, the assumption of rigid and heavy particles is often not valid. For example, microplastics or microgels, such as silicone particles, are in many cases soft and deformable. Further, biological particles cannot be treated as rigid and heavy particles since, for example, fungal capsules or cell membranes are deformable. [4] Wastewater treatment plants have been designed in the past mostly using rigid particle sedimentation for design calculations. But in the process, increasing amounts of microplastics enter the wastewater. Shape factors and empirical formulations are used to account for the sedimentation velocity of microplastics, which obviously differs from that of other heavier particles. [5] Furthermore, several polymers have a density in the range of that of water, *i.e.*, the density ratio is in the range of unity. These particles are called nonheavy particles. Studies show that a significant proportion of microplastics cannot be removed from wastewater in sewage treatment plants and end up in the environment. [6] The motion of biological particles such as bacteria or blood cells in flows is often described using, *e.g.*, challenging soft capsule models or, *e.g.*, flexible bond models in computational

fluid dynamics (CFD) - discrete Eement methods (DEM) simulations. [7],[8] It is assumed, that elastic solid beads could also serve as good models for biological particles. [9] Additionally, such soft particle models are of particular interest in the field of microfluidics, like transportation of soft particles through rectangular micro ducts. Here, however, not only the link between shape, material properties (deformability) and fluid dynamics plays a role, but also the influence of the surrounding walls. [10],[11],[12],[13]

While the literature regarding the dynamics of rigid particles is vast and consolidated, the research and knowledge regarding the dynamics of elastic particles is still incomplete in places and it remains of great interest to the scientific community. [9],[14] Even comparatively simple particle dynamics, such as the sedimentation of elastic spheres in an unbounded fluid, is only described in basic theory or is based on numerical calculations. [15],[16] Thereby, it is well known from related fields like liquid-liquid separation, for example in drop settling or bubble rise in fluids, that the deformation of dispersed particles has a significant influence on the particle dynamics. [17],[18] There are numerous studies, experimental as well as numerical and theoretical, which relate the dynamics under deformation to characteristic quantities like, *e.g.*, viscous forces, cohesion forces or hydrostatic pressure. [19],[20],[21],[22]

However, relationships between sedimentation velocity and elastic properties are still missing. Basic research is necessary at this point. Therefore, we perform sedimentation experiments, which allow insights into the dynamics of elastic solid spheres at low Reynolds numbers in a rectangular duct. Trajectories and resulting dynamics are recorded on a macroscopic scale. With the data obtained, both the transient and the steady-state sedimentation of deformable solid particles under wall influence can be quantitatively determined and related to the deformability.

2.3 Theoretical background

A rigid spherical particle with radius R,volume V_P and density ρ_P sediments due to gravitational acceleration $\mathbf{g}$ with velocity U_P in an unbounded fluid. The fluid density is ρ and the fluid dynamic viscosity η. Furthermore, the particle starts from rest at $t = 0$ s and, initially, the fluid velocity field around the particle is $|U_\mathbf{f}|= 0$ m·s^{-1}. In the stationary state the particle sediments in the Stokes regime with the particle Reynolds number $Re_\mathrm{P} = 2U_\mathrm{P}R\rho\eta^{-1} \ll 1$. The equation of motion of a nonheavy particle with a particle-to-fluid density ratio $\gamma = \rho_\mathrm{P}/\rho \rightarrow 1^+$ (quasi neutrally buoyant particles) can be described with the Basset-Boussinesq-Oseen (BBO) equation according to Basset, Boussinesq and Oseen. [23],[24],[25] The BBO equation results from the force balance around the particle with $F_\mathbf{I}+F_\mathbf{g}+ F_\mathbf{Buoyancy}+F_\mathbf{St}+F_\mathbf{AM}+F_\mathbf{B}= 0$ (see Fig. 2.1*(a)*). The differential equation for the particle velocity U_P in direction of the gravitational

acceleration reads as [17],[26]

$$\rho_P V_P \frac{\mathrm{d}U_P}{\mathrm{d}t} = (\rho_P - \rho) g V_P - 6\pi\eta R U_P - \frac{1}{2}\rho V_P \frac{\mathrm{d}U_P}{\mathrm{d}t} - 6R^2\sqrt{\rho\pi\eta}\int_0^t \frac{\dot{U}_P(\tau)}{\sqrt{t-\tau}}\,\mathrm{d}\tau. \tag{2.1}$$

The overdot denotes a time-derivate and τ is a dummy time variable for integration. The term on the left side of Eq. 2.1 is the inertial force F_I. The inertial force is equaled by the gravitational force F_g and the buoyancy $F_{Buoyancy}$. F_{St} denotes the drag force resulting from Stokes´s law. [27] The third term on the right is the added mass force F_{AM} which arises because the acceleration of the particle requires acceleration of the fluid surrounding it. The fourth term is the Basset history force F_B. The Basset history force includes past acceleration and represents the effect of the diffusion of vorticity around the sphere due the temporal delay in boundary layer development. [17],[28]

When a rigid particle starts sedimenting from rest, it first undergoes a transient phase until it reaches a stationary, terminal sedimentation velocity. The two acceleration forces F_{AM} and F_B lead to a more extended transient phase compared to heavy particles (see Fig. 2.1 *(b)*). In the steady state ($\frac{\mathrm{d}U_P}{\mathrm{d}t} = 0$), where the gravitational force and buoyancy balance the drag and the acceleration forces vanish, Eq. 2.1 results in the terminal Stokes velocity

$$U_{St} = \frac{2R^2\Delta\rho g}{9\eta}. \tag{2.2}$$

The previous equations are valid for particles sedimenting in an unbounded fluid. The influence of walls on the terminal velocity of a rigid sphere between parallel plane walls was first treated by Faxén. [29] A detailed overview of empirical equations and of mathematical methods for calculating the influence of walls on particle dynamics is given by Happel and Brenner. [2] In principle, the following statement can be made: if particles sediment in the presence of walls, drag exerted on the sphere is increased and thus the terminal velocity is reduced. While there are numerous empirical as well as theoretical approaches to calculate drag coefficient corrections for cylindrical pipes, drag corrections for confined spaces with plane walls are mostly based on computational studies. For example, in a computational study, Swan and Brady calculated the terminal velocity of a spherical particle sedimenting along a channel with two parallel walls in dependence of the wall distance. [30] Since they assume the space between the two walls as infinite, the real terminal velocity is estimated to be even lower. These effects would be expected in confined spaces like in a rectangular duct. Hensley and Papavassiliou performed CFD simulations to calculate the drag exerted on a sphere moving in the center of a square microduct with width W. [31] For a spherical particle that moves with $Re_P = 0.1$ in a square microduct they proposed a correction of the Stokes´s drag. Using their correction factor, the particle velocity in a rectangular duct reduces to

$$U_{P,corr} = \frac{1}{1 + 5\frac{R}{W}} U_{St}. \tag{2.3}$$

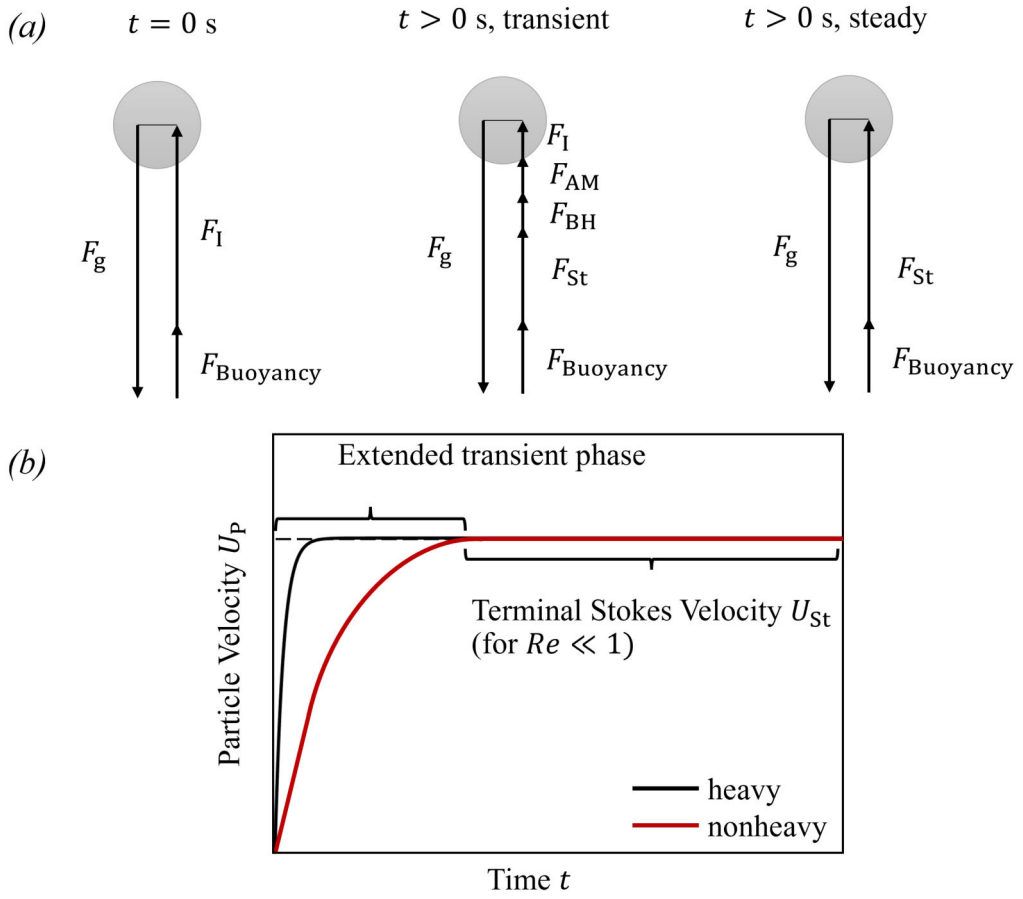


Figure 2.1: *(a)* Force balance around a spherical particle at different times during sedimentation; *(b)* Exemplary velocity curve of a sedimenting sphere with particle-to-fluid density ratio $\gamma \gg 1$ (heavy) and one with particle-to-fluid density $\gamma \rightarrow 1$ (nonheavy)

In contrast to rigid solid particles, there is little knowledge available with respect to deformable, elastic solid particles. In 1980, Murata derived an expression for the terminal sedimentation velocity of an elastic sphere in an unbounded fluid. According to Murata´s calculations, when a sphere sediments in the low Reynolds number regime with $Re_P \ll 1$, it deforms into a prolate spheroid in direction of the gravitational acceleration. [15] This deformation into a prolate spheroid would reduce the drag acting on the elastic body. Hence, the terminal sedimentation velocity increases. [2] By series expansion with the perturbation parameter α and in terms of specific constants K_0 and K_1, Murata derived the following expression for the terminal sedimentation velocity of an elastic sphere

$$U_{St,el} = \frac{2R^2\Delta\rho g}{9\eta}(1 + 2\alpha^2 K_0 + \frac{1}{5}\alpha^2 K_1) = U_{St}(1 + \Delta_{el,M}). \tag{2.4}$$

In this equation, the terminal velocity for rigid particles is extended by an elastic component of the terminal velocity $\Delta_{\mathrm{el,M}}$. The perturbation parameter α relates the viscous stresses to the elastic, mechanical stresses with $\alpha = U_{\mathrm{St}}\eta G^{-1}R^{-1} \ll 1$. α can therefore be interpreted as dimensionless elastocapillary number and, since it is much smaller than unity, small deformations are assumed. The elastic constants K_0 and K_1 are calculated from the solid material properties ($K_{0,1} = f(G, \lambda, \rho_{\mathrm{P}}, R, g)$). G and λ denote Lamé´s constants with $G = E[2(1+\nu)]^{-1}$ and $\lambda = E\nu[(1+\nu)(1-2\nu)]^{-1}$. E represents Young´s elastic modulus and ν the Poisson´s ratio of the elastic solid material.

To the best of our knowledge, the theoretically derived velocity from Eq. 2.4 has not yet been verified by experimental data. Furthermore, it is not known whether the equation, or the increase in sedimentation velocity respectively, is analogous in the case of sedimentation in a bounded fluid. It is not yet known whether walls as in a rectangular duct have an additional influence not captured by Murata´s calculations.

In the following, we hence investigate the sedimentation of elastic spheres under small deformation and in a bounded fluid domain.

2.4 Methods

2.4.1 Experimental setup

Sedimentation of rigid and elastic model particles was performed in a rectangular duct. As a vessel for the experiments, a glass container of 140 mm x 140 mm x 500 mm (W x D x H) was used, see Fig 2.2.

The container was filled up to a height of around 450 mm with silicone oil which is a Newtonian fluid. The silicone oil had a nominal viscosity of 1000 cSt. The choice of the model particle size together with the choice of a high viscosity liquid ensured that Re_{P} is always much smaller than 1. This condition allowed to investigate the same conditions as small, elastic microparticles would experience in aqueous liquids. The spheres were hold with a pipette under weak vacuum and then immersed in the liquid. The wall distance of the sphere center to all sides was about $d \approx 11R$. (see Fig. 2.2 *(b)*). After immersion, the vacuum was released. The sphere began to fall without rotation due to gravity. This ensured that the spheres began to sediment at an initial velocity of $U_{\mathrm{P}} = 0\ \mathrm{m{\cdot}s^{-1}}$ (starting from rest). High-resolution videos of the sedimentation experiments were recorded by a DSLR camera (Nikon® D7200 with Sigma® 50 mm f1.4 objective lens). Subsequently, the velocities were evaluated with a self-programmed image processing tool in MATLAB. The tool tracked the centroid of the recorded pixel disc in each image extracted from the video at fixed timesteps and calculated the velocity. During the experiments, the container with silicone oil was illumi-

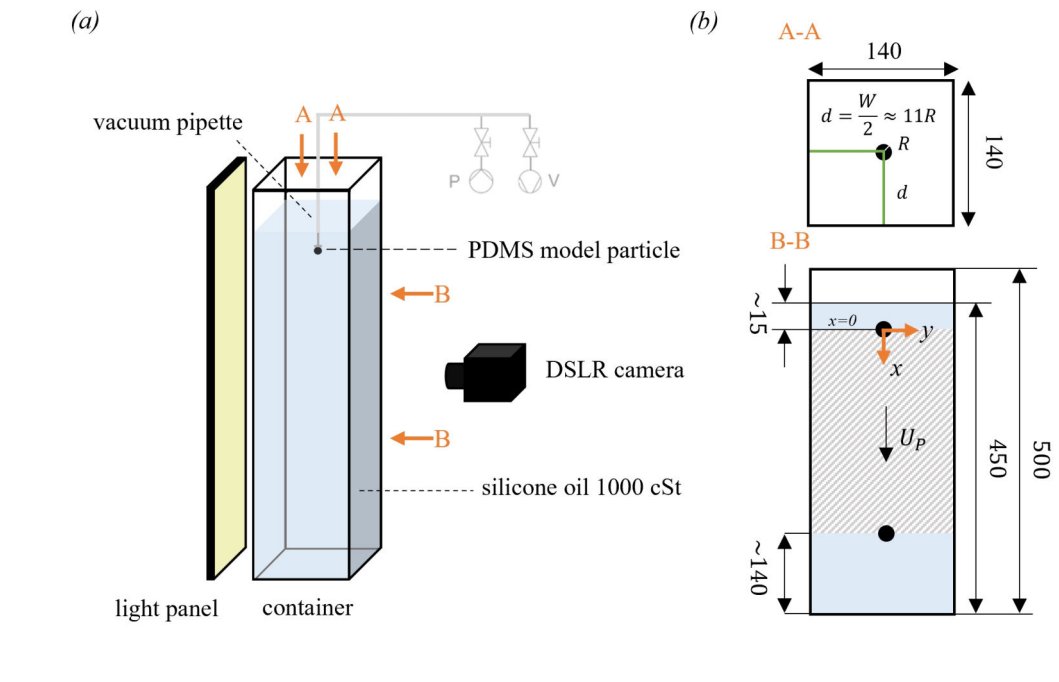


Figure 2.2: *(a)* Schematic experimental setup: spherical particles sediment in a rectangular container with square base in silicone oil with a nominal viscosity of 1000 cSt. The particles were immersed hanging on a vacuum pipette. By flooding the pipette with air, the spheres were released; *(b)* Dimensions (in mm) and coordinates: (A-A) top view and (B-B) view from optical axis. The particles were placed in the center of the container so that the wall distance to all walls is $d \approx 11R$. In the standard experiments the spheres were immersed around 15 mm deep. The origin of coordinates which is used in the evaluation lies in the center of the sphere after it was completely detached from the pipette. Dashed area: measurement range

nated from the opposite side of the camera by a collimated light panel. This ensured a straight projection of the model particle recorded by the camera sensor and allowed for the assumption, that the recorded centroid of the disc corresponds to the center of mass of the sphere.

2.4.2 Model particle fabrication

Elastic model particles were fabricated from polydimethylsiloxane (PDMS) by casting. To vary Young´s modulus of the particles, mixtures of two PDMS types were prepared in different mixing ratios. The fabrication procedure was based on the report by Palchesko *et al.* [32] First, base blends of commercially available PDMS elastomer Sylgard™ 184 (Dow Corning®) and PDMS Dielectric Gel Sylgard™ 527 (Dow Corning®) were prepared according to the manufacturer's specifications. The recommended mixing ratios (Sylgard 184 silicone oil: curing agent in a 10:1 ratio; Sylgard 527 part A: part B in a 1:1 ratio) were used. Each base blend was colored black with 1 w-% iron oxide powder. The production of base blends in the recommended mixing ratio ensured that complete cross-linking could take place for both components. This is

of crucial importance for the mechanical stability of the mixture of both PDMS types. Each base blend was degassed. Hereafter, the base blends were mixed with each other in a 1:1 ratio and a 1:5 ratio, respectively. Pure Sylgard 184, respectively the again degassed mixtures of Sylgard 184 and Sylgard 527, were poured into a mould for hemispheres. The hemisphere moulds had a diameter of 12 mm. The casted hemispheres were hardened for 12 h at 60 °C. For at least another 36 h, they were cured at room temperature. Two hemispheres were bonded together with a thin film of the corresponding newly produced PDMS compound avoiding ridges and asymmetries. The bonded spheres were cured for at least another 48 h at room temperature. The shape deviation of the bonded hemispheres compared to a perfect sphere with radius R was evaluated prior to the experiments with high-resolution images. For all experiments it was shown that the measured area corresponds well to the calculated area of a disc with radius R resulting from circle fitting. Hence, shape factors of the model particles do not differ notably from a value of 1.

In the standard case, experiments were performed with the spheres in the dry state after fabrication. For comparison, spheres that had remained in silicone oil after the first experiment showed slight swelling effects. It was observed that size, weight and consequently the density of the sphere changed over time. This suggests that the spheres swell by diffusion of the silicone oil into the elastomer-gel matrix. However, a significant change in the material properties was only observed after the spheres had been immersed in the oil for at least two days. Consequently, swelling effects are not to be expected during the short period of the experiment. A defined initial state could be ensured for the experiments.

To compare soft PDMS spheres with rigid spheres whose density is in a range comparable to that of PDMS, spheres made of epoxy resin were fabricated. Blends of Casting Resin MS 1000 by Weicon® were mixed according to the manufacturer´s recommendations and colored black with 1 w-% iron oxide powder. The same hemisphere moulds as for the soft spheres were used to cast the hemispheres. The hemispheres were hardened according to the manufacturer´s recommendation. The following steps were analogous to the fabrication of the soft spheres.

2.4.3 Material properties

The solid density of the spheres was determined directly after the sedimentation experiments. This ensured to be able to correctly represent the current state of the density. The solid density was determined using a hydrostatic balance (Sartorius® ENTRIS BCE 224i-1s analytical balance + density determination kit YDK03 for determination of solid and liquid densities). The balance has a readability of 0.1 mg. Density measurements were performed in distilled water. The density of silicone oil was also determined hydrostatically at room temperature. The corresponding material data for the solid and liquid density can be found in Tab.

2.1. The dynamic viscosity η of the silicone oil under experimental conditions was measured to be about 980 mPa·s using a rotational viscometer (IKA® Rotavisc lo-vi).

The elastic material properties were determined experimentally by means of compression tests. Cylindrical specimens of the PDMS mixtures also used in the model experiments were fabricated. The compression tests were in accordance with DIN ISO 7743:2016-08. [33] A Schenk Trebel RSA25 universal testing machine with a piezoelectric load cell and potentiometric displacement sensor was used to record the force-displacement measurement data in a displacement-controlled test ($v_{\Delta l}$ = 10 mm·min^{-1}), see Fig. 2.8 in the chapter appendix. To avoid friction effects, silicone oil with a viscosity of 1000 cSt was used as lubricant. The Young's elastic modulus of each specimen was determined from the slope of the compressive stress-strain curve in the linear-elastic range of small deformations. The experimentally determined averaged Young's moduli are shown in Tab. 2.1.

Table 2.1: Measured material properties

Material properties			
Liquid density	ρ	971.28 ± 0.134	kg· m^{-3}
Liquid dynamic viscosity	η	0.9797 ± 0.012	Pa· s
Solid densities			
Epoxy resin	ρ_{Epoxy}	1159.21 ± 1.17	kg· m^{-3}
Sylgard 184	ρ_{Syl184}	1040.01 ± 1.90	kg· m^{-3}
Sylgard 184:527 1:1	ρ_{Mix11}	1004.75 ± 1.32	kg· m^{-3}
Sylgard 184:527 1:5	ρ_{Mix15}	987.59 ± 1.9	kg· m^{-3}
Young´s moduli			
Epoxy resin	E_{Epoxy}	2.9[1)]	GPa
Sylgard 184	E_{Syl184}	1712 ± 82.55	kPa
Sylgard 184:527 1:1	E_{Mix11}	936 ± 33.44	kPa
Sylgard 184:527 1:5	E_{Mix15}	135 ± 13.14	kPa

[1)] According to manufacturer information.

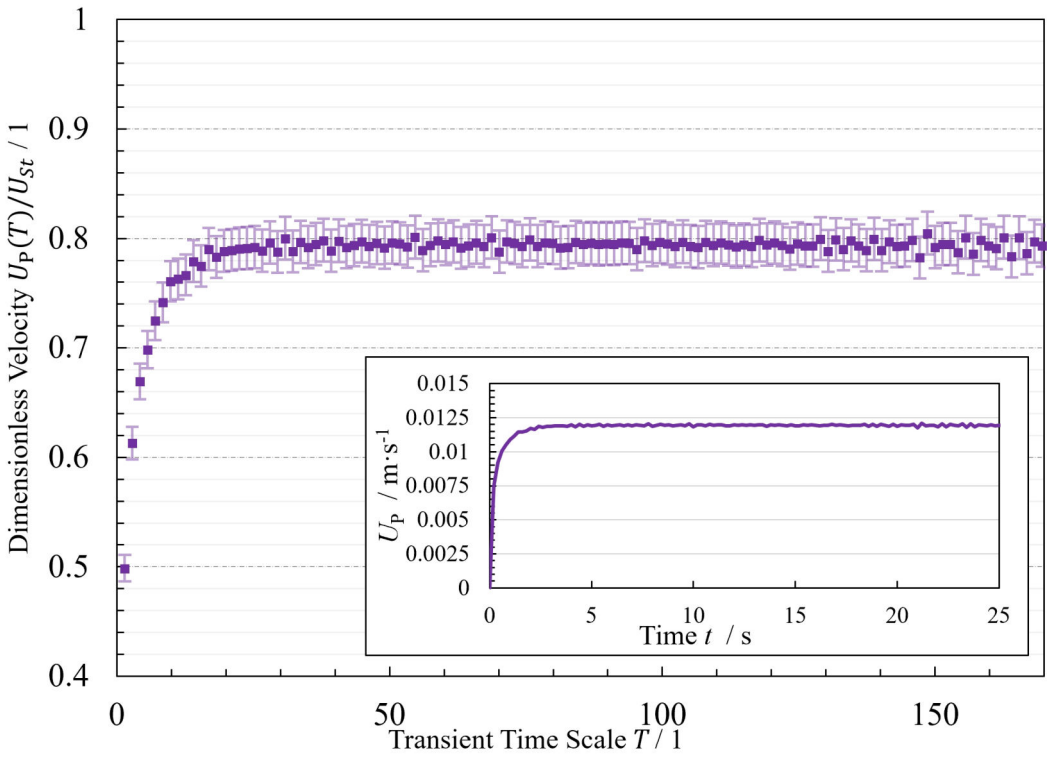


Figure 2.3: Dimensionless velocity plotted over the transient time scale of a sphere which starts sedimentation from rest. The sphere was made of epoxy resin with $E_■ = 2.9$ GPa, $\rho_{P,■} = 1159.21 \pm 1.17$ kg· m^{-3}, $R_■ = 6 \cdot 10^{-3}$ m, $Re_{P,■} = 0.179$, $\gamma_■ = 1.19$; Insert: absolute values of the measured particle velocity plotted over time.

2.5 Results and Discussion

2.5.1 Velocity measurements

2.5.1.1 Reference: rigid spheres

Results for the velocity measurements of the nonheavy rigid spheres made of epoxy resin show typical velocity curves for rigid particles under wall influence, see Fig. 2.3. As expected, sedimentation shows two phases. After the initial, transient phase the rigid spheres reach the terminal velocity, the second phase of sedimentation dynamics.

The results are presented as absolute $U_P - t$ diagram and in a dimensionless representation. As will be shown, the experiments with varying elasticity are not directly comparable on the dimensional time scale. The difference in density between materials and the mixtures lead to much faster sedimentation for the rigid

spheres compared to the elastic spheres. Anyway, the dimensional quantities are shown for the sake of completeness.

The nondimensionalization of the velocity is performed by U_{St} from Eq. 2.2 as characteristic scale. The dimensionless velocity is plotted over the time scale resulting from the viscous diffusion time. This dimensionless time is also known as transient time scale T. [34]

$$T = \frac{\eta t}{4\rho R^2} \tag{2.5}$$

The measured terminal velocity of the rigid sphere is $U_{P,term,\blacksquare} = 11.9$ mm·s^{-1}. The terminal Stokes velocity resulting from the measured material properties after Eq. 2.2 is $U_{St,\blacksquare} = 15.0 \pm 0.4$ mm·s^{-1}. Hence, the measured terminal velocity in the experiment is reduced to about 80 % of the velocity in an unbounded fluid. This is due to wall effects stemming from the four container walls, even though the particle sediments more than 11 times its radius away from the walls. This reduction is in accordance with existing literature data based on calculations. For example, according to Swan and Brady´s numerical calculations, a particle would reach a terminal velocity of approximately 85-90 % of the Stokes velocity when the sphere sediments at a distance of $d \approx 11R$ between two infinite walls. [30] Since in their calculations just two parallel walls were assumed, a reduction to a value in the measured range of our experiments with four walls is realistic. Specifically with respect to four walls, a good agreement of the experimental values is obtained with Eq. 2.3 stemming from the increase in drag. With the correction factor found by Hensley and Papavassiliou in CFD simulations, a dimensionless velocity of $U_{P,corr}/U_{St} = 0.82$ is expected for the width of the container of 140 mm and a radius of 6 mm. [31]

Because the investigated particles classify as nonheavy, the transient phase is more extended than it would be the case for the sedimentation of particles with high particle-to-fluid-density ratio $\gamma \gg 1$. Solving the differential equation Eq. 2.1 with respect to U_P neglecting the Basset history force, the theoretical terminal velocity for the epoxy resin spheres would be reached after about 0.1 seconds. In contrast, the experimental determined terminal velocity is reached after a time of about 3 seconds during the sphere sediments about 30 mm $\approx 5R$. Correspondingly, in the present case, initial effects like the added mass force and the Basset history force must be considered to describe the complete sedimentation dynamics adequately.

2.5.1.2 Elastic, deformable spheres

Velocity curves of elastic, deformable spheres significantly differ from those of the rigid spheres. Elasticity affects both the dynamic evolution of sedimentation as well as the terminal sedimentation velocity. This effect is the stronger the lower the Young´s modulus E becomes, see Fig. 2.4 *(a)-(c)*.

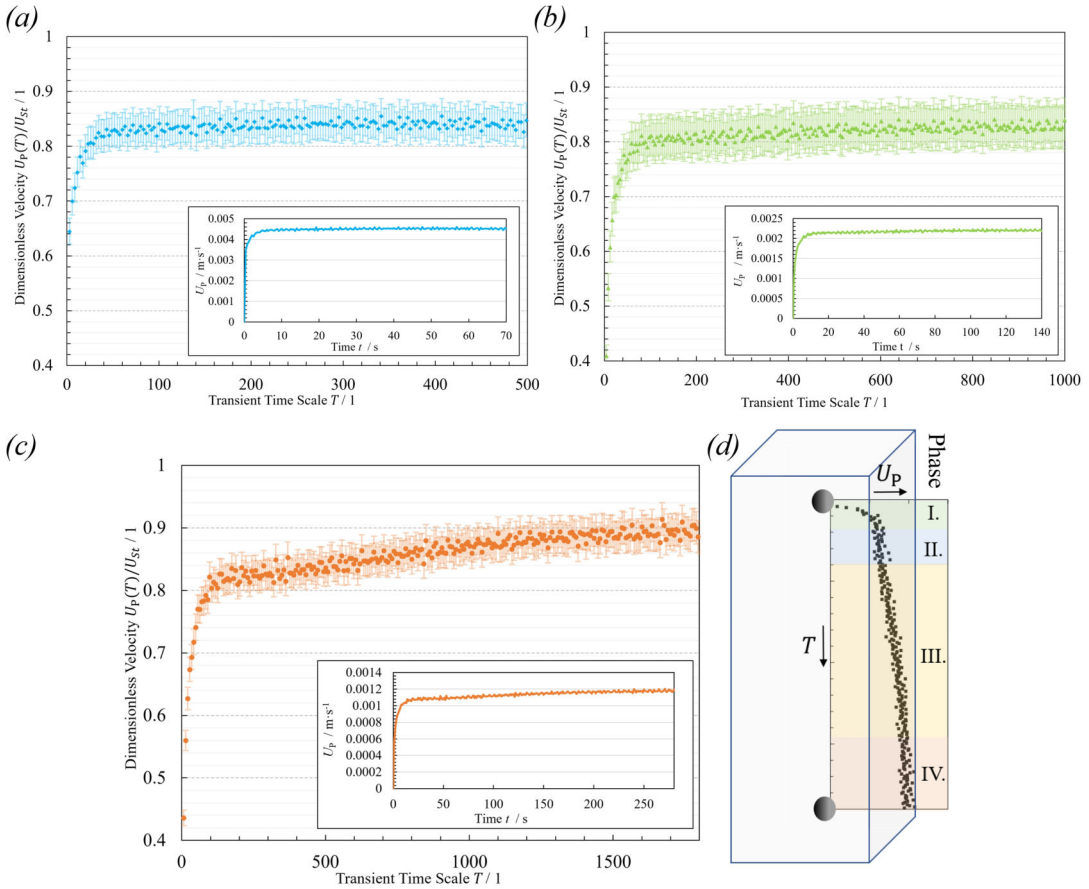


Figure 2.4: Dimensionless velocity plotted over the transient time scale of a sphere which starts sedimentation from rest made of *(a)* Sylgard 184 with $E_\blacklozenge = 1712 \pm 82.55$ kPa, $\rho_{P,\blacklozenge} = 1040.01 \pm 1.9$ kg·m^{-3}, $R_\blacklozenge = 0.00593$ m, $Re_{P,\blacklozenge} = 0.061$, $\gamma_\blacklozenge = 1.07$; *(b)* Sylgard 184 : Sylgard 527 in a 1:1 mixing ratio with $E_\blacktriangle = 936 \pm 33.44$ kPa, $\rho_{P,\blacktriangle} = 1004.75 \pm 1.32$ kg·m^{-3}, $R_\blacktriangle = 0.00598$ m, $Re_{P,\blacktriangle} = 0.032$, $\gamma_\blacktriangle = 1.03$; *(c)* Sylgard 184 : Sylgard 527 in a 1:5 mixing ratio with $E_\bullet = 135 \pm 13.14$ kPa, $\rho_{P,\bullet} = 987.59 \pm 1.9$ kg·m^{-3}, $R_\bullet = 0.006$ m, $Re_{P,\bullet} = 0.016$, $\gamma_\bullet = 1.02$; Inserts *(a)-(c)*: absolute values of the measured particle velocities plotted over time; *(d)* schematic of elastic particle sedimentation showing the four phases of sedimentation

While the differences in the sedimentation of rigid and elastic spheres are not yet obvious at first glance for the PDMS spheres with the highest Young´s modulus of $E_{SYL184} = 1712$ kPa (Fig. 2.4 *(a)*), a reduction of the Young's modulus by about half ($E_{MIX11} = 936$ kPa, Fig. 2.4 *(b)*) already leads to a clearer visibility of the differences. The additional influence of elasticity is most evident with the lowest Young´s modulus of $E_{MIX15} = 135 \pm 13.14$ kPa (Fig. 2.4 *(c)*). It is evident that the sphere's increase in velocity is not uniform but happens in several stages. For the softest sphere, no clear steady-state condition was established within the measuring range. Based on the last measured values from $T \approx 1800$ ($t \approx 260$ s), a terminal velocity of $\bar{U}_{P,term,\bullet} \approx 1.2$ mm·s^{-1} can be estimated. These values exceed the actual measuring range (*cf.* Fig. 2.2 *(b)*). The measuring range was selected in such a way that there is at least 140 mm (same as width and depth of the container) of space to the ground to exclude ground effects such as deceleration of the sphere. Values below the measuring range were nevertheless recorded by the camera and were considered in this case. All

measured averaged terminal velocities and calculated Stokes's terminal velocities can be found in Tab. 2.2. In the following, we divide the sedimentation of the elastic spheres in four phases (Fig. 2.4 *(d)*). The phases

Table 2.2: Velocity measurements

E/kPa	$\bar{U}_{\mathrm{P,term}}$/mm·s^{-1}	U_{St}/mm·s^{-1}
1712 ± 82.55	4.5 ± 0.0	5.4 ± 0.2
936 ± 33.44	2.2 ± 0.0	2.7 ± 0.1
135 ± 13.14	1.2 ± 0.0	1.3 ± 0.04

are: I. the transient acceleration and II. the first plateau. The dimensionless velocity on the first plateau is comparable with the dimensionless velocity of the rigid spheres as will be discussed in chapter 3.5.2. The rigid plateau is followed by phase III, the second acceleration. Ultimately, the elastic spheres reach phase IV, a second plateau on which the elastic spheres reach their terminal sedimentation velocity. The principles and distinguishing features of the individual phases will be discussed in detail below.

The error bars shown in Fig. 2.3 and Fig. 2.4 were calculated by means of systematic and statistical measurement errors. Systematic errors in our measurements include, for example, measurement inaccuracies of the measuring instruments or errors when scaling the data from image velocimetry (pixels to real length units). Statistical measurement errors include the deviations within multiple measurements of a measured quantity. Here, the error analysis was carried out just for the terminal Stokes velocity. The representation of the uncertainty for the time scale T was omitted at this point for the sake of clarity.

Furthermore, only single experiments are presented in the figures. Experiments were performed with different specimens fabricated from each material and at least two measurements were performed for each specimen. Only experiments in which the sphere sedimented without rotation were considered. It was shown that the experiments are consistent and reproducible in terms of quality and quantity within the scope of the deviations described above.

It should also be noted that the starting point for velocity measurement is the first image where the sphere is completely detached from the vacuum pipette. This inevitably leads to the fact that the time $T = 0$ may differ between the individual experiments (depending on the time step size selected for the evaluation).

2.5.2 Phase I & II: transient acceleration, rigid plateau and elastic time scale

When the dynamics of rigid and elastic spheres are compared, similarities arise during the initial phases. First, all soft model particles presumably reach a first plateau (II) after a first, transient acceleration phase

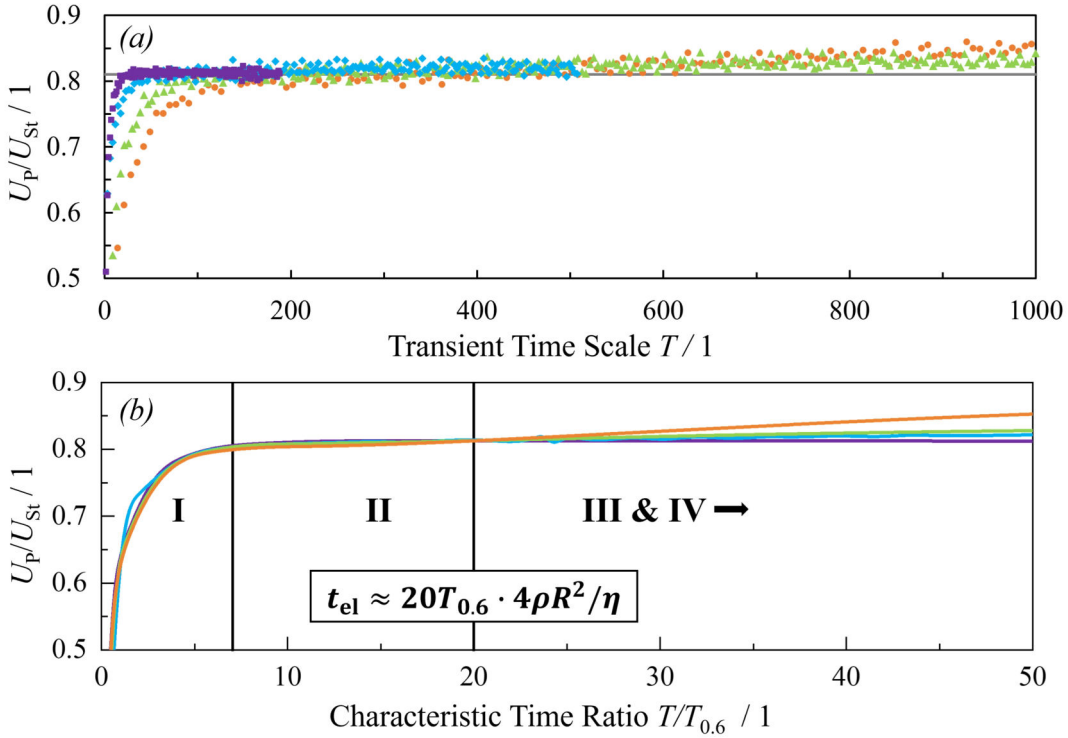


Figure 2.5: *(a)* Dimensionless velocities of the experiments from Fig. 2.3 and 2.4 (■ epoxy resin, ♦ Sylgard 184, ▲ Mix 1:1, ● Mix 1:5) fitted to a value of 0.81 at the first plateau and plotted against the transient time scale; *(b)* Interpolated dimensionless velocities of the experiments from Fig. 2.3 and 2.4 (— epoxy resin, — Sylgard 184, — Mix 1:1, — Mix 1:5) adjusted to a value of 0.81 at the first plateau and plotted against the characteristic time ratio $T/T_{0.6}$. The interpolation was performed with cubic B-splines for the sake of clarity of the representation.

(I). This plateau lies at a value between ≈ 0.8 and ≈ 0.83 considering the mean value of the dimensionless velocity in this range. This velocity is just the same as the terminal velocity of the rigid spheres within the uncertainty of the measurements. It is hence reasonable to assume that all particles – both rigid and soft – initially reach the same reduced stationary state, which is only due to the wall influence.

However, the velocity-time behavior of the different spheres is not directly comparable to each other due to the different density ratios following from the individual mixing ratios (Tab. 2.1) needed to fabricate spheres of varying elasticity. Consequently, inertial influences are different for each type of sphere, see the different slopes of the velocity curves for different elasticities at low times in Fig.2.5 *(a)*. For a better overview, we slightly shifted all curves within the measurement uncertainty to a reference value of 0.81 within the second phase. To make the experimental data of all experiments comparable on the time scale, the time delay of the increase due to inertia must be eliminated. One way to do this is reported by R.B. Moorman in 1955 in his dissertation. [35]

If the transient range is resolved, an inflection point of the velocity-time curve appears. This point marks the time from which the frictional forces become more significant and ultimately more dominant than the

inertial forces in the transient range. Experimentally Moorman determined this inflection point to be located at about 60 % of the terminal velocity, *i.e.*, $U_P/U_{St} \approx 0.6$ at the corresponding time $T_{0.6}$. R.B. Moorman could map similar curves from the sedimentation of rigid spheres on a universal curve upon scaling T with $T_{0.6}$. [34] Following the same procedure, also the sedimentation velocities for elastic spheres fall on top of each other within the first two phases (Fig. 2.5 *(b)*).

Attaining this universal curve supports the assumption that at the beginning of the sedimentation, elastic spheres follow the same principles as rigid spheres: inertial and frictional forces determine the transient acceleration until a steady state is reached. For the investigated spheres, any elastic effects obviously kick in at a time scale that is larger than the time scale for establishing this first plateau.

In the experiments, after reaching the first plateau, all curves of the elastic spheres start to rise again from a characteristic time ratio of $T/T_{0.6} \approx 20$ (see Fig. 2.5 *(b)*). This allows an estimation and calculation of a time t_{el} with

$$t_{el} = \frac{20 T_{0.6} \cdot \rho R^2}{\eta} \tag{2.6}$$

From this time on, an elastic effect leads to a significant change in the particle dynamics and to an increase in the sedimentation velocity due to elasticity. Furthermore, t_{el} marks the end of the second sedimentation phase.

It should be mentioned that the normalization after Moorman in Fig. 2.5 was performed with respect to the sedimentation velocity in an unbounded fluid ($U_P/U_{St} \approx 0.6$). It remains to be clarified whether in the case of wall influence and consequently lower velocities, the inflection point shifts accordingly, here to a point for T at $U_P/U_{St} \approx 0.6 * 0.81$. Experimentally, the consequences for $T_{0.6}$ are not large due to the steep increase in velocity. An experimental investigation of this inflection point would however require a large temporal resolution of the transient phase and is a potential field for further investigations. In the present case, the chosen approach is viable insofar as a mapping of the curves on top of each other could be established.

2.5.3 Phase III: second acceleration

As described above, a second, elastic acceleration starts about the characteristic time t_{el}. Alternatively, the sedimentation velocity can be considered as a function of position in the direction of gravitational acceleration (Fig. 2.6).

All elastic spheres sediment with a velocity comparable to the rigid sphere´s velocity until the position $x_{el} \approx 10 \cdot R$ is reached. At this characteristic elastic onset position, the second acceleration begins. The

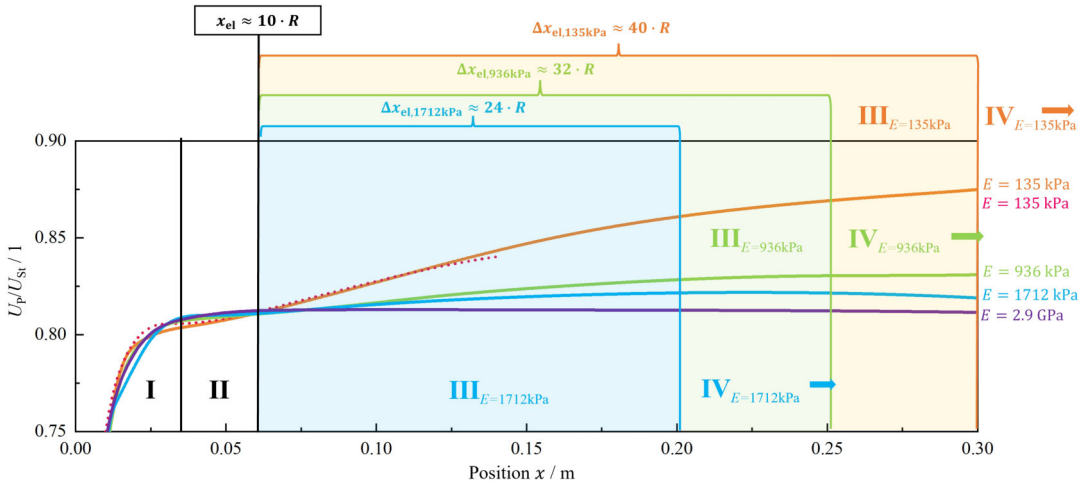


Figure 2.6: Interpolated dimensionless velocities of the experiments from Fig. 2.3 and 2.4 (— epoxy resin, — Sylgard 184, — Mix 1:1, — Mix 1:5, · · · · Mix 1:5 deep immersed) fitted to a value of 0.81 at the first plateau and plotted against the position x within the measuring range ($x < 0.3$ m) – rigid sedimentation behavior is found until position $x_{el} \approx 10 \cdot R$ is reached.

extension of the second acceleration, *i.e.*, the distance Δx_{el} between the characteristic onset x_{el} and the second plateau with the final velocity $\bar{U}_{P,term}$, depends on the elasticity of the sphere. The more deformable ($E \downarrow$) the sphere is, the longer is the distance Δx_{el} until the stationary state is reached. For the present data, the length of the second acceleration phase due to elasticity can be approximately described in terms of the sphere radius R as function of the Young´s Modulus E (in Pa)

$$\frac{\Delta x_{el}}{R} \approx \frac{E}{10^5 \text{Pa}} + 41 \tag{2.7}$$

As already described in section 2.5.1.2, the sphere with the lowest Young´s modulus only reached the terminal velocity at the last measured values that are not part of the measuring range ($x < 0.3$ m). For this reason, the second plateau of the softest sphere is not visible in Fig. 2.6. It is possible that the second acceleration phase has not yet been fully completed by this sphere.

2.5.4 Phase IV: Second plateau - elastic terminal velocity

After the second acceleration discussed in the section before, the fourth phase of sedimentation of elastic spheres starts. In this final phase, the elastic spheres reach the terminal sedimentation velocity. The more deformable the spheres are, the faster are the spheres and the higher is the measured increase in velocity relative to the first plateau (see Fig. 2.6). The measured relative increase to the rigid sedimentation velocity $\Delta x_{el,exp}$ reaches up to nearly 9% for the softest spheres (exact values see Tab. 2.3). To our knowledge, no

equation exists describing the increase in velocity of elastic spheres in a bounded fluid. There is merely the expression proposed by Murata for sedimentation in an unbounded fluid (Eq. 2.4). It predicts an increase to the terminal Stokes velocity of $\Delta x_{\mathrm{el,M}}$. [15] Hence, the increase in sedimentation velocity obtained experimentally is not directly comparable to the sedimentation velocity for elastic spheres proposed by Murata in Eq. 2.4. However, a comparison of Murata´s predicted increase and the experimentally obtained increase can be used to shed light on possible additional wall influences on the increase in velocity. In general, the terminal velocity of an elastic sphere can be thought to be influenced by the sphere's shape that evolves according to its elasticity.

A deformation may already occur in an unbounded fluid. Furthermore, additional wall-related forces may occur. It is known that bodies moving close to an elastic wall are subjected to an additional elastic lift force away from the wall as well as to an altered drag force. [36],[37] Similar forces might also occur during sedimentation of soft bodies in a bounded fluid.

The increase according to Murata $\Delta x_{\mathrm{el,M}}$ can be determined using known material parameters. No exact measured values for the Poisson´s ratio of the PDMS mixtures are available. Therefore, the increase according to Murata was calculated for various Poisson´s ratios. Based on measurements for pure Sylgard 184, it is assumed that the Poisson's ratio of all mixtures has a value between $\nu = 0.490$ and $\nu = 0.499$. [38] The percentage increase from the experimental data is calculated from the mean values of the velocities of the first plateau and the second plateau.

Comparing the calculated increase according to Murata´s equation to the measured increase in the experiments, shows that the values fundamentally differ in the order of magnitude, but slightly correlate in the prefactor (see Tab. 2.3). The measured increase in velocity relative to the first plateau is up to a factor 10^{10} higher than the percentage increase predicted by Murata. In total, the increase according to Murata $\Delta x_{\mathrm{el,M}}$ in an unbounded fluid is almost negligible for Poisson´s ratios in the previously mentioned range. In contrast, the measured increase of nearly 9% is not negligible, particularly with regard to applications. Exemplarily, Tab. 2.3 shows the percentage increases $\Delta x_{\mathrm{el,M}}$ for a Poisson's ratio of 0.491 assumed for all PDMS mixtures.

Although the values of Δx_{el} do not fit to each other at the first glance, a closer look on the measured increase compared to the predicted increase shows that they just seem to differ by a factor α^{-2} and some constant $C(\nu)$ which depends on the Poisson´s ratio (see Fig. 2.7).

Calculation of the specific constants K_0 and K_1 from Murata's equation suggests that the sphere deforms into a prolate ellipsoid while sedimentation. Yet, this deformation is small, since the perturbation parameter α (viscous stresses vs. mechanical stresses) $\ll 1$. In order to evaluate deformation during the experiments, the isoperimetric quotient was determined for each timestep. It is defined as $(4 \cdot Area \cdot \pi)/Perimeter^2$ and gives the ratio of the measured area to the area of a disc with the same perimeter as the perimeter measured

Table 2.3: Experimental values of $\Delta x_{\mathrm{el,exp}}$ and theoretical values of $\Delta x_{\mathrm{el,M}}$ calculated with a Poisson´s ratio of $\nu = 0.491$

E/kPa	$\Delta x_{\mathrm{el,exp}}$/%	$\Delta x_{\mathrm{el,M}}$/%	$0.025 \cdot \Delta x_{\mathrm{el,M}} \cdot \alpha^{-2}$/%
1712	1.39	$1.24 \cdot 10^{-10}$	1.30
936	2.71	$2.60 \cdot 10^{-10}$	3.37
135	8.96	$17.65 \cdot 10^{-9}$	8.64

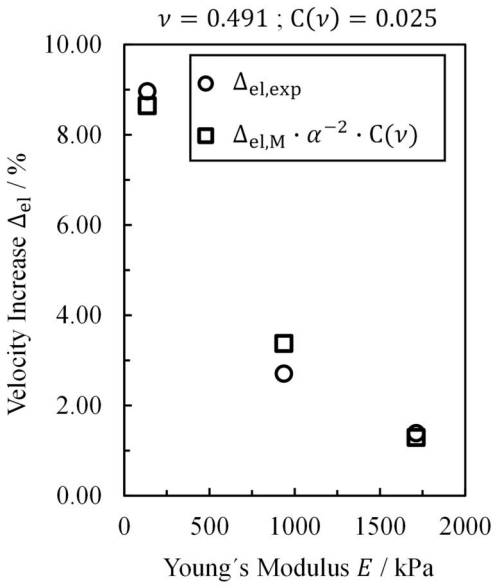


Figure 2.7: Experimental determined and by factor $\alpha^{-2} \cdot C(\nu)$ fitted values of the velocity increase to the rigid velocity plotted against the Young´s modulus E

for the particles. Large deformation of the particle would lead to a change in the isoperimetric quotient over time. In our experiments, this ratio was found to be constant over time for all experiments. Consistently, no apparent deformation could be detected with the optical resolution of our measurement method, where also $\alpha \ll 1$.

Also, elastohydrodynamic lubrication theories, which predict wall lift and drag forces, typically consider small surface deformations that are not easily observable. At the same time, the effect of such wall-related forces is macroscopically significant. From the comparison of Murata's calculation in an unbounded fluid and the experiments in a bounded fluid, it is hence likely that wall-related forces influence the terminal velocity. After all, if lift-forces existed on the particle, they could pinch together the particle from all four sides.

2.5.5 Influencing factors and future directions

In order to further investigate the effect of walls on the terminal sedimentation velocity, more experiments are needed especially with varying radius to container size ratios. Experiments already show that this would require either very large container dimensions or the development of a specialized particle release mechanism. Experiments with spheres of $R \approx 4$ mm made from the 1:5 mixture of Sylgard 184 and Sylgard 527 showed that such small spheres are not heavy enough to overcome adhesion to the pipette on their own. Pushing the spheres however leads to completely different initial conditions and hence sedimentation dynamics.

In addition, particle image velocimetry (PIV) experiments or CFD simulations might help to shed light on the hydrodynamic mechanisms under wall influence by visualizing the fluid streamlines. The plane container walls and the four corners of the container could lead to an altered flow profile around the sphere compared to the axisymmetric profile assumed for unbounded sedimentation in the Stokes flow regime. In the case of elastic spheres, these asymmetries in the hydrodynamics could cause elastohydrodynamic lift forces and the pinch already mentioned in chapter 2.5.4. Furthermore, coupled Fluid - Structural mechanics - Interaction (FSI) simulations might help to investigate and to understand these elastohydrodynamic interactions. Such FSI simulations could also shed light on the magnitude of deformation caused by the hydrodynamic forces which could not be resolved with the optics used in the experiments.

Also, the pressure in the system might play a role since it could in principle deform the particles. To check any possible influence of hydrostatic pressure on the elastohydrodynamic acceleration, experiments with a larger immersion depth were performed (red dotted curve in Fig. 2.6). The same sphere as considered in section 2.5.1.2 that has a Young´s modulus of 135 kPa was immersed about 55 mm deeper before release. No influence of the hydrostatic pressure (at least not at this immersion depths) could be observed for phases I and II and also not for the beginning of phase III. This is consistent with the assumptions and also with the behavior of rigid spheres, like which the elastic spheres behave during the initial times. Deeper immersed spheres however do not reach the same terminal velocity as initially less immersed spheres (see Fig. 2.9 in the appendix). This saturation takes place significantly before any possible influence of the bottom of the container would be assumed ($x > 0.24$ m). Hence, the length of elastohydrodynamic acceleration as described in Eq. 2.7 may depend on further variables that remain to be investigated.

Under the here investigated conditions, the sedimentation dynamics of elastic particles could be well described in four phases. Both the characteristic elastic time t_{el} and the characteristic onset position x_{el} show a dependence on the particle radius. Especially in the case of small and highly deformable particles, it could be possible that elastic effects would kick in earlier. Then it would no longer be possible to distinguish between the acceleration phases and effectively two phases would be observed. However, the resulting overall time of acceleration to reach the terminal velocity would still be much longer than in the case of comparable

rigid particles.

2.6 Conclusion

In this paper, we presented experimentally derived characteristics of sedimentation of elastic, deformable and nonheavy spheres in a rectangular duct. The experiments gave fundamental insights into the fluid-particle dynamics of elastic particles in bounded fluids and at low Reynolds numbers. We observed that the sedimentation of elastic spheres under the influence of walls differs fundamentally from that of rigid spheres.

Sedimentation of rigid and elastic spheres with a radius of 6 mm was performed in a rectangular duct at low Reynolds numbers. Sedimentation dynamics of rigid spheres was as expected. Velocities of 81% of the Stokes velocity were measured for the rigid spheres. The reduction of the velocity is due to the influence of the four surrounding plane walls in the rectangular duct. The measured reduction in velocity was expected and agrees with theoretical calculations from literature. The experiments with the elastic model particles showed a completely different velocity-time behavior, or velocity-displacement behavior respectively, than rigid particles. It appears that elastic effects kick in at a comparatively large time scale, such that the sedimentation of elastic spheres could be described by four phases instead of two phases as for rigid particles. The first phase showed a transient acceleration and the second phase a first velocity plateau that corresponds to the dimensionless velocity of the rigid spheres. Thereafter, for all elastic spheres a second acceleration began after a distance of about $10 \cdot R$. This characteristic onset position corresponds to a time of $t_{\mathrm{el}} \approx 20T_{0.6} \cdot 4\rho R^2\eta^{-1}$. From this characteristic time on, the elasticity has a significant influence on the sedimentation of elastic spheres in the bounded fluid. The third phase of sedimentation showed further acceleration that depends strongly on the Young's modulus. The more deformable the spheres were, the longer the second acceleration lasted and the further the distance was until the terminal velocity of the second plateau was reached. It was shown, that the softest spheres sedimented more than $50 \cdot R$ until the terminal velocity of the second plateau was reached. Furthermore, the measured percentage increase $\Delta x_{\mathrm{el,exp}}$ compared to the rigid velocity plateau was found to be up to 9 %. This long-term unsteady behavior and the much higher terminal velocities both are relevant for calculations, but they also have a significant impact on applications, *e.g.*, process design, since these deviations from the known rigid particle behavior are not negligible.

With the help of our experimental data and the characteristic quantities obtained so far, it is already possible to make some easy-to-calculate statements about the expected terminal velocity of elastic (micro)particles under wall influence. Our findings and their discussions regarding the gaps that still exist, also

encourage a great deal of further research. Our findings can be used as a basis for following investigations in this area, which in our opinion, especially with respect to the associated applications, has been little studied experimentally but also theoretically in the past. In particular, we see a lot of potential in conducting further experiments with more variations of Young's modulus and of the ratio of the radius to the duct size. Even sedimentation of elastic spheres in an unbounded fluid remains to be investigated experimentally. An overarching goal for the future would be the modeling of the relationship between the elastic material parameters and the particle dynamics. With the help of analytical expressions of the forces acting on particles or the sedimentation velocity as a function of the Young's modulus, the computational effort, *e.g.* for CFD simulations including elastic particle dynamics, would be greatly reduced.

Declaration of Interests. The authors report no conflict of interest.

Acknowledgements. Funded by the Deutsche Forschungsgemeinschaft (DFG, German Research Foundation) – Project-ID 172116086 – SFB 926. The experiments and simulations were performed in frame of subproject A10 "Elastohydrodynamic interactions of particles flowing over microstructured surfaces" in the Collaborative Research Center 926 (CRC926 MICOS).

2.7 Chapter Appendix

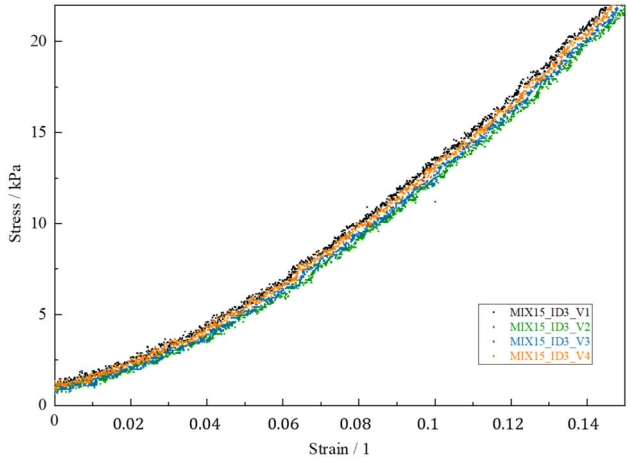


Figure 2.8: Stress-strain curve of four cycles (load and unloading) of a test with a cylinder fabricated from a Sylgard 184 and Sylgard 527 in a 1:5 mixing ratio lubricated with silicone oil; Since no standard bodies for testing were used and the recorded displacement of the sensor is not adjusted to the sample height, there are intercepts (curve does not start at point (0/0)). To determine Young's moduli and thereby exclude initial and frictional effects, in this example the slopes of in total 0.05 absolute strain in the range of small deformations are determined by a linear fit (here in the range [0.025;0.075]).

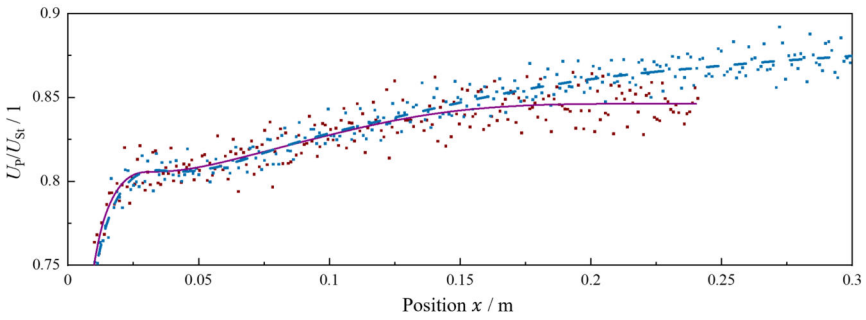


Figure 2.9: Measured dimensionless velocity and interpolation curves of experiments of spheres with Young´s modulus $E_{MIX15} = 135 \pm 13.14$ kPa (– – –Mix 1:5 immersed 15 mm deep, —— Mix 1:5 immersed 70 mm deep) fitted to a value of 0.81 at the first plateau and plotted against the position x within the measuring range ($x < 0.3$ m for 15 mm immersion; $x < 0.24$ m for 70 mm immersion).

Updates. Figures, Equations, Tables and references are renumbered to provide a consistent and clear allocation in this thesis. The general style, like colors and fonts are changed to provide a uniform format. The notation is changed for the following symbols to avoid double occupations (original paper changed to this thesis):

Fluid velocity	U	U_f
Dummy time variable	s	τ

3

Inertial forces and elastohydrodynamic interaction of spherical particles in wall-bounded sedimentation experiments at low Re_P number

Contents

3.1 Abstract **36**
3.2 Introduction **36**
3.3 Theoretical background **40**
3.4 Methods **44**
3.4.1 Experimental setup and particle tracking velocimetry 44
3.4.2 Fabrication of model particles and the soft layer 45
3.5 Results and Discussion **48**
3.5.1 Sedimentation of rigid and elastic spheres near a plane, rigid wall 48
3.5.2 Sedimentation of a rigid sphere near a plane, elastic wall 63
3.6 Summary and Conclusions **68**
3.7 Chapter Appendix **74**

Chapter 3 presents an updated reprint of the following manuscript: I.Noichl and C. Schönecker. Inertial forces and elastohydrodynamic interaction of spherical particles in wall-bounded sedimentation experiments at low Re_P number.

Manuscript currently in preparation for submission to Journal of Fluid Mechanics.

3.1 Abstract

Unsteady, wall-bounded sedimentation of spherical particles at low Reynolds numbers $Re_P \lessapprox 0.1$ under the influence of small elastic deformation was investigated experimentally. The complete kinematics of both elastic and rigid spheres sedimenting from rest and from various distances near a rigid or an elastic plane wall in a rectangular duct were recorded. Several specific phenomena related to the influence of fluid inertia and superimposed elastohydrodynamic effects were identified and discussed. Among these phenomena is an *inertial wall attraction*, *i.e.*, particles approach the wall while being accelerated from rest. It was found, that this initial attraction was a purely hydrodynamic phenomenon which occurred in all experiments at $Re_P \lessapprox 0.1$. After the initial stage, rigid spheres sedimenting at $Re_P \approx O(10^{-1})$ near the wall behaved in the classic way, showing linear migration due to hydrodynamic lift forces. Non-classic evolution of the particle velocity with respect to the wall distance was observed for both rigid and soft spheres sedimenting at $Re_P \approx O(10^{-2})$. Sedimentation was persistently unsteady and the spheres decelerated although the wall distance was increased. In the case of very soft spheres, the instationarities in the kinematics were superimposed by additional nonlinearities. This superimposed, weaker effect is attributed to the non-trivial coupling between particle-fluid inertial forces and effects due to small elastic deformation, *i.e.,* an *elastohydrodynamic memory* effect is assumed to be the underlying physical mechanism. Instationarities were also observed during the sedimentation of rigid spheres along an elastic wall. For example, in the near-wall region, elastohydrodynamic interactions damped the dynamics during mass acceleration. Meanwhile, persistent undulating motion towards the wall was observed, *i.e., elastohydrodynamic particle trapping* instead of hydrodynamic lift was observed. The results gained from the experiments give deep insights into the unsteady dynamics of sedimenting particles at low Re_P with elastic interaction and are of importance, *e.g.*, for the understanding of micro-particle transport and the locomotion of swimming micro-organisms near surfaces. They illustrate the breakdown of classic assumptions applied in particle sedimentation if walls and various other influences are present.

3.2 Introduction

Particle-laden fluid flows are ubiquitous in our daily lives. From the flow of our blood cells through the cardiovascular system to the purification of wastewater in sewage treatment plants - particles of every conceivable shape or morphology in interaction with fluids are found everywhere. Typically, these particle-laden fluids are within or flow through confined spaces, such as reactors, pipelines and tubes or blood vessels.

In other words, the particles do not only interact with the (flowing) fluid but also with surrounding walls. These interactions of particles, the surrounding fluid and a confining wall can lead to phenomena, to which everyone of us is exposed to – perhaps without knowing it. The best example of such a phenomenon, is the Fåhraeus effect. Robin Fåhraeus described in 1929 the effect, that blood cells migrate laterally from the walls of blood vessels in direction of the vessel axis. A cell-free plasma layer is formed along the vessel walls, which is of crucial importance for the functionality of the cardiovascular system and for immune defense. [39] Today it is known, that the Fåhraeus effect in blood vessels is subject to the principle of elasto-inertial focusing, which is a combined effect of inertial focusing and elastic forces. The part of elastic forces can originate either from elasticity of the particle, the walls or from viscoelastic properties of the fluid. [40] Segré and Silberberg were the first researchers, who, in 1961, reported observations on the phenomenon of particle collection of rigid particles in viscous fluids due to fluid inertia. In their experiments, they observed radial particle displacements in Poiseuille flows of suspensions. Today known as Segré-Silberberg effect, it describes that macroscopic, rigid and spherical particles collect into a thin, annular region when an initially uniform dilute suspension is passed in laminar flow through a straight cylindrical tube. [41] Segré and Silberberg recognized the potential of this effect as particle sorting mechanism. In recent years, the principle of inertial focusing has attracted increasing interest in the field of microfluidics. [40],[42],[43],[44] This interest is based mainly on the numerous possible applications in, for example, the field of biomedical diagnostics. For example, it is well-known, that infectious diseases like COVID-19 can alter the physical properties of blood cells, including morphological or mechanical features. [45] For this reason, deformability cytometry techniques are promising in the field of real-time diagnostics but also in the field of material characterization of deformable micro-particles. [46] What the focusing techniques from the field of inertial microfluidics have in common: the word “inertial” refers mostly to separately imposed advective fluid inertia, *i.e.*, the particles are moved by and with the fluid.

The lateral migration of particles perpendicular to walls like in the Segré-Silberberg effect is due to a combination of advective inertia induced lift forces directed towards the wall and wall-induced lift forces directed away from the wall. The former are induced by shear gradients, *i.e.* the particle experiences locally a shearing due to gradients in the velocity (*cf.,* parabolic flow profiles in cylindrical tubes). The mechanism was first described by P.G. Saffman in 1965. [47] The latter lift forces are induced solely by the presence of the wall and can also emerge if the fluid is quiescent (not separately advected).

The time reversal symmetry of the steady Stokes equations and the symmetry in front of and behind the point at the surface closest to the wall would actually imply the absence of normal forces in the creeping flow regime. [48] This would be especially true if both the fluid Reynolds number and the particle Reynolds number are close to zero ($Re_P \ll 1$), *i.e.,* if the particle itself translates with small inertia and momentum transferred to the fluid is very small. But why do normal forces like wall-induced hydrodynamic lift emerge

anyway? The simple answer is: inertia of the surrounding fluid is per se finite. In that moment, in which a particle starts translating through a fluid, a disturbance flow is generated and the fluid around the particle accelerates. In this case, Stokes's assumptions of reversibility are no longer valid in the far-field of the particle and the equations of motion must be supplemented by the influence of fluid inertia as recognized by Carl Wilhelm Oseen in 1910. [49] The inertial contribution is indeed small for low Reynolds numbers. However, if a sphere translates in the presence of a wall, these small inertial contributions are enough to induce a lift force directed normally to the wall due to symmetry-breakings in the disturbance flow. It was Carl Wilhelm Oseen´s PhD student, Hilding Faxén, and later Vasseur and Cox who described the lateral migration of a rigid particle in a viscous fluid and in the presence of plane walls theoretically. [29],[50] These theoretical approaches refer purely to rigid and perfectly spherical particles with small but finite inertia. However, there are several other effective mechanisms than pure fluid inertia that can invoke the symmetry breaking that leads to lift forces. Such mechanisms are, *e.g.,* elastic deformation of the particle or of the confining wall. These deformations also induce a symmetry-breaking, which leads to so called elastohydrodynamic lift forces. [36],[51] Theoretical work on lift forces in the presence of a wall usually assume a steady motion of the object, or steady relative velocity, respectively. [51],[52] Furthermore, experimental and theoretical work on particle dynamics including elastohydrodynamic effects is mostly performed with small gap sizes between the particle and the wall, or the elastic layer, respectively, to make use of, *e.g.* elastohydrodynamic lubrication theory. [53],[54],[55],[56],[57]

If the active motion of small particles in a viscous fluid is assumed to be governed by the steady Stokes equations, the hydrodynamics after self-propulsion can be effectively described theoretically using multipole expansions of fundamental singularities. A key class of microswimmers studied in this context are so called squirmers, which propel themselves by generating tangential surface deformations and oscillations by cilia motion. [58],[59] The leading-order singularity is the Stokeslet, which represents the fundamental solution of Stokes equations of the flow induced by a point force in the fluid. Higher-order singularities, *i.e.* derivatives of the Stokeslet, include force dipoles, or the Stresslet, respectively, and the source dipole. The presence of boundaries, such as walls or interfaces, alters these singularity solutions due to no-slip or stress conditions. So called hydrodynamic imaging is the principle of sensing objects remotely based on disturbances generated by moving or inert objects such as small particles in the flow field. [60] This principle is applied in modeling flow fields near walls by introducing fictitious singularities that enforce the required boundary conditions, analogous to the method of electrical images in electrostatics. [61],[62],[63] In fact, theoretical squirmer dynamics are strongly influenced by walls, *e.g.*, walls modify the propulsion efficiency, the squirmer´s orientation and the stability near surfaces. [64],[65],[66],[67] Many experimentally observed phenomena can be constructed and simulated using the squirmer model and multipole analysis near walls. Nevertheless, the flow field generated by the singularities is instantaneous and, except of gravity, most mod-

els do not account for body forces.

In reality, however, particles with finite mass and finite body size also undergo transient phases of motion, *e.g.,* through spontaneous, time-depended self-propulsion or during the transient phase of gravitational acceleration like in sedimentation processes. [68],[69],[70] During transient phases of particle motion, unsteady forces related to inertia of mass act on a particle. An example for such an unsteady force acting on a particle during mass acceleration from rest is the Basset history force classifying as a so called memory effect. [23],[71] This type of inertial force is particularly relevant in an otherwise quiescent liquid when mass inertia of the particle is small but finite. As a consequence, steady-state conditions are no longer valid and the complete transient dynamics or kinematics must be taken into account.

Experimental investigations on the complete kinematics are rare and, especially, investigations of single elastic spheres sedimenting in the Reynolds number regime $Re_P \lessapprox 0.1$ and in which the influence of bounding plane walls is precisely addressed are not available to date. Complete kinematics in this context includes the spatio-temporal resolution of the entire trajectory from the beginning of the acceleration, *e.g.,* when starting from rest. Fully resolved kinematics were reported, for example, for rising bubbles in viscous liquids or for sedimentation of rigid spheres in a cylindrical tube filled with a viscoelastic liquid. [72],[73] Generally, in the past the light was often directed towards the description of drag and lift forces of drops and bubbles. [74] However, the underlying physics of bubbles and drops in liquids cannot be easily applied to the interaction of deformable solids with liquids. All the gaps and limitations with respect to transient dynamics in the literature prevent detailed insights into particle dynamics which are highly relevant for biotechnological applications, *e.g.,* particle sedimentation along surfaces coated by biofilms. [1] One possible reason for the experimental gaps could be that it is difficult to spatially and temporarily resolve the kinematic phenomena in the µm-range and especially in the near-wall region, where very small Reynolds numbers $Re_P \lessapprox 0.1$ naturally occur.

In this report, we therefore attempt to shed light on the phenomena of transient particle dynamics with and without elastohydrodynamic wall interactions using an experimental approach. The focus is on spontaneous particle sedimentation from rest in an otherwise quiescent fluid within a rectangular duct. Both elastic and rigid spheres were examined, which started at various distances from elastic and from rigid walls. The experiments were performed in a scaled experimental design in the cm-range. The advantage of this scaling is that the kinematics could be detected much more precisely in space and time than this would be possible on the µm-scale. The paper is structured as follows: section 3.3 reviews the fundamental theory of classic Newtonian particle dynamics in fluids to calculate relevant forces and velocities of a flowing, single particle at low Reynolds numbers. Furthermore, the applicability and the limitations of existing theory are discussed. In section 3.4, the experimental methods such as the fabrication of polymer spheres and the optical measurement methods for tracking the particle kinematics are explained. In the first part of section 3.5, data

of experiments with rigid and elastic model particles sedimenting at different particle Reynolds numbers at various distances to rigid walls are presented. In the context of the observed kinematics, the different types of inertial forces and their origins are reviewed and discussed. Additionally, 3D computational fluid dynamics (CFD) studies of a falling sphere in a rectangular fluid domain were carried out to validate the measured velocities and to gain insights into the principal fluid flow field during the experiment. In the second part of section 3.5, results of experiments with rigid spheres sedimenting along an elastic wall are presented and discussed.

3.3 Theoretical background

In the following, a brief overview of the basic equations, which form the basis for the physical understanding of the data shown in the next sections, is given.

The unsteady equation of motion of a rigid, spherical particle in a spatially nonuniform, time-dependent fluid flow in the absence of any rigid boundaries, *e.g.*, walls or other particles, is described by the Maxey-Riley (MR) equation. [75]

$$\begin{aligned} m_\mathrm{P}\frac{\mathrm{d}\boldsymbol{U}_\mathrm{P}}{\mathrm{d}t} = (m_\mathrm{P}-m_\mathrm{f})\boldsymbol{g} + m_\mathrm{f}\left.\frac{\mathrm{D}\boldsymbol{U}_\mathrm{f}}{\mathrm{D}t}\right|_{\boldsymbol{X}_\mathrm{P}(t)} &- \frac{1}{2}m_\mathrm{f}\frac{\mathrm{d}}{\mathrm{d}t}\left.\left(\boldsymbol{U}_\mathrm{P}-\boldsymbol{U}_\mathrm{f}-\frac{R^2}{10}\nabla^2\boldsymbol{U}_\mathrm{f}\right)\right|_{\boldsymbol{X}_\mathrm{P}(t)} \\ &- 6\pi\eta R\left.\left(\boldsymbol{U}_\mathrm{P}-\boldsymbol{U}_\mathrm{f}-\frac{R^2}{6}\nabla^2\boldsymbol{U}_\mathrm{f}\right)\right|_{\boldsymbol{X}_\mathrm{P}(t)} \\ &- 6\pi\eta R^2\int_0^t \frac{\mathrm{d}\tau}{\sqrt{\pi\nu\,(t-\tau)}}\frac{\mathrm{d}}{\mathrm{d}\tau}\left.\left(\boldsymbol{U}_\mathrm{P}-\boldsymbol{U}_\mathrm{f}-\frac{R^2}{6}\nabla^2\boldsymbol{U}_\mathrm{f}\right)\right|_{\boldsymbol{X}_\mathrm{P}(\tau)} \end{aligned} \tag{3.1}$$

The Maxey-Riley equation results from the force balance around a sphere with mass $m_\mathrm{P} = \frac{4}{3}\pi R^3\rho_\mathrm{P}$. R is the radius of the spherical particle and ρ_P is the solid density of the particle. The sphere starts from rest and translates through an incompressible, Newtonian fluid with density ρ and dynamic viscosity η. $\nu = \eta/\rho$ is the kinematic viscosity of the fluid. $m_\mathrm{f} = \frac{4}{3}\pi R^3\rho$ is the mass of the fluid displaced by the sphere. The particle translates with velocity $\boldsymbol{U}_\mathrm{P} = \frac{\mathrm{d}\boldsymbol{X}_\mathrm{P}(t)}{\mathrm{d}t} = \begin{pmatrix} U_\mathrm{P} & U_\mathrm{P,y} & U_\mathrm{P,z}\end{pmatrix}^T$ in a Lagrangian reference frame through the fluid in which $\boldsymbol{X}_\mathrm{P}(t)$ is the position of the particle center at a certain time t. The fluid motion satisfies the incompressible Navier-Stokes equations whose solution is an Eulerian velocity field $\boldsymbol{U}_\mathrm{f} = \boldsymbol{u}_\mathrm{f}\left(\boldsymbol{X}_\mathrm{P}(t), t\right)$ from the point of view of the particle center. This velocity field is the net velocity field of, on the one hand, a global background flow which is imposed independently of the particle's motion. An example for such an imposed flow is a Poiseuille flow through a tube. On the other hand, the velocity $\boldsymbol{U}_\mathrm{f}$ at time t contains the local disturbance flow around the sphere caused by the previous motion of the sphere. The term on the left side of Eq. 3.1 is the inertia of the spherical particle due to acceleration of the particle´s mass $\boldsymbol{F}_\mathrm{I}^P$. The

inertia is balanced by the gravitational force $\boldsymbol{F}_{\mathrm{G}}$, buoyancy $\boldsymbol{F}_{\mathrm{Buoyancy}}$, advective fluid inertia $\boldsymbol{F}_{\mathrm{I}}^{f}$, added mass $\boldsymbol{F}_{\mathrm{AM}}$, viscous drag $\boldsymbol{F}_{\mathrm{D}}^{ub}$ and the Basset history force $\boldsymbol{F}_{\mathrm{B}}$, respectively (terms on the right side of Eq. 3.1 in the order of appearance). If the fluid is quiescent, unbounded, and $Re \rightarrow 0$ ($\boldsymbol{U}_{\mathrm{f}} = \begin{pmatrix} 0 & 0 & 0 \end{pmatrix}^{T}$), Eq. 3.1 reduces to the Basset-Boussinesq-Oseen (BBO) equation, in which all terms in Eq. 3.1 containing $\boldsymbol{U}_{\mathrm{f}}$ disappear. [23],[24],[25] The terms of order $R^2\nabla^2\boldsymbol{U}_{\mathrm{f}}$ in Eq. 3.1 which arise in the added mass term, the viscous drag and the Basset history force are known as Faxén terms since they were originally derived by Hilding Faxén in his dissertation. [2] The so called Faxén´s law reads

$$\boldsymbol{F}_{\mathrm{D}}^{ub} = -6\pi\eta R\left(\boldsymbol{U}_{\mathrm{P}} - \boldsymbol{U}_{\mathrm{f}} - \frac{R^2}{6}\nabla^2\boldsymbol{U}_{\mathrm{f}}\right)\Big|_{\boldsymbol{X}_{\mathrm{P}}(t)} \tag{3.2}$$

and modifies Stokes´s drag force, or Stokes´s law for viscous drag on a sphere, respectively, with an additional fluid inertia term that takes into account the curvature of the disturbance flow induced by the sphere. [27],[75] If there is a background flow involved in addition to the disturbance flow, the fluid inertia term $m_{\mathrm{f}}\frac{\mathrm{D}\boldsymbol{U}_{\mathrm{f}}}{\mathrm{D}t}\Big|_{\boldsymbol{X}_{\mathrm{P}}(t)}$ plays a significant role in the Maxey-Riley equation. $\frac{\mathrm{D}}{\mathrm{d}t} \equiv \frac{\partial}{\partial t} + (\boldsymbol{U}_{\mathrm{f}} \cdot \nabla)$ is the material derivative in the background flow. The term accounts for advective inertia due to fluid motion acting on the sphere. The Maxey-Riley equation in this form is only valid, when the particle size is small compared to the characteristic scales of the spatial variations of the undisturbed background flow. For the case when the size of the particle is appreciable relative to characteristic length scale of the flow, Rallabandi extended the fluid inertia term to include the influence of curvature in the nonuniform background flow on advective inertia. [76] Such scenarios can be found, for example, in microfluidic channels, where vortex formation due to cavities, takes place and where particles move within these vortices. [77]

As mentioned previously, both the BBO equation and the MR equation are valid only when a rigid, spherical particle is moving in an unbounded fluid. The influence of walls on the steady dynamics of spherical particles suspended in quiescent fluids or in (non)uniform flows is an ongoing part of intensive research for many years. When a particle translates in the vicinity of a wall and when both mass inertia and fluid inertia are present (Re is small but finite), symmetry breaking due to the wall leads to an increased drag $\boldsymbol{F}_{\mathrm{D}}^{wb}$ and a wall-induced lift force $\boldsymbol{F}_{\mathrm{L}}^{wi}$. However, analytical expressions for the drag force in wall-bounded fluids $\boldsymbol{F}_{\mathrm{D}}^{wb}$ or the wall-induced hydrodynamic lift force $\boldsymbol{F}_{\mathrm{L}}^{wi}$ are described only for several special cases, *e.g.*, for one plane wall, linear shear flows, etc. A good overview of wall corrections for stationary drag and for wall lift models is given by Shi and Rzehak (2020) or by Ekanayake et al. (2021). [78],[52]

The wall-induced hydrodynamic lift force as a function of the lift coefficient c_{L} can be expressed by

$$F_{\mathrm{L}}^{wi} = c_{\mathrm{L}}R^2\rho U_{\mathrm{P}}^2. \tag{3.3}$$

Ekanayake *et al.* (2021) developed a generalised lift model valid for arbitrary distances d between the particle and the wall and proposed the following lift coefficient c_L for non-rotating particles moving with $Re_\mathrm{P} \leq 0.05$ in a quiescent fluid parallel to a plane wall: [52]

$$c_\mathrm{L} = \frac{18\pi}{32 + 2\left(\frac{d}{L_\mathrm{S}}\right) + 3.8\left(\frac{d}{L_\mathrm{S}}\right)^2 + 0.049\left(\frac{d}{L_\mathrm{S}}\right)^3} + 0.4353\left(\frac{R}{d}\right) - 1.198\left(\frac{R}{d}\right)^2 + 0.7792\left(\frac{R}{d}\right)^3. \tag{3.4}$$

The first fractional term corresponds to the lift coefficient in Takemura's outer-region model, where $L_\mathrm{S} = \eta/\rho U_\mathrm{P}$ is the Stokes length scale. [79]

What existing models for wall-induced lift forces on spherical particles in quiescent liquids without imposed fluid flow (absence of shear) have in common: the wall-induced lift force is always positive and directed perpendicularly to the wall, *i.e.*, it leads to a migration of the sphere away from the wall.

In 1922, Faxén was the first who derived an equation for the steady drag force when a spherical particle is sedimenting in the presence of a plane wall. He used his previously formulated unbounded drag force $\boldsymbol{F}_\mathrm{D}^{ub}$ from Faxén´s law (Eq. 3.2) to calculate the influence on drag due to the disturbance flow induced by the sphere which is then reflected at the plane wall. This reflection in turn causes a background flow which affects the resulting stationary force on the sphere leading to an expression for the drag force in a bounded fluid $\boldsymbol{F}_\mathrm{D}^{wb}$. Using Faxén´s $\boldsymbol{F}_\mathrm{D}^{wb}$, the corrected Stokes´s velocity near a single plane wall, *i.e.*, the dimensionless velocity $U_\mathrm{P}/U_\mathrm{St}$ in direction of gravitational acceleration, can be calculated as follows. [29],[2]

$$\left(\frac{U_\mathrm{P}}{U_\mathrm{St}}\right)_{\mathrm{F},\bullet|} = 1 - \frac{9}{16}\left(\frac{R}{d}\right) + \frac{1}{8}\left(\frac{R}{d}\right)^3 - \frac{45}{256}\left(\frac{R}{d}\right)^4 - \frac{1}{16}\left(\frac{R}{d}\right)^5 \tag{3.5}$$

The index "$\bullet|$" illustrates that it is the corrected dimensionless velocity for a sphere in the close vicinity of one plane wall. In the other spatial directions, the fluid is unbounded. The velocity U_St results from Stokes´s law and is the theoretical velocity of a sphere which falls stationary due to gravity in an unbounded, incompressible fluid. [27] U_St results from balancing Stokes´s drag, gravity and buoyancy and reads

$$U_\mathrm{St} = \frac{2R^2\Delta\rho g}{9\eta}. \tag{3.6}$$

Thus, with the dimensionless velocity $U_\mathrm{P}/U_\mathrm{St}$ from Eq. 3.5, the influence of the wall on the steady velocity can be read directly. Faxén´s Eq. 3.5 is only valid in the creeping flow regime when $Re_\mathrm{P} \to 0$. If the Reynolds number is slightly larger, *e.g.*, of $O(10^{-1})$, the theoretical (dimensionless) velocities must be extended by the so-called Oseen correction terms, *cf.* Eq. 3.8 in section 3.5.1.1 and Eq. 3.13 in appendix A1 (the equations are explained in connection with the respective results for a rigid sphere sedimenting at $Re_\mathrm{P} \approx O(10^{-1})$).

Faxén also derived and calculated numerically the terms to correct Stokes´s velocity of a sphere that

sediments mid-way between two parallel plates (index "|•|"):[2]

$$\left(\frac{U_\mathrm{P}}{U_\mathrm{St}}\right)_{\mathrm{F},|\bullet|} = 1 - 1.004\left(\frac{R}{d}\right) + 0.418\left(\frac{R}{d}\right)^3 - 0.169\left(\frac{R}{d}\right)^5. \tag{3.7}$$

The discussed corrections are valid within the previously mentioned restrictions which are, on the one hand, rigidity and sphericity. On the other hand, the correction factors were derived by the assumption of stationary motion in the creeping flow regime ($Re_\mathrm{P} \rightarrow 0$). These assumptions help in theory to make particle dynamics accessible by various mathematical methods, *e.g.*, series expansions. However, these assumptions represent reality in only very limited and isolated cases. There is especially little knowledge and experimental work available which deals with the influence of the presence of walls during the unsteady motion of particles, *e.g.*, when they accelerate from rest due to their inertia of mass. [2],[80] Furthermore, common theories about the influence of elasticity of the particles or the walls, respectively, on the dynamics are available only for certain exceptional cases. One example for such a case is the steady motion of an elastic particle in an unbounded fluid. [15],[9] For example, Murata expanded the theoretical Stokes´ drag around a perturbation parameter $\alpha = U_\mathrm{St}\eta G^{-1}R^{-1}$ to derive the influence of small elastic deformation on the sedimentation velocity. α relates the viscous stresses to the elastic, mechanical shear stresses. If α is much smaller than unity, small deformations ($\Delta R \approx \alpha R$) are assumed. G denotes the shear modulus of the elastic material with $G = E[2(1+\nu)]^{-1}$. E represents Young´s elastic modulus and ν the Poisson´s ratio of the elastic solid. However, it was shown that Murata´s theory cannot be applied on sedimentation in bounded fluids, *i.e.* measured sedimentation velocities of soft spheres in the center of a rectangular duct were significantly larger than predicted by Murata´s theory. Nevertheless the theory correctly predicts an increase in velocity since it predicted the deformation into a prolate spheroid for the corresponding solid and liquid material properties. [70] Another case, or configuration, respectively, for which theoretical models with limitations exists, is the already mentioned translation of an object at very small distances between the elastic object and/or the elastic wall or a membrane. In this case, elastohydrodynamic lubrication theory is applicable, *i.e.*, the Reynolds equations for thin fluid films hold. [81],[36],[55],[56],[82],[51] In real systems, however, a complex interplay of the various effects like wall interaction at larger distances, elastohydrodynamic interaction and inertial forces takes place and cannot be considered in isolation from one another.

3.4 Methods

3.4.1 Experimental setup and particle tracking velocimetry

Sedimentation experiments of spherical model particles were performed in a rectangular duct. As a vessel for the experiments, a glass container of 140 mm x 140 mm x 500 mm (W x D x H) was used, *cf.* Fig. 3.1 *(a)*. The container was filled up to a height of around 450 mm with silicone oil. The silicone oil had a nominal viscosity of 1000 cSt (measured value of $\eta = 0.9797 \pm 0.012$ Pa·s using a rotational viscometer IKA® Rotavisc lo-vi). The liquid density at room temperature was measured to be $\rho = 971.28 \pm 0.134\,\mathrm{kg \cdot m^{-3}}$ using an analytical balance (Sartorius® ENTRIS BCE 224i-1s). The choice of these setup properties allowed to investigate the same conditions as small microparticles would experience in aqueous liquids because $Re_\mathrm{P} \ll 1$. The spheres were hold with a pipette under weak vacuum and then immersed in the liquid. The pipette tip was equipped with a soft silicone cap which adapted to the shape of the object to be held. This and the weak vacuum prevented the object from being deformed beforehand. The sphere was positioned at the midplane between two opposing walls, having a distance d to the nearest wall, *cf.* top view in Fig. 3.1 *(a)*. The vacuum was released by slowly opening a valve and flooding the tube with air. This ensured that the spheres were not pushed away from the pipette by air. The silicone oil penetrated the gap between the sphere and the pipette cap, causing the sphere to detach and begin to fall due to gravity. This procedure ensured an initial sedimentation velocity of $U_{\mathrm{P,\,t=0s}} = 0\,\mathrm{m \cdot s^{-1}}$ (starting from rest) while the fluid was initially quiescent $\boldsymbol{U}_{\mathrm{f,\,t=0s}} = \begin{pmatrix} 0 & 0 & 0 \end{pmatrix}^T$. After immersion and between two experiments, a rest period was inserted to exclude the influence of imposed fluid motion and backflows within the closed tank.

High-resolution videos of the sedimentation experiments were recorded by a DSLR camera (Nikon® D7200 with Sigma® 50 mm f1.4 objective lens). During the experiments, the container with silicone oil was illuminated from the opposite side of the camera by a collimated light panel. This ensured a sharp contour of the model particle recorded by the camera sensor. The DSLR camera recorded videos of the experiments with a resolution of 1.920 px ($W_{\mathrm{px,\,vid}}$) x 1.080 px ($H_{\mathrm{px,\,vid}}$). The videos were recorded with the maximum frame rate of 25 frames per second (fps). To avoid blurring effects or artifacts at the edges of the image (*e.g.*, due to spherical aberration), the camera was aligned so that the object was recorded in the center of the image. The optical plane of the camera was aligned perpendicular to the closest wall of the container, which had a negligible inclination of $\varepsilon \lessapprox 0.2^\circ$ in relation to the vertical in the direction of gravity. Before starting the experiment, an image with higher resolution (3.368 px ($W_{\mathrm{px,\,start}}$) x 6.000 px ($H_{\mathrm{px,\,start}}$)) was captured. With this start image, the scaling from pixel values to real-length values was performed in each evaluation by scaling via the pipette diameter (known real-length in the image). This procedure allowed to

determine the radius of a sphere with an accuracy of ≈ 1% of its radius (size of a pixel $l_{\text{px, start}} \approx 6.6 \cdot 10^{-5}$ m, *cf. Supplementary information* (SI) in the dissertation appendix A.1 §2). Subsequently, the trajectories and velocities were evaluated with a self-programmed image processing tool in MATLAB®. The principle of particle tracking is illustrated in Fig. 3.1 *(b)* and *(c)*. The center of the spheres (centroid of the pixel disks) and the radii of the best-fit circles around the spheres were calculated by the image processing tool. The optical resolution of the camera system during video recording allowed tracking of the centroid in the accuracy range of about 3.5 % of the radius (size of a pixel in the video $l_{\text{px, vid}} \approx 2 \cdot 10^{-4}$ m). The time step between two video images must therefore be chosen large enough to ensure that the centroid of the disc has moved in a distinguishable way. The detail from optical tracking (yellow box in Fig. 3.1 *(b)*) shows, that the deviation from a vertical in the image was properly resolved optically. Furthermore, it was checked in each evaluation that the spheres moved within the initial optical plane (xy-plane) in order to exclude 3D effects, *e.g.*, by evaluating the black discs pixel area A_{px}, its perimeter P_{px} and calculating the isoperimetric quotient $Q = 4\pi A_{\text{px}} P_{\text{px}}^{-2}$ over time. Further details on optical image tracking accounting for the robustness of the measurement method can be found in the provided *SI*. Furthermore, the reliability of the measurement technique was proven with measurements of rigid spheres in the center of the tank by comparison with existing literature for rectangular channels, *cf.* [70].

3.4.2 Fabrication of model particles and the soft layer

The spheres used for the experiments in this study were from the same fabrication batches also used in our previous study in the center of the duct. [70]

Elastic model particles with Young´s elastic moduli of $E \approx 1712$ kPa, $E \approx 936$ kPa and $E \approx 135$ kPa (softest sphere) were fabricated from polydimethylsiloxane (PDMS) mixtures (Sylgard™ 184 and SylgardTM 527, Dow Corning®) by casting and bonding of hemispheres. Base blends of the PDMS elastomers were prepared according to the manufacturer's specifications (Sylgard™ 184 silicone oil: curing agent in a 10:1 ratio and Sylgard™ 527 part A: part B in a 1:1 ratio). Each base blend was colored black with 1 w-% iron oxide powder and degassed. Hereafter, the base blends were mixed with each other in a 1:1 ratio ($E \approx 936$ kPa) and a 1:5 ratio ($E \approx 135$ kPa), respectively. Pure Sylgard™ 184, respectively the again degassed mixtures of Sylgard™ 184 and Sylgard™ 527, were poured into a mould for hemispheres. The casted hemispheres were hardened for 12 h at 60 °C. For at least another 36 h, they were cured at room temperature. The measured Young´s elatsic modulus of hardened Sylgard™ 184 base blend was $E \approx 1712$ kPa (for details regarding the measurement of elastic properties, *cf.* [70]). In the next step, two hemispheres were bonded together with a thin film of the corresponding newly produced PDMS compound avoiding ridges and asymmetries. A detailed shape analysis is provided in §2 in the SI of the dissertation appendix A.1.

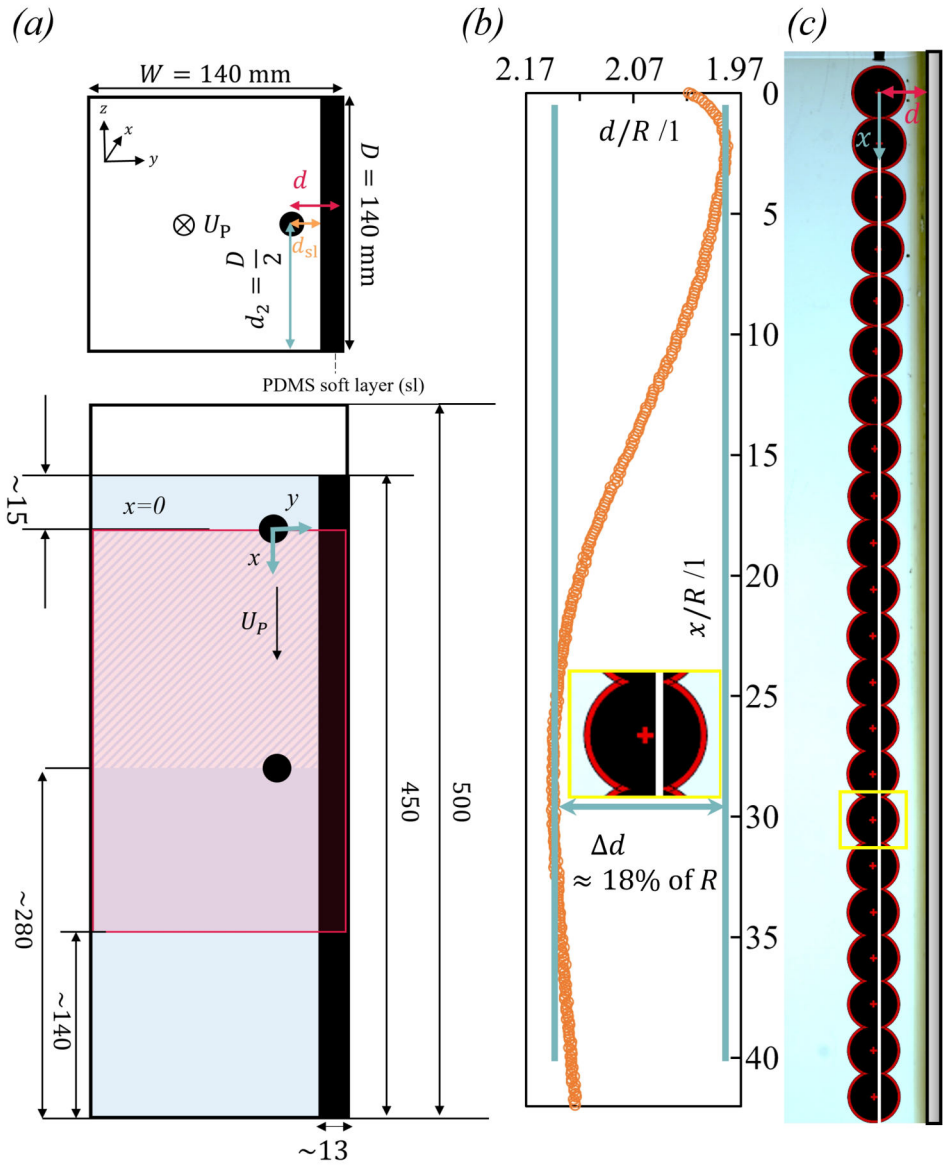


Figure 3.1: *(a)* Container dimensions in mm (top view and front view); Red area: measurement range of experiments near the rigid (glass) wall. The inclination in relation to the vertical (direction of $\boldsymbol{g}$) of the right glass wall is $\varepsilon \lessapprox 0.2°$ (widened downwards); Dashed area: measurement range of experiments near the PDMS soft layer; Principle of particle tracking: *(b)* Example of a trajectory represented as $(d/R) - (x/R)$-plot; *(c)* merged images of a sedimenting sphere showing the centers and radii of the sphere calculated at different positions. The white line indicates a vertical through the centroid aligned with the vertical of the image.

The bonded spheres were cured for at least another 48 h at room temperature. The PDMS spheres had a radius of $R \approx 6$ mm. The material properties relevant for the experiments are listed in Tab. 3.1 and Tab. 3.2 in Chapter 3.5.1. By changing the mixing ratios to vary the Young´s elastic modulus E, the density of the material inevitably changes. The variations in the particle-to-fluid density ratio $\gamma = \rho_P/\rho$ are small (especially those between the PDMS mixtures ($\gamma \approx 1.02 - 1.07$)). However, this had a significant influence

on the hydrodynamics, as will be shown in the next chapter.

Rigid, not manually deformable, spheres with a radius of $R \approx 6$ mm and a larger Young´s modulus of 2.9 GPa (according to manufacturer´s specifications) were fabricated by casting and bonding of hemispheres from epoxy resin (casting resin MS 1000 by Weicon®). Furthermore, commercially available hard polymer spheres with a radius of $R \approx 4$ mm were purchased. The measured density of $\rho_{\mathrm{R4mm}} = 1036.4 \pm 2.7$ kg·m^{-3} and the rigidity of the material suggest polystyrene (PS). The solid density of the rigid and elastic spheres was determined directly after each sedimentation experiment. This ensured to correctly represent the current state of the density. Changes in material properties due to diffusion of oil into the polymer and resulting swelling effects at the surface are avoided due to the short period of time of the experiments, *cf.* density curve Fig. A.2 in §1 in the SI of the dissertation appendix A.1. The solid density was determined using a hydrostatic balance (Sartorius® ENTRIS BCE 224i-1s analytical balance + density determination kit YDK03 for determination of solid densities). The balance has a readability of 0.1 mg. Density measurements were performed in distilled water.

To equip the rectangular duct with an additional soft layer, a PDMS plate with a thickness of $h_{\mathrm{sl}} \approx 13$ mm was fabricated by casting. Base blends of Sylgard™ 184 and Sylgard™ 527, Dow Corning®, were prepared according to the manufacturer´s specifications and colored black with 1 w-% iron oxide powder. The base blends were mixed in a 1:5 mixing ratio, *cf.* fabrication of the softest spheres. The degassed PDMS mixture was poured into a shallow rectangular laboratory dish and hardened for 12 h at 60 °C. The soft layer in the dry state had the same physical properties as the softest spheres (Young´s modulus $E_{\mathrm{layer,0}} \approx 135$ kPa and a solid density of $\rho_{\mathrm{s,\,layer,0}} \approx 987$ kg·m^{-3}). The soft layer was bonded on a stainless-steel sheet by a thin epoxy resin coating. The bonded soft layer was immersed into the container with silicone oil and fixed on one of the walls (see Fig. 3.1 *(a)*). For the soft layer, changes in the material properties due to diffusion of oil into the polymer, mainly the changes in solid density and the Young´s elastic modulus, must be considered. The change in density over time was investigated with a remaining part of the soft layer. For this purpose, samples of the material were immersed in silicone oil for different periods of time and the density was determined. It was shown that the density remained constant after 14 days, *i.e.*, the sample was saturated. After this time, no change in density was observed anymore, see Fig. A.2 in §1 in the SI of the dissertation appendix A.1. It is assumed, that the oil saturated layer had a smaller Young´s elastic modulus. However, the exact value could not be measured experimentally. All experiments in the vicinity of the soft layer were carried out after saturation to ensure, at least qualitatively, the same properties of the soft layer for all experiments.

3.5 Results and Discussion

The first part of this section deals with the sedimentation of particles with various radii and various Young´s moduli in the vicinity of plane, rigid walls in a rectangular container. In this part, the spheres are assessed in terms of their elasticity (division into rigid and soft spheres), as Young's elastic modulus E is the material property that obviously changes the most. However, the change in E led to small variations in the density ratio γ and consequently in the particle Reynolds number Re_P. As becomes clear after evaluating the data, these small variations in the particle Reynolds number are even superior to the elastic effects. It will be shown, that elastic effects only come into play at very large time scales, *i.e.*, when $Re_P \lesssim O(10^{-2})$.

In section 3.5.2, results of sedimentation experiments of rigid spheres in the container equipped with an additional soft layer are presented.

3.5.1 Sedimentation of rigid and elastic spheres near a plane, rigid wall

3.5.1.1 Sedimentation of large spheres $R \approx 6$ mm with varying density and Young´s elastic modulus at varying initial distance to a plane wall

In this subsection, the study is focused on the influence of varying density and elasticity on the kinematics of sedimenting spheres near rigid walls. All particles had the same size, but varying Young's moduli and slightly varying densities. Experiments were performed at two different distances to the nearest wall: in an intermediate region between the duct center and one of the walls ($d/R \approx 4$) and close to one of the walls ($d/R \approx 2$). Corresponding results can be found in Fig. 3.2 ($d/R \approx 4$) and Fig. 3.3 ($d/R \approx 2$), respectively.

Fig. 3.2 and Fig. 3.3 show exemplary measurements of specimens for the respective experiment (wall distance/Young´s modulus combination). All experiments were performed with at least three different spec-

Table 3.1: Physical properties and reference quantities from experiments shown in Fig. 3.2 (sphere sedimentation experiments with a wall distance of $d/R \approx 4$)

Specimen	E /kPa	ρ_s/ kg·m^{-3}	$\overline{\gamma}$	R /mm	$\overline{Re}_{Peak}$	$U_{th,\,ub}$ /mm·s^{-1}
■ (rigid)	$2.9 \cdot 10^6$	1160.83 ± 3.9	1.2	6.0	$14.3 \cdot 10^{-2}$	14.9 ± 0.5
▲ (soft)	1712 ± 82.55	1036.70 ± 0.1	1.07	6.2	$5.0 \cdot 10^{-2}$	5.6 ± 0.1
♦ (soft)	936 ± 33.44	1007.16 ± 1.03	1.04	6.0	$2.5 \cdot 10^{-2}$	2.9 ± 0.1
● (soft)	135 ± 13.14	989.40 ± 0.9	1.02	6.0	$1.2 \cdot 10^{-2}$	1.5 ± 0.1

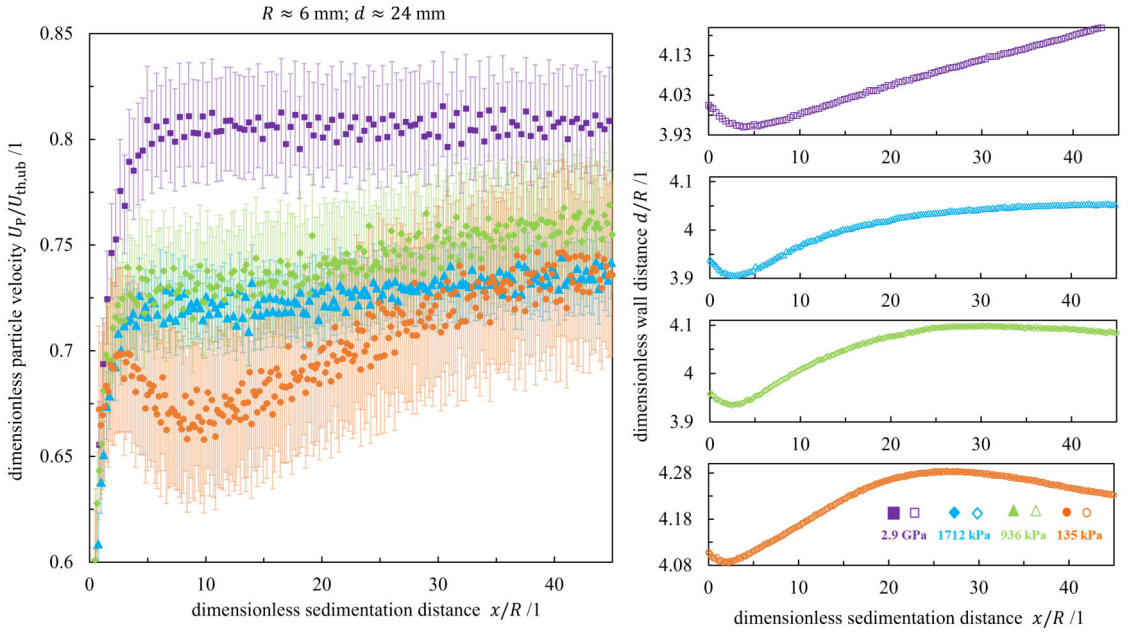


Figure 3.2: Left: dimensionless particle velocity $U_P/U_{th,ub}$ plotted against the dimensionless sedimentation distance x/R of sedimenting rigid and soft spheres with a radius of $R \approx 6$ mm in the vicinity of a plane, rigid wall. The spheres start from an initial dimensionless wall distance of $d/R \approx 4$; Right: corresponding trajectories as $(x/R) - (d/R)$-plot

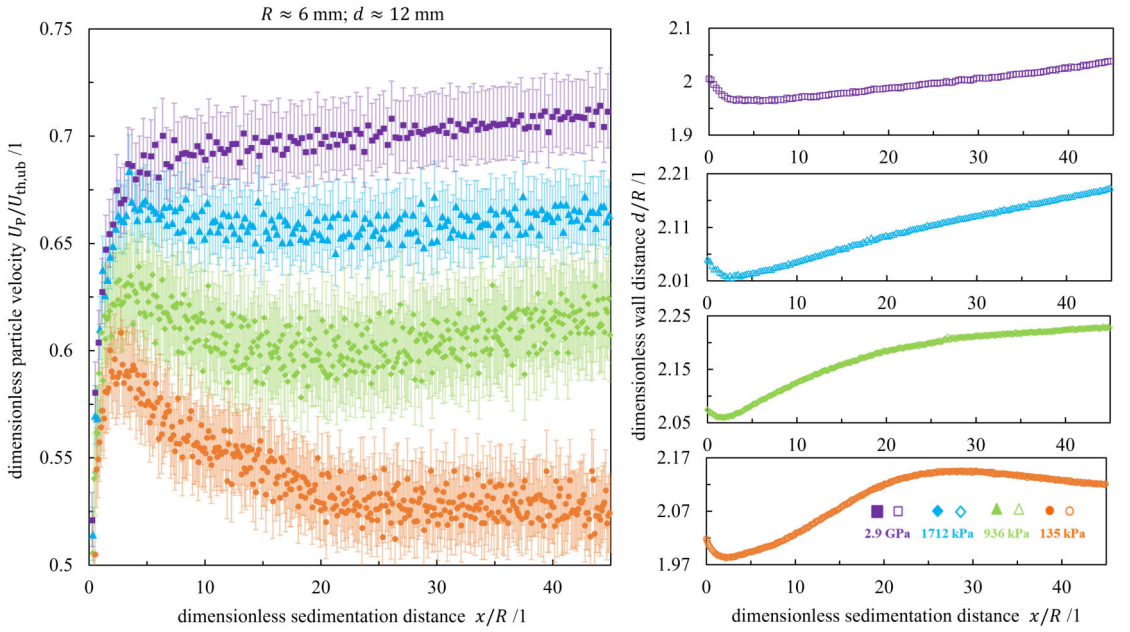


Figure 3.3: Left: dimensionless particle velocity $U_P/U_{th,ub}$ plotted against the dimensionless sedimentation distance x/R of sedimenting rigid and soft spheres with a radius of $R \approx 6$ mm in the vicinity of a plane, rigid wall. The spheres start from an initial dimensionless wall distance of $d/R \approx 2$; Right: corresponding trajectories as $(x/R) - (d/R)$-plot

imens and at least one repetition per specimen was performed. The experiments were reproducible and are representative within the shown deviations, *cf.* a complete measurement series for the softest spheres is

Table 3.2: Physical properties and reference quantities from experiments shown in Fig. 3.3 (sphere sedimentation experiments with a wall distance of $d/R \approx 2$)

Specimen	E /kPa	ρ_s/ kg·m^{-3}	$\overline{\gamma}$	R /mm	$\overline{Re}_{\mathrm{Peak}}$	$U_{\mathrm{th,\,ub}}$ /mm·s^{-1}
■ (rigid)	$2.9 \cdot 10^6$	1159.85 ± 1.51	1.2	5.9	$11.4 \cdot 10^{-2}$	14.2 ± 0.4
▲ (soft)	1712 ± 82.55	1037.05 ± 0.25	1.07	6.0	$4.2 \cdot 10^{-2}$	5.3 ± 0.1
♦ (soft)	936 ± 33.44	1007.16 ± 1.03	1.04	6.0	$2.1 \cdot 10^{-2}$	2.8 ± 0.1
● (soft)	135 ± 13.14	988.24 ± 0.39	1.02	6.0	$0.9 \cdot 10^{-2}$	1.3 ± 0.1

provided in §4 in the SI of the dissertation appendix A.1. Different measurements were not averaged, as the smallest changes in the initial conditions (*e.g.* the initial wall distance) have a considerable influence on the further development of the kinematics. Averaging could result in certain effects not becoming apparent with the necessary clarity. In Fig. 3.2 and Fig. 3.3, the theoretical velocity in the unbounded fluid, $U_{\mathrm{th,ub}}$, is used as reference for the measured particle velocity U_{P}. U_{P} is the velocity magnitude in direction of x, *i.e.*, the direction of gravitational acceleration $\boldsymbol{g}$. On the one hand, this kind of representation allows a direct comparison of the measured velocity of spheres with varying density. On the other hand, the direct influence of the wall compared to unbound sedimentation can also be read off. $U_{\mathrm{th,ub}}$ is calculated by balancing the forces acting on a sedimenting particle in the steady state as shown in Eq. 3.8.

$$6\pi\eta R U_{\mathrm{th,ub}} \left(1 + \frac{3}{16} Re_{\mathrm{P,th}}\right) = \frac{4}{3}\Delta\rho g \pi R^3 \tag{3.8}$$

In Eq. 3.8, Stokes´s drag is corrected by a factor of $O(Re)$. This correction term was introduced by Carl Wilhem Oseen in 1910. It accounts for the influence of inertia on the drag force at small but finite Reynolds numbers. Due to the acceleration of mass of the sphere, the velocity field at sufficient distance (the disturbance velocity field) deviates significantly from the velocity field assumed by Stokes. The disturbance increases drag which the fluid exerts on the surface of the sphere. [49] The theoretical particle Reynolds number was calculated by $Re_{\mathrm{P,th}} = U_{\mathrm{th,ub}} 2R\rho/\eta$. For very small Reynolds numbers, the correction term can be neglected and the theoretical velocity results in the Stokes´s velocity, see Eq. 3.6. Assessing the Reynolds number in the experiments, $\overline{Re}_{\mathrm{Peak}}$ in Tab. 3.1 and Tab. 3.2 corresponds to the measured mean Reynolds number shortly after the first transient acceleration phase. As will be discussed, the velocity shows a peak in this area in some cases. $\overline{Re}_{\mathrm{Peak}}$ is of $O(10^{-1})$ for the rigid spheres and of $O(10^{-2})$ for the soft spheres. The assumption that $U_{\mathrm{th,ub}}$ corresponds to U_{St} is valid in good approximation for the soft spheres. However, the influence of mass inertia on the drag of rigid spheres must be considered. Since Stokes´s drag is smaller than Oseen´s drag, neglecting the inertial correction term for the rigid spheres would result in an overestimation of the theoretical velocity (and consequently in an underestimation of the dimensionless

velocity). Therefore, the velocities from experiments with the rigid spheres are nondimensionalized with the theoretical velocity calculated by solving Eq. 3.8 and those of the soft spheres with $U_{\mathrm{th,ub}} = U_{\mathrm{St}}$. The error bars shown in the dimensionless velocity curves result from the statistical uncertainties in calculating $U_{\mathrm{th,ub}}$.

From the purple curves in Fig. 3.2 and Fig. 3.3 the following observations for rigid spheres can be made. The velocity curve of the rigid sphere which was released from an initial wall distance in the intermediate region (purple, left diagram in Fig. 3.2) is qualitatively comparable with a velocity curve of a rigid, heavy sphere sedimenting in an unbounded fluid. The velocity curve shows one acceleration phase in the very beginning followed by an approximately constant velocity. The sphere accelerated from rest until a dimensionless velocity of $U_{\mathrm{P,\blacksquare},4}/U_{\mathrm{th,ub}} \approx 0.80$ was reached. The measured velocity was reduced compared to the theoretical value in the unbounded fluid due to the influence of the four surrounding container walls. The value in the intermediate region is slightly lower than the one in the center at $d/R \approx 11.7$. For comparison, the dimensionless velocity in the center calculated with $U_{\mathrm{th,ub}}$ from Eq. 3.8 was measured to be $U_{\mathrm{P,\blacksquare},11.7}/U_{\mathrm{th,ub}} \approx 0.82$. [70][1]

Despite the velocity curve being very classic over the whole process of sedimentation, a close look at the trajectory of the rigid sphere sedimenting in the intermediate region shows unexpected behavior in the very beginning (purple, upper right panel in Fig. 3.2). In the first part, the sphere moved towards the wall, *i.e.*, the distance to the wall was reduced after the sphere was released. The movement from the initial position to a minimum in wall distance took place within the initial acceleration of the spheres. For the rigid spheres, the position of the minimum wall distance corresponds approximately to the end of the mass acceleration phase. This is why this part is referred to as *inertial wall attraction* in the following. To the best of our knowledge, this kinematical phenomenon has not yet been reported before. The inertial wall attraction was observed in all sedimentation experiments near a rigid plane wall, including those of soft spheres. The phenomenon will be discussed more intensively in the next subsection 3.5.1.3.

When the first acceleration phase was finished, the rigid sphere showed linear migration away from the wall with $x \sim d$. This is due to the wall-induced hydrodynamic lift force $\boldsymbol{F}_{\mathrm{L}}^{\mathrm{wi}}$, which acts perpendicularly to the wall. [52],[78] Such migration away from the wall was shown experimentally by Vasseur and Cox in 1977. [50] Vasseur and Cox found that a sphere between two plane parallel walls migrated away from the closer wall until an equilibrium position mid-way between the plates is reached. The alignment of sedimenting particles in the centerline between boundaries was shown numerically, too. [83] The large, rigid spheres in the experiments shown here did not reach an equilibrium position (independent from the release position). This suggests that migration was not yet finished during the measurement, *i.e.*, the container is

[1] Measurement from section 4.1.1 in [70]: U_{St} was used as reference for the velocity of the rigid spheres. For this reason, a smaller value for the dimensionless velocity was reported there.

too short for the sphere to reach the centerline.

All in all, one can say that, in the intermediate sedimentation region, the wall-induced lift only affects the trajectory in a noticeable manner but not the velocity. A more detailed curve analysis and further comparisons with theoretical values can be found in §I-a) in the chapter appendix 3.7.

In contrast to sedimentation in the intermediate region, the effect of the wall-induced lift force $\boldsymbol{F}_{\mathrm{L}}^{\mathrm{wi}}$ on both the dimensionless velocity and the trajectory is obvious for a sedimenting rigid sphere in the close vicinity to a wall (Fig. 3.3, purple curves). In the beginning, there is again an inertial wall attraction during the initial acceleration phase. Thereafter, the velocity keeps increasing. This is due to the decreased drag when increasing the distance to the wall.

The theoretical dimensionless velocity of a sphere sedimenting near a plane wall at $d/R \approx 2$ is $\left(U_{\mathrm{P}}/U_{\mathrm{th,ub}}\right)_{\mathrm{FO},\,\bullet\mid}\Big|_{d/R=2} = 0.72$ (Faxén´s equation with additional Oseen terms, *cf.* Eq. 3.13 in the appendix A1). This value is in the range of the measured value at this distance.
All in all, sedimentation experiments of rigid spheres show the expected, classic behaviour of sedimentation near walls. Furthermore, the measured values reflect the theoretical approximations.

The velocity curves and trajectories of the soft spheres differ fundamentally from that of the rigid spheres. Both in the intermediate region when starting from $d/R \approx 4$ (Fig. 3.2) and in the near-wall region when starting from $d/R \approx 2$ (Fig. 3.3), none of the soft spheres reached a stationary state within the measurement range. The softer the spheres were, *i.e.*, the smaller Re_{P} was, and the smaller the distance from the wall was, the more unexpected the velocity curves and trajectories are. The spheres decelerated after a shortened mass acceleration phase reaching a reduced peak in velocity, although the distance to the wall is significantly increased. This completely contradicts the classic ideas of wall-induced hydrodynamic lift and its consequences. Non of the soft spheres reached the theoretically predicted value calculated with the corresponding wall distances. Furthermore, the velocity curves and trajectories become curvier, *i.e.*, more non-linear, the softer the spheres were (and thus, the smaller Re_{P} was). A closer look at the curves reveals a number of relevant points and characteristics of the underlying dynamics which are of great importance for further modelling. One example are inflection points at a specific sedimentation distance of $x/R \approx 10$, *cf.* orange curve in Fig. 3.2. A detailed curve analysis can be found in the appendix.

If the velocity curves of the softest sphere type at various wall distances d are compared directly with each other, another interesting fact emerges. Fig. 3.9 in the appendix shows a direct comparison of exemplary velocity curves from sedimentation experiments with wall distances of $d/R \approx 2$, $d/R \approx 4$ and $d/R \approx 11.7$ (center; from previous report [70]) in one figure. It is shown that the curve in the intermediate region can be composed from parts of the other two curves by shifting the curves upwards or downwards (bright curves in Fig. 3.9), *i.e.*, the sedimentation velocity in the intermediate region is a mixture of the other two curves.

This composition works only for the softest spheres for which $Re \rightarrow 0$. This is consistent with the fact that only in this regime the Stokes´s equations are approximately linear and the principle of superposition of several hydrodynamic forces is valid. [84] This observation raised the question of whether elastic effects, *i.e.* small elastic deformations, could be the main reason for the observed long-time unsteady kinematics. Or, whether there were additional and perhaps purely hydrodynamic phenomena responsible for the unsteady sedimentation over such large time scales. Therefore, experiments with rigid spheres having particle Reynolds numbers of $O(10^{-2})$ like the soft spheres were performed. By keeping the Reynolds number constant while elastic effects were excluded, the impact of purely hydrodynamic effects should become apparent.

3.5.1.2 Sedimentation of rigid spheres ($R \approx 4$ mm; $d/R \approx 2$) at $Re_{\mathrm{P}} \approx O(10^{-2})$

Experiments with smaller, rigid spheres which had a radius of $R \approx 4$ mm and which started at an initial wall distance of $d/R \approx 2$ to the nearest wall were performed. The measured peak Reynolds number $\overline{Re}_{\mathrm{Peak}}$ of these experiments was $O(10^{-2})$. Hydrodynamically, these experiments are thus comparable to the experiments with the softest spheres discussed in the previous subsection. Fig. 3.4 shows a representative measurement of the velocity (blue-green in the upper left diagram) and a trajectory (blue-green in the bottom left diagram) of a sedimenting small, rigid sphere with a radius of $R \approx 4$ mm released from an initial distance of $d \approx 8$ mm (dimensionless wall distance $d/R \approx 2$). For better comparability, the curves of the large, rigid sphere and the large soft sphere with a Young´s modulus of $E \approx 135$ kPa (softest) from Fig. 3.3 are shown again. The diagrams on the right show mapped fit curves of the experiments with comparable $\overline{Re}_{\mathrm{Peak}}$. The corresponding material and size properties (solid densities ρ_{s} and radii R) and reference quantities are given in Tab. 3.3.

A direct comparison of experiments with rigid spheres in the near-wall region at different Reynolds numbers (a decrease from $Re_{\mathrm{P}} \approx O(10^{-1})$ to $Re_{\mathrm{P}} \approx O(10^{-2})$) shows that the deceleration behavior after the initial mass acceleration also occurs with rigid spheres. Consequently, the strong deceleration is not an elastic effect and some other effect seems to be the primary reason for the overall unsteadiness. Further-

Table 3.3: Physical properties and reference quantities from experiments shown in Fig. 3.4

Specimen	ρ_{s}/ kg·m^{-3}	$\overline{\gamma}$	R /mm	$\overline{Re}_{\mathrm{Peak}}$	$U_{\mathrm{th,\,ub}}$ /mm·s^{-1}
■ (rigid)	1159.85 ± 1.51	1.2	5.9	$1.14 \cdot 10^{-1}$	14.2 ± 0.4
● (soft)	988.24 ± 0.39	1.02	6.0	$0.9 \cdot 10^{-2}$	1.3 ± 0.1
■ (rigid)	1034.5 ± 2.8	1.07	4.1	$1.1 \cdot 10^{-2}$	2.3 ± 0.1

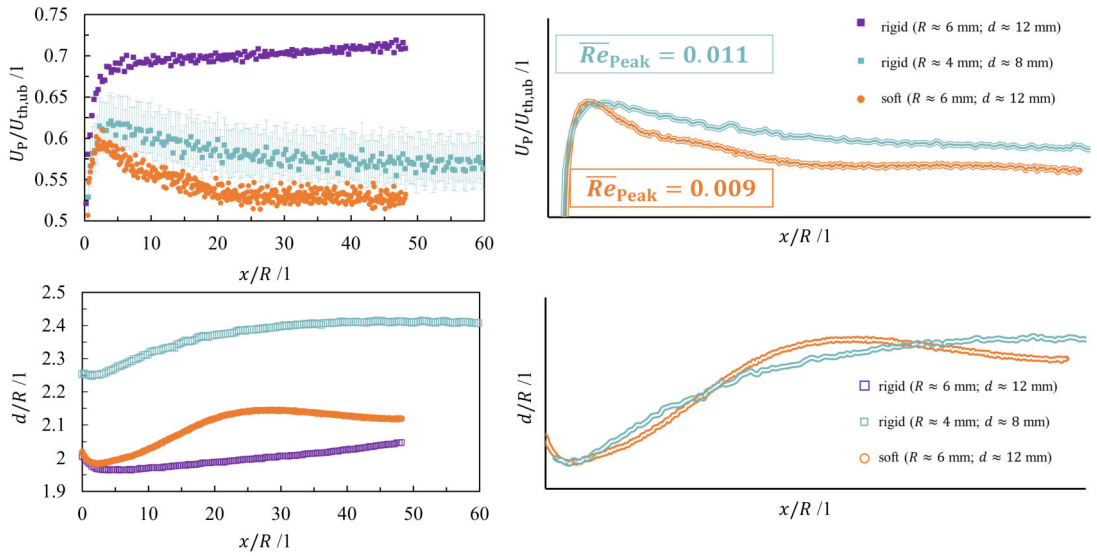


Figure 3.4: Upper left: dimensionless particle velocity $U_P/U_{th,ub}$ plotted against the dimensionless sedimentation distance x/R of a large rigid sphere with $R \approx 6$ mm (purple), a small rigid sphere with $R \approx 4$ mm (blue-green) and a large soft sphere with $R \approx 6$ mm (orange); Bottom left diagram: corresponding trajectories ($(x/R) - (d/R)$-plot); Right figures: qualitative fit curves of the small, rigid sphere and the large, soft sphere mapped on each other at the point of peak velocity or minimum wall distance, respectively.

more, based on the detailed curve analysis (see §III) in the chapter appendix 3.7), it is concluded that the nonlinearities in the particle kinematics during the migration phase and the second attraction phase, *i.e.*, the curvature, were induced by elasticity. However, the elastic interaction seems only to be of secondary importance and appears to superimpose the primary effects which seem to be of purely wall-induced, hydrodynamical nature.

We attribute the wall-induced hydrodynamic effects that cause the instationarities to forces related to the inertia of the surrounding fluid. In order to clarify the term "inertial forces", the different types of inertia involved in the sedimentation process and their different origins are reviewed.

Inertia due to mass acceleration

During acceleration, the inertial forces which are related to the inertia of mass determine the particle dynamics. These are the inertial forces which depend on the unsteady particle velocity ($\mathrm{d}\boldsymbol{U}_P/\mathrm{d}t \neq 0$). On the one hand, there is the pure mass inertia $m_P \frac{\mathrm{d}U_P}{\mathrm{d}t}$ which results from accelerating the mass of the particle from rest. And on the other hand, there are coupled particle-fluid inertial forces, *e.g.* the added mass or the Basset history force during the initial mass acceleration (*cf.* Eq. 3.1). In the sedimentation process, these inertial forces are decisive for the appearance of the velocity curve during the initial acceleration phase. In general, if particle-fluid inertial forces are important (especially when $\rho_P/\rho \to 1$), they lead to an extended transient mass acceleration phase compared to heavier particles, *i.e.*, a less steep increase of the velocity curve in the beginning.

Inertia due to fluid advection

Another type of inertial forces that can act on a particle are inertial forces due to fluid advection. Advective inertia can either originate from disturbance flows. Disturbance flows are the flows caused by advection of the fluid volume V_P, which was displaced by the particle, see Faxén´s law in Eq. 3.2. Or advective inertia on a particle can originate from separately imposed background flows. In general, advective inertial forces are forces which depend on the velocity of the surrounding fluid $\boldsymbol{U}_f$, *cf.* Eq. 3.1.

Hydrodynamic history effects

The most unintuitive and least understood type of inertial forces are the long-time persistent unsteady forces or hydrodynamic history effects, respectively. In this case, “long-time persistent” means time scales that go far beyond the initial mass acceleration. The Basset force is also a history force, but refers specifically to the phase shortly after acceleration from rest, *i.e.*, before mass inertia decays and drag forces become dominant. Hydrodynamic history effects can result, for example, from inhomogeneities in *e.g.* the shape or the material composition, or, *e.g.* from deformations of the surface. The unsteady forces come into play, when such inhomogeneities disturb the surrounding fluid, or fluid flow respectively, and the object sediments so slow, that ”it can feel the hydrodynamic history in the fluid produced by itself”.

M.V. Díaz (2021) proposed to add, in addition to the Basset history force, a second history force to the force equilibrium of the BBO equation. This additional history force has a non-singular kernel to account for inhomogeneities. [85] The regarded unsteady forces could also play a role, when spherical or non-spherical objects sediment in a time-dependent background flow, like oscillating flows. [86],[87],[88],[83]

Among other things, Feng and Joseph concluded from their simulations in 1995, that the presence of walls also tends to enhance unsteady inertial effects. In their report they stated: ”In the literature, the practice of completely ignoring the unsteady effects of inertia at low Reynolds numbers is overwhelming.”[71] This circumstance of ignorance, intentionally or unintentionally, has not changed much until today. The literature is partly very confusing concerning these unsteady effects of inertia. This is certainly also due to the fact that it is difficult to clearly distinguish between the different origins and influences on such unsteady forces, as the three types of inertial forces are coupled in many cases.

3.5.1.3 CFD simulation of the fluid flow field in a rectangular container - studying the origin of fluid inertia in the system

The assumption of a quiescent fluid within the container is only valid in the beginning at $t = 0$ s. However, as concluded, the flow field inside the container during sedimentation seems to play an important role for the particle kinematics. The visualization and measurement of the flow field using experimental methods, such

as particle image velocimetry, is difficult to implement in these experiments due to the high viscosity of the fluid. In order to gain insights into the hydrodynamics and the flow field, a computational fluid dynamics (CFD) simulation of a sedimenting rigid sphere with a radius of $R = 6$ mm and with the original container dimensions as computational domain was performed. The simulations were performed with COMSOL Multiphysics® by solving the differential equation resulting from the force balance around a sphere which falls due to gravity through a fluid domain. The sphere dynamics were coupled to the surrounding flow field.

The fluid velocity field in the spatial frame of the container, $\boldsymbol{u}_\mathrm{f}$, is calculated by solving the time-dependent Stokes´s flow equations, or creeping flow equations, respectively, for an incompressible, Newtonian fluid. The equation for the conservation of momentum reads

$$\rho \frac{\partial \boldsymbol{u}_\mathrm{f}}{\partial t} = \nabla \cdot \left[-p\boldsymbol{I} + \eta \left(\nabla \boldsymbol{u}_\mathrm{f} + (\nabla \boldsymbol{u}_\mathrm{f})^T \right) \right] + \boldsymbol{f}_\mathrm{ext} \tag{3.9}$$

and the continuity equation for the conservation of mass reads

$$\rho \nabla \cdot \boldsymbol{u}_\mathrm{f} = 0. \tag{3.10}$$

The last term in Eq. 3.9, $\boldsymbol{f}_\mathrm{ext}$, is the volume force density, or external applied force density, respectively, and reads

$$\boldsymbol{f}_\mathrm{ext} = -\rho \left(\frac{\mathrm{d}\boldsymbol{U}_\mathrm{P}}{\mathrm{d}t} + g \right). \tag{3.11}$$

Thus, the fluid is accelerated by the motion of the sphere and the sphere´s acceleration $\frac{\mathrm{d}\boldsymbol{U}_\mathrm{P}}{\mathrm{d}t}$ is the coupling parameter. The governing equation for the velocity of the sphere in direction of the gravitational acceleration $\boldsymbol{g}$ is described by the ordinary differential equation Eq. 3.12.

$$m_\mathrm{P} \frac{\mathrm{d}\boldsymbol{U}_\mathrm{P}}{\mathrm{d}t} = m_\mathrm{P} g + 2\pi \int_S r \boldsymbol{e}_g \cdot \left[-p\boldsymbol{I} + \eta \left(\nabla \boldsymbol{u}_\mathrm{f} + (\nabla \boldsymbol{u}_\mathrm{f})^T \right) \right] \boldsymbol{n} dS \tag{3.12}$$

Eq. 3.12 results from the force balance around the sphere, $\boldsymbol{F}_\mathrm{I}^P = \boldsymbol{F}_\mathrm{G} + \boldsymbol{F}_\mathrm{Buoyancy} + \boldsymbol{F}_\mathrm{D}$. Unlike in the Maxey-Riley equation (Eq. 3.1) and the Basset-Boussinesq-Oseen equation, the Basset force $\boldsymbol{F}_\mathrm{B}$ and the added mass $\boldsymbol{F}_\mathrm{Am}$ were neglected in the simulations to reduce the computational effort. In Eq. 3.12, r is the radial coordinate of the surface S of the sphere, $\boldsymbol{e}_g$ is the unit vector in direction of $\boldsymbol{g}$ and $\boldsymbol{n}$ is the corresponding normal vector on the sphere´s surface. The integral term in Eq. 3.12 is the force, which the fluid exerts on the surface of the particle, *i.e.*, the buoyancy and drag force are calculated by integrating the component of the fluid stress tensor in direction of $\boldsymbol{g}$. It was implemented in COMSOL with the built-in operation $\boldsymbol{F}_\mathrm{Buoyancy} + \boldsymbol{F}_\mathrm{D}$= `intop(-spf.T_stressx)`.

The simulated domain had the same cross-sectional dimensions as the glass container used in the exper-

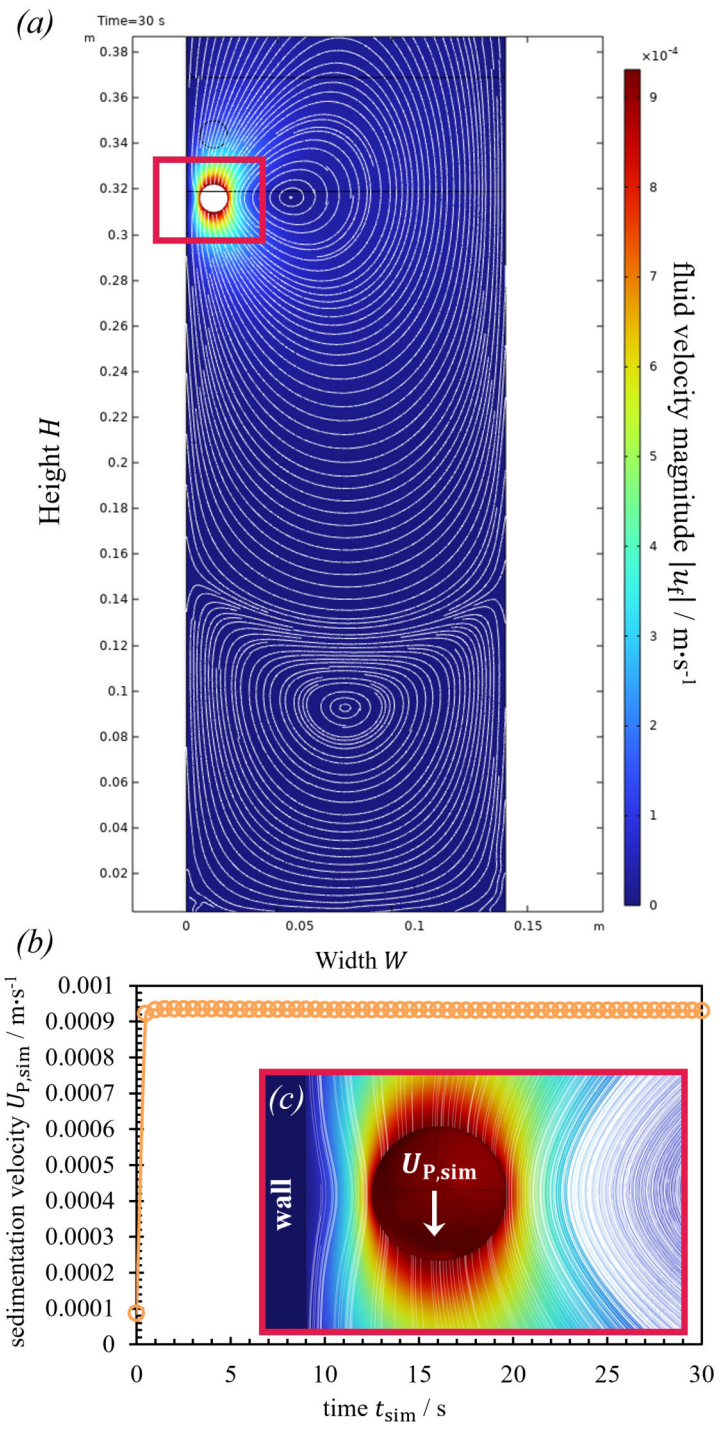


Figure 3.5: 3D simulation of a rigid sphere with a density of $\rho_s = 987.59\ \mathrm{kg{\cdot}m^{-3}}$ sedimenting at a distance of $d = 12$ mm from a no-slip boundary (magnitude of fluid velocity as contour plot and velocity streamlines on the symmetry plane (half plane trough the container)). *(a)* 2D Streamline plot of the entire simulation domain after $t_{sim} = 30$ s; *(b)* simulated sedimentation velocity plotted against the simulation time; *(c)* 3D streamline plot corresponding to a close-up of *(a)*

iments. The measured mean values from the experiments were used as physical properties of the fluid. The solid densities used to solve Eq. 3.12 were $\rho_{P,sim} = 987.59\ kg{\cdot}m^{-3}$ and $\rho_{P,sim} = 1159.8\ kg{\cdot}m^{-3}$, respectively. Applying appropriate symmetry conditions, the computation of an eighth of the domain was sufficient as a model for the sedimentation in the center of a rectangular channel, *cf.* Fig. A.7 in §3 in the SI of the dissertation appendix A.1. In contrast, the 3D domain of the model for sedimentation in the near-wall region ($d_{sim}/R = 2$) could only be reduced by half, which resulted in a high computational effort. In order to fulfill the symmetry conditions for the entire simulation and to keep the mesh parameters around the sphere surface constant, the distance between the sphere and the boundaries of the simulation domain had to be fixed. Therefore, no spatial displacement towards or away from the wall due to lift forces could be simulated with this model. The center of the sphere had a constant distance to the no-slip boundary of $d_{sim} = 12$ mm for the near-wall model and $d_{sim} = 70$ mm, respectively, for the center model. The immersion depth, *i.e.*, the distance of the center of the sphere to the liquid-gas interface, was $h_{I,1\&2} = 56$ mm (simulation 1 and 2) and $h_{I,3} = 156$ mm (simulation 3), respectively. The liquid-gas interface was modeled as open boundary with zero normal stress. The sphere was moving in the fluid domain using a moving mesh approach, *cf.* Fig. 4.1 in Chapter 4. The sphere was not modeled as a solid body but as a hollow space having the mass of the sphere. This means, that fluid-structural mechanics interactions such as deformations were explicitly not taken into account in this simulation, as the focus of the simulations was on the flow field produced by the fluid displacement of a spherical object. By using these methods, the calculation effort remained manageable in contrast to fully coupled 3D fluid-structural mechanics simulations.

The simulated particle velocities over time showed in general a short transient acceleration phase which went instantaneously over into a stationary state, *cf.* Fig. 3.5 *(b)*. This is reasonable because the solved ODE only consists of steady state forces, *i.e.*, the dynamics were undamped. The terminal velocities in the simulations and in the corresponding experiments were of same order of magnitude. The simulated velocities of the spheres with higher density were slightly larger than the measured velocities ($\Delta_{sim;d=70;1159.21} = +5.9$ % in the center and $\Delta_{sim;d=12;1159.8} = +8.3$ % in the near-wall region). The simulated particle velocity in the duct center of the sphere with lower density ($\rho_s \approx 988\ kg{\cdot}m^{-3}$) was in good agreement with the measured velocity at the first plateau (the simulated dimensionless velocity in the center was $\left(U_{P,sim}/U_{St}\right)_{d=70;987.59} \approx 0.84$ and the mean measured value of the first plateau $\left(U_{P,exp,1st}/U_{St}\right)_{d=70;987.59} \approx 0.83$, *cf.* section 4.2 in the previous report [70]. Unlike in the center, the simulated velocity in the near-wall region is significantly larger ($\Delta_{sim;d=12;987.59} = +16.5$ %) than the measured peak velocity ($U_{P,exp,Peak} = 0.8\ mm{\cdot}s^{-1}$, *cf.* Fig. 3.3). An overview of all values is shown in Tab. 3.4 in appendix A2.

Remarkably, the dimensionless velocity resulting from the simulated particle velocity in the near-wall region ($\left(U_{P,sim}/U_{St}\right)_{d=12;987.59} \approx 0.71$) is of same order of magnitude as the dimensionless values of the experiments and simulations for the sphere with higher density ($\left(U_{P,exp}/U_{th,ub}\right)_{d=12;1159.85} \approx 0.70$ and

$\left(U_{\mathrm{P,sim}}/U_{\mathrm{th,ub}}\right)_{d=12;1159.8} \approx 0.73$). This supports the observation made in the previous section, that the mass acceleration of spheres sedimenting at $Re_{\mathrm{P}} \approx O(10^{-2})$ is interrupted prematurely at $\left(U_{\mathrm{P,exp,Peak}}/U_{\mathrm{St}}\right)_{d=12;988.24} \approx 0.61$. The simulations cannot reproduce these kinematics, *i.e.*, this early interruption followed by a decrease in velocity. One obvious reason for this is that the sphere is fixed at a constant distance from the wall, which limits the evolution of the dynamics as they occur in reality.

The 2D contour plot with streamlines in Fig 3.5 *(a)* which shows the magnitude of the velocity field on the half plane of the container illustrates, that the disturbance around a falling sphere is not only limited to a small area around the sphere. Rather, the disturbed area is asymmetric, extended and reaches dimensions in the order of the characteristic length scales of the sphere.

The streamlines indicate the formation of a slow but noticeable background flow between the sphere and the walls. Due to fluid reflections at the wall far away from the sphere, a large vortex is formed. This vortex moves downwards along with the sphere. The size of this vortex depends on the width of the container and the wall distance. Furthermore, it is extended in the region above and below the sphere. The shape of the vortex is influenced by the free boundary (the liquid-gas interface), if the sphere begin to fall close to the interface (simulation 1 and 2). In this case, the far-wall vortex is asymmetric in shape. In contrast, the vortex is symmetrical when the sphere starts to sediment deeper in the fluid domain (simulation 3). The close-up in Fig. 3.5 *(c)* shows, that the far-wall vortex also influences the local disturbance flow field around the sphere. The disturbance flow field is pushed in laterally by the vortex. Vortex formation during sphere sedimentation has already been reported in numerical 2D studies in the past. [83] Also, Vasseur and Cox concluded from their calculations in 1977, that the drag on a sphere which is sedimenting far away from a plane wall (in the outer region) can be reduced due to a potential flow induced by reflections from the wall. [50]

Furthermore, the simulations illustrate the formation of another vortex on the bottom of the closed container. If the sphere began to fall close to the interface at $H = 0.4 - h_{\mathrm{I,1\&2}} = 0.344$ m, the vortex extends approximately to a height of $H = 0.14$ m, which corresponds to the container width. To exclude effects resulting from this bottom vortex, only the area above this height was considered in the evaluation of the experiments, *cf.* Fig. 3.1 *(a)* in the methods section.

More interesting insights into the dynamics were gained by evaluating the fluid stresses and the resulting forces directly on the surface of the sphere, *cf.* the integral term in Eq. 3.12. The diagram in Fig. 3.6 shows the calculated normal forces $F_{\mathrm{y,i}}$ of a sphere with density $\rho_{\mathrm{s}} = 987.59$ kg·m^{-3}. The inserts represent plots of the underlying total stresses τ_{y} in direction normal to closest wall (Fig. 3.6 *(a)*) and the viscous stresses, σ_{x}, at the surface in direction of gravity (Fig. 3.6 *(b)*).

The spheres in simulation 1 and 2 started from an immersion depth of $h_{\mathrm{I,1\&2}} = 56$ mm to the open boundary (interface). Simulation 1 (hollow circles) was performed with a higher temporal resolution (*i.e.*, smaller numerical time step which resulted in a high computational effort). The simulation was performed

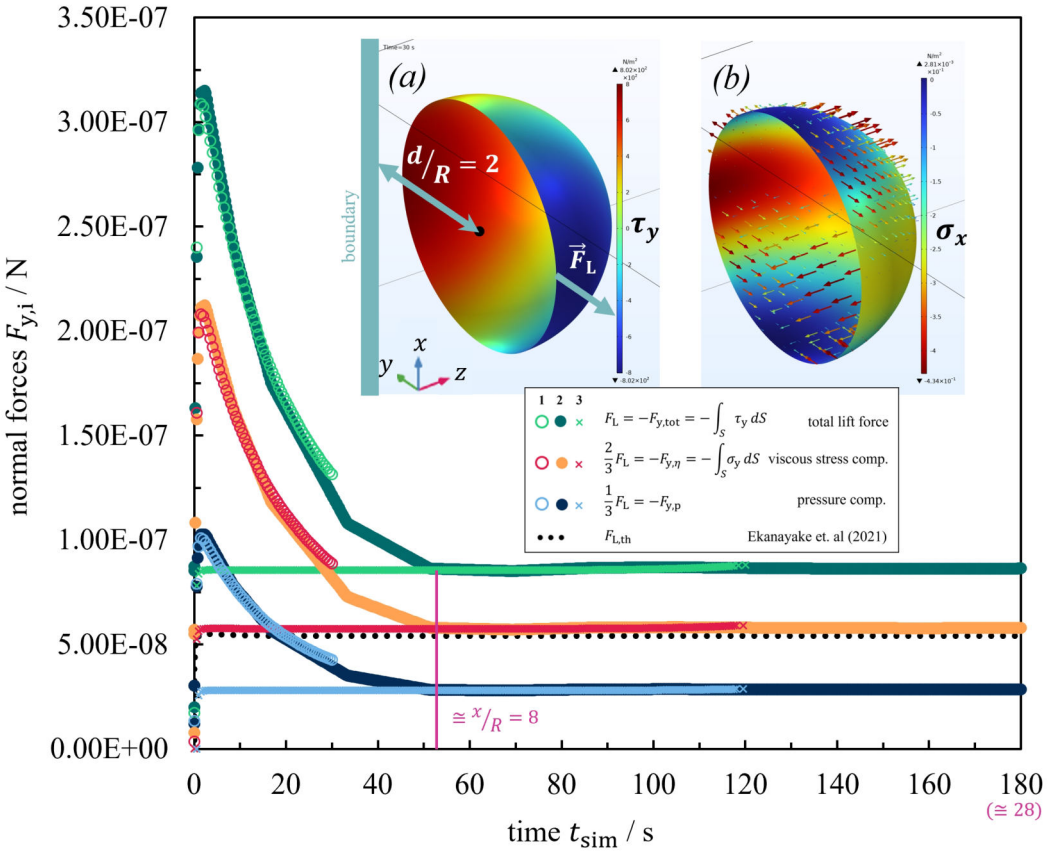


Figure 3.6: Forces $F_{y,i}$ acting on the surface of a sphere in direction normal to the near no-slip boundary (3D simulations of a rigid sphere with a density of $\rho_s = 987.59$ kg·m^{-3} sedimenting at a distance of $d = 12$ mm ($d/R = 2$) from the wall). Simulation 1 (hollow circles) and simulation 2 (filled circles) started from an immersion depth of $h_{I,1\&2} = 56$ mm and from rest. Simulation 3 (crosses) started from an immersion depth of $h_{I,3} = 156$ mm to the free surface on top. The theoretical value $F_{L,th}$ was calculated with the lift coefficient proposed by [52]. Insert *(a)*: contour plot of total stresses $\tau_{y,\,sim1}$ on the sphere surface at $t_{sim1,max} = 30$ s; Insert *(b)*: contour plot of viscous stresses parallel to $\boldsymbol{g}$ ($\sigma_{x,\,sim1}$) on the sphere surface at $t_{sim1,max} = 30$ s. Arrows: viscous stress magnitudes in y- and z-direction.

up to a simulation time of $t_{sim1,max} = 30$ s. In simulation 2 (filled circles) the computational effort was reduced by selecting larger time steps. This reduces accuracy, especially in the transient phase. However, this allowed a total time of $t_{sim2,max} = 180$ s to be simulated, which is more comparable to the large time scale in the experiment. A simulation time of 180 s corresponds to a dimensionless sedimentation distance of $x/R \approx 28$. The modelled sphere in simulation 3 started from an immersion depth of $h_{I,3} = 156$ mm in order to elucidate the influence of the interface on top.

In simulations 1 and 2, the total forces in direction of y, $F_{y,tot}$, are strongly time depended up to a time $t_{sim} \approx 50$ s (corresponding to a sedimentation distance of $x_{sim}/R \approx 8$). This long time, as well as the large distance x/R, goes far beyond the initial phase of mass acceleration. Since both simulations, *i.e.* simulations with small and large time-steps, show the same time dependence over such long time scales, numerical rea-

sons for this force overshoot are excluded. The maximum magnitude of the force overshoot is more than 3.6 times larger than in the stationary state. Such an overshoot was also observed in the simulation of spheres with a higher density ($Re_P \approx O(10^{-1})$), but this was considerably lower with 1.1 times the steady-state value, *i.e.* smaller force gradients were observed.

The simulated total lift force was compared with values of the total lift force of the model for translational motion parallel to one plane wall which was proposed by Ekanayake *et al.*, *cf.* equations 3.3 and 3.4. [52] The theoretical value was calculated with the simulated velocities $U_{P,sim}$. The theoretical lift force is instantaneously steady. Consequently, the strong time dependence of the lift force at the beginning cannot be mapped with the existing model and any fluctuations in the particle velocity, which originate, for example, from numerical inaccuracies. Apart from the initial time dependence, the stationary values are of the same order of magnitude, with the steady lift force in a rectangular duct being larger compared to the lift force induced by a single plane wall (note: the apparent correspondence with the viscous component of our simulations is a coincidence). Remarkably, dynamical switching points were also identified in the experiments at $x/R \approx 10$. After comparable length and time scales, the kinematics of particles sedimenting at lower particle Reynolds number ($Re_P \approx O(10^{-2})$) in the experiments show phenomena like switching from deceleration to acceleration, *cf.* for example the orange curve in Fig. 3.2 and the detailed curve analysis §II-a) in the chapter appendix 3.7.

In contrast to immersion near the interface, the normal forces of simulations in which the sphere was deeply immersed at the beginning (simulation 3, crosses) do not show this time dependence. This indicates that the proximity to the interface has a significant influence on the dynamics in this simulation. The large force gradients are probably a direct consequence of the vortex formation and its initial asymmetry caused by the interaction of the far-wall vortex with the interface. In the experiments, the immersion depth was less ($h_{I,exp} \approx 15$ mm, *cf.* Fig. 3.1). The influence of the interface on the vortex in the container was therefore perhaps even more pronounced and could be the cause of the unsteady phenomena at the beginning, *i.e.* the *inertial wall attraction*.

Another quantity that can be estimated by the simulations is the local deformation caused by the shear stresses. The maximum total shear stresses in the y and z direction are located in the gap between the sphere and the wall and are $|\tau_{y;z}|_{max} \approx 800$ Pa. Assuming linear elasticity, this corresponds to a linear deformation of $\Delta R_{y;z} = |\tau_{y;z}|_{max} E^{-1} R \approx 35$ µm. The approximation of the deformation with the purely viscous component in direction of gravity ($|\sigma_x|_{max} = 0.434$ Pa, *cf.* Fig. 3.6 *(b)*) leads to much smaller theoretical deformations due to shear. Based on the shear modulus $G \approx E/3$, the approximate deformation would be $\Delta R_x = 3|\sigma_x|_{max} E^{-1} R \approx 0.06$ µm. This shear deformation is almost negligible in absolute terms and at first glance it cannot be assumed that these small deformations purely due to viscous shear would have an influence on the kinematics (*cf.* perturbation parameter α from Murata discussed in our previous report).

[15],[70] Nevertheless, it should be mentioned that these small shear deformations are distributed asymmetrically on the surface of the sphere and are largest in the area between the sphere and the wall, see 3.6 *(b)*, red area of the contour plot. This should be taken into account with regard to memory forces and the long time scales on which they act.

3.5.1.4 Conclusions for rigid and elastic particles sedimenting near a plane rigid wall and and discussion of possible mechanisms

Inertial forces associated with fluid advection play a decisive role during the mass acceleration phase both at $Re_{\mathrm{Peak}} \approx O\left(10^{-1}\right)$ and $Re_{\mathrm{Peak}} \approx O\left(10^{-2}\right)$. Apart from time $t = 0$ s, the fluid around a sedimenting sphere in a rectangular duct is not quiescent and advection of the fluid in the background may be significant due to vortex formation between the sphere and the walls. Further influencing factors, such as proximity to interfaces, *e.g.*, liquid-gas interfaces, can have an effect on the formation of these background flows and significantly influence the kinematics.

Rallabandi presented in 2021 a modification of the Maxey–Riley equation 3.1. In Rallabandis modification, the inertia of a spatially varying background flow which is appreciable on the particle scale, *e.g.,* in the case of large vortex radii, is included. He concluded, that the additional force contributions due to flow curvature amplify inertial Faxén terms threefold, *i.e.,* these forces are dominant compared to wall-induced lift forces predicted by Faxén [76] And this is exactly the case with the vortex background flow and the time-dependent lift forces observed in the CFD simulations. In the very beginning of mass acceleration, when the velocity of the sphere is small compared to the peak velocity ($Re_{\mathrm{P},\, t \gtrsim 0\,\mathrm{s}} \ll Re_{\mathrm{Peak}}$), the spatial curvature of the vortex instantly induces forces that are dominant compared to the Faxén forces, *i.e.* the stationary lift forces. In the experiments, where the spheres were not fixed and were free to migrate and to rotate, these forces due to the vortex background flow may alter the trajectory in such a way that the sphere appears to be attracted instead of repelled from the wall.

When inertia due to the acceleration of mass decays, drag and inertial forces of the fluid, or lift forces respectively, associated with Faxén forces begin to dominate and lead to migration of the sphere away from the wall. This only applies if the sphere sediments with $Re_{\mathrm{Peak}} \approx O\left(10^{-1}\right)$. In contrast to spheres with $Re_{\mathrm{Peak}} \approx O\left(10^{-1}\right)$, not only inertial forces due to fluid advection but also particle-fluid inertial forces like the Basset history force and added mass play a role for spheres with smaller density accelerating to $Re_{\mathrm{Peak}} \approx O\left(10^{-2}\right)$. As a consequence, the sum and coupling of these types of inertial forces during the mass acceleration phase damp the dynamics in this regime and result in a shift to large time scales. At this large times scales, the unsteady forces (*cf.* type *Hydrodynamic history effects*) kick in and become apparent.

At larger Re_P, the spheres are simply too fast to sense the small contributions of their disturbance flow, reflections from the wall or other unsteady forces. The coupling of inertial forces in the special case of elastic objects near walls leading to the superimposed nonlinearities (fluid advection, hydrodynamic history and deformability-induced forces) might also be summarized and referred to as *elastohydrodynamic memory effect*. One consequence of the elastohydrodynamic memory effect is the nonlinear lift after the inertial attraction phase. Another consequence is the second nonlinear attraction phase of the soft spheres observed at the end of the measurement.

The reversal of signs with respect to the velocity (*cf.* deceleration although increasing the wall distance) is attributed to wall-induced unsteady forces and important for both the rigid spheres and the elastic spheres sedimenting at low Reynolds numbers $Re_{\mathrm{Peak}} \approx O\left(10^{-2}\right)$.

One may ask now why the attraction and the nonlinearities in the trajectory have never been detected in experiments in the past. Indeed, the migration towards the wall is small and a precise measurement technique is needed. Since applications within the considered Reynolds number regime usually can be found in the field of microsystems, the resolution of such small distances is technically challenging. This applies in particular to optical measurements in the vicinity of interfaces and solid walls. The relative increase Δd from the minimum wall distance to the maximum wall distance after migration was approximately 20% of the radius (*cf.* Fig. 3.1 *(b)* and axis scales in Fig. 3.2 and Fig. 3.3 (right)). This difference would be very small in absolute terms especially for microscopic spheres and may therefore not have been noticed until now. With our measurement method on the macroscopic scale, we were able to measure these differences accurately.

3.5.2 Sedimentation of a rigid sphere near a plane, elastic wall

In subsection 3.5.1, the focus was on the sedimentation of rigid and elastic spheres near a rigid wall. It was found that there was a large influence of the particle Reynolds number on the dynamics. Inertial forces determined the sedimentation dynamics while elastic effects only kick in at large time scales and were of secondary importance.

In this subsection, sedimentation of rigid spheres with radii of $R \approx 6$ mm and $R \approx 4$ mm were performed in the vicinity of an elastic wall. The larger spheres were denser, thus having a larger particle Reynolds number ($Re_P \approx O(10^{-1})$) than the smaller spheres ($Re_P \approx O(10^{-2})$), *cf.* material data in Tab. 3.3 in the previous section. An elastic layer with a thickness of approximately 13 mm was fixed on one of the inner walls of the container. The other dimensions and the arrangement of the sphere in the container during the experiments

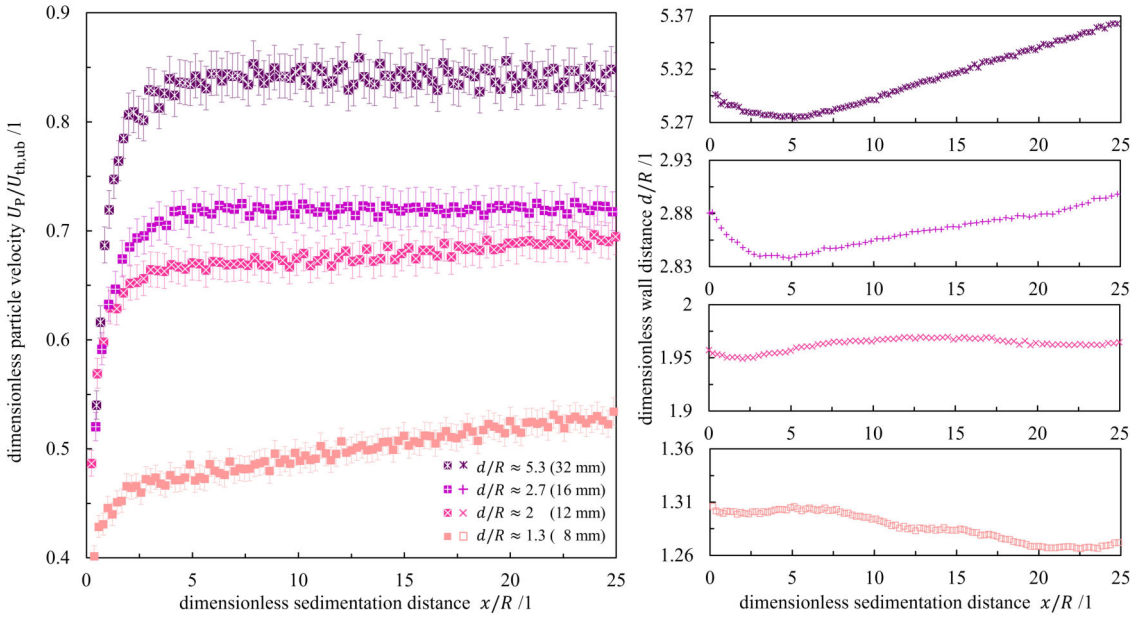


Figure 3.7: Left: dimensionless particle velocity $U_P/U_{th,ub}$ plotted against the dimensionless sedimentation distance x/R of sedimenting rigid spheres ($E \approx 2.9$ GPa) with a radius of $R \approx 6$ mmn and higher density $\rho_s \approx 1159$ kg·m^{-3} in the vicinity of a plane, soft layer ($E \leq 135$ kPa) starting from various initial wall distances $d/R \approx 1.3$ (8 mm), $d/R \approx 2$ (12 mm), $d/R \approx 2.7$ (16 mm) and $d/R \approx 5.3$ (32 mm); Right: corresponding trajectories as $(x/R) - (d/R)$-plot

were maintained, see Fig. 3.1.[2]

The pairing "rigid sphere near elastic wall" at various Reynolds numbers is compared with the corresponding experiments of "rigid spheres near rigid wall". Since the influence of inertial forces on the sedimentation of the "rigid sphere near rigid wall" pairing is known from previous experiments and simulations, deviations in the experiments from this subsection can clearly be attributed to the elasticity of the wall.

3.5.2.1 Rigid spheres ($R \approx 6$ mm) sedimenting at $Re_P \approx O(10^{-1})$ near a plane, elastic wall

Fig. 3.7 shows velocity curves as dimensionless $(x/R) - \left(U_P/U_{th,ub}\right)$-plot (left) and trajectories as dimensionless $(x/R) - (d/R)$-plot (right) of the denser, rigid spheres ($\rho_s \approx 1159$ kg·m^{-3}; $E \approx 2.9$ GPa) with a radius of $R \approx 6$ mm sedimenting in the vicinity of a plane, soft layer ($E \leq 135$ kPa). The spheres were released from various wall distances $d/R \approx 1.3$ (8 mm), $d/R \approx 2$ (12 mm), $d/R \approx 2.7$ (16 mm) and $d/R \approx 5.3$ (32 mm).

While there is no specific influence of the elastic wall on sedimentation in the intermediate region be-

[2]The measurement range covered a distance of $x \approx 150$ mm, see dashed area in Fig. 3.1. This was the maximum distance over which a plane elastic layer could be ensured experimentally. The lower part of the soft layer is susceptible to penetration of a thin film of oil between the glass and the plate with the elastic layer during insertion of the soft layer. Therefore, only the upper area of the container which was vertically aligned was considered to avoid additional influences stemming from the soft incline.

tween the duct center and the wall, the kinematics of the large, dense spheres differ from those in the vicinity of rigid plane walls when sedimenting in the near-wall region of the elastic layer, (*cf.* equivalent near the rigid wall in Fig. 3.3).

The spheres released at a distance of $d/R \approx 2$ to the elastic layer accelerated to a velocity plateau. The plateau velocity and the corresponding Reynolds number are in good agreement with the values from the rigid wall after finishing the mass acceleration phase and before starting the migration. A second increase in velocity could be observed after approximately $x/R \approx 10$. However, there was no noticeable increase in wall distance and migration appeared to be interrupted.

Sedimentation of rigid spheres starting closest at the elastic wall at $d/R \approx 1.3$ ($d \approx 8$ mm) showed no implementation of a velocity plateau after mass acceleration, see lowest curve in Fig. 3.7. It appears more as if the second part of the mass acceleration phase (the part of decaying mass inertia) was damped. The sphere reached a velocity of only $U_P/U_{th,ub} \approx 0.47$ after the short, steep mass acceleration phase followed by a phase of less steep increase in velocity starting from $x/R \approx 3$.[3] The total increase in velocity in the range $3 \leq x/R \leq 25$ was quite large for the short distance covered. Considering this large increase in velocity, the trajectory seems all the more surprising. After a short period of sedimentation at almost constant wall distance, the sphere started to decrease the wall distance. While decreasing the distance to the wall, the sphere showed some wave-like, undulatory movement. The undulating trajectory appears as if there is a "battle" between attractive and repulsive forces. Finally, the spheres find themselves in a kind of trap, which is why this behavior was named *elastohydrodynamic particle trapping*. The elastohydrodynamic trapping can clearly be attributed to an elastic effect or elastohydrodynamic effect, respectively, since this behavior did not occur in experiments near the rigid wall.

More details on the curve analysis can be found in §i) in the chapter appendix 3.7.

3.5.2.2 Rigid spheres ($R \approx 4$ mm) sedimenting at $Re_P \approx O(10^{-2})$ near a plane, elastic wall

To investigate the influence of inertial forces on sedimentation near an elastic layer, experiments at lower particle Reynolds number ($Re_P \approx O(10^{-2})$) were performed. Experiments were performed with less dense, rigid spheres ($\rho_s \approx 1038.3 \pm 1.6$ kg·m^{-3}) with a radius of $R \approx 4$ mm. The spheres were of the same type as used for the experiments near the rigid wall in subsection 3.5.1.2. Fig. 3.8 shows velocity curves as dimensionless $(x/R) - \left(U_P/U_{th,ub}\right)$-plot (left) and trajectories as dimensionless $(x/R) - (d/R)$-plot (right) of

[3] A value for the velocity of a rigid sphere starting at $d/R \approx 1.3$ near a rigid wall for comparison could not be measured. A dimensionless wall distance of $d/R \approx 1.5$ was the minimal wall distance in experiments near the rigid wall which could be implemented. Implementation of smaller gap sizes was not possible due to constructional restrictions in the experimental setup. The measured dimensionless velocity of a large, rigid sphere with $R \approx 6$ mm starting at $d/R \approx 1.5$ near a rigid wall was $U_{P,\blacksquare,1.5}/U_{th,ub} \approx 0.56$, see Fig. A.10 in §4 in the SI of the dissertation appendix A.1

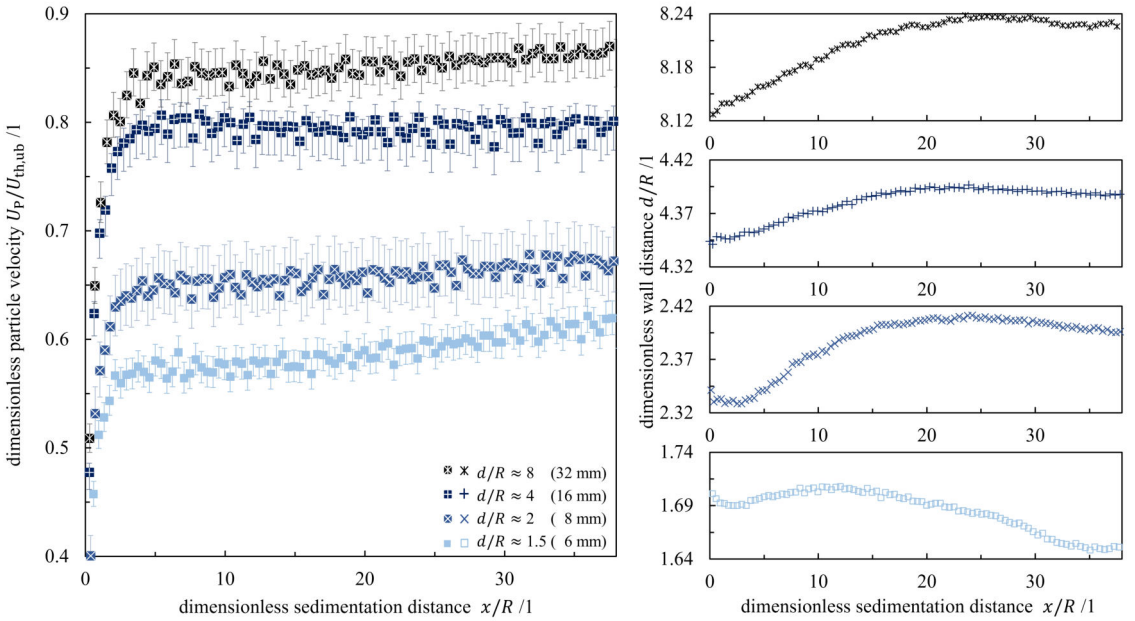


Figure 3.8: Left: dimensionless particle velocity $U_P/U_{th,ub}$ plotted against the dimensionless sedimentation distance x/R of sedimenting rigid spheres with a radius of $R \approx 6$ mm and lower density $\rho_s \approx 1038.3 \pm 1.6$ kg·m^{-3} in the vicinity of a plane, soft layer ($E \leq 135$ kPa) starting from various initial wall distances $d/R \approx 1.5$ (6 mm),$d/R \approx 2$ (8 mm), $d/R \approx 4$ (16 mm) and $d/R \approx 8$ (32 mm); Right: corresponding trajectories as $(x/R) - (d/R)$-plot

spheres sedimenting at $Re_P \approx O(10^{-2})$ in the vicinity of a plane, soft layer ($E \leq 135$ kPa). The initial wall distances were $d/R \approx 1.5$ (6 mm), $d/R \approx 2$ (8 mm), $d/R \approx 4$ (16 mm) and $d/R \approx 8$ (32 mm).

In these experiments, it was more difficult to identify clear trends in the kinematics for sedimentation at distances $d/R \gtrapprox 2$. Some of the experiments showed two stages of acceleration and others catenary velocity curves. In general, the dynamics appeared to be sensitive to changes in the initial conditions and the conditions during the experiment. A detailed curve analysis for the curves of experiments shown in Fig. 3.8 can be found in §ii) in the chapter appendix 3.7.

In contrast to the experiments of this sphere type near the rigid wall at $d/R \approx 2$, none of the spheres sedimenting at the elastic wall showed that strong deceleration and persistent smaller velocity after the initial mass acceleration, *cf.* Fig. 3.4.

The trajectory of the experiment at $d/R \approx 2$ ($d \approx 8$ mm) in Fig. 3.8 is curvy and shows a clear second attraction phase in the end although the sphere accelerated strongly at this stage. This behaviour is reminiscent of the trajectory of the softest spheres at $d/R \approx 2$ near the rigid wall (●, orange trajectory on the right Fig. 3.3). This supports the assumption that nonlinearities and curvature in the kinematics are elasticity-induced effects coupled with inertial forces, *e.g.* history effects. However, there were also trajectories recorded which show an undulating movement towards the soft wall. It is possible that the elastic effects which lead to the late, second attraction in the previous case, set in earlier in these experiments or were dominant compared

to the inertial forces. No clear trend could be determined under which conditions the respective type of kinematics occurred.

In contrast, the trend for spheres which started closest to the soft wall at $d/R \approx 1.5$ ($d \approx 6$ mm) was clear. All spheres which started at $d/R \approx 1.5$ showed an undulating motion towards the wall although being accelerated strongly, *i.e.*, *elastohydrodynamic trapping* was observed.

3.5.2.3 Mechanisms near a soft wall

The comparison between the kinematics near rigid walls and near elastic walls shows clearly, that the pairings "elastic sphere near rigid wall" and "rigid sphere near elastic walls" differ fundamentally. This applies in particular to the sedimentation in the near-wall region close to the elastic wall where elastohydrodynamic effects appear to dominate in both Reynolds number regimes, $Re_\mathrm{P} \approx O(10^{-1})$ and $Re_\mathrm{P} \approx O(10^{-2})$.

Using the elastohydrodynamic (EHD) lubrication theory and the Lorentz reciprocal theorem, Bertin *et al.* (2022) obtained the forces acting on a sphere which translates with velocity U_P along an elastic surface. [51] In their soft-lubrication model, they found an additional inertial-like term for the force in direction of U_P. The inertial term depends on the acceleration of the sphere $\frac{\mathrm{d}\boldsymbol{U}_\mathrm{P}}{\mathrm{d}t}$ and the elastic material properties of the soft surface. Consequently, their model predicts increasing drag if the sphere accelerates in the vicinity of a soft layer, *i.e.*, the term depending on $\frac{\mathrm{d}\boldsymbol{U}_\mathrm{P}}{\mathrm{d}t}$ acts as a damping term in the differential equation. These mathematical predictions are consistent with our experimental observation of a damped mass acceleration phase of spheres sedimenting in the near-wall region at $d/R \lessapprox 2$ independent of the Reynolds number.

Attractive phases, or trapping phases, respectively, likely to the observations made in our experiments were also found by Urzay in 2010. Urzay made an asymptotic analysis and used numerical methods to investigate the influence of the triple interaction of hydrodynamic, intermolecular (electric double layer produced by solvents leading to attractive or repulsive forces) and substrate deformation effects on the motion of a solid sphere translating along a soft substrate. [89] With his theoretical studies, he predicted so called elastohydrodynamic adhesion regimes in which spherical, solid particles move towards soft substrates which are then entrapped near the surface without direct contact. It was assumed, that the elastohydrodynamic adhesion, *i.e.*, the phenomenon of sticking without contact, was produced by the interaction of elastic instabilities in form of surface bifurcations in the substrate with hydrodynamic and intermolecular forces.

For soft solids like the PDMS used in our experiments it is known that the surface can show undulation, creases or wrinkles under certain circumstances like compression of the material. [90],[91],[92] It is conceivable that the compression induced by the fluid pressure in the gap between the sphere and the surface also led to surface instabilities in form of small, local deformations, *i.e.* surface undulations. Such surface

undulations might influence the surrounding fluid velocity field and consequently the fluid inertial forces acting on the sphere. This could explain the superimposed undulating motion while moving towards the wall which was observed both for the denser spheres sedimenting at $Re_P \approx O(10^{-1})$ and for the sphere with lower particle Reynolds number of $Re_P \approx O(10^{-2})$. Since the surface deformations appear to be small, it is obvious why the undulation was only noticeable for the denser spheres that sedimented closest to the wall while the undulations were already measurable for larger wall-distances for spheres sedimenting at $Re_P \approx O(10^{-2})$. The fluid needed less time for reflection at the deformed wall. As a result, even the denser spheres had enough time to interact with the deformed wall. The spheres sedimented at $Re_P \approx O(10^{-2})$ still had enough time to interact with the elastic wall at larger distances. However, at larger wall distances, the fluid inertial forces, *e.g.* history forces, become more and more dominant again. If the sphere sediments in that transition region, this can lead to the observed ambiguity in the kinematics.

All in all, further discussions about the many variations and data sets from the experiments in the transition region at Reynolds numbers $Re_P \approx O(10^{-2})$ are not expedient at this point. For this Reynolds number regime, no clear tendencies were shown to date where the dynamic switching points are and which kinematical behavior can be attributed to elastic effects or which to inertial forces. The dynamical system reacts very sensitive to the various influences (inertia, material properties, distance to walls in all directions, etc.). Which effect finally prevails seems to depend on the smallest nuances. This is a classic example of an unstable, nonlinear system. It is difficult to predict what effect a particular change will have on the system. Data science methods like Machine Learning (ML) could be promising methods to make predictions based on the data sets gained from such experiments.

3.6 Summary and Conclusions

In this study, the sedimentation of spherical particles starting from rest near a plane wall within a rectangular duct was investigated. The experiments were performed at low particle Reynolds numbers ($Re_P \lessapprox O(10^{-1})$). Additionally, elastohydrodynamic interactions were involved in the sedimentation experiments, both for the case of elastic particles as well as for an elastic wall. A multitude of new and unknown phenomena such as persistent unsteady motion, nonlinear kinematics and specific characteristics of the kinematics, *e.g.* the *inertial wall attraction* or *elastohydrodynamic trapping* near soft walls, were found. These phenomena have their origin in the complex coupling of inertial forces and elastic effects, or elastohydrodynamic effects, respectively. It was shown, that inertial forces such as inertia due to fluid advection and hydrodynamic history determine the dynamics at particle Reynolds number $Re_P \approx O(10^{-2})$ and that it is inevitable to include

these forces in the context of modelling particle dynamics at small, but finite Reynolds numbers.

The kinematics of rigid and elastic spheres which sedimented due to gravity along a wall inside a rectangular glass container were measured by a camera system and analyzed by image processing. By using high viscosity silicone oil, macroscopic spheres with a radius of $R \approx 6$ mm and $R \approx 4$ mm sedimented in the same hydrodynamic regime as µm-sized particles in aqueous liquids.

Sedimentation of rigid and elastic spheres near a plane, rigid wall

While rigid spheres sedimenting with particle Reynolds numbers of $Re_P \approx O(10^{-1})$ showed the kinematics as they were predicted by classic wall-lift and drag models, spheres with decreasing Young´s moduli and smaller density (lower Reynolds numbers $Re_P \approx O(10^{-2})$) became more and more untypical. At first sight, the trajectories and the particle velocities showed a noticeable dependence on the elastic modulus of the material used. The more elastic the spheres were, the more nonlinear were the velocity curves and the trajectories. This was also the case when the particles sedimented far away from the wall, for example in the intermediate region between the center of the duct and one wall. A detailed curve analysis showed that the trajectories and the velocity curves contradicted in parts the theories about hydrodynamic interactions of rigid particles with rigid walls, *i.e.*, existing wall-lift models for the steady motion were not applicable to describe the motion of the soft spheres in these experiments. For example, in the very beginning, the softest particles accelerated due to their mass to a reduced velocity compared to the theoretical velocity in the unbounded fluid. However, after reaching a peak in velocity, the elastic sphere abruptly stopped to accelerate and decreased the velocity strongly. All this happened, although the sphere simultaneously increased the wall distance by migration more than rigid ones did. For clarification, existing wall-lift models predict a larger velocity when increasing the wall-distance due to a reduction in drag acting on the sphere. In other cases, it was vice versa. The spheres decreased the wall distance while accelerating, *i.e.*, the spheres seemed to be attracted by the wall.

With respect to such attraction phases, a to date unrecognized kinematical phenomenon of sedimenting particles with small but finite mass inertia in the vicinity of plane walls, the *inertial wall attraction* during mass acceleration, was observed. Both the rigid and the elastic particles with Reynolds numbers in the range $10^{-2} \lessapprox Re_P \lessapprox 10^{-1}$ decreased the wall distance during the first mass acceleration phase, *i.e.*, they migrated towards the wall instead migrating away from it after they were released from rest. We relate this phenomenon to the interplay between advection of the surrounding fluid in the beginning of sedimentation (vortex formation) in combination with symmetry breaking due to the confining walls and the liquid-gas interface which was in proximity to the release position. The inertial wall attraction is a purely hydrodynamic, wall and interface induced inertial effect occurring for all particles sedimenting in this hydrodynamic regime

under these experimental conditions.

Further comparisons of the kinematics of rigid spheres with those of the elastic spheres at comparable Reynolds number revealed that the inertial forces were of primary importance for the deceleration behavior after the initial acceleration phase. Since rigid spheres sedimenting at $Re_P \approx O(10^{-2})$ also decelerated after the initial acceleration phase although increasing the wall distance, it became clear that this effect is not related to elasticity. Unlike the soft spheres, the decrease in velocity was almost linear and the total decrease was smaller than the one of the soft spheres. For this reason, these other nonlinearities, *i.e.*, the curvatures in the velocity curves and trajectories of the soft spheres, are attributed to the influence of elasticity. However, the elasticity-induced effects were superimposed and only of secondary order.

To shed light on the flow field and possible mechanisms behind the inertial forces leading to the contradictory acceleration and deceleration of the sphere with respect to the migration behavior, a computational fluid dynamics (CFD) simulation of a sphere moving through a rectangular fluid domain was performed. Forces due to fluid-structure interactions were explicitly not calculated and the sphere was not modeled as a solid body but as a hollow sphere with the mass of a solid. However, deformations of the elastic bodies could be estimated using the simulated fluid shear stresses. Only the steady forces such as gravity, buoyancy and the steady drag force acting on the sphere´s surface were calculated to reduce the computational effort. Using a moving mesh approach, we were able to show that the lift forces during acceleration due to gravity are strongly time-dependent in the vicinity of open boundaries. The calculated fluid velocity field showed that the disturbance around the sphere is not limited to a small area around the sphere, but that the disturbance flow expands and reaches dimensions in the range of the sphere´s diameter. Furthermore, the streamlines indicate the formation of a slow but noticeable background flow between the sphere and the wall due to reflections of the fluid from the wall. It was shown that a large vortex is formed between the sphere and the walls far away. The curvature of the streamlines forming this vortex is comparable with the curvature of the sphere´s surface, *i.e.*, the velocity gradients stemming from the reflections at the wall and the resulting advective inertia are also appreciable for the particle. Such inertial forces due to advective inertia are already known *e.g.*, from the Saffman lift force. In the beginning of sedimentation, when the surrounding fluid is still almost quiescent, the flow curvature-induced inertial forces might be dominant compared to the (repulsive) wall-induced Faxén lift forces. Theses forces combined with symmetry breaking at the wall and at the free liquid-gas interface might alter the sphere´s trajectory and the sphere is attracted instead of repelled from the wall. This mechanism would explain the inertial wall attraction which was observed in the experiments of all spheres sedimenting at $Re_P \approx O(10^{-1})$ down to $Re_P \approx O(10^{-2})$. For the rigid spheres sedimenting at higher Reynolds number $Re_P \approx O(10^{-1})$, the Faxén wall-lift forces began to dominate as the inertia due to mass decayed and led to migration of the sphere away from the wall, as predicted by classic hydrodynamic, wall-lift models. In contrast to spheres with $Re_P \approx O(10^{-1})$, it seemed that the inertial forces due to fluid

advection, or flow curvature-induced lift forces, respectively, and the particle-fluid inertial forces like the Basset history force persist longer for the spheres sedimenting at $Re_P \approx O(10^{-2})$. The (fluid) inertial forces just did not seem to loose their relevance when the inertia due to mass decayed. Instead, the sum of all inertial forces, or the coupling of the different types of inertial forces respectively, damp the dynamics during the initial mass acceleration phase in such a way that the result is a shift to very large time scales. At this large time scales, additional forces, such as wall-induced, unsteady forces or unsteady forces due to deformability, can kick in. The peculiar behavior of decreasing velocity although increasing the wall distance was attributed to such wall-induced, unsteady (history) forces. In the special case of elastic interaction, the effect resulting from the complex coupling of inertial forces due to fluid advection, history forces and elasticity-induced forces leading to the superimposed nonlinearities was named *elastohydrodynamic memory effect.*

Sedimentation of a rigid sphere near a plane, elastic wall

Instationarities were also observed in sedimentation of rigid particles along an elastic wall which was immersed and fixed at the inner side of one wall of the rectangular duct. However, there were clear differences compared to the pairings of elastic or rigid particles near a rigid wall. It was shown, that, even in the region close to the wall, it does definitely matter, if the pairing is ”elastic particle near rigid wall” or ”rigid particle near elastic wall”. This insight has concrete implications on the idea of the underlying physical mechanisms and the assumptions in mathematical models.

Sedimentation of rigid spheres at $Re_P \approx O(10^{-1})$ in the intermediate region between the center of the duct and the walls showed that the kinematics were influenced by the presence of the surrounding walls. The velocity was lowered compared to the theoretical velocity in the unbounded fluid and both inertial wall attraction and migration away from the wall was observed. However, elasticity of the nearest wall had no specific influence on the kinematics, *i.e.*, on the appearance of the curves. In contrast, when sedimenting in the near-wall region of the elastic layer ($2 \gtrapprox d/R > 1$) the kinematics started to differ from those in the vicinity of rigid plane walls. While the counterpart at rigid walls started to increase the velocity linearly after the mass acceleration phase, there was a delay in increasing the velocity in the close vicinity to an elastic wall. It appeared as if the second part of the mass acceleration phase was damped and as if the mass inertial forces decayed much more slowly. However, at the end of this damped acceleration phase, the spheres accelerated strongly again. Especially considering this strong acceleration, the trajectories in this area were again very surprising. While decreasing the distance to the wall during the phase of strong acceleration, the spheres showed a superimposed wave-like, undulatory movement. Since the spheres appeared to be trapped between certain distances to the wall and not repelled from it, it was spoken of *elastohydrodynamic trapping* in this context. For spheres sedimenting at particle Reynolds number $Re_P \approx O(10^{-1})$, the elastohydrodynamic

interaction was only noticeable at small wall distances. Only within small distances, the spheres at higher particle Reynolds number had enough time, to interact with the deformed wall, *i.e.* the fluid reflected at the deformed wall reached the rigid particle within the given time.

Experiments in proximity to the elastic wall were also performed with spheres sedimenting at lower Reynolds numbers of $Re_P \approx O(10^{-2})$. In this hydrodynamic regime, the sphere did still have enough time to interact with the soft wall even at larger wall distances. However, the influence of inertial forces like hydrodynamic history was present as well. The presence of inertial forces led to ambiguities in the kinematics which made it difficult to highlight clear qualitative trends in both the measured velocities and the trajectories of experiments in this Reynolds number regime. This was especially true for the experiments of spheres starting at initial wall distances in the transition region ($d/R \gtrapprox 2$), *i.e.*, shortly before entering the near-wall region of the elastic wall. In this region, there seemed to be some kind of competition between inertial forces and elasticity-induced effects. The system reacted sensitively to small changes in the experimental conditions, *e.g.*, the initial wall distance. Therefore, the system can be regarded as unstable. Specific conclusions about which effects are induced by inertial forces and which by elasticity cannot be drawn to date. In contrast, the results of experiments which were performed relatively far away from this transition region and in the near-wall region showed clear trends. For example, the undulation towards the soft wall in the near-wall region, the *elastohydrodynamic trapping,* was observed in all experiments, *i.e.*, the elastohydrodynamic interaction was dominant at small gap sizes.

Overall consequences

The kinematics measured in our experiments illustrated how complex the interactions between hydrodynamics, walls and elasticity are. The experiments showed that many phenomena in the field of particle-laden fluid flows near walls are still undescribed and therefore do not yet found application in common dynamic models. Especially, the instationarities and nonlinearities, which were shown in particular at very small Reynolds numbers in interaction with elasticity, cannot be represented or approximated with existing stationary models for rigid bodies. The common assumption that the drag on a solid body at particle Reynolds numbers $Re_P < 1$ is adequately described by the stationary Stokes' drag loses its validity at the latest in the presence of walls. The experiments of this study show impressively that there are still large differences even in the creeping flow regime ($Re_P \lessapprox O(10^{-1})$) if the density of the body changes slightly and the Reynolds number varies by an order of magnitude of 10^{-1}. But it is precisely this range of Reynolds numbers that is highly relevant for applications, for example in the flow of microorganisms, blood flow or the wastewater treatment of water contaminated with microplastics. Sedimentation also plays a decisive role in otherwise highly dynamic processes, *e.g.* in bioreactors where microscopic, biological particles have to be transported

close to a catalytic surface. If stagnant dead spaces are created, *e.g.* by microstructures or obstacles, the particles can reach the surface only by less effective mechanisms like sedimentation. It is therefore important to understand the sedimentation process at low Reynolds numbers in detail. In order to develop more accurate models for the motion of microscopic particles in liquids, fluid inertial forces, unsteady history forces and other effects such as elastohydrodynamic effects must be taken into account, even if the computational effort for this still seems very high at present. A combination of further experiments, direct numerical simulations and data science methods, such as machine learning, may be the key in the future to better distinguish between the individual effects and to develop effective mathematical models to describe the motion of microscopic particles. Unfortunately, Sir George Gabriel Stokes did not have these modern methods because it was he himself, who already knew in 1851: "The formula ($-\boldsymbol{F} = 6\pi\eta R\boldsymbol{U}$) determines, in the particular case of a sphere, that part of the whole resistance which depends on the first power of the velocity, even though the part which depends on the square of the velocity be not wholly insensible."[27]

Declaration of Interests. The authors report no conflict of interest.

Acknowledgements. Funded by the Deutsche Forschungsgemeinschaft (DFG, German Research Foundation) – Project-ID 172116086 – SFB 926. The experiments and simulations were performed in frame of subproject A10 "Elastohydrodynamic interactions of particles flowing over microstructured surfaces" in the Collaborative Research Center 926 (CRC926 MICOS).

3

3.7 Chapter Appendix

A1 Additional analysis Sec. 3.5

Additional analysis Sec. 3.5.1 - sedimentation near rigid wall

I) Detailed curve analysis for rigid spheres sedimenting at $Re_P \approx O(10^{-1})$

I-a) Rigid sphere near rigid wall in the intermediate region ($d/R \approx 4$)

Although there was a noticeable migration away from the wall of the rigid sphere which was released from $d/R \approx 4$, there was no noticeable increase in velocity. The rigid sphere increased its wall distance by more than 20 % of its radius ($\Delta d \geq 0.2R$) over a sedimentation distance of $\approx 40R$. A theoretical estimate of the increase in velocity resulting from the wall-induced lift of the nearest wall can be obtained by calculating the theoretical dimensionless velocities at the beginning and at the end of the experiment. As mentioned before, the influence of inertia on the drag of a sedimenting rigid sphere must be considered since the Reynolds number $\overline{Re}_{\mathrm{Peak}}$ is of $O(10^{-1})$. For such a purpose, Faxén´s Eq. 3.5 has been extended with additional Oseen terms of $O(Re)$. [34] The corrected dimensionless velocity for a sphere with larger mass inertia near a plane wall given by

$$\left(\frac{U_P}{U_{\mathrm{th,ub}}}\right)_{\mathrm{FO},\bullet|} = 1 - \frac{3}{16}Re_{\mathrm{P,th}} - \frac{9}{16}\left(\frac{R}{d}\right)\cdot\chi + \frac{1}{8}\left(\frac{R}{d}\right)^3 - \frac{45}{256}\left(\frac{R}{d}\right)^4 - \frac{1}{16}\left(\frac{R}{d}\right)^5 \tag{3.13}$$

with

$$\chi = 1 - \frac{4}{3}\left(\frac{Re_{\mathrm{P,th}}}{4\,(R/d)}\right) + \frac{23}{16}\left(\frac{Re_{\mathrm{P,th}}}{4\,(R/d)}\right)^3 - .... \tag{3.14}$$

According to Eq. 3.13, the rigid sphere with the corresponding material properties at $d/R \approx 4$ would have a theoretical dimensionless velocity of approximately $\left(U_P/U_{\mathrm{th,ub}}\right)_{\mathrm{FO},\bullet|}\Big|_{d/R=4} = 0.86$. This theoretical value is, of course, larger than the measured value of about 0.8 since Eq. 3.13 considers only the influence of one wall on the velocity. Consequently, the velocity is overestimated. Nevertheless, Eq. 3.13 can be used to estimate a theoretical increase in velocity due to the wall-induced lift stemming from the closest wall. The theoretical increase is calculated with the measured wall distances between positions $x/R \approx 5$ (starting the migration) and $x/R \approx 45$ (end of measurement). This results in a small linear increase of

$\Delta_{5\ldots45}\left(U_P/U_{th,ub}\right)_{FO,\bullet|} \approx 0.008$. The measured dimensionless velocity only shows an increase of approximately $\Delta_{5\ldots45}\left(U_P/U_{th,ub}\right) \approx 0.002$ over the whole measurement range. Therefore, the dimensionless velocity appeared almost stationary after the transient acceleration in the experiments.

I-b) Rigid sphere in the near-wall region ($d/R \approx 2$)

Interestingly, the increase in wall distance $\Delta d \approx 0.1R$ at $d/R \approx 2$ is smaller than in the intermediate region. However, the measured increase in velocity is larger than in the intermediate region ($\Delta_{5\ldots45}\left(U_P/U_{th,ub}\right)_{FO,\bullet|} \approx 0.02$). This larger influence on the velocity is consistent with the theoretical estimations. Eq. 3.13 predicts a theoretical increase of $\Delta_{5\ldots45}\left(U_P/U_{th,ub}\right)_{FO,\bullet|} \approx 0.012$. The theoretical dimensionless velocity of a sphere sedimenting near a plane wall at $d/R \approx 2$ is $\left(U_P/U_{th,ub}\right)_{FO,\bullet|}\Big|_{d/R=2} = 0.72$. The measured mean dimensionless velocity at $x/R \approx 27$, *i.e.*, where the sphere in the experiments again reached a distance of $d/R \approx 2$ due to migration, is $U_{P,\blacksquare,2}/U_{th,ub} \approx 0.7$.

II) Detailed curve analysis for soft spheres sedimenting at $Re_P \approx O(10^{-2})$

II-a) Soft spheres in the intermediate region ($d/R \approx 4$)

Velocity: The soft spheres with the largest and the intermediate Young´s modulus ($E \approx 1712$ kPa (▲, blue) and $E \approx 936$ kPa (♦, green)) which were released from $d/R \approx 4$ (Fig. 3.2) accelerated due to their mass to a mean dimensionless velocity of approximately $U_P/U_{th,ub} \approx 0.72\ldots0.73$. This was less than for the rigid sphere at this distance. After the initial acceleration due to its mass, the spheres sedimented with approximately constant velocity up to $x/R \approx 10$. After sedimentation of this distance, the spheres continued to accelerate, *i.e.*, acceleration became apparent again. The soft sphere with largest E accelerated up to a dimensionless velocity of $\left(U_{P,\blacktriangle}/U_{th,ub}\right)_{Max} \approx 0.736$. This corresponds to an increase in velocity of $\Delta\left(U_{P,\blacktriangle}/U_{th,ub}\right) \approx 0.015$ with respect to the first plateau. The spheres with intermediate E accelerated up to $\left(U_{P,\blacklozenge}/U_{th,ub}\right)_{Max} \approx 0.76$ ($\equiv \Delta\left(U_{P,\blacklozenge}/U_{th,ub}\right) \approx 0.03$ with respect to the first plateau). Such an acceleration in multiple stages was also observed when the spheres sedimented in the duct center. [70] Unlike with the release in the duct center, no second plateau with a terminal sedimentation velocity was established in the intermediate region.

The kinematics of sedimentation experiments of the softest spheres ($E \approx 135$ kPa (●,orange)) which were released at $d/R \approx 4$ showed a completely different, and, at first sight, surprising and unexpected behavior. After releasing the sphere, it accelerated up to a peak in dimensionless velocity of $\left(U_{P,\bullet}/U_{th,ub}\right)_{Peak} \approx 0.698$. Then, the sphere changed abruptly from acceleration to deceleration. The sphere decelerated until a minimum velocity of $\left(U_{P,\bullet}/U_{th,ub}\right)_{Min} \approx 0.66$ was reached. Interestingly, the dynamical behavior again changed at the sedimentation distance of $x/R \approx 10$. From this dynamic switching point, the sphere accelerated again strongly up to $\left(U_{P,\bullet}/U_{th,ub}\right)_{Max} \approx 0.74$. The velocity curve is overall nonlinear. While such an

unsteady and nonlinear behavior may seem surprising at first sight, it should be noted that the fact that sedimenting particles may accelerate and decelerate has already been observed experimentally in viscoelastic fluids, *i.e.*, where further influence factors play a role. [73]

Wall distance: Nonlinearities are also shown in the trajectories of the soft spheres (Fig. 3.2, right side). In general, the trajectory is the curvier, the more deformable the spheres were. The inertial attraction phase of all soft spheres was followed by a repulsion phase, or migration, respectively. The smaller the Youngs´s modulus was, the steeper is the trajectory, *i.e.*, the larger was the migration rate $d'(x)$. The trajectory of the soft sphere with largest E (blue) flattens in the end. The intermediate soft and the softest sphere (green and orange) instead migrated to a maximum in wall distance and then turned back to the wall, *i.e.*, they decreased the wall distance again.

If the trajectory of the softest sphere (orange) is compared with its velocity curve, the acceleration behavior becomes even more unintuitive. After the inertial wall attraction, the sphere decelerated although the wall distance increased strongly. Trajectory and velocity contradict each other from the perspective of wall-bounded models for the drag force like Faxén´s drag force model, see Eq. 3.5. In principle, the change from deceleration to acceleration would also suggest a change in direction of the trajectory. However, the trajectory shows an inflection point. At this point, there is a change from progressive increase to degressive increase in wall distance. This in turn suggests the decay of some kind of unsteady force at that point. Inflection points in the kinematics are already known from velocity curves during the first transient acceleration. A. B. Basset developed a decay function for the complete fall of a sphere starting from rest in an unbounded fluid. The resulting velocity curve is "S"-shaped and shows an inflection point when inertial forces such as inertia due to mass ($\boldsymbol{F}_{\mathrm{I}}^{\mathrm{P}} = m_{\mathrm{P}} \frac{\mathrm{d}\boldsymbol{U}_{\mathrm{P}}}{\mathrm{d}t}$) decay and drag becomes dominant. [23],[34] The velocity curve of softest spheres which started sedimentation from $d/R \approx 4$ shows an additional inflection point. However, the additional inflection point is not within the first transient acceleration, but at a much later time at position $x/R \approx 26$. At this position, the trajectory shows a maximum in wall distance. From this position on, the sphere started to return to the wall, *i.e.*, there is a second wall attraction phase. Meanwhile, the increase in velocity became degressive. It is already obvious from Fig. 3.2 that the shape of the velocity curves and trajectories continuously changes the softer the spheres become.

II-b) Soft spheres in the near-wall region ($d/R \approx 2$)

Velocity: Also, for the soft spheres released at a wall distance of $d/R \approx 2$, there is a clear influence that continuously emerges with increasing deformability or decreasing particle Reynolds number Re_{P}, respectively, see Fig. 3.3 (left side). As for the spheres released at a larger distance, there is an acceleration phase during which inertial wall attraction occurs, in the very beginning. The behavior that spheres decelerate

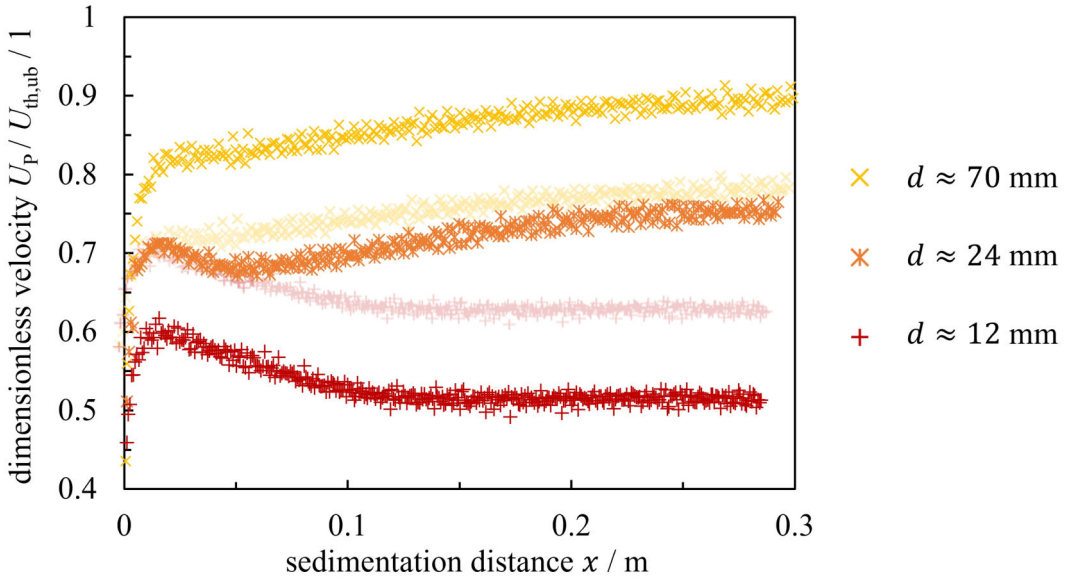


Figure 3.9: Dimensionless particle velocity $U_P/U_{th,ub}$ plotted against the sedimentation distance x of sedimenting soft spheres ($E \approx 135$ kPa) with a radius of $R \approx 6$ mm in the vicinity of a plane, rigid wall. The spheres started from various wall distances of $d \approx 12$ mm ($d/R \approx 2$); $d \approx 24$ mm ($d/R \approx 4$) and $d \approx 70$ mm (center of a rectangular duct); Bright curves: upwards and downwards shifted curves, matched on the point of the peak velocity of the intermediate curve.

after this first acceleration, which was already observed for the softest sphere released at the larger distance, is more prominent at shorter wall distance. Here, all soft spheres accelerated to a peak in velocity and then decelerated. The more deformable the spheres were and the lower the particle Reynolds number Re_P was, the lower was the peak velocity. All peak velocities were lower than the velocity of the rigid spheres at that initial distance and the theoretical velocity calculated with Eq. 3.5 $(U_P/U_{St})_{F,\bullet}|_{d/R=2} = 0.721$. Furthermore, the soft spheres had longer deceleration phases the more deformable they were and the lower the particle Reynolds number Re_P was.

The soft sphere with largest E (▲, blue) decelerated slightly after the first acceleration phase (see Fig. 3.3, left). Then, the sphere accelerated again to approximately the peak velocity. As with the rigid sphere, this could be related to the fact that drag is notably decreased by the sphere moving almost constantly away from the wall after the inertial wall attraction (see Fig. 3.3, right). The migration rate $d'(x)$ was higher than the migration rate of the rigid spheres at that distance. The soft sphere with intermediate Young´s modulus (♦, green) decreased the dimensionless velocity more than the stiffer one ($\Delta\left(U_{P,\blacklozenge}/U_{th,ub}\right) \approx -0.04$). At position $x/R \approx 20$ the sphere began to accelerate again. This sphere did not reach the peak velocity within the measurement range again. The velocity curves of spheres with the largest and intermediate Young´s modulus could possibly be described by catenaries, *i.e.,* hyperbolic functions. The migration phase of spheres

with intermediate E started with a progressive increase in wall distance. Like in the experiments with this Young´s modulus starting from a larger initial distance, the trajectory shows an inflection point at $x/R \approx 10$. There, the migration went over into degressive increase.

The softest sphere (●, orange) which started from $d/R \approx 2$ decreased its dimensionless velocity most. The peak in dimensionless velocity after the mass acceleration phase $\left(U_{\mathrm{P},\bullet}/U_{\mathrm{th,ub}}\right)_{\mathrm{Peak}} \approx 0.6$ was reduced to $\left(U_{\mathrm{P},\bullet}/U_{\mathrm{th,ub}}\right)_{\mathrm{Min}} \approx 0.52$, *i.e.,* a total decrease of $\Delta\left(U_{\mathrm{P},\bullet}/U_{\mathrm{th,ub}}\right) \approx -0.08$.

Wall distance: The softer the spheres were, the more nonlinear the migration became. The trajectory of the soft sphere with intermediate Young´s modulus flattens in the end. The trajectory of the softest sphere is qualitatively comparable with the one sedimenting in the intermediate region. The softest sphere decreased the wall distance again at the end although the dimensionless velocity remained almost constant in this phase.

III) Detailed curve analysis for rigid spheres sedimenting at $Re_{\mathrm{P}} \approx O(10^{-2})$

Velocity: The small, rigid sphere accelerated to a peak in velocity of $\left(U_{\mathrm{P},\blacksquare}/U_{\mathrm{th,ub}}\right)_{\mathrm{Peak}} \approx 0.61$. The dimensionless peak velocity is in the same range as the $\left(U_{\mathrm{P}}/U_{\mathrm{th,ub}}\right)_{\mathrm{Peak}}$ of the softest sphere which had a comparable Reynolds number. The fact that, at the same particle Reynolds number, both the small rigid sphere as well as the larger soft sphere accelerated to the same reduced peak velocity and then decelerated implies that the velocity reduction after the first transient phase is a hydrodynamics-dependent quantity and not an elasticity-induced effect. After reaching the peak, the small sphere decelerated in good approximation linearly to a dimensionless velocity of $\left(U_{\mathrm{P},\blacksquare}/U_{\mathrm{th,ub}}\right)_{\mathrm{Min}} \approx 0.57$, *i.e.,* a total decrease of $\Delta\left(U_{\mathrm{P},\blacksquare}/U_{\mathrm{th,ub}}\right) \approx -0.04$. This decrease is approximately half the decrease of the softest sphere. This in turn implies that elasticity enhanced deceleration, *i.e.,* elasticity led to a larger deceleration rate. Thereafter, the small sphere sedimented stationary with the reduced velocity $\left(U_{\mathrm{P},\blacksquare}/U_{\mathrm{th,ub}}\right)_{\mathrm{Min}}$.

Wall distance: The initial dimensionless wall distance of the small sphere in the experiment was $d/R \approx 2.25$. This is initially further away from the wall than the experiments used for the comparison. However, experimentally, it became more difficult to set the initial distance accurately the smaller the spheres were. Like all previously considered experiments, the small sphere reduced the wall distance after releasing it from the pipette. The inertial wall attraction was also observable during the first transient acceleration phase. However, the total decrease in wall distance $\Delta\left(d/R\right)_{R=4mm} = \left(d/R\right)_0 - \left(d/R\right)_{\mathrm{min}} \approx -0.01R$ due to the inertial wall attraction was much smaller than for the larger spheres ($\Delta\left(d/R\right)_{R=6mm} \approx -0.04R$). After the inertial wall attraction, the sphere increased the wall distance progressively and changed quickly to a degressive increase. After a sedimentation distance of approximately 40R was reached, the trajectory flattens. From there on, the sphere sedimented at an equilibrium wall distance without further migration. Mapping the trajectories on each other at the point of minimum wall distance shows that the total increase

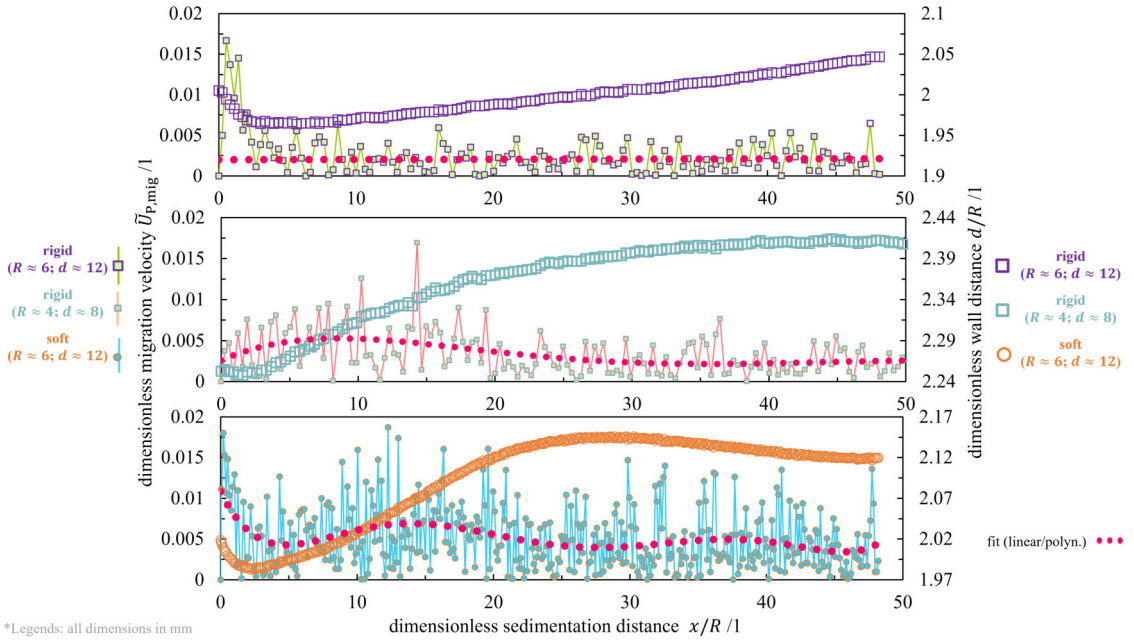


Figure 3.10: Dimensionless migration velocity $\widetilde{U}_{\mathrm{P,mig}}$ of a rigid sphere ($R \approx 4$ mm and $R \approx 6$ mm) and a soft sphere ($R \approx 6$ mm; $E = 135$ kPa) sedimenting near a plane, rigid wall plotted against the dimensionless sedimentation distance x/R (filled symbols with lines). Red, dotted curves: linear fit curve (top) and polynomial fits with $n = 5$ (middle) and $n = 6$ (bottom) of the measured migration velocity; Hollow symbols: corresponding trajectory ($(x/R) - (d/R)$-plot); The spheres started from an initial position of $d/R \approx 2$.

$\Delta(d/R) = (d/R)_{\mathrm{max}} - (d/R)_{\mathrm{min}}$ is of the same order of magnitude (see right diagram in Fig. 3.4). Unlike the soft spheres, the small rigid spheres had no second attraction phase at the end. Additionally, the trajectory of the soft sphere shows larger curvature during the migration phase compared to the small, rigid sphere.

Migration velocity: The curvature in the trajectory is directly related to the migration velocity $U_{\mathrm{P,y}}$. $U_{\mathrm{P,y}}$ is the velocity directed perpendicularly to the sedimentation velocity. Fig. 3.10 shows measurements of the dimensionless migration velocity $\widetilde{U}_{\mathrm{P,mig}} = U_{\mathrm{P,y}}/U_{\mathrm{th,ub}}$ of a large, rigid sphere ($R \approx 6$ mm) with $Re_{\mathrm{P}} \approx 10^{-1}$(top), a small, rigid sphere ($R \approx 4$ mm) with $Re_{\mathrm{P}} \approx 10^{-2}$(middle) and a soft sphere ($R \approx 6$ mm) with $Re_{\mathrm{P}} \approx 10^{-2}$(bottom). All experiments were performed with an initial wall distance of $d/R \approx 2$. The corresponding trajectories are also plotted in the diagram on the secondary axis.

The migration velocity curve of the large, rigid sphere ($R \approx 6$ mm; $Re_{\mathrm{P}} \approx O(10^{-1})$; top diagram) is still in line with expectations. The migration velocity is small and scatters around a constant value. Consistently, linear migration leads to a stationary migration velocity ($\widetilde{U}_{\mathrm{P,mig}} = U_{\mathrm{P,y}}/U_{\mathrm{th,ub}} \approx 0.0021 \pm 0.0015$, *i.e.*, 0.2 % of the theoretical sedimentation velocity in an unbounded fluid $U_{\mathrm{th,ub}}$, *cf.* Tab.3.3). During the initial acceleration phase (or the inertial wall attraction, respectively), there is a peak in velocity. The peak velocity is several times larger than the constant migration velocity. After the inertial attraction was finished, the velocity decreased abruptly. The velocity curve of the small, rigid sphere ($R \approx 4$ mm; $Re_{\mathrm{P}} \approx O(10^{-2})$; middle) shows more fluctuations of the velocity during the migration phase. The maximum of $\widetilde{U}_{\mathrm{P,mig}}$ was

during the migration phase and was approximately 0.5 % of $U_{\mathrm{th,ub}}$ (cf. the fit curve). The maximum is located approximately at the inflection point which appears at a sedimentation distance of $\approx 10R$. After the maximum was reached, the velocity decreased to a small and constant velocity which is comparable with the dimensionless, terminal migration velocity of the large sphere.

The migration velocity of the soft spheres ($R \approx 6$ mm; $Re_{\mathrm{P}} \approx O(10^{-2})$; bottom) fluctuated strongly over the entire measurement range. For the softest sphere a peak in migration velocity during the inertial wall attraction phase was detected. The $\widetilde{U}_{\mathrm{P,mig}}$ in this phase is of same order of magnitude as in the experiments with the large, rigid spheres. The velocities during the migration phase were overall larger than for the small, rigid spheres. The maximum in the mean migration velocity (*cf.* the fit curve) is also located at the inflection point which appears at a sedimentation distance of $\approx 10R$. This corresponds to the inflection point in the trajectory. Unlike the rigid spheres, no constant velocity after the migration phase was detected for the soft spheres. The dimensionless migration velocity after the migration phase was in general larger ($\widetilde{U}_{\mathrm{P,mig}} = U_{\mathrm{P,y}}/U_{\mathrm{th,ub}} \approx 0.0049 \pm 0.0038$ for $x/R > 10$). Additionally, a second peak in velocity was detected during the second attraction phase. However, the second peak was of smaller order of magnitude as the velocities during the inertial attraction and during the migration phase (*cf.* polynomial fit curve).

Additional analysis Sec. 3.5.2 - sedimentation near elastic wall

i) Detailed curve analysis for rigid spheres sedimenting at $Re_{\mathrm{P}} \approx O(10^{-1})$

i-a) Rigid sphere near elastic wall in the intermediate region ($d/R \approx 2.7$; $d/R \approx 5.3$)

Velocity curves of spheres released in the intermediate region from initial wall distances of $d/R \approx 2.7$ and $d/R \approx 5.3$ are qualitatively comparable with velocity curves of rigid spheres released near rigid walls, *cf.* rigid sphere in the intermediate region at $d/R \approx 4$ in subsection 3.5.1.1. The corresponding trajectories are also qualitatively comparable with those at rigid walls in the range of dimensionless sedimentation distances of $0 < x/R \leq 25$. Inertial wall attraction during the mass acceleration phase was followed by linear migration away from the nearest wall and towards the centerline. The migration rate $d'(x)$ was of same order as in the intermediate region at the rigid wall (approximately $0.1R$ increase in wall distance per $25R$ of sedimentation distance). Thus, while sedimentation was clearly influenced by the walls in this area between the center of the duct and the walls, elasticity of the wall had no specific influence on the kinematics, *i.e.*, on the appearance of the curves.

i-b) Rigid sphere near elastic wall in the near-wall region ($2 \gtrapprox d/R > 1$)

The spheres released at a distance of $d/R \approx 2$ to the elastic layer accelerated to a velocity plateau of $U_{\mathrm{P}}/U_{\mathrm{th,ub}} \approx 0.67$. The average particle Reynolds number during the constant phase was $\overline{Re}_{\mathrm{P}} \approx 1.18 \cdot 10^{-1}$. Since the plateau velocity and the corresponding Reynolds number are in good agreement with the values

from the rigid wall after finishing the mass acceleration phase, the elastic layer had no significant influence on the velocity during the mass acceleration phase. The total increase in velocity from the end of the first acceleration phase to $x/R \approx 25$ was $\Delta\left(U_P/U_{th,ub}\right) \approx 0.024$. This was a larger increase than in the equivalent experiments at the rigid wall which was only ≈ 0.01 in the range $5 \leq x/R \leq 25$. This large increase in velocity within this short range would suggest a larger migration rate $d'(x)$, *i.e.*, a steeper trajectory, if the drag on sphere was assumed to be dependent on the wall distance in the classic, direct manner. However, there was no noticeable increase in wall distance at all. The sphere sedimented with almost constant wall distance along the elastic layer.

In contrast, sedimentation of rigid spheres starting closest at the elastic wall at $d/R \approx 1.3$ ($d \approx 8$ mm) reached a velocity of only $U_P/U_{th,ub} \approx 0.47$ after the steep mass acceleration phase followed by a phase of less steep increase in velocity starting from $x/R \approx 3$. The total increase in velocity in the range $3 \leq x/R \leq 25$ was $\Delta\left(U_P/U_{th,ub}\right) \approx 0.056$ which is quite large for the short distance covered.

ii) Detailed curve analysis for rigid spheres sedimenting at $Re_P \approx O(10^{-2})$

ii-a) Rigid sphere near elastic wall in the intermediate region ($d/R \approx 4$ and $d/R \approx 8$)

After the mass acceleration phase, the sphere which started farthest away from the wall at $d/R \approx 8$ ($d \approx 32$ mm) accelerated to a constant dimensionless velocity plateau of $U_P/U_{th,ub} \approx 0.85$. From $x/R \approx 15$ on, the sphere accelerated and increased velocity slightly $\Delta\left(U_P/U_{th,ub}\right) \approx 0.010$ in the range $15 < x/R \leq 45$). During the phase of constant velocity, the sphere increased the wall distance linearly with large migration rate $d'(x)$. During the second acceleration phase, however, the wall distance remained almost constant.

The velocity of the sphere which started at $d/R \approx 4$ ($d \approx 16$ mm) appeared to be approximately constant. A closer look on this curve and on curves from other experiments (not plotted here) shows, that the curves are partially reminiscent of the hanging curves (catenaries) discussed for the least soft spheres shown in Fig. 3.3 (▲, blue curve on the left), which sedimented at a closer distance of $d/R \approx 2$ to the rigid wall. This fact is interesting regarding the comparable density of these two spheres and the particle Reynolds number, which was of comparable order of magnitude. The trajectory of the sphere started at $d/R \approx 4$ shown on the right of Fig. 3.8 showed a less steep increase in wall distance than the sphere started farther away. After the migration, the sphere sedimented at a approximately constant distance to the wall.

There were also velocity curves within the measurement series at $d/R \approx 4$ (min. 8 experiments per series with different specimens of this sphere type) which showed two stages of acceleration (not shown in Fig. 3.8). This behaviour is comparable to the least soft spheres sedimenting at the same wall distance ($d/R \approx 4$) near the rigid wall.

ii-b) Rigid sphere near elastic wall in the near-wall region ($2 \gtrapprox d/R > 1$)

The fact that both catenary curves and two stages of acceleration were measured for the velocity also ap-

plied to the spheres which started at distances in the near-wall region at $d/R \approx 2$ ($d \approx 8$ mm) and $d/R \approx 1.5$ ($d \approx 6$ mm). In sedimentation experiments shown in Fig. 3.8, the two lower velocity curves showed the case of two stages of acceleration. In other experiments within these two series of measurement, the velocity curve was a hanging, catenary curve, as discussed for the wall distance $d/R \approx 4$.

A2 Simulations

Experimental vs. simulated dimensionless sedimentation velocities in the near-wall region

$\left(U_{\mathrm{P,exp}}/U_{\mathrm{th,ub}}\right)_{d=12;1159.85} \approx 9.9/14.2 \approx 0.70$

$\left(U_{\mathrm{P,sim}}/U_{\mathrm{th,ub}}\right)_{d=12;1159.8} \approx 10.7/14.6 \approx 0.73$

$\left(U_{\mathrm{P,exp,Peak}}/U_{\mathrm{St}}\right)_{d=12;988.24} \approx 0.8/1.3 \approx 0.61$

$\left(U_{\mathrm{P,sim}}/U_{\mathrm{St}}\right)_{d=12;987.59} \approx 0.93/1.31 \approx 0.71$

Table 3.4: Simulated sedimentation velocity for solid densities $\rho_s \approx 988$ kg·m^{-3} and $\rho_s \approx 1159$ kg·m^{-3} in the center and in the near-wall region of a rectangular duct

d /mm	ρ_s / kg·m^{-3}	$U_{\mathrm{P,\,exp}}$ /mm·s^{-1}	$U_{\mathrm{P,\,sim}}$ /mm·s^{-1}	Δ_{sim}
70	1159.21	11.9	12.60	+5.9 %
70	987.59	1.1 (1st plateau) 1.2 (2nd plateau)	1.10	-0.4 %
12	1159.8 (Sim) 1159.85 (Exp)	9.9	10.73	+8.1 %
12	987.59 (Sim) 988.24 (Exp)	0.8 (Peak)	0.93	+16.5 %

Updates. Figures, Equations, Tables and references are renumbered to provide a consistent and clear allocation in this thesis. The general style, like colors and fonts are changed to provide a uniform format.

Equation 3.7 was added in section 2.3.

4 Computational fluid dynamics simulations of single particle sedimentation in a rectangular duct

Contents

4.1 Abstract . . . 85
4.2 Introduction . . . 86
4.3 Methods . . . 89
4.3.1 Parameter and numerical settings . . . 89
4.3.2 Geometry and Mesh . . . 91
4.4 Results . . . 94
4.4.1 Particle velocity and flow field . . . 95
4.4.2 Fluid stresses on the surface . . . 101
4.4.3 Traction forces, drag and lift . . . 105
4.5 Conclusions . . . 111
4.6 Chapter appendix . . . 115

4.1 Abstract

The sedimentation of a sphere in a rectangular fluid domain was modeled and computed using three-dimensional computational fluid dynamics (3D CFD) simulations. The transient dynamics of a sphere falling near a plane wall ($d/R = 2$) and close to an open boundary representing the liquid–air interface were solved and coupled with the time-dependent creeping flow equations for a Newtonian fluid with high viscosity. The primary goal of the simulations was to visualize the flow field within the rectangular container used in prior experiments, where experimental techniques such as particle image velocimetry were not feasible due to the

fluid's high viscosity. The simulation employed a moving mesh approach based on an Arbitrary Lagrangian-Eulerian (ALE) formulation with a co-moving domain surrounding the sphere. Two particle densities were simulated, corresponding to particle Reynolds numbers of $Re_P \approx O(10^{-1})$ and $Re_P \approx O(10^{-2})$, respectively. The computed fluid velocity field and streamlines revealed the formation of a large vortex between the particle and the distant wall, which, during the initial acceleration phase, was influenced by the open boundary. Additionally, the particle velocity and traction forces in both the direction of fall and normal to the wall were analyzed. The resulting drag force agreed well with predictions from Faxén's law, indicating that the nearest wall predominantly determines the drag. The simulated lift force exhibited strong spatial and temporal variations during the early stages of sedimentation, especially at $Re_P \approx O(10^{-2})$, which could be attributed to the proximity of the interface and the size of the vortex. These simulations provide valuable insights into the experimental dynamics. On one hand, they serve to validate experimental results; on the other, they offer a deeper understanding of specific kinematic features observed in the experiments, such as *inertial wall attraction*.

4.2 Introduction

The sedimentation of single particles in confined geometries, such as closed vessels or ducts, is a fundamental problem in fluid mechanics with significant implications across various scientific and engineering disciplines. Unlike unbounded sedimentation, where a particle settles in an infinite domain, confined sedimentation involves complex interactions between the particle, the surrounding fluid, and the nearby solid boundaries. This added complexity influences both the trajectory of the particle and the structure of the induced flow field. At the core of numerous applications lies the need to accurately predict how a particle interacts with the confining geometry and how the flow field evolves around it. The confinement can significantly alter the flow structure compared to unbounded sedimentation, leading to deviations in drag force, settling velocity, and trajectories. These effects are particularly pronounced in the low Reynolds number regime, which is the typical regime in microfluidics and many biological systems. In many cases, however, it is difficult or even impossible to visualize the flow field experimentally, *e.g.* by using particle image velocity (PIV). This applies to applications in the creeping flow regime, *e.g.* in small-scale applications in microfluidics or in very viscous systems in which viscous fluids such as oil are used. In small-scale or very viscous systems, it is either challenging to resolve the flow field due to the optical resolution. Or a homogeneous distribution of tracer particles or dyes, such as fluorophores, is difficult to implement.

Numerical simulation of the flow field, *i.e.*, CFD simulation, is therefore a widely used method for gain-

ing access to the properties of the flow field or calculating certain forces or stresses that act on the surface of flowing particles. However, even for simple physical problems, such as the sedimentation of a single sphere falling in a closed simulation volume, a number of challenges arise. These challenges mainly concern the model setup, in particular the type of meshing of the simulation domain, as well as the temporal resolution of the numerics, *i.e.* the time step size used for the calculation. It is easy to see that a fully resolved 3D simulation of large models of an application at small Reynolds numbers leads to an enormous numerical effort in the form of computing power and time.

This is due to one of the hallmark features of low Reynolds number flow, which is the long-range nature of hydrodynamic interactions. When a particle moves through a viscous fluid at $Re_\mathrm{P} \approx 0$, it disturbs the surrounding fluid in a way that decays only algebraically with distance. For example, the velocity field induced by a point force (Stokeslet), *i.e.*, the disturbance, in an unbounded domain decays only as $1/r$. [25]

In confined geometries, such as a closed vessel, disturbances caused by the particle reflect at the boundaries and interact with the particle in a nontrivial way. This makes the fluid response highly nonlocal, with the motion of a single particle influenced not just by its immediate vicinity but by the global configuration of the domain. Furthermore, if $Re_\mathrm{P} \approx 0$ and gravitational or buoyant forces are weak, the particle settles extremely slowly. In practical terms, this means that the simulation must resolve long physical timescales to observe the full trajectory. But not only the long physical time scale is challenging, but also the numerical time stepping. Particularly for the case of time-dependent problems with large gradients of the calculation variables such as the particle velocity, *e.g.* in the transient phase when the sphere starts falling from rest, there are special requirements for the numerical time step size. For this reason, in simulations in which variables such as the drag force on a body are to be calculated as accurately as possible, often only the stationary case is considered. Furthermore, the models are often set up in such a way that the fluid only flows around the body but the body is not moving, *i.e.* it is fixed within the simulation geometry. This is sufficient for calculating drag forces, as at a given velocity it is initially irrelevant whether the body moves through the fluid with a certain velocity or the fluid is flowing around the fixed body with this velocity.

For example, Hensley and Papavassiliou (2019) performed 3D CFD simulations in Ansys Fluent® to calculate the drag on spheres and cylinders in a square microduct. They fixed the particle on the center line of the duct and imposed a laminar flow with a given velocity which resulted a particle Reynolds number of $Re_\mathrm{P} = 0.1$. [31] Ekanayake followed a similar approach to calculate the drag and lift on a particle using direct numerical simulations. However, the main aim was to analyze the influence of a single wall in order to develop a corresponding drag and lift model for a sphere under the influence of a shear flow. The size of the simulation domain was chosen large enough and the results were validated that the other three boundaries of the rectangular simulation domain had no influence on the calculated drag and lift. [93] In 2021, their model was extended for translating particles. The sphere was allowed to translate with a moving reference frame

and the steady-state Navier-Stokes equations were solved. However, the particle velocity was previously set to a fixed value and the shear flow was stationary. [52] The examples mentioned above have in common that the particles were only simulated as empty places in the simulation mesh, *e.g.* as a hollow sphere without fluid-structure interaction. Furthermore, the complete transient dynamics could not be captured with these models.

A sphere in a domain with plane walls can not be simulated in 2D. Calculating a circular object between parallel walls in 2D means simulating an infinitely long cylinder between two infinitely plane walls. Although these physics do not reflect the physics that happens to a spherical particle in a 3D space between two or four plates, the simplification into 2D is interesting and useful. The simplification allows the calculation of additional forces in the model with a significantly lower calculation effort than in the 3D model. For example, Ghosh and Stockie (2015) used the immersed boundary method to simulate the transient sedimentation of circular particles in 2D, *i.e.*, an infinitely long cylinder between two plates. They presented complete kinematics and could show that the 2D disc rotates while falling. Additionally, they incorporated an expression for the added mass term in their simulation which enables a more accurate modeling of the physics in the transient regime at low Reynolds numbers. [83]

A large number of researchers are investigating sedimentation dynamics in viscoelastic fluids. A number of 3D simulations have already been conducted and published, specifically investigating the influence of walls on sedimentation behavior. These studies report transient sedimentation behavior in the form of a velocity overshoot at the beginning of sedimentation. [94],[95],[96]

Simulations that probably have the greatest agreement with the experiments of this thesis were recently carried out by Villone and Maffetone. [97] They performed fully three-dimensional finite element method (FEM) simulations with an arbitrary Lagrangian–Eulerian (ALE) mesh formulation (*cf.* section Methods 4.3.1) of soft beads in the center and close to a wall in a rectangular fluid domain. The simulation method is closely related to the approach in this chapter. However, they included fluid-structure interaction. In their model, the bead was modeled as a soft solid, *i.e.* the particle deformaility was modeled trough a neo-Hookean hyper-elastic constitutive equation. They also reported velocity overshoots and fluctuations at the beginning and long-term transient sedimentation behavior. However, their model failed to capture the behavior of the spheres in the center, which was experimentally measured in the experiments of this thesis, *cf.* Chapter 2. This could be related, among other things, to their model setup (particularly the meshing), which could potentially lead to numerical inaccuracies at very low velocities, *i.e.* very small Reynolds number like in our experiments. This point will be discussed again in the results section. Nevertheless, their results also led them to the conclusion that there is a complex interplay between elasticity, confinement and acceleration of the particle, *i.e.* inertia of the particle.

A brief summary of the most important results of the simulations and how they relate to the experimen-

tal results of this work has already been presented in Chapter 3 in section 3.5.1.3. This chapter goes into more detail on the challenges of modeling the simulation of sedimentation at very low Reynolds numbers $0.1 \gtrapprox Re_P \gtrapprox 0.01$. Although the simulations reproduce the experiment in terms of geometry, the model cannot reproduce the physics in the form of fluid-structure interactions. The focus of the simulations was always on the representation of the velocity field. Nevertheless, interesting insights into the transient dynamics of a rigid sphere in a closed simulation volume can be obtained. These insights can help to explain some of the phenomena observed during the experiments.

The chapter is structured as follows: The first part of the Methods section 4.3.1 deals with the simulation parameters and in particular with the time step settings, as these have a decisive influence on the results. The second part (Section 4.3.1) discusses the geometry and the type of meshing and explains why this model differs from existing literature. The Results chapter 4.4 is divided into three parts: presentation of the velocities and the flow fields in Section 4.4.1, presentation of the fluid stresses on the surface of the sphere in 4.4.2, and finally the forces resulting from the fluid stresses parallel to the direction of fall (traction and drag) as well as the forces normal to the closest wall (lift), *cf* Section 4.4.3 . Simulations were performed for two Reynolds number ranges: $Re_P \approx 0.1$ ($\rho_s = 1159.8$ kg·m^{-3}) and $Re_P \approx 0.01$ ($\rho_s = 987.59$ kg·m^{-3}).

4.3 Methods

4.3.1 Parameter and numerical settings

CFD simulations were carried out in which the sedimentation of a rigid sphere with a radius of $R = 6$ mm close to a wall (wall distance $d/R = 2$) in a rectangular container was modeled. The sphere was modeled as a hollow space inside a fluid domain, *i.e.*, fluid-structure interactions were not involved. The container dimensions were similar to those in the experiments, *cf.* Chapters 2 and 3. The simulations were conducted in COMSOL Multiphysics® by solving the differential equations derived from the force balance acting on a sphere with a specific solid density falling under gravity through a fluid. The fluid was modeled as a Newtonian fluid with a density of $\rho = 971.3$ kg·m^{-3} and a dynamic viscosity of $\eta = 0.9797$ Pa·s. The motion of the sphere was coupled with the surrounding flow field by coupling the creeping flow equations with the force balance around the sphere, *cf.* the governing equations 3.9-3.12 were reported in Chapter 3.5.1.3.

Four different simulations are presented. In total three simulations were carried out for a sphere with a density of $\rho_s = 987.59$ kg·m^{-3}. This model corresponds to the density of the softest sphere in Chapters 2 and 3 and to a Reynolds number of $Re_P \approx O(10^{-2})$. Simulation 1 with $\rho_s = 987.59$ kg·m^{-3} (Sim 1) had a

high temporal resolution, *i.e.* a higher numerical accuracy. The relative tolerance was manually set (*User controlled*) to a value of 0.001, *cf.* Fig. 4.1.

The relative tolerance defines the maximum acceptable error, relative to the solution's magnitude, for

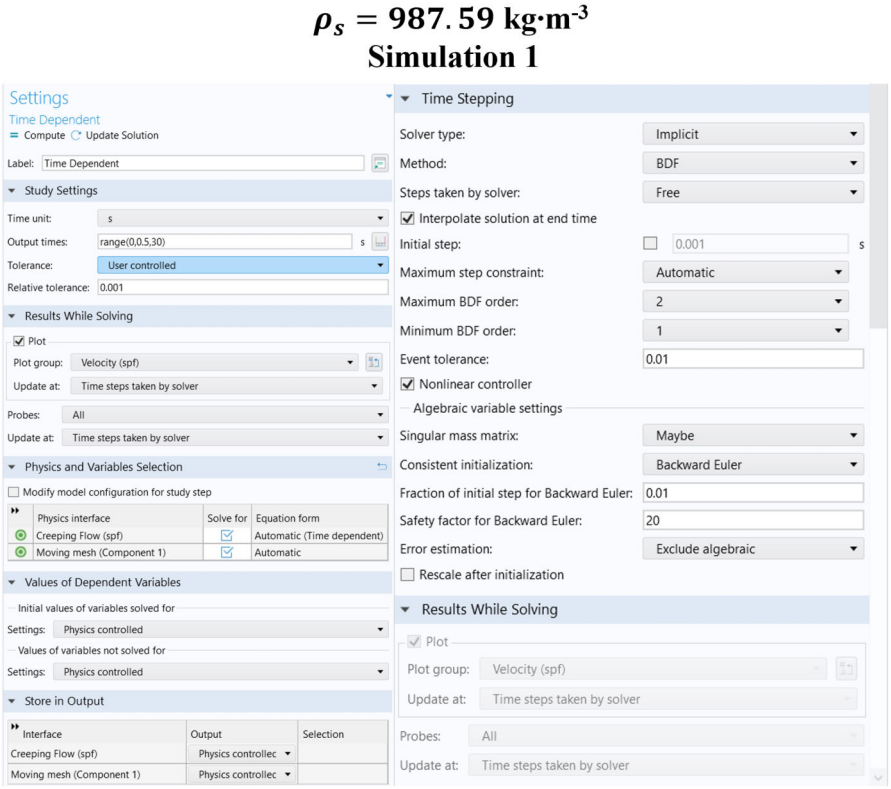


Figure 4.1: Study settings and time stepping settings of simulation 1 of a sphere with a density of ρ_s = 987.59 kg·m^{-3} sedimenting in a rectangular fluid domain.

each iterative step of the solver. Lowering the relative tolerance to smaller numbers results in smaller time steps. This increases solution accuracy, but also the solving time. For example, simulation 1 computed for more than 71 hours on an 1 TB RAM workstation (temporary RAM requirement: 765 GB) to simulate 30 s ($\equiv t_{\mathrm{sim,max}}$ of simulation 1) of the sedimentation process.

Simulation 2 (Sim 2) used a coarser time stepping, which was automatically chosen by the solver. The *Tolerance* setting was changed to *Physics controlled*. In order to force the solver not to select too large time steps, the output time step was reduced from 0.5 s to 0.25 s. Note: the output time steps are not solution time steps or numerical time steps, respectively. The result at the output time is interpolated to this value if the numerical time step does not match the output time. Simulation 2 computed for 12 hours 40 minutes and required 737 GB of RAM.

In simulation 3 with the lower density, the geometry was changed in order to model a deeper immersion of the sphere. The center of the sphere was placed 100 mm below the one in simulations 1 and 2, leading to

an immersion depth of $h_{I,3} = 156$ mm. The numerical settings were similar to simulation 1, *i.e.*, the numerical accuracy was high. The deep immersion simulation computed for 68h 40 min and required temporarily a maximum RAM of 745 GB for a simulation time of $t_{sim,max} = 120$ s.

In addition to the lower density, one simulation was carried out for a sphere with a density of $\rho_s = 1159.8$ kg·m^{-3} with high temporal resolution .This density corresponds to the stiff spheres in Chapters 2 and 3 and a Reynolds number of $Re_P \approx O(10^{-1})$. The time stepping settings were similar to simulation 1 ($\rho_s = 987.59$ kg·m^{-3}) and the output time step size was 0.25 s. The simulation computed 73 hours and 45 minutes and required temporarily a maximum RAM of 757 GB. The simulation was interrupted when the velocity decreased after a steady phase of sedimentation, *i.e.* when the sphere almost reached the bottom of the container. This shows that, due to the increased density, the entire sedimentation process -not merely the initial phase- could be simulated with a comparable computational effort at higher Reynolds numbers.

4.3.2 Geometry and Mesh

The near-wall model of sedimentation is based on the model for sedimentation in the center of a rectangular duct, which was developed in frame of Xiangqian Wu´s master thesis *"3D Computational Fluid Dynamics (CFD) simulation of the sedimentation of spheres and rods in a rectangular duct"*, (2021).

If the sphere falls along the center line of the rectangular duct and does not leave the center axis (fixed position), the simulation domain can be reduced to 1/8 by selecting suitable symmetry conditions, see Fig. A.7 in the SI of the dissertation appendix A.1. In the case of off-center sedimentation, the diagonal symmetry planes of the square cross-section are omitted. This means that only a reduction to half the container volume is possible.

Fig. 4.2 shows the simulation mesh of simulation 1 of a sphere with density $\rho_s = 987.59$ kg·m^{-3} at a simulation time of $t_{sim} = 0$ s (Fig. 4.2 *(a)*) and $t_{sim} = 30$ s (Fig. 4.2 *(b)*) and close ups of the mesh elements in mesh domain 1 (Fig. 4.2 *(c)*) and the fine mesh around the sphere cavity (Fig. 4.1 *(d)*).

The simulation domain modeling the fluid had a total height of $H_{sim} = H_1 + H_2 + H_3 = 0.4$ m. It is is divided into three areas: fluid domain 1 ($H_1 = 0.031$ m), fluid domain 2 ($H_1 = 0.05$ m) and fluid domain 3 ($H_3 = 0.319$ m). Domain 1 and 3 were discretized with a so-called *Swept* mesh. The surfaces at the bottom and the free surface on top, were divided into triangles and then extruded in the x-direction (direction of fall), leading to triangular prisms. Domain 1 was divided into 100 equal parts in the x-direction and domain 3 into 200 equal parts, *cf.* close up in Fig. 4.2 *(c)*. The meshes generated in this way were implemented as a moving mesh with an Arbitrary Lagrangian-Eulerian (ALE) formulation.

The ALE method is a meshing technique that blends the strengths of both Lagrangian and Eulerian ap-

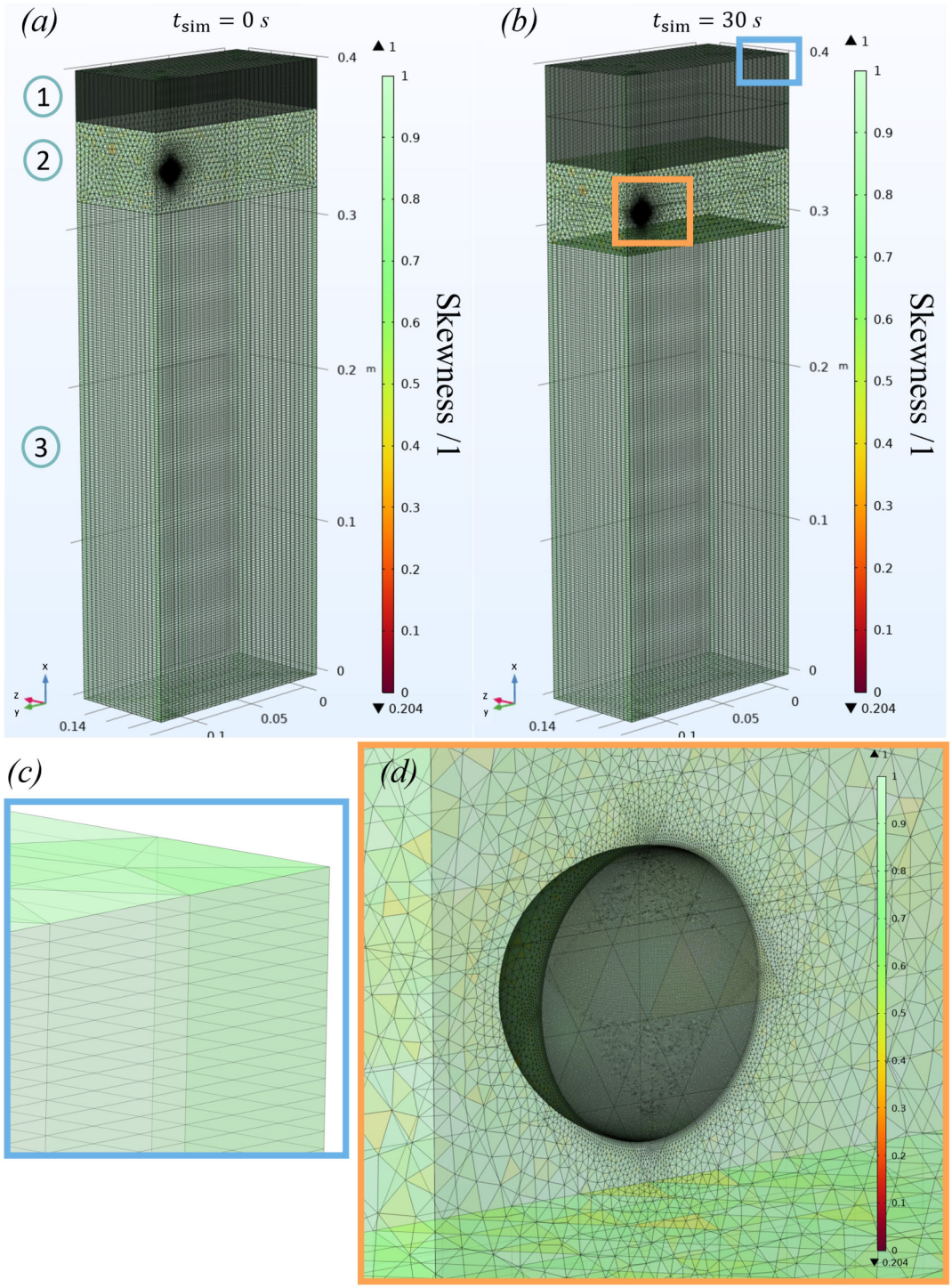


Figure 4.2: Mesh of simulation 1 of a sphere with density ρ_s = 987.59 kg·m^{-3} at *(a)* simulated time of t_{sim} = 0 s and *(b)* t_{sim} = 30 s. Close ups of the mesh elements in mesh domain 1 *(c)* and the fine mesh around the sphere cavity *(d)*. Mesh quality parameter is the *skewness* of the mesh cells (color legend)

proaches, making it particularly well-suited for simulations involving moving or deforming domains, such as in fluid-structure interaction (FSI) problems or in sedimentation processes. In continuum mechanics, partial

differential equations governing physical phenomena are typically formulated in either a spatial (Eulerian) or material (Lagrangian) coordinate system. The Eulerian formulation observes physical quantities at fixed spatial locations, while the Lagrangian formulation follows individual material points as they deform or move. The latter is especially advantageous in structural mechanics and other areas involving anisotropic solid materials. Conversely, when modeling fluids, it is often impractical to track individual material points. Instead, interest lies in field quantities (*e.g.*, pressure, temperature, concentration) at fixed spatial positions, favoring an Eulerian framework. However, a limitation of the pure Eulerian approach is its inability to handle moving domain boundaries, as the domain itself evolves while the coordinate system remains fixed in space. To address this, the governing equations can be reformulated with respect to a coordinate system in which the domain boundaries remain stationary, The new coordinate system is called *mesh coordinate system* . This coordinate system is initially aligned with the domain's geometry and establishes a one-to-one mapping to the current spatial configuration. As the domain deforms, this mapping may become distorted, degrading mesh quality. To mitigate this, a remeshing procedure can be applied: the simulation is paused, a new mesh is generated in the deformed configuration, and physical quantities are interpolated onto it. Upon resuming, the new mesh coordinates serve as the reference, now differing from the original geometry coordinates. Consequently, the mesh moves independently of both the material and spatial frames. When the mesh follows the material motion, the ALE formulation reduces to the Lagrangian case; when the mesh remains fixed in space, it becomes purely Eulerian. Thus, ALE provides a flexible intermediate framework, enabling simulations with moving boundaries while avoiding the constraints of fully Lagrangian or Eulerian descriptions. [98]

The displacement of the mesh in the simulation was defined by the force equilibrium around the sphere, *i.e.*, the calculated displacement in x-direction from Eq. 3.12. Domains 1 and 3 can only deform in direction of x and not normal to the walls. The elements in domain 1 were stretched and the elements in zone 3 were compressed.

An additional section (domain 2) with a fixed, tetrahedral mesh was introduced. A fully deforming ALE mesh over the complete geometry would lead to a large mesh distortion and nonphysical behavior, as was found in the master thesis of X. Wu (2021). Decoupling an area around the sphere from the rest of the moving mesh has a number of further advantages. Firstly, it can effectively ensure finer meshing of the sphere surface without the large calculation effort that would be required for the ALE mesh, *cf.*, Fig. 4.2 *(d)*. Very fine meshing of the surface of the sphere is important because the velocity and thus the displacement of the overall mesh is derived from the fluid stress tensor around the surface of the sphere, *cf.* the integral term in Eq. 3.12. If the surface of the sphere is not sufficiently discretized, this results in an inaccuracy of the integral value. In particular, if the forces acting on the surface of the sphere are small (and consequently the velocity is small), convergence problems arise. In addition, vortices form in the areas between the sphere

and the outer walls and thus also influence the fluid stresses on the sphere surface, see streamline plots in section 4.4.1. A fine resolution of the mesh in this area is therefore also given from this point of view. A mesh refinement study and mesh independence study for to element size in domain 2 was performed, *cf.*, master thesis X. Wu (2021). The maximum element size was set to $6 \cdot 10^{-5}$ m. The maximum element size of the triangles defining the prisms in the swept meshes was set to 0.004 m. It should be noted that this special type of meshing with a co-moving, finely meshed zone is the distinguishing feature from the references mentioned in the introduction Chapter 4.2, especially those of Ekanayake *et al.* (2021) and Villone & Maffettone (2024). [52],[97]

The mesh elements in Fig. 4.2 are colored according to the mesh quality parameter *Skewness*. Skewness is the default quality measure in COMSOL. In terms of skewness, the mesh is of good quality. However, since *Swept* was chosen as meshing method in domains 1 and 3, a different quality parameter must be considered for these areas: the *volume vs. edge lengths*. Fig. 4.3 shows the meshes of simulation 2 of a sphere with density $\rho_s = 987.59$ kg·m^{-3} at simulated times of $t_{sim} = 1$ s and $t_{sim} = 100$ s colored with regard to the previously mentioned parameter *volume vs. edge lengths*.

The quality parameter *Volume vs. edge lengths* is based on a quotient of element edge lengths and element volume. This quality measure is primarily sensitive to anisotropy of the volume. Anisotropy in terms of volume describes the different degrees of expansion of a solid in relation to the spatial directions. It is particularly present in the mesh cells in domain 1 at the start of the simulation. The cells have a large triangular base area compared to the height in x-direction. At later times, *i.e.* when the mesh cells in the upper domain have been stretched, the mesh is of good quality. However, at this point, the poor mesh quality must be accepted. If the subdivision in the x-direction is reduced (*i.e.* less than 100 sections in the x-direction), the problem is merely shifted in the other direction, *i.e.* at some point the base area of the prism is small compared to the height of the prism. Possible problems with the numerics, which result from the poor mesh quality in this area at the beginning of the simulation, will play a role in the following Chapter 4.4 Results when considering the initial acceleration phase.

4.4 Results

In this chapter, the results for the simulation with a density of $\rho_s = 1159.8$ kg·m^{-3} are shown first in a separate diagram. The results of the three simulations with a density of $\rho_s = 987.59$ kg·m^{-3} follow and are presented in joint diagrams.

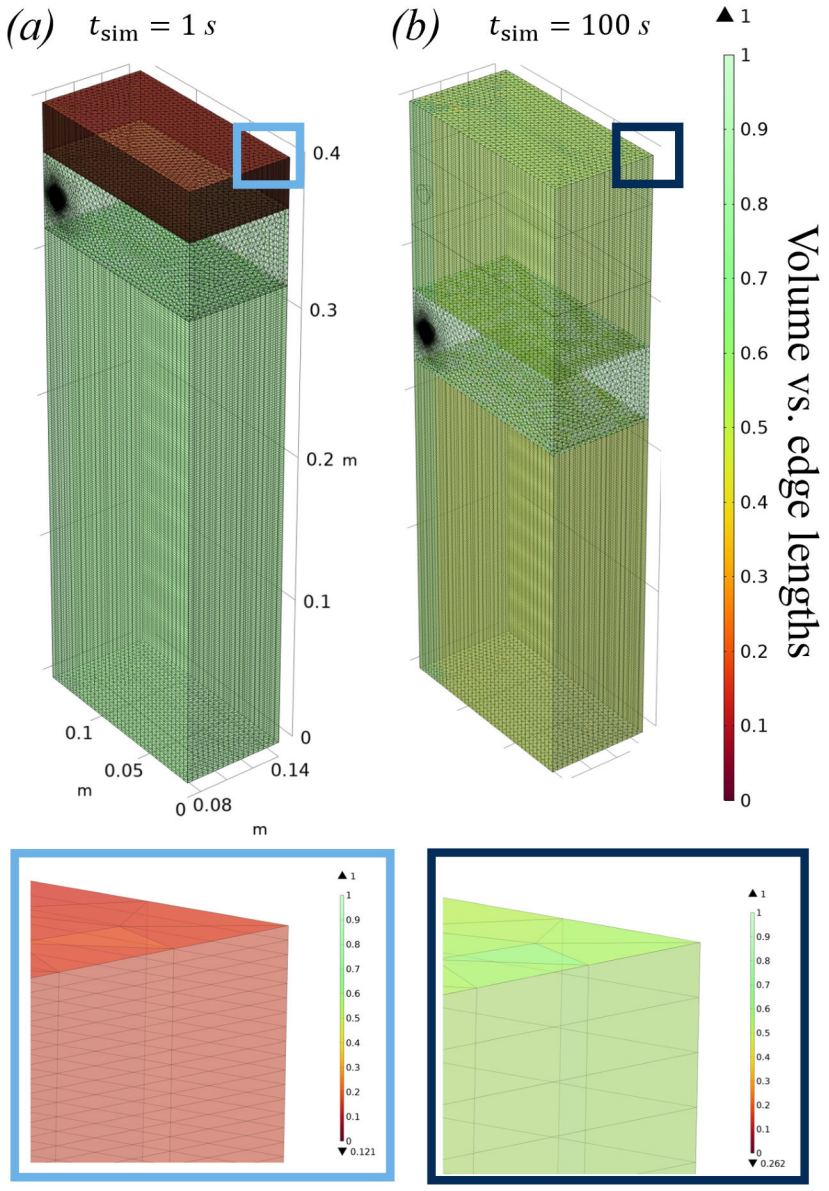


Figure 4.3: Mesh of simulation 2 of a sphere with density $\rho_s = 987.59\ kg{\cdot}m^{-3}$ at *(a)* simulated time of $t_{sim} = 1$ s and *(b)* $t_{sim} = 100$ s. Close ups below: mesh elements in mesh domain 1 at the given times. Mesh quality parameter is *Volue vs. edge lengths* (color legend)

4.4.1 Particle velocity and flow field

The sedimentation velocity $U_{P,sim}$ is presented as a a function of the simulation time t_{sim} or the dimensionless sedimentation distance x_{sim}/R, respectively. Fig. 4.4 shows the t_{sim}-$U_{P,sim}$-diagram of the simulation with a density of $\rho_s = 1159.8\ kg{\cdot}m^{-3}$ ((x_{sim}/R)-$U_{P,sim}$-diagram in the insert).

The sedimentation curves show expected behavior. After a steep increase during acceleration, the sphere reaches immediately a steady velocity of $\overline{U}_{P,sim} = 10.73\ mm{\cdot}s^{-1}$. This is to be expected, as no additional

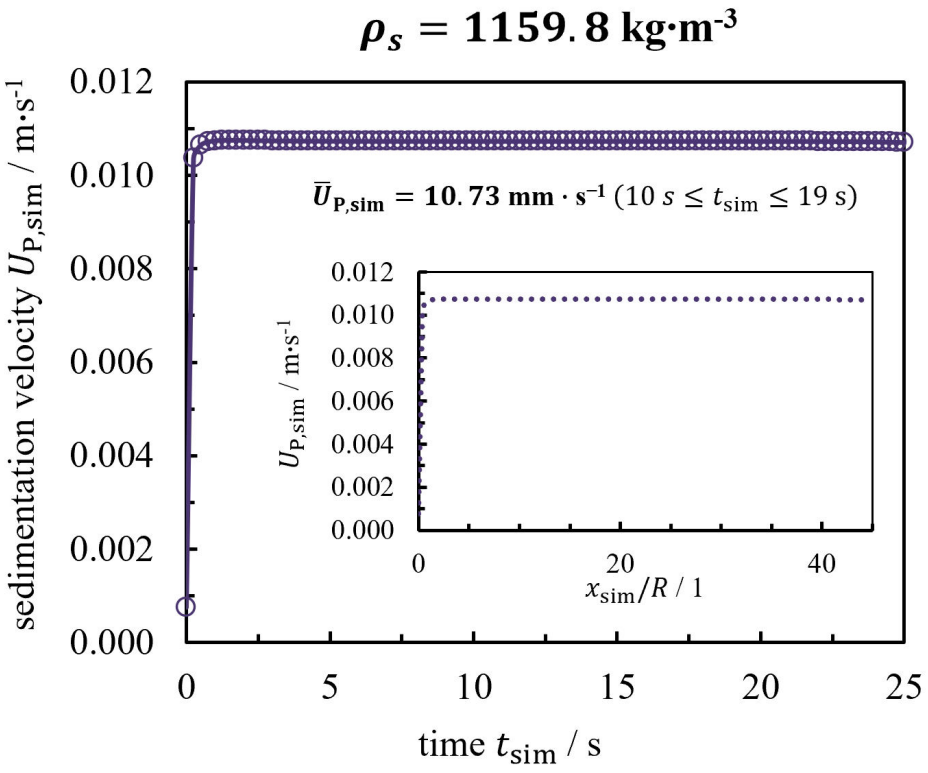


Figure 4.4: Simulated particle velocity $U_{P,sim}$ plotted against the simulation time t_{sim} of a sphere (R = 6 mm) with density ρ_s = 1159.8 kg·m^{-3} ($Re_P \approx O(10^{-1})$) sedimenting at a distance of d_{sim}/R = 2 from a plane no-slip boundary in a rectangular fluid domain. (x_{sim}/R)-$U_{P,sim}$-diagram

inertial forces, such as the Basset force, are calculated in the force equilibrium, which extend the initial acceleration or delay it in time.

However, a more precise resolution in the range +/- 1% around the stationary velocity reveals that there is a short overshoot before the velocity becomes stationary, see Fig. 4.5.

The overshoot of the simulation of a sphere with ρ_s = 1159.8 kg·m^{-3} is $\Delta \approx 0.2$ %, *i.e.* negligibly small with respect to the stationary velocity. The (x_{sim}/R)-$U_{P,sim}$-diagram shows, that the overshoot in velocity decayed after a sedimentation distance of (x_{sim}/R) $\approx$ 10.

Fig. 4.5 shows the simulated velocity at the interpolated output time steps (Δt = 0.25s = const.) and at the solver time steps. The curves fit perfectly, *i.e.* the overshoot does not result from inaccuracies in the interpolation. Furthermore, the solver has selected small time steps during the overshoot (the relative tolerance was set to 0.001 in this simulation, *cf* Section 4.3.1). An influence of the temporal resolution in the numerics is therefore rather unlikely. More likely is an influence of the mesh quality due to the fact that the mesh cells still have a poor mesh quality at the beginning with regard to the anisotropy of the volume (*cf* discussion in section 4.3.1). It is conceivable that an improvement in mesh quality occurs when domain 1 has stretched by approximately 10R.

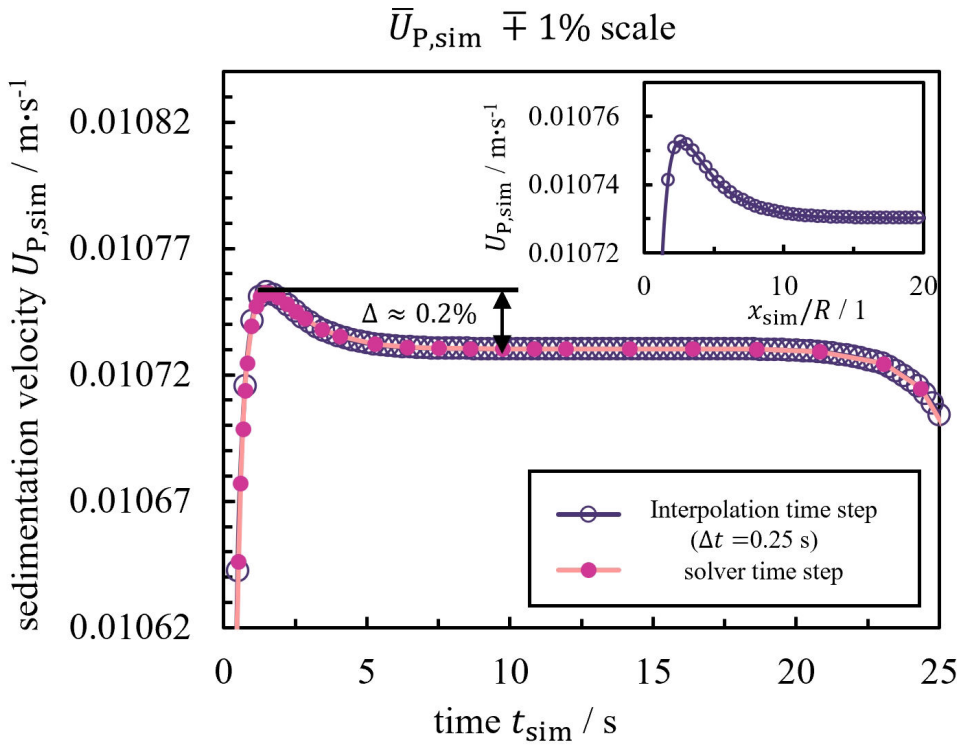


Figure 4.5: $\overline{U}_{P,sim}$+/- 1% scale of the simulated particle velocity $U_{P,sim}$ plotted against the simulation time t_{sim} of a sphere (R = 6 mm) with density ρ_s = 1159.8 kg·m^{-3} ($Re_P \approx O(10^{-1})$) sedimenting at a distance of d_{sim}/R = 2 from a plane no-slip boundary in a rectangular fluid domain. Insert: (x_{sim}/R)-$U_{P,sim}$-diagram

Fig. 4.6 shows the t_{sim}-$U_{P,sim}$-diagram of the simulations with a density of ρ_s = 987.59 kg·m^{-3} ((x_{sim}/R)-$U_{P,sim}$-diagram in the insert). The diagram is presented directly in the $\overline{U}_{P,sim}$+/- 1% scaling ($\overline{U}_{P,sim}$ of simulation 2).

Simulation 1 and 2 both show an overshoot. Simulation 2 reached a steady velocity after $t_{sim} \approx 60$ s. No steady-state value was reached in Simulation 1, as the simulation was terminated prematurely due to the long simulation duration. Even at this Reynolds number, the overshoot is not visible on the complete axis scaling, *cf.* Fig. 3.5 in Chapter 3.5.1.3 showing the curve for simulation 2 on the complete axis scale. In the experiments, a decrease in velocity was also measured after a peak in velocity was reached after the initial acceleration. However, the velocity decreased over a longer period of time and over a longer distance. In addition, the overshoot in the simulation is comparatively small with respect to the steady velocity, *i.e.* only 0.5% in simulation 1 and 1% in simulation 2 (the spheres in the experiments decreased the velocity ≈ 8 %). A comparison of the simulated velocity with a complete series of measurements of spheres of this density can be found in the dissertation appendix A.1 in §4, Fig. A.9. This figure also shows graphically that the simulated velocity and the measured velocity deviate significantly from each other, *i.e.* the simulated steady-state velocity is ≈ 16.5 % larger than the measured velocity at the peak. All simulated and experimental values were summarized and compared in Tab. 3.4 in the previous chapter appendix 3.7 §A2. A comparison

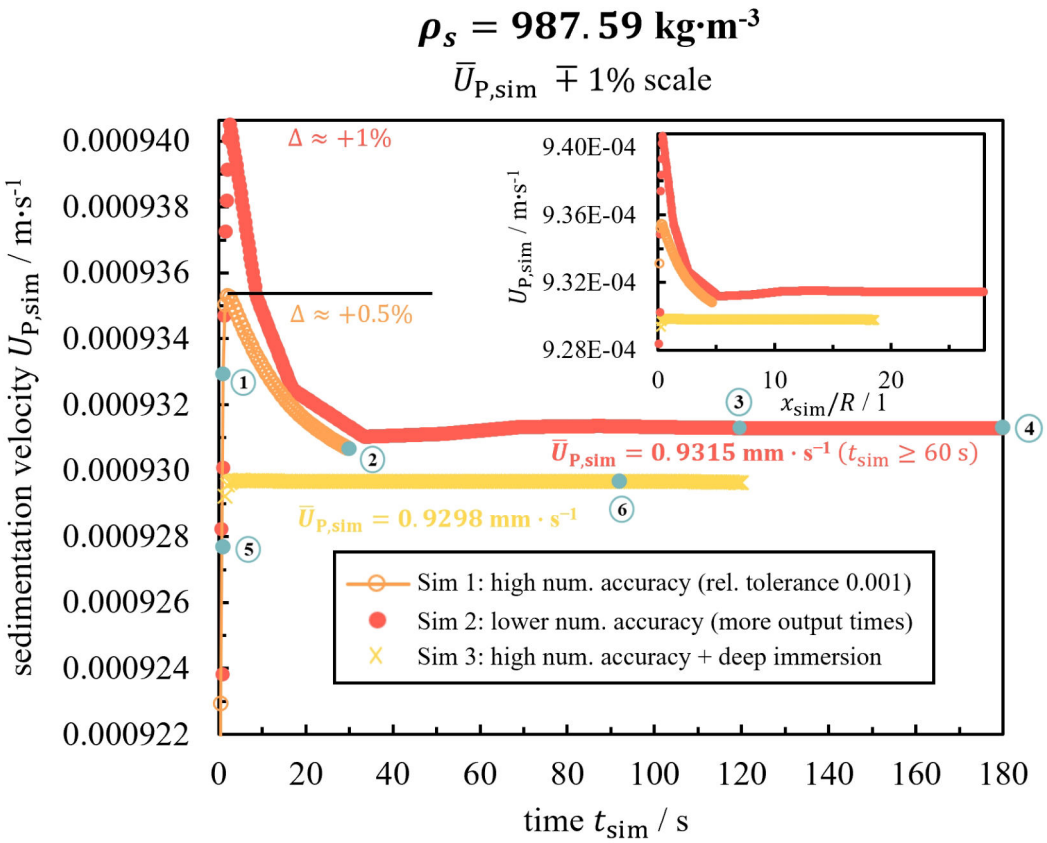


Figure 4.6: $\overline{U}_{P,sim}$+/- 1% scale of the simulated particle velocities $U_{P,sim}$ plotted against the simulation time t_{sim} of a sphere (R = 6 mm) with density ρ_s = 987.59 kg·m^{-3} ($Re_P \approx O(10^{-2})$) sedimenting at a distance of d_{sim}/R = 2 from a plane no-slip boundary in a rectangular fluid domain. Insert: (x_{sim}/R)-$U_{P,sim}$-diagram. Simulations were performed with various numerical settings and various immersion depths.

between the simulation and a theoretical value will follow in section 4.4.3.2 dealing with the drag force.

The velocity curve of simulation 2 in the (x_{sim}/R)-$U_{P,sim}$-diagram shows, that the large overshoot decays after $\approx 5R$. Then the velocity increases slightly and becomes constant after $\approx 10R$.

Although improved numerics leads to a reduction in the overshoot, the overshoot cannot be completely eliminated even with a very small time step size. The overshoot can only be eliminated when the sphere is immersed at a lower position inside the container, see yellow crosses (Sim 3) in Fig. 4.6. The steady-state velocity at deep immersion depth is smaller than that of simulation 2. However, it appears that the curve of Sim 1 would approach the steady-state value of Sim 3 at later times.

In conclusion, the improved numerics leads to a lower and more accurate velocity. A deeper immersion depth eliminates the overshoot. There are two possible origins for the overshoot: on the one hand, the poor numerics due to the bad mesh quality in domain 1 or, from a purely spatial point of view, the immersion depth, *i.e.*, the proximity to the open boundary on top of the container. The former cause is partly contradicted by the fact that the overshoot also appears with the small time step sizes and is larger for the slower

spheres than for the faster spheres. If the mesh cells in domain 1 were too small (flat) for the numerics, the calculation of a higher velocity at the beginning, or larger displacements, respectively, would suffer more and lead to poorer results. However, the reverse is the case.[1] Furthermore, the curve of simulation 1 also appears to approach the more accurate value of the simulation with a deeper immersion depth (Sim 3; for the evaluation of accuracy, see section 4.4.3.2). Nevertheless, the numerical influence cannot be completely ruled out. An influence is even likely. However, the spatial aspect, *i.e.* the proximity to the free boundary on top of the container, seems to be of greater importance. This aspect will be clarified in more detail by evaluation of the flow field and the streamlines. In Fig. 4.6, specific points (number 1-6) at certain simulation times are labeled. The flow field is analyzed at these points in the following.

Fig. 4.7 shows the velocity field (contour plot) and the streamlines of point 1 ($t_{\mathrm{sim}} = 1$ s) and 2 $t_{\mathrm{sim}} = 30$ s labeled on the curve of simulation 1 in Fig. 4.6.

Fig. 4.7 shows that a large vortex between the sphere and the far wall has already formed after a simu-

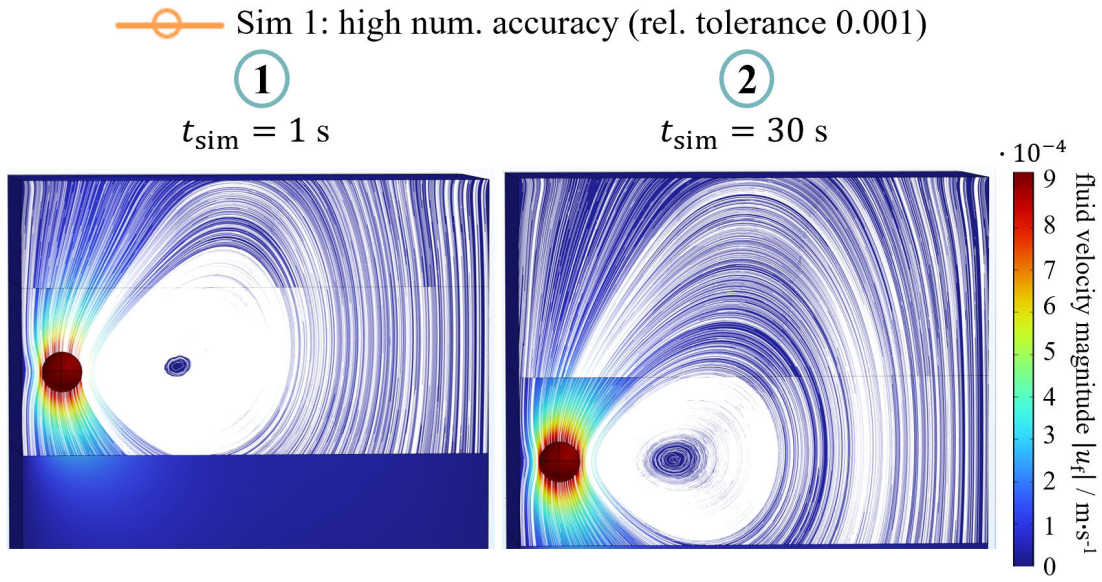


Figure 4.7: Velocity field of the fluid (contour plot) and streamlines of simulation 1 of a sphere ($R = 6$ mm) with density $\rho_{\mathrm{s}} = 987.59$ kg·m^{-3} ($Re_{\mathrm{P}} \approx O(10^{-2})$) sedimenting at a distance of $d_{\mathrm{sim}}/R = 2$ from a plane no-slip boundary in a rectangular fluid domain at simulation time $t_{\mathrm{sim}} = 1$ s (point 1, left) and $t_{\mathrm{sim}} = 30$ s (point 2, right). The sphere started sedimenting in proximity to the open boundary on top.

lation time of $t_{\mathrm{sim}} = 1$ s. The vortex is not symmetrical at the beginning (in terms of its appearance upwards and downwards). When the vortex moved downwards with the sphere, symmetry forms. However, still at $t_{\mathrm{sim}} = 30$ s, the vortex is influenced by the boundary on top, *cf.* the complete view of the flow field at this point in Fig. 4.8.

[1] An estimate of the quality of the discretization, *i.e.*, the relation between cell size Δx_{i} and the choice of time step Δt_{i}, can be made, *e.g.* with the CFL (Courant-Friedrichs-Lewy) number ($CFL = U_{\mathrm{P,sim}} \Delta t_{\mathrm{i}} / \Delta x_{\mathrm{i}}$. The CFL number indicates whether a point in a mesh cell passes a cell completely or skips the cell, *e.g.* if the velocity is too large. Skipping cells leads to poorer results. The larger the CFL number, the poorer is the result.[99] COMSOL checks such conditions internally when calculating with time-dependent solvers.

The complete expansion of the vortex in the x-direction becomes apparent as distance from the free

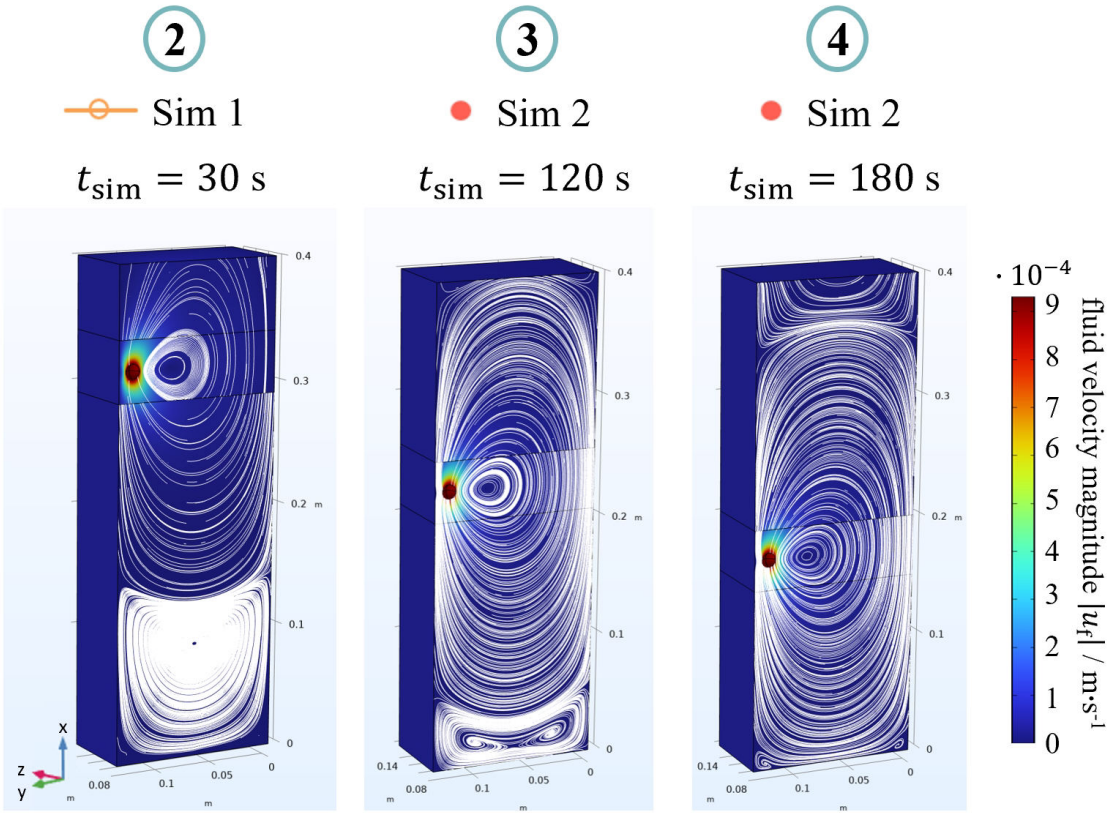


Figure 4.8: Velocity field of the fluid (contour plot) and streamlines of simulation 1 of a sphere (R = 6 mm) with density ρ_s = 987.59 kg·m^{-3} ($Re_P \approx O(10^{-2})$) sedimenting at a distance of d_{sim}/R = 2 from a plane no-slip boundary in a rectangular fluid domain at simulation time t_{sim} = 30 s (point 2, left) and of simulation 2 at time t_{sim} = 120 s (point 3, center) and t_{sim} = 180 s (point 4, right). The sphere started sedimenting in proximity to the open boundary on top.

boundary increases (t_{sim} = 120 s, point 3). At this point, the second vortex at the bottom of the container disappears gradually, and a further decoupled flow formation forms in the upper area of the container (especially visible at the end time of simulation 2 at t_{sim} = 180, point 4).

Fig. 4.9 shows the velocity field (contour plot) and the streamlines of point 5 (t_{sim} = 1 s) and point 6 t_{sim} = 90 s labeled on the curve of the deep immersion simulation (Sim 3) in Fig. 4.6.

If the sphere starts the sedimentation 100 mm deeper (almost at mid-height), the complete vortex is already formed after t_{sim} = 1 s over the entire container height, *cf* Fig. 4.9 (left, point 5). The velocity field and the streamlines around the sphere at any later point in time (here shown at time t_{sim} = 90 s (point 6, bottom right)) are identical to those at the beginning. Since there is no overshoot in the velocity curve and the same numerical settings were used as in simulation 1, it can be concluded that the overshoot is related to the proximity to the free boundary, *i.e.* to the asymmetrical vortex in the beginning. This is also supported by the fact that the overshoot decays after $\approx 5R$. Based on the initial immersion depth of simulation 1 and 2 ($h_{I,1\&2}$ = 56 mm $\equiv 9R$), this results in a distance to the interface of approximately $14R$ until the veloc-

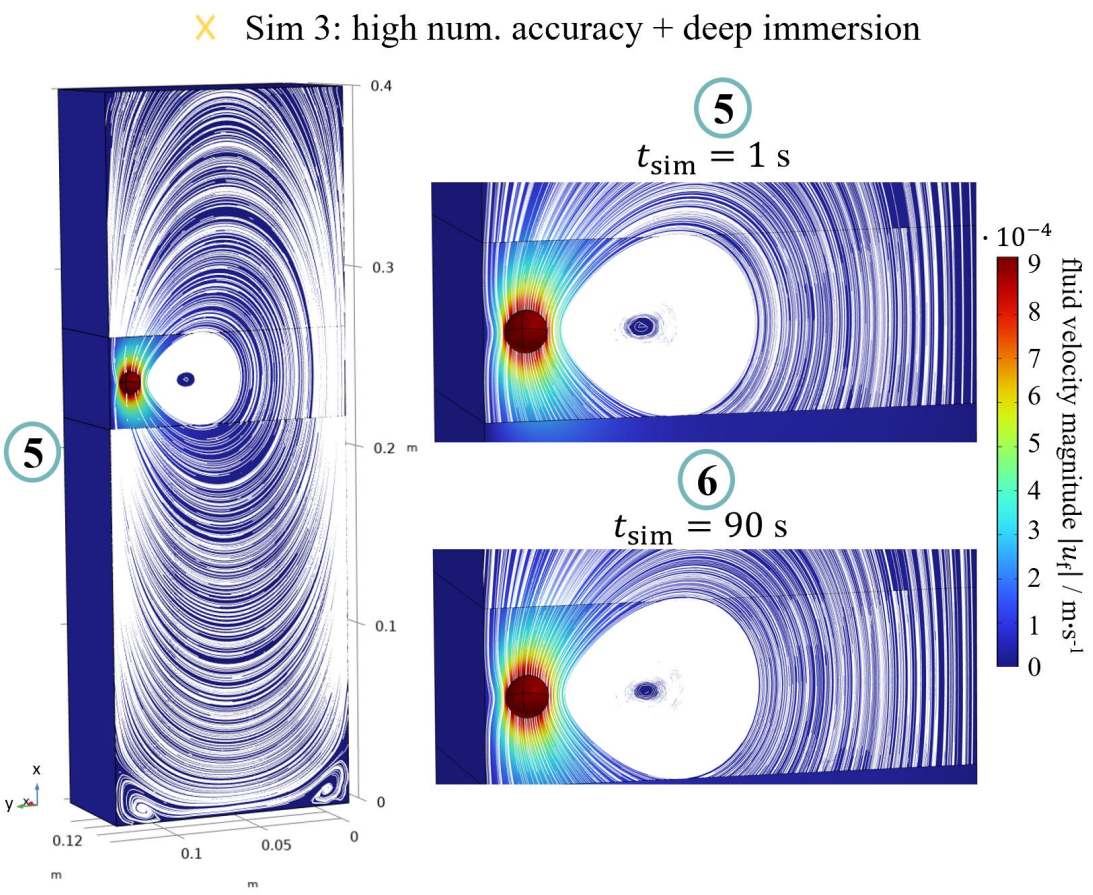


Figure 4.9: Velocity field of the fluid (contour plot) and streamlines of simulation 3 of a sphere (R = 6 mm) with density ρ_s = 987.59 kg·m^{-3} ($Re_P \approx O(10^{-2})$) sedimenting at a distance of d_{sim}/R = 2 from a plane no-slip boundary in a rectangular fluid domain at simulation time t_{sim} = 1 s (point 5, left and top right) and t_{sim} = 90 s (point 6, bottom right). The sphere started sedimenting with a larger immersion depth.

ity approaches the stationary value. $14R$ corresponds to slightly more than half the width of the container ($W/2 \approx 11.7R$). Furthermore, this size corresponds well with the radius of the vortex (measured from the center of the vortex towards the far wall). The dynamics thus seem to depend on the characteristic size of the vortex, which in turn depends on the size of the container (*i.e.*, the confinement), the sphere size and the position of the sphere (*i.e.*, the wall distance).

4.4.2 Fluid stresses on the surface

In this section, the fluid stresses on the sphere surface are presented. The fluid stresses at a specific simulation time t_{sim} are presented as a matrix. The stress components are shown in $x-$, $y-$ and $z-$ directions on the surface of the sphere (vertical subdivision). In addition, the stress tensor $\vec{\tau}$ (referred to as *total traction*, as this is the output designation in COMSOL) is divided into its viscous stress component $\vec{\sigma}$ and the pres-

sure component $-p\boldsymbol{I}$ (horizontal subdivision). The respective legends show the minima (triangle pointing downwards) and maxima (triangle pointing upwards) of the stresses.[2] The components in x-direction are shown with reversed colors in order to display the largest stress magnitudes more intuitively in red.

Fig. 4.10 shows the calculated fluid stresses of the simulation with a density of $\rho_s = 1159.8$ kg·m^{-3} ($Re_P \approx O(10^{-1})$) at time $t_{sim} = 2.25$ s. This simulation time corresponds to the velocity maximum during the overshoot, *cf.* Fig. 4.5.

Fig. 4.10 shows the calculated fluid stresses of the simulation with a density of $\rho_s = 1159.8$ kg·m^{-3} ($Re_P \approx O(10^{-1})$) at time $t_{sim} = 10$ s. At this simulation time, sedimentation was steady.

The calculated fluid stresses of the simulation with a density of $\rho_s = 987.59$ kg·m^{-3} ($Re_P \approx O(10^{-2})$) at time $t_{sim} = 16$ s (unsteady) and at time $t_{sim} = 100$ s (steady) are shown in the chapter appendix 4.6 in Fig. 4.18 and 4.19.

The plots of the fluid stresses of the transient and steady state do not differ qualitatively, both in the simulation with a density of $\rho_s = 1159.8$ kg·m^{-3} ($Re_P \approx O(10^{-1})$) and with a density of $\rho_s = 987.59$ kg·m^{-3} ($Re_P \approx O(10^{-2})$).

Differences between the transient and steady-state regimes are only quantitatively evident in the viscous component. The viscous stresses are slightly larger during the transient phase than during the stationary phase.The pressure component changes naturally due to the increase in hydrostatic pressure.

The asymmetry of the x-component of the viscous stresses is also interesting (plot middle left): the largest viscous stress magnitude in x-direction (direction of fall) is not at the stagnation point (the point of highest pressure on the lower hemisphere), but exactly on the point of minimal gap size between the sphere surface and the wall, *cf.* a direct comparison on a smaller axis scaling between the transient and steady regime is shown in Fig. 4.17 in the chapter appendix 4.6.

A quantity that can be estimated with the fluid stresses is the local deformation on a specific point on the surface. In the case of spheres with a density of $\rho_s = 987.59$ kg·m^{-3} ($Re_P \approx O(10^{-2})$), which were the softest spheres in the experiments, the maximum total traction in the y and z direction are $|\tau_{y;z}|_{max} \approx 678$ Pa (unsteady) and $|\tau_{y;z}|_{max} \approx 1420$ Pa (steady) and in the x-direction $|\tau_x|_{max} \approx 733$ Pa (unsteady) and $|\tau_x|_{max} \approx 1480$ Pa (steady). Assuming linear elasticity, this corresponds to a linear deformation of $\Delta R_{y;z} = |\tau_{y;z}|_{max} E^{-1} R \approx 30 - 33$ µm in the unsteady regime and $\Delta R_{y;z} = |\tau_{y;z}|_{max} E^{-1} R \approx 63 - 65$ µm in the steady phase. The approximation of the deformation with the purely viscous component in direction of gravity ($|\sigma_x|_{max} = 0.434$ Pa leads to much smaller theoretical deformations due to fluid shear. Based on the shear modulus $G \approx E/3$, the approximate deformation due to fluid shear would be $\Delta R_x = 3|\sigma_x|_{max} E^{-1} R \approx 0.06$ µm. This shear deformation is almost negligible in absolute terms and at first glance it cannot be as-

[2] Only the figures for the x- and y-component show the correct fluid stress minima and maxima (mirror symmetry). For the z-component, the minima shown in the figures do not match the actual minima (the minima, or negative values of the stresses, respectively, lie on the hemisphere, which was not explicitly included in the simulation).

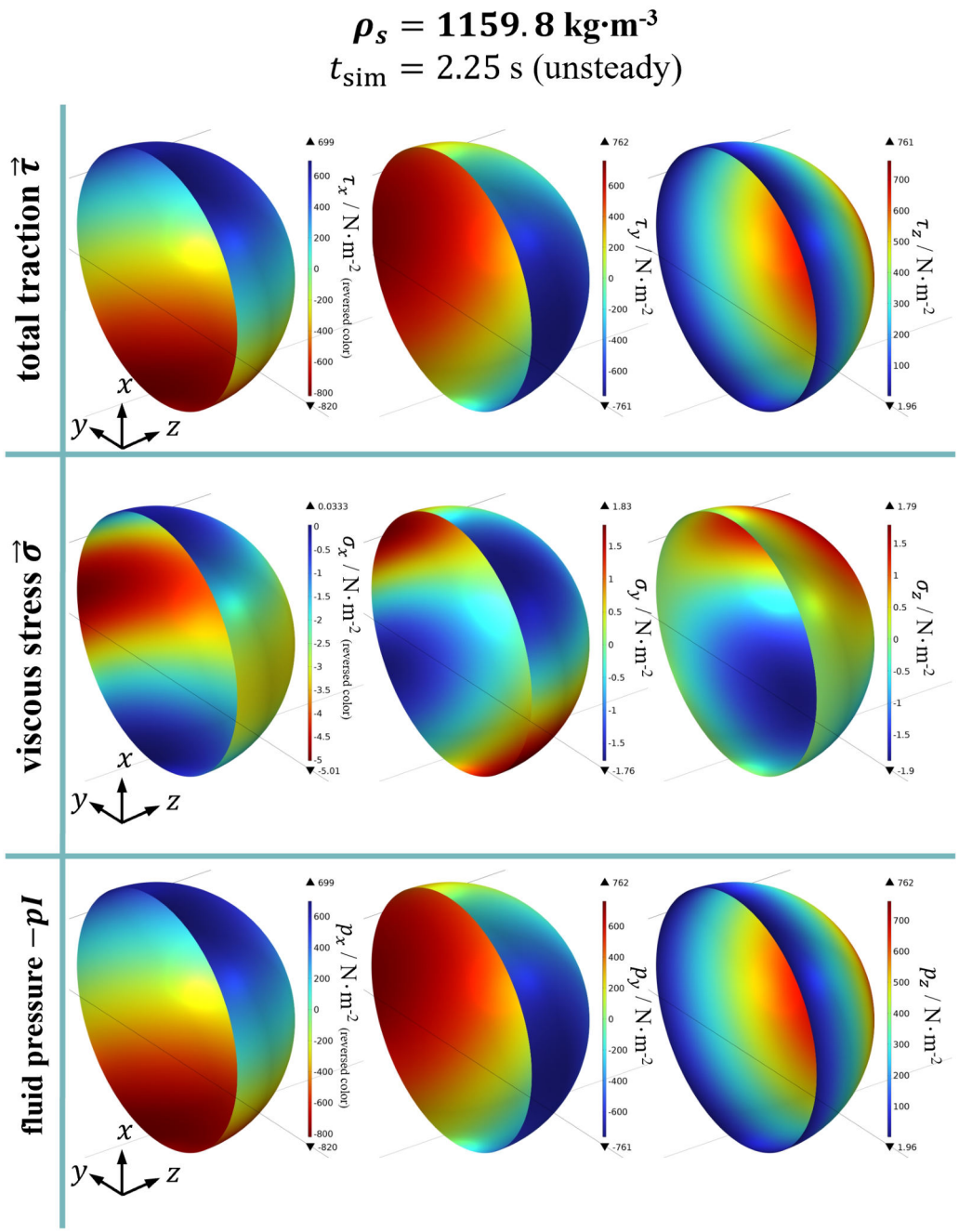


Figure 4.10: Simulated fluid stresses on the surface of a sphere ($R = 6$ mm) with density $\rho_s = 1159.8$ kg·m^{-3} ($Re_P \approx O(10^{-1})$) sedimenting at a distance of $d_{sim}/R = 2$ from a plane no-slip boundary in a rectangular fluid domain at time $t_{sim} = 2.25$ s (unsteady).

sumed that these small deformations purely due to viscous shear would have an influence on the kinematics (*cf.* perturbation parameter α from Murata discussed in our previous report). [15],[70] Nevertheless, it should be mentioned that these small shear deformations which are asymmetrically distributed on the surface of the sphere and are largest in the area between the sphere and the wall could have an influence on the

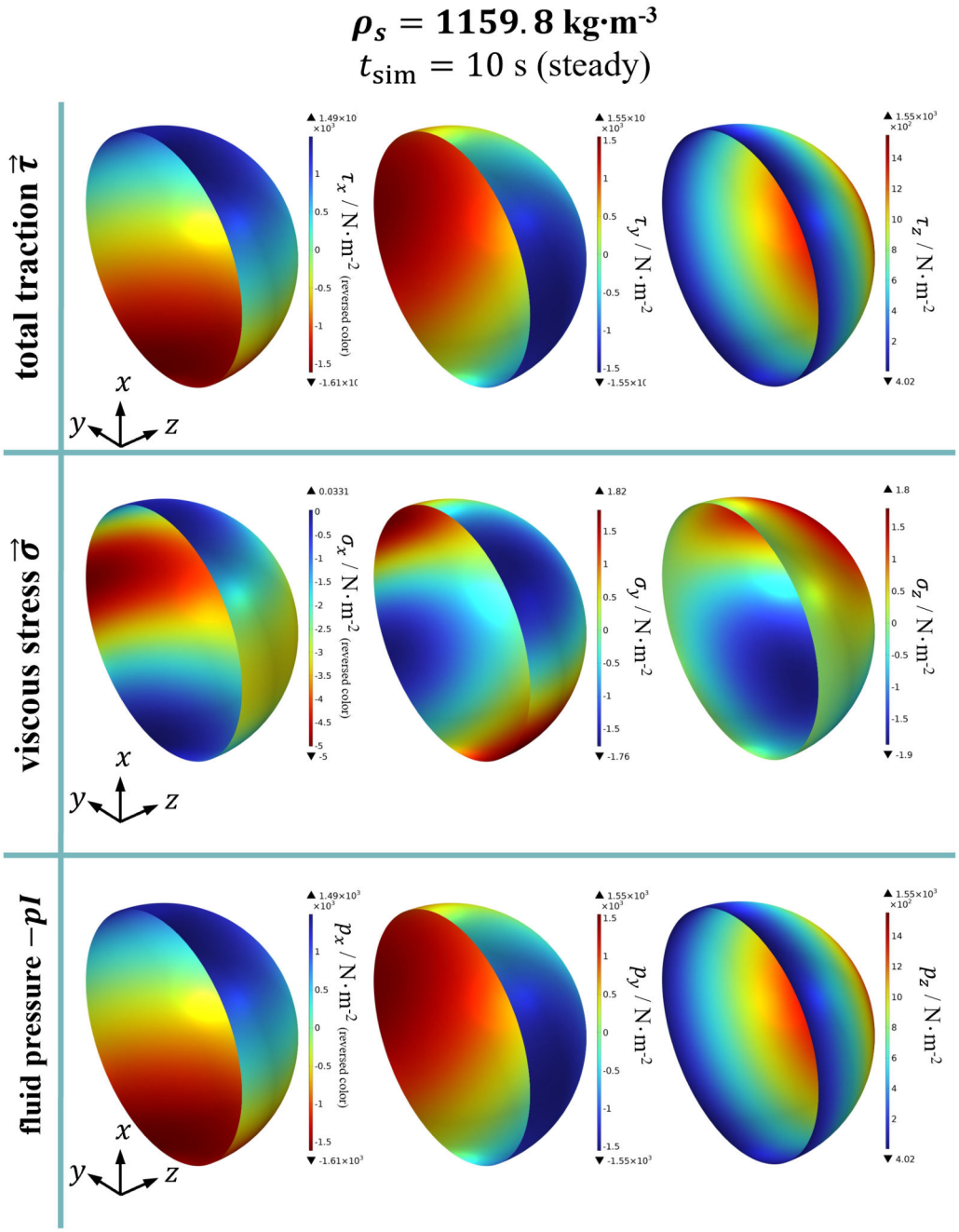


Figure 4.11: Simulated fluid stresses on the surface of a sphere ($R = 6$ mm) with density $\rho_s = 1159.8\ \mathrm{kg{\cdot}m^{-3}}$ ($Re_P \approx O(10^{-1})$) sedimenting at a distance of $d_{\mathrm{sim}}/R = 2$ from a plane no-slip boundary in a rectangular fluid domain at time $t_{\mathrm{sim}} = 10$ s (steady).

dynamics anyway. These small deformations should be taken into account with regard to memory forces and the long time scales on which they act. In other words, the sedimenting sphere has plenty of time to interact with the wall, and even small deformations in the gap can change the flow field, which is then reflected back from the wall, etc.

4.4.3 Traction forces, drag and lift

In this section, the forces resulting from the integration over the sphere surface of the fluid stresses discussed in the previous section are analyzed. Integration of the complete stress vector τ_i results in the total traction forces $F_{i,tot}$ exerted by the fluid (designation taken from COMSOL). The components of the traction forces (viscous component and pressure component) in the direction of fall (referred to as *tangential forces* in the following) and the components in the direction normal to the nearest wall, *i.e.* in the y-direction, are considered. The force in z-direction cannot be calculated for the reasons of symmetry. However, the force is also of little relevance. It should be mentioned that only half the force is obtained by integrating the stresses from the simulation. In the diagrams, the force for a complete sphere is presented. Due to the symmetry, this simply corresponds to twice the force resulting from the simulation. It should also be mentioned that the forces calculated from the fluid stresses represent the forces of an imaginary fluid element shell around the sphere and that the resulting forces are considered from the reference frame of the fluid, *i.e.*, these are the active forces (*"actio"*). However, when dealing with the forces acting on a body in the sense of classical Newtonian mechanics (*e.g.* inertia, drag, lift, ect.), the opposite forces are meant, *i.e.*, the reaction forces (*"reactio"*). For this reason, all forces resulting from the fluid stresses are shown with a negative sign.

4.4.3.1 Traction forces in fall direction and drag calculation of simulation with $\rho_s = 1159.8$ kg·m^{-3} ($Re_P \approx O(10^{-1})$)

Fig. 4.12 shows the simulated tangential forces $-F_{x,i}$ (traction forces in fall direction) of the sphere with a density of $\rho_s = 1159.8$ kg·m^{-3} ($Re_P \approx O(10^{-1})$) plotted against time t_{sim}.

Furthermore, the drag force resulting from the simulation ($F_{D,sim}$) and the theoretical drag force resulting from Faxén´s law are plotted, *cf.* Eq. 4.1. [29]

$$F_{D,th} = \frac{6\pi\eta R U_{P,sim}}{1 - \frac{9}{16}\left(\frac{R}{d}\right) + \frac{1}{8}\left(\frac{R}{d}\right)^3 - \frac{45}{256}\left(\frac{R}{d}\right)^4 - \frac{1}{16}\left(\frac{R}{d}\right)^5} \tag{4.1}$$

The figure shows that the simulated drag is not equal to the integral of the viscous part of the fluid stress vector, *i.e.* $F_{x,\eta} \neq F_{D,sim}$. The drag acting on the sphere as it sediments corresponds to the total (negative) traction force reduced by the sphere´s buoyancy, see Eq. 4.2.

$$F_{D,sim} = -\int_S \tau_x \mathrm{d}S - \frac{4}{3}\pi R^3 \rho g \tag{4.2}$$

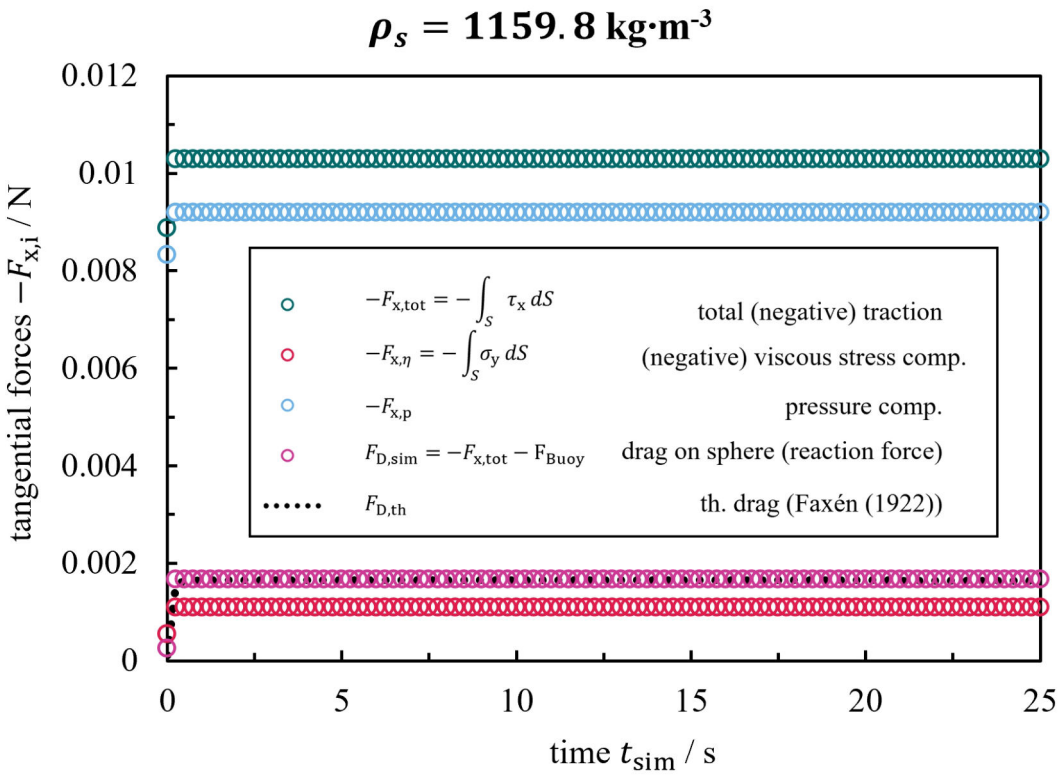


Figure 4.12: Simulated tangential forces $-F_{x,\,i}$ (traction forces in fall direction) of a sphere ($R = 6$ mm) with density $\rho_s = 1159.8$ kg·m^{-3} ($Re_P \approx O(10^{-1})$) sedimenting at a distance of $d_{sim}/R = 2$ from a plane no-slip boundary in a rectangular fluid domain plotted against time t_{sim}. Dotted line: theoretical drag (Eq. 4.1).

The largest proportion of the total traction force stems from the pressure component of the fluid stresses ($F_{x,\,p} \approx 0.89 F_{x,\,tot}$). In Fig. 4.13, the components are therefore considered separately on the respective resolved axis scaling.

The diagram on top in Fig. 4.13 shows the total force (green circles) over the simulation time t_{sim}, or over the dimensionless sedimentation distance x_{sim}/R (insert), respectively. $F_{x,\,tot}$, like the simulated velocity curve, shows a short overshoot at the beginning. At the end, the force increases rapidly. The breakdown of the total force into its components reveals that the overshoot originates solely from the viscous component. Compared to the overshoot of the velocity, however, the overshoot of the force is negligible. This becomes clear in the joint plot of the simulated drag $F_{D,sim}$ and the theoretical drag $F_{D,th}$, *cf.* Fig. 4.14.

The theoretical value according to Faxén's model behaves qualitatively like the velocity curve. The stationary value calculated with Faxén's equation underestimates the simulated value by only ≈ -1.2 %.

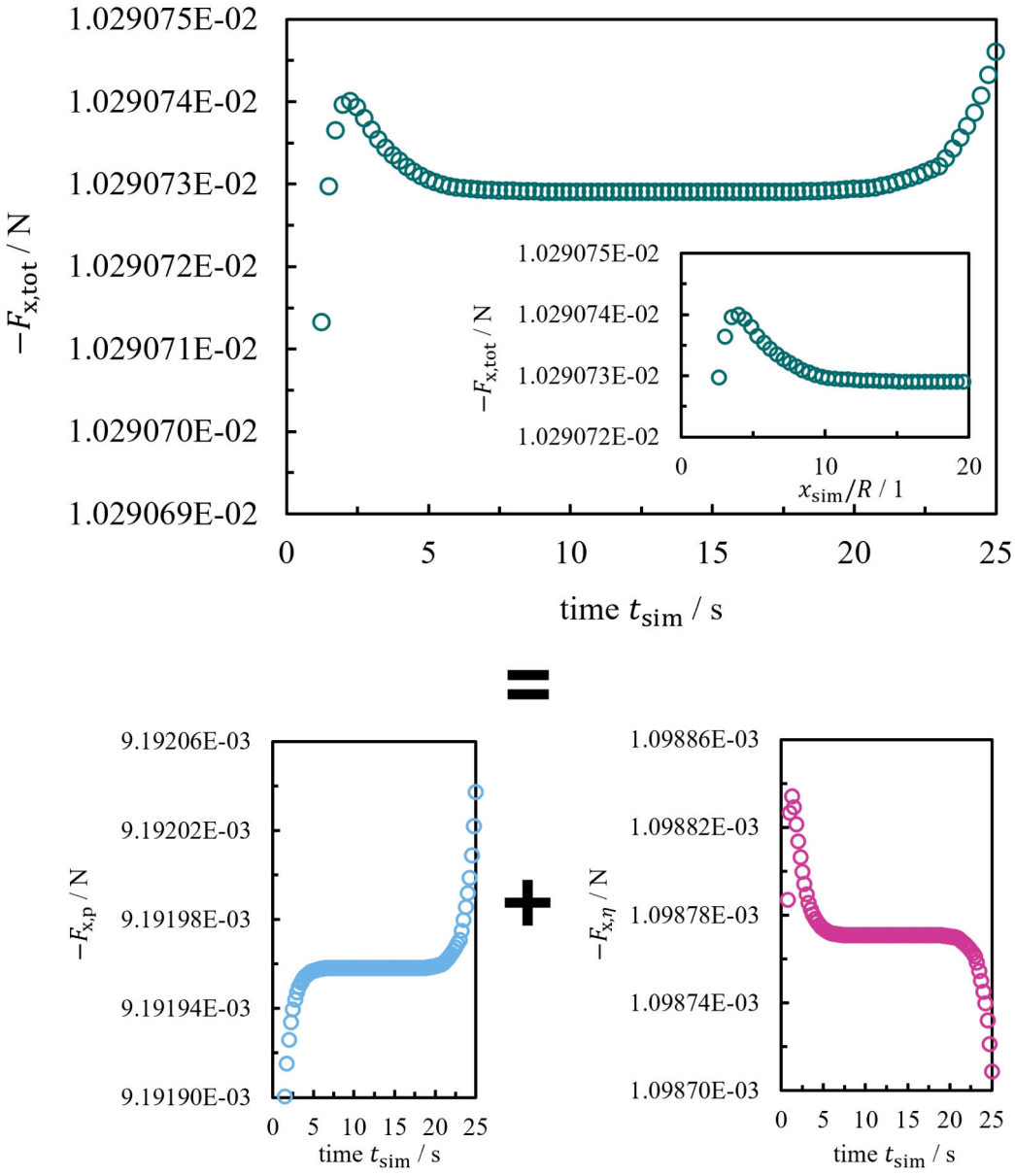


Figure 4.13: Resolved axis scaling of simulated tangential forces $-F_{i,x}$ of a sphere (R = 6 mm) with density ρ_s = 1159.8 kg·m^{-3} ($Re_P \approx O(10^{-1})$) sedimenting at a distance of $d_{sim}/R = 2$ from a plane no-slip boundary in a rectangular fluid domain plotted against time t_{sim}.Top: total traction; Bottom: pressure component (left) and viscous component (right).

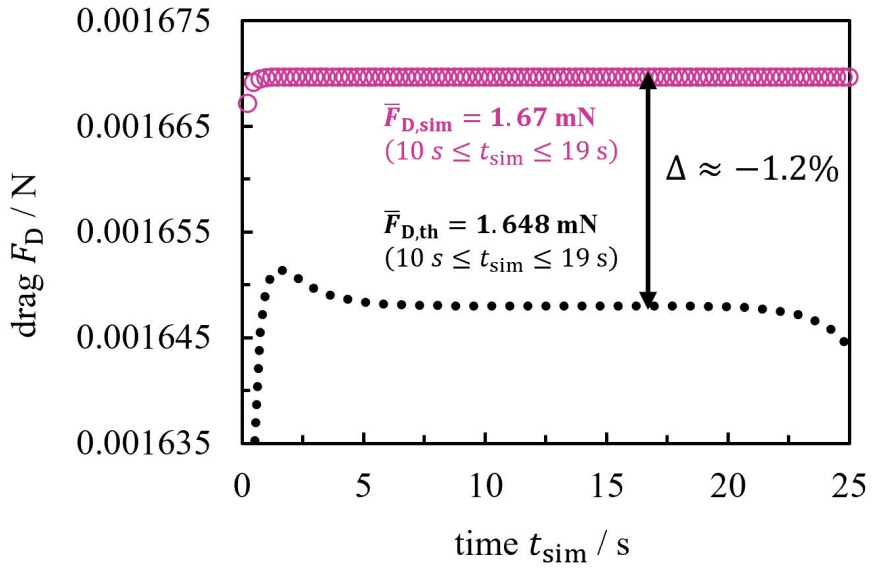


Figure 4.14: Calculated drag from the simulation of a sphere (R = 6 mm) with density ρ_s = 1159.8 kg·m^{-3} ($Re_P \approx O(10^{-1})$) sedimenting at a distance of d_{sim}/R = 2 from a plane no-slip boundary in a rectangular fluid domain plotted against time t_{sim} in comparison with the theoretical value calculated with Faxén´s equation 4.1

.

4.4.3.2 Traction forces in fall direction and drag calculation of simulation with ρ_s = 987.59 kg·m^{-3} ($Re_P \approx O(10^{-2})$)

Fig. 4.15 shows the individual components tangential forces of the three simulations of the sphere with a density of ρ_s = 987.59 kg·m^{-3} ($Re_P \approx O(10^{-2})$) directly resolved with the respective axis scaling.

The forces are shown from top to bottom in the same way as they would appear in the overview in a single diagram (see Fig. 4.20 in the chapter appendix, where the legend can also be found). As can be seen there, an overall representation in one diagram is not useful. The drag forces and the viscous component can no longer be resolved, as they only amount to approximately 1% of the total force.

The curves of simulation 2 (lower numerical accuracy, release close to open boundary) show that poorer numerics have a negative effect on the simulation result, especially at the beginning.

As with the velocities, it can be seen that the curves from simulation 3 (high numerical resolution + deep immersion) directly reach the stationary value without an overshoot or any other instationarities. The curves of the pressure component ($-F_{x,p}$) and the viscous component ($-F_{x,\eta}$) of simulation 1 behave qualitatively like the curves at higher density, *i.e.* larger velocities (see Fig. 4.13). The pressure force of simulation 1 increases and runs asymptotically towards the value of simulation 3. The viscous component in turn shows an overshoot and then also approaches the value of simulation 3. This supports the assumption already made that simulation 1 is numerically correctly resolved and that the transient behavior up to $x_{sim}/R \lessapprox 10$ is ac-

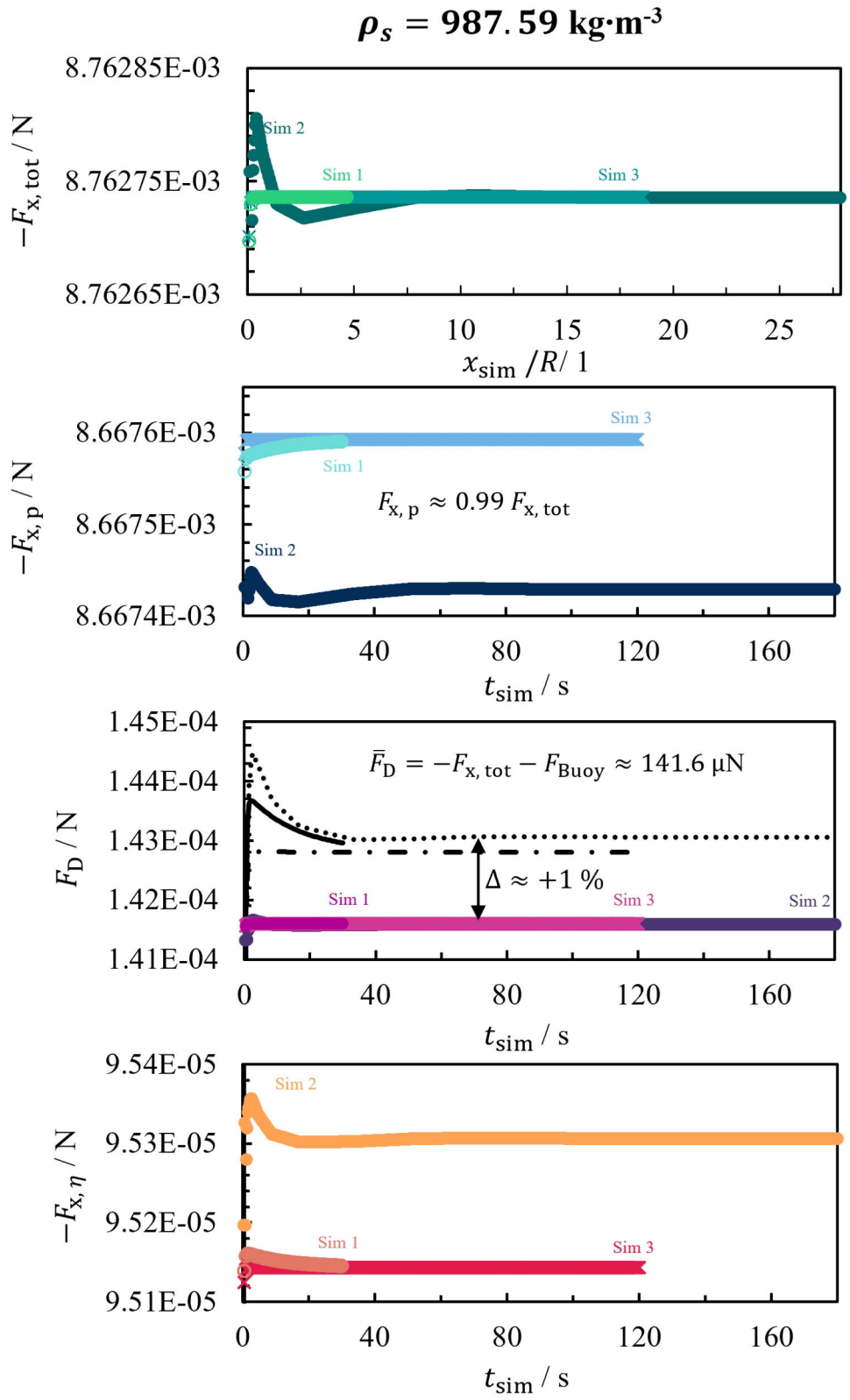


Figure 4.15: Resolved axis scaling of the tangential forces $-F_{x,\,i}$ (traction forces in fall direction) of a sphere ($R = 6$ mm) with density $\rho_s = 987.59$ kg·m^{-3} ($Re_P \approx O(10^{-2})$) sedimenting at a distance of $d_{sim}/R = 2$ from a plane no-slip boundary in a rectangular fluid domain plotted against time t_{sim} (x_{sim}/R). Three simulations are shown: high num. accuracy (Sim 1), lower num accuracy (more output times) (Sim 2) and high num. accuracy + deep immersion (Sim 3). Black (dotted) lines: theoretical drag (Eq. 4.1); Total traction, pressure component, drag in comparison with Faxén´s value, viscous component (from top to bottom).

tually caused by the proximity to the open boundary.

4.4.3.3 Traction forces in direction normal to the wall and lift force calculation

Fig. 4.16 shows the simulated normal forces $-F_{\mathrm{y,\,i}}$ (forces pointing normal to the nearest wall) of the sphere with a density of $\rho_{\mathrm{s}} = 1159.8\ \mathrm{kg{\cdot}m^{-3}}$ ($Re_{\mathrm{P}} \approx O(10^{-1})$) plotted against the dimensonless sedimentation distance x_{sim}/R. The corresponding figure for the simulations with a density of $\rho_{\mathrm{s}} = 987.59\ \mathrm{kg{\cdot}m^{-3}}$ ($Re_{\mathrm{P}} \approx O(10^{-2})$) was shown and discussed in detail in Chapter 3.5.1.3.

The total (negative) traction force in y-direction, $-F_{\mathrm{y,tot}}$, corresponds to the lift force F_{L} acting on the

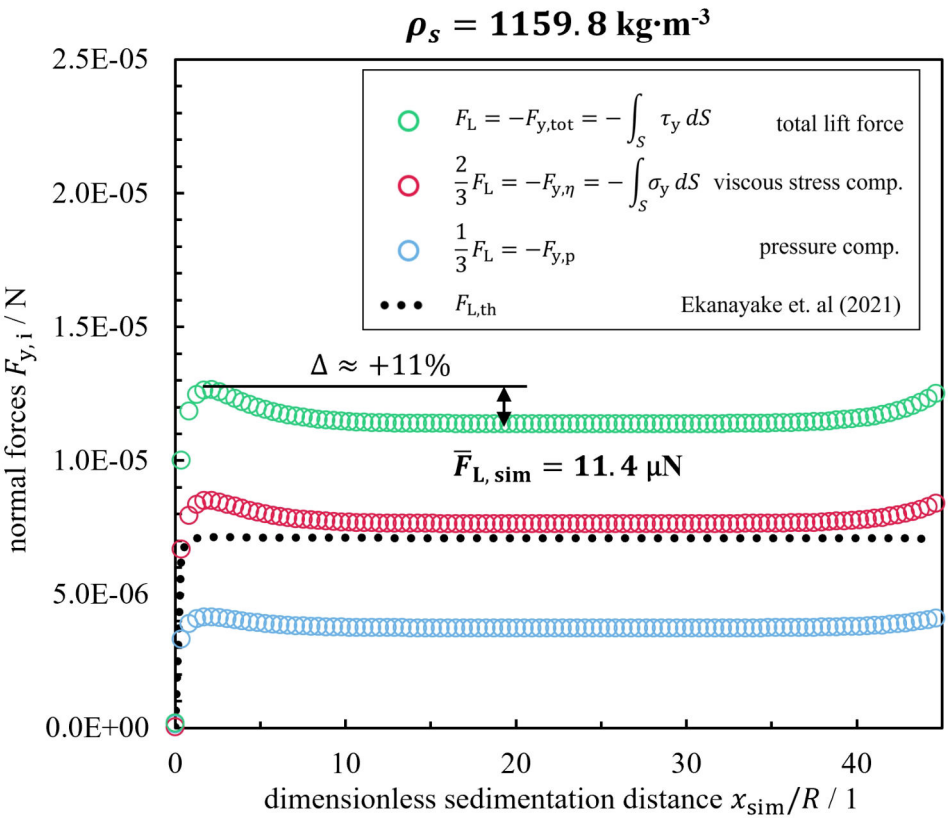


Figure 4.16: Simulated normal forces $-F_{\mathrm{i,y}}$ (traction forces in y-direction) of a sphere ($R = 6$ mm) with density $\rho_{\mathrm{s}} = 1159.8\ \mathrm{kg{\cdot}m^{-3}}$ ($Re_{\mathrm{P}} \approx O(10^{-1})$) sedimenting at a distance of $d_{\mathrm{sim}}/R = 2$ from a plane no-slip boundary in a rectangular fluid domain plotted against the dimensionless sedimentation distance x_{sim}/R. Dotted line: theoretical lift force calculated with the simulated particle velocity and the model of Ekanayake *et al.* (Eq. 3.4).

sphere. As with the drag, the lift force is the reaction force to the fluid traction forces in y-direction and would cause the sphere to move away from the wall (what is not possible in this simulation).

The viscous component accounts for 2/3 of the total force and the pressure component for 1/3. These

are the coefficients that also appear in the viscous stress tensor for a Newtonian, incompressible fluid.

The simulated lift force of a sphere with a density of $\rho_s = 1159.8$ kg·m^{-3} ($Re_P \approx O(10^{-1})$ overshoots by 11%. For comparison: in the simulation with a lower density it was 260%, *cf.* Fig. 3.6.

The simulated total lift force was compared with values of the total lift force of the model for translational motion parallel to one plane wall which was proposed by Ekanayake *et al.*, *cf.* equations 3.3 and 3.4 in the previous Chapter 3. [52] The theoretical value was calculated with the simulated velocity $U_{P,sim}$. The theoretical lift force is instantaneously steady. The small overshoot in velocity has consequently no influence on the magnitude of the lift force.

Apart from the initial time dependence, the stationary values are of the same small order of magnitude. However, the steady lift force from the simulations are larger compared to the lift force from the model of Ekanayake *et al.*, which is a model for a single plane wall (the model underestimated the simulated value by $\Delta \approx -37$ % for both simulated densities).

It is important to emphasize again that the oveshoot of the lift force by 260% in the simulations with low density ($\rho_s = 987.59$ kg·m^{-3} ($Re_P \approx O(10^{-2})$)) and small immersion depth $h_{I,1\&2} = 56$ mm to the open boundary (interface) was completely independent of the numerics. The curve of simulation 1 and 2 were almost identical, while the curve of simulation 3 ($h_{I,3} = 156$ mm) directly shows a stationary force. This suggests that the proximity to the surface and in particular the influence on the vortex during acceleration is the reason for the unsteady behavior at the beginning.

4.5 Conclusions

3D Computational Fluid Dynamics (CFD) simulations of a sphere with varying density ($\rho_s = 987.59$ kg·m^{-3} ($Re_P \approx O(10^{-2})$) and $\rho_s = 1159.8$ kg·m^{-3} ($Re_P \approx O(10^{-1})$)) sedimenting in a rectangular fluid domain in the vicinity of a plane no-slip boundary were performed. The same dimensions and properties (container dimensions, sphere size, material properties, etc.) were used as in the experiment. With the help of the simulations, interesting insights could be gained, for example into the appearance of the flow field during sedimentation in a rectangular duct.

The differential equation around a falling sphere was solved using the finite element method in COMSOL Multiphysics® and was coupled with the creeping flow equations of the surrounding fluid via the mass inertia term. By applying suitable symmetry-conditions, only one half of the container had to be simulated in the near-wall simulation. This reduced the computational effort enormously. The sphere was not simulated as a solid, but as a hollow space having the mass of the solid sphere. Therefore, no fluid-structure

interactions were considered, *i.e.* the simulation only modeled rigid spheres. A moving mesh approach with an Arbitrary Lagrangian-Eulerian (ALE) formulation was chosen to simulate the fall of the sphere in the fluid domain. The special feature of the method used is that a co-moving, non-deforming mesh domain was inserted around the sphere. This prevented a strong distortion of the mesh around the sphere and allowed a fine spatial resolution around the sphere. With this method, the fluid flow field around the sphere could be simulated in great detail. The walls of the container were modeled as no-slip boundaries and the boundary on top was modeled as open boundary with zero normal forces. Spheres with a density of $\rho_s = 987.59\ \mathrm{kg{\cdot}m^{-3}}$ ($Re_P \approx O(10^{-2})$) and $\rho_s = 1159.8\ \mathrm{kg{\cdot}m^{-3}}$ ($Re_P \approx O(10^{-1})$) were simulated, which started at an immersion depth of $h_{I,1\&2} = 56$ mm and at a distance of $d/R = 2$ to the nearest wall. To determine the influence of the open boundary on the sedimentation, an additional simulation was carried out in which the sphere was immersed at a larger depth ($h_{I,3} = 156$ mm). In addition, a mesh independence study was carried out and the influence of the numerical parameters (time step sizes) on the simulation results was investigated.

The simulated velocities of the spheres in the near-wall region with higher density were slightly larger than the measured velocities ($\Delta_{sim;d=12;1159.8} = +8.3$ %). However, the simulated velocity in the near-wall region of the sphere with lower density is significantly larger ($\Delta_{sim;d=12;987.59} = +16.5$ %) than the measured peak velocity in the experiment ($U_{P,exp,Peak} = 0.8\ \mathrm{mm{\cdot}s^{-1}}$). Remarkably, the dimensionless velocity resulting from the simulated particle velocity in the near-wall region ($\left(U_{P,sim}/U_{St}\right)_{d=12;987.59} \approx 0.71$) is of same order of magnitude as the dimensionless values of the experiments and simulations for the sphere with higher density ($\left(U_{P,exp}/U_{th,ub}\right)_{d=12;1159.85} \approx 0.70$ and $\left(U_{P,sim}/U_{th,ub}\right)_{d=12;1159.8} \approx 0.73$). This supports the observation made in the previous section, that the mass acceleration of spheres sedimenting at $Re_P \approx O(10^{-2})$ is interrupted prematurely at $\left(U_{P,exp,Peak}/U_{St}\right)_{d=12;988.24} \approx 0.61$. The simulated velocity curves show a small overshoot at both Reynolds numbers, qualitatively similar at first glance to the peak in the experiments of the softest spheres in the near-wall region. However, the overshoot in the simulation only occurred for a short time and at a short distance, *i.e.*, it does not correspond by far to the long-term transient behavior in the experiments. The overshoot in velocity could be attributed in parts to numerical inaccuracies on the one hand and to the proximity to the open boundary on the other, *i.e.* the overshoot did not occur if the sphere started sedimentation deeply immersed. If the velocity field and the streamlines of the surrounding fluid were considered, a large vortex formed between the sphere and the wall far away. This vortex also affected the local velocity field around the sphere. If the sphere started close to the open boundary, the vortex was influenced by the interface, which manifested itself in the form of asymmetries. It was also shown that the distance to the open boundary, from which the dynamics became stationary, corresponds approximately to the characteristic size of the vortex, *i.e.* the vortex radius. The radius of the vortex is approximately equal to half the width of the container. The dynamics are therefore also dependent on the characteristic sizes of the confinement. It is conceivable that precisely such a vortex also occurred in the experiments during the

acceleration phase and that the asymmetries of the vortex led to the special features in the kinematics, *e.g.* in the form of *inertial wall attraction*.

The simulations were also used to calculate the fluid stresses on the sphere surface as it falls. It was found that the viscous stresses in the direction of fall, which cause shear on the surface of the sphere, were largest at the point of the smallest distance between the sphere and the wall, *i.e.* at the point where $d/R = 2$, and are distributed asymmetrically on the sphere surface. In addition, the total stresses pointing normally to the outer walls were largest at these points, *i.e.* the walls cause a lateral compression on the the sphere. The deformation caused by the total stresses was estimated by assuming linear elasticity. The deformations would be in the range between approximately 30 and 60 µm. The pure shear stresses in the gap between the nearest wall and sphere would only lead to small deformations in the range 0.06 µm. Although the deformations being small, they could have a significant influence with regard to memory forces acting on very long time scales.

From the fluid stresses on the surface, the traction forces acting on the surface can be deduced by integration, and from this in turn the corresponding reaction forces, such as drag and lift. For spheres with a density of $\rho_s = 1159.8$ kg·m^{-3}, a drag force of $\overline{F}_{D,sim,\,1159.8} = 1.67$ mN was calculated and for a density of $\rho_s = 987.59$ kg·m^{-3}, the simulated drag was $\overline{F}_{D,sim,\,987.59} = 141.6$ µN. The simulated drag forces correspond in good approximation to the theoretical value at the simulated velocity, which results from the drag model of Faxén for a sphere translating in the vicinity of one plane wall. The closest wall therefore determines the drag significantly and the other walls have less influence.

The simulated lift force of a sphere with density $\rho_s = 1159.8$ kg·m^{-3} was $\overline{F}_{D,sim,\,1159.8} = 11.4$ µN and for the sphere with a density of $\rho_s = 987.59$ kg·m^{-3} the lift was $\overline{F}_{D,sim,\,987.59} = 86.3$ nN. The simulated lift forces of the spheres that started near the surface show a strongly time-dependent behavior in the form of an overshoot of 11% for the spheres of higher density and even 260 % in the simulation with spheres of lower density. In this case, the numerics had no effect on the result, but the overshoot can be attributed without doubt to the proximity to the open boundary on top.

In summary, these simulations provided insights into the dynamics within the experiment from the last two chapters that are otherwise difficult or impossible to access. This applies in particular to the flow field, which cannot be visualized by experimental methods (*e.g.* PIV) in a viscous medium. In addition, important forces such as drag or lift, could be quantified. Probably the most important result of the simulations is that the proximity to the interface had such a decisive influence. It would not have been conceivable beforehand that possible causes for the special kinematic features, such as inertial wall attraction, might be related to the proximity to the liquid-gas interface.

In the future, the simulation model could be extended to include fluid-structure interaction (FSI). However, initial attempts to implement FSI have shown that the main difficulty here lies in the implementation of

a second moving mesh in order to couple the deformation to the fluid mechanics. In addition, it would also be interesting to carry out investigations in which other mass inertial forces are also taken into account in this model, *e.g.* the added mass or the Basset history force. It is conceivable that interesting insights could also be gained here, particularly with regard to how the free interface affects the dynamics when it is shifted to even longer time scales.

4.6 Chapter appendix

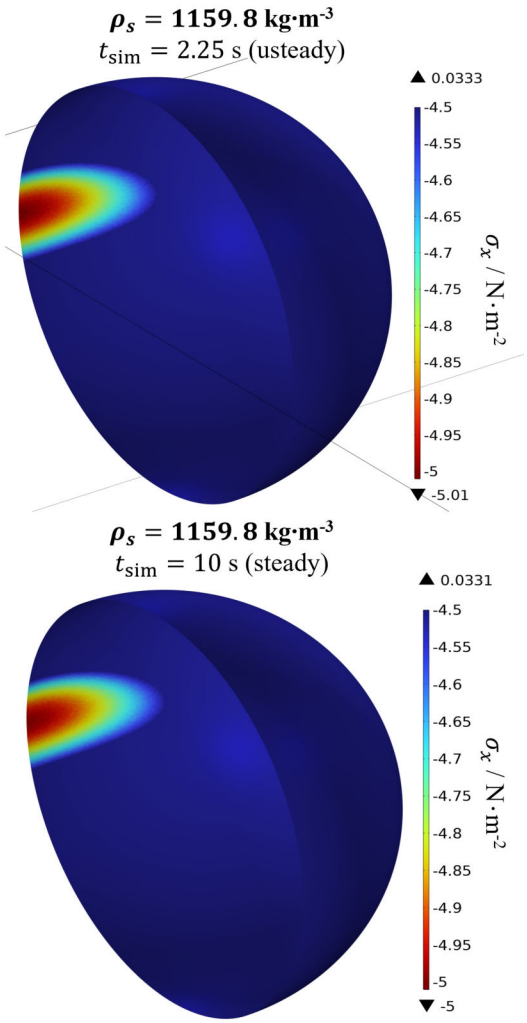


Figure 4.17: Small axis scaling of the simulated x-component of the viscous stress σ_x on the surface of a sphere ($R = 6$ mm) with density $\rho_s = 1159.8$ kg·m^{-3} ($Re_P \approx O(10^{-1})$) sedimenting at a distance of $d_{sim}/R = 2$ from a plane no-slip boundary in a rectangular fluid domain at time $t_{sim} = 2.25$ s (unsteady, top) and $t_{sim} = 10$ s (steady, bottom).

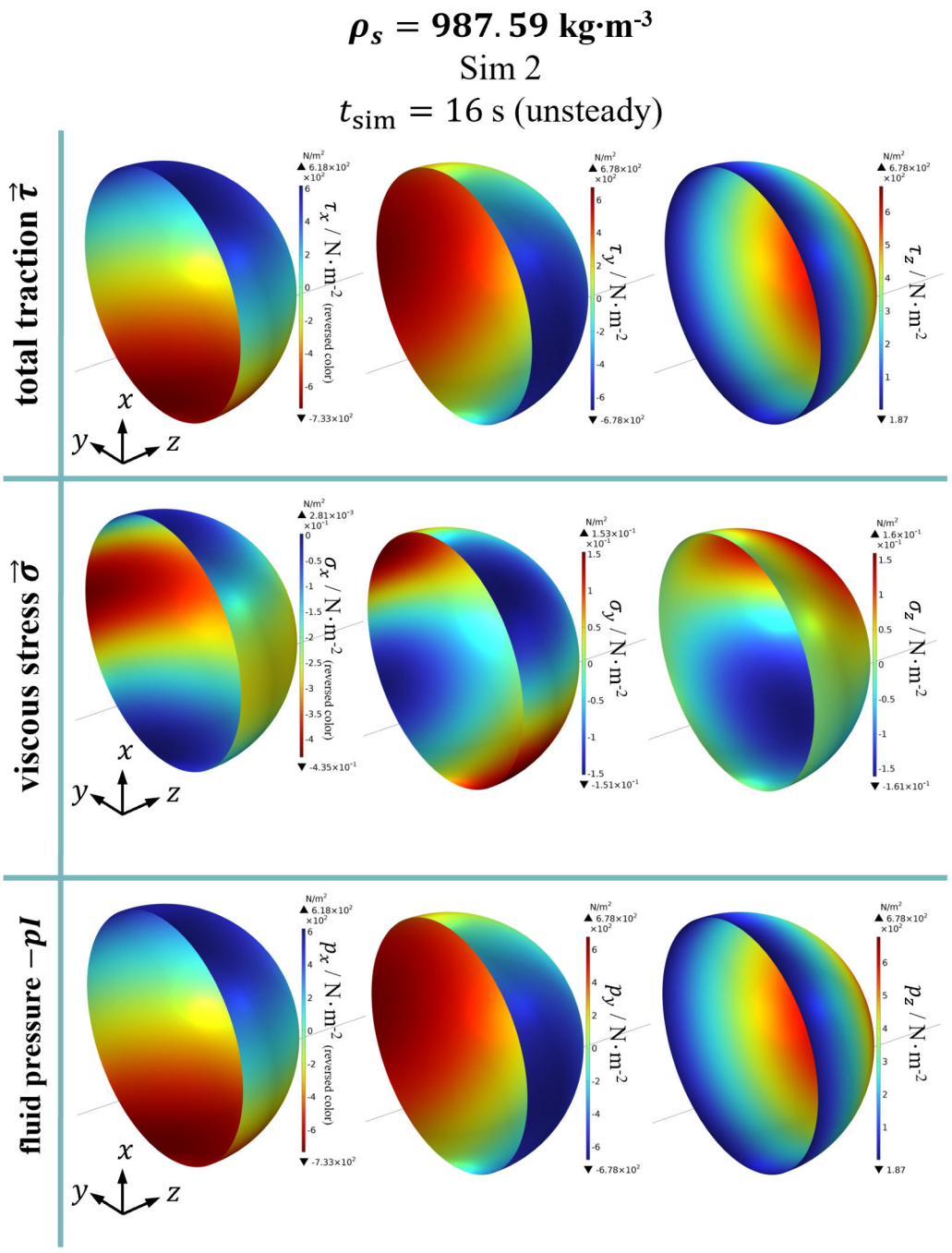


Figure 4.18: Simulated fluid stresses on the surface of a sphere ($R = 6$ mm) with density $\rho_s = 987.59$ kg·m^{-3} ($Re_P \approx O(10^{-2})$) sedimenting at a distance of $d_{sim}/R = 2$ from a plane no-slip boundary in a rectangular fluid domain at time $t_{sim} = 16$ s (unsteady).

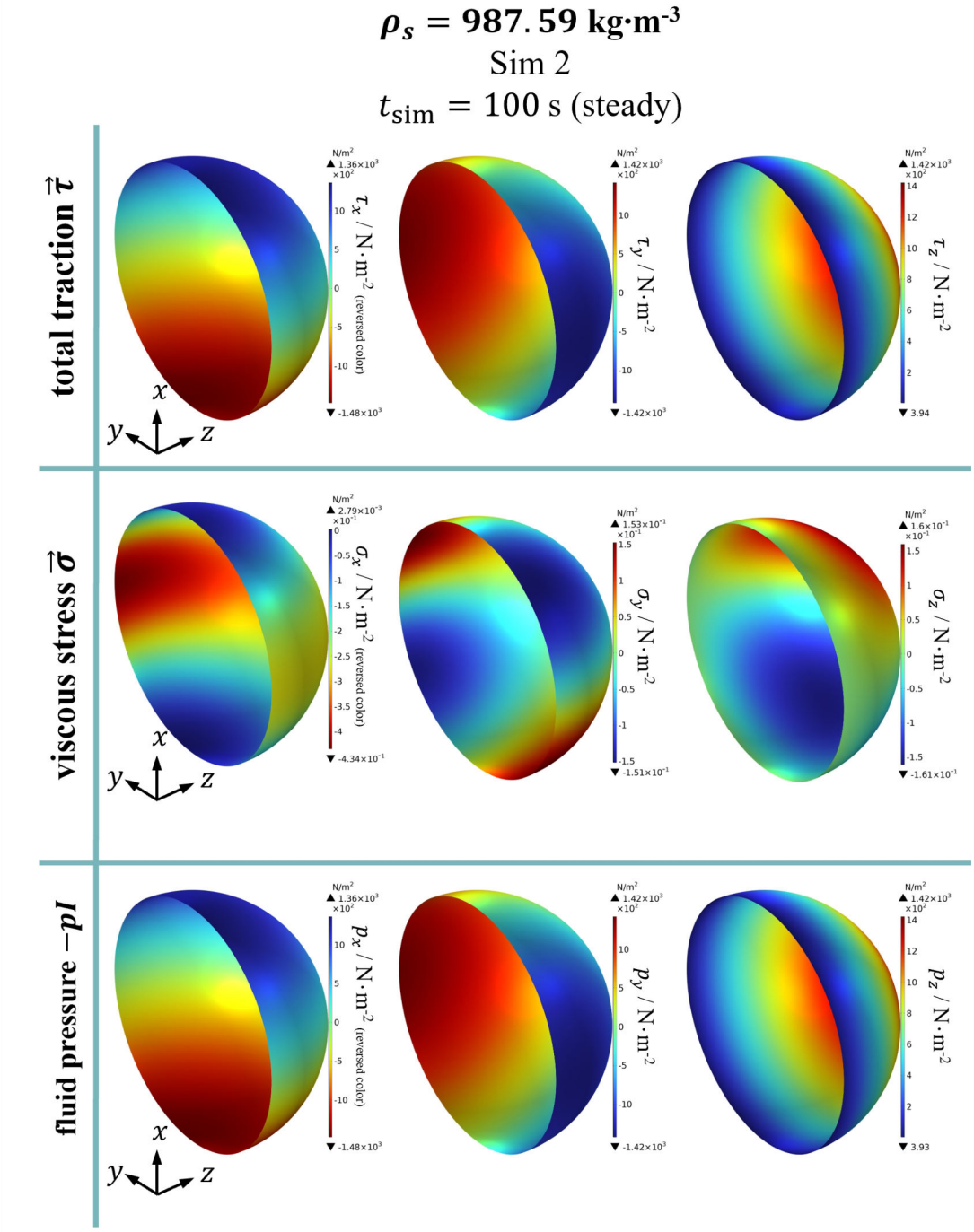


Figure 4.19: Simulated fluid stresses on the surface of a sphere ($R = 6$ mm) with density $\rho_s = 987.59$ kg·m^{-3} ($Re_P \approx O(10^{-2})$) sedimenting at a distance of $d_{sim}/R = 2$ from a plane no-slip boundary in a rectangular fluid domain at time $t_{sim} = 100$ s (steady).

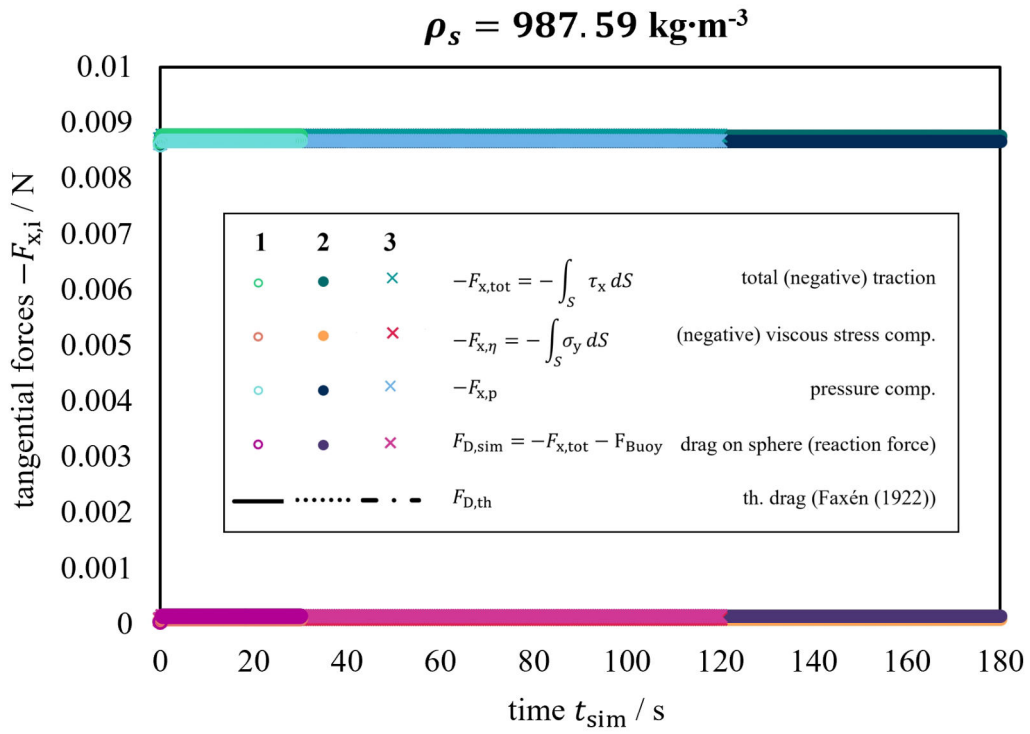


Figure 4.20: Simulated tangential forces $-F_{x,i}$ (traction forces in fall direction) of a sphere ($R = 6$ mm) with density $\rho_s = 987.59$ kg·m^{-3} ($Re_P \approx O(10^{-2})$) sedimenting at a distance of $d_{sim}/R = 2$ from a plane no-slip boundary in a rectangular fluid domain plotted against time t_{sim}. Three simulations are shown: high num. accuracy (Sim 1), lower num. accuracy (more output times) (Sim 2) and high num. accuracy + deep immersion (Sim 3). Black (dotted) lines: theoretical drag (Eq. 4.1).

5 Low *Re* kinematics of short, cylindrical rods accelerating axially aligned from rest in a rectangular duct

Contents

5.1 Abstract . . . 119
5.2 Introduction . . . 120
5.3 Theory . . . 125
5.4 Methods . . . 131
5.4.1 Experimental setup and definitions . . . 131
5.4.2 Data acquisition - Particle tracking velocimetry of cylindrical particles . . . 134
5.4.3 Model particle fabrication and soft wall fabrication . . . 136
5.5 Results and Disucssion . . . 138
5.5.1 Kinematics of short, cylindrical rods falling near rigid, plane walls . . . 138
5.5.2 Kinematics of short, cylindrical rods falling near a soft, plane wall . . . 161
5.6 Conclusions and outlook . . . 165
5.7 Chapter Appendix . . . 170

5.1 Abstract

The kinematics of rods with small aspect ratios $l/r \approx 5-6$ sedimenting at particle Reynolds numbers $Re_P = \rho|\vec{U}|l\eta^{-1} \lessapprox 0.1$ in a rectangular tank filled with a viscous Newtonian fluid were investigated. The rods were initially aligned axially with respect to their cylinder axis (orientation angle $\theta = 0°$) and released from rest at various distances from the plane walls. Both rigid, non-deformable rods - sedimenting at $Re_P \approx O(10^{-1})$ and $Re_P \approx O(10^{-2})$ (by varying the density) - and soft, deformable rods - sedimenting

at $Re_P \approx O(10^{-2})$ - were examined. Sedimentation experiments were conducted near both rigid and elastic plane walls. To investigate wall elasticity effects, the experimental setup was equipped with an additional thick, soft elastic layer. The results for rigid rods at $Re_P \approx O(10^{-1})$ were stable and reproducible even in close proximity to the walls. These were compared with theoretical predictions obtained by combining a semi-empirical velocity estimate for axial translation in an unbounded fluid which is based on slender-body theory (Kharrouba *et al.* (2021), *Phys. Rev. Fluids* 6, 044308) with wall correction factors known from sedimentation involving spheres in a rectangular duct. Good agreement was observed for axially falling cylinders in the center of a square duct and up to orientation angles of $\theta \approx 15^\circ$ for inclined cylinders near plane walls. At $Re_P \approx O(10^{-2})$, the kinematics showed instabilities and increasing nonlinear behavior with increasing deformability. Due to sensitivity to small variations in initial conditions, results were not reproducible and could only be analyzed qualitatively. However, through sorting and classification techniques, characteristic kinematic features - particularly those associated with elastohydrodynamic interactions - were identified. These include, for example, the drifting of soft rods at a nearly constant orientation angle near a wall. In contrast, non-deformable rods at similar Reynolds numbers predominantly exhibited flipping behavior. These kinematic patterns closely resemble the motion of red blood cells (RBCs) in shear flow, with tank-treading (drifting) observed in soft, deformable cells and tumbling in stiffer ones. The ability to replicate and accurately measure such microscale behaviors at a macroscopic level offers new opportunities for data acquisition and validation in modeling particle flows with elastic interactions in the low-Reynolds-number regime.

5.2 Introduction

Sedimentation of cylindrical or rod-shaped particles is significant in a wide range of applications, including environmental and biological contexts. For example, in water systems, sedimentation of cylindrical particles is observed with biological materials, such as rod-shaped bacteria like *Bacillus subtilis*, or rod-shaped natural fibres like wood fibers. [100] Similarly, engineered approaches to microplastic removal often focus on non-spherical particles, including fragments and fibers, which must settle out of suspension for effective extraction from wastewater. [101] Modeling the sedimentation dynamics of these cylindrical particles is critical to understanding and predicting their behavior in fluids, yet presents notable challenges due to their anisotropic shape, *i.e*, the hydrodynamic forces vary with the spatial direction. While the dynamics of spherically isometric particles in unbounded fluids up to Reynolds numbers of $Re_P \approx O(10^{-1})$ are well-described by classic models such as Stokes' law or Oseen´s equations, non-spherical particles like cylinders introduce

additional complexities, *e.g.* the dependence on their orientation. [27],[49],[2] Thus even the simplest case of sedimentation, falling in an unbound fluid, becomes a multi variable problem.
Various mathematical models have been developed to address these challenges, including slender-body theory and computational approaches that account for rotational and translational dynamics. [2],[102],[103],[104] Empirical models and adaptations of Stokes' law have also been proposed for cylinders, though these often rely on approximations that only hold for specific shapes (*e.g.* prolate ellipsoid), sizes (*e.g.* large aspect ratios), or flow conditions (*e.g.* steady flow conditions). [2]. A large number of numerical studies of cylindrical bodies and on prolate spheroids at different Reynolds numbers can be found in the literature. [105],[106],[107],[108],[109],[110],[111],[112]

Unlike spherical particles, which have a simple geometric symmetry leading to constant hydrodynamic forces in all directions, cylinders interact with fluid flows in ways that can lead to tumbling, reorientation, and variable drag coefficients. The flat ends and the edges of the cylinder have a considerable influence on the dynamics. Particularly with short, rod-shaped cylinders, the edge effects are no longer negligible. These edge effects are less important the longer the cylinder is compared to its diameter (or the larger the aspect ratio l/r is, respectively; with l the half-length of the cylinder and r the radius of the cylinder). And they are also less important if the cylinder falls horizontally, *i.e.*, perpendicularly to its cylinder axis. If the cylinders fall with their flat side forward, such as in the axial fall, or if the flat face is subjected to a flow, edge effects must be incorporated. However, this case is often less considered in the literature or, for the sake of simplicity, the focus is often only on the horizontal translation and rotation parallel to a wall. [113] In recent years, axial alignment with the flow and variation of the inclination (*i.e.*, the orientation angle θ) has been increasingly taken up again. For example, slender body theory can map edge effects, or shorter aspect ratios respectively, more accurately the larger the order of the approximation is. For example, Kharrouba *et al.* (2021) used numerical simulations to calculate the drag force on fixed cylinders as a function of their aspect ratio and the direction of flow. The results of the simulations and experimental results were then adapted to a 4th order slender body approximation resulting in an analytical equation for the drag force with an empirical term incorporating edge effects. Furthermore, they included inertial corrections to capture various Reynolds number regimes in their drag model. [110]

The complexity in modeling particle dynamics increases all the more if the liquid is confined, *i.e.*, if the anisotropic particles interact with walls. The Mestre and Russel (1975) made a slender body analysis to approximate the translation of a slender cylinder near a plane wall. They approximated the force on the slender body by distributions of point forces, so called Stokeslets, along the cylinder axis and an image system in the wall. Using this method, they derived drag forces for cylinders translating axially and perpendicularly along a wall and cylinders approaching axially or perpendicularly a wall. However, they also made clear that these cases of orientation only represent special cases of cylinder translation which can not be measured

in experiments, as cylinders rotate near walls and fixed orientation angles cannot be maintained during the experiments. Their approximation is only valid for slender bodies and $r \ll d$, with d the wall distance. [114] In 1977, Russel *et al.* used a slender body analysis and an image system to derive an integral equation for the case of very long rods near walls. The integral equation was solved numerically and compared with experiments with aluminum wires ($l/r \approx 59 - 69$) in oil from various wall distances at with various initial orientation angles. Their theoretical approximation and their experiments showed so-called glancing and reversing as ways in which the rod turns near wall, depending on the initial angle and initial wall distance. What theory and experiments had in common is that the turns were symmetric under time reversals, *i.e.* after the turn the particles tend to the initial inclination to the horizontal but with the opposite sign. [115] Both approaches mentioned above are limited to slender bodies and become inaccurate as soon as edge effects of the cylinder play a role. Koens and Montenegro-Johnson used de Mestres slender body analysis which is only valid if $r \ll d$ and matched it with asymptotic expansions in r of the Stokes´s equations, which are valid if $r \to d$. However, they only specified an integral form for a resistance tensor without analytically representing its components. A simple comparison with the axial case parallel to a flat wall is therefore difficult. [116] Another study on the drag force of a finite cylinder moving parallel (but perpendicular to the cylinder axis) along a long wall while rotating is presented by Teng *et al.* (2022). There is also a comprehensive review of different methods and models near walls presented. [117]

Ui *et al.* (1984) performed experiments of axially falling cylinders in the center of a cylindrical tube at low Reynolds number and compared their results with slender body models and beads-on-a-shell models. They varied the tube diameter, measured the stationary velocities and calculated the dimensionless drag on the sphere under wall influence. Using an extrapolation method proposed by Brenner (1962), they could derive the drag on an axially falling cylinder in an unbounded fluid from the wall-bounded drag. [118],[119] Vice versa, the resistance corrected for the wall influence can be calculated entirely from the known force experienced by the particle in an unbounded fluid, providing (i) that the wall correction is already known for a spherical particle and (ii) that the particle is small in comparison to its distance from the boundary.
In the absence of fluid inertia, *i.e.* if $Re_\mathrm{P} = 0$, particles falling obliquely in an unbounded fluid should also maintain their angle, *i.e.* no torque is induced. However, since inertia is finite, various theoretical and experimental studies are concerned with the influence of inertia (induced, advective inertia and fluid inertia, *e.g.* during sedimentation, *cf.* chapter 3) on the dynamics of cylindrical rods. [120],[121],[110],[111],[112]

Cabrera *et al.* (2022) studied experimentally the sedimentation of tungsten rods with aspect ratios of $l/r = 8$ and $l/r = 16$ with particle Reynolds number $Re_\mathrm{P} = |\vec{U}|l\rho\eta^{-1} \approx 0.105 - 0.150$, or $Re_\mathrm{P} \approx 0.255 - 0.390$ respectively in a square tank. [122] The tungsten particles were negligibly small with respect to the tank dimensions. Their focus was on the influence of particle inertia on the forces and torques of the particles during steady sedimentation after the particles were released with various inclination an-

gles. Their measurements showed a nonnegligible scatter in particle trajectories (translational and angular) which they related to particle mass inhomogeneities and (or) a weak induced flow when releasing particles. They compared their results to a slender rod model, *i.e.*, a 1st order approximation corrected for the effect of inertia which was proposed by Khayat and Cox in 1989. [123] This model was able to approximate the dynamics the better the higher the aspect ratio was. They also compared their experimental results with a spheroid model. The spheroid model could not reproduce the dynamics appropriately for any of the aspect ratios considered.

The study of Cabrera *et al.* represents a time-dependent study in so far that the orientation angles varied with time due to inertial torques. An approach to investigate inertial torques on fibers without involving time-dependent orientation is to create particles with asymmetric mass distributions or shapes that generate gravitational and viscous torques, and then measure the orientation they adopt during steady sedimentation. Roy *et al.* used this procedure and showed theoretically and experimentally that fibers with an asymmetric radius or mass density distribution undergo a supercritical pitch-fork bifurcation from vertical to oblique settling. Their results show that the orientation of the particles as a function of the flow regime is not necessarily unique and may be unstable. The smallest investigated Reynolds number, based on the half-length, was of $Re_P \approx O(1)$. [121]

Additional complexities in the dynamics arise, if deformability is involved in the system. Both experimental and theoretical investigations on the sedimentation deformable fibers (*e.g.*, microplastic fibers) at small Reynolds number $Re_P \lessapprox O(1)$ are available, *i.e.* experiments with small particles with large aspect ratio which could bend or were curly. [124],[125],[101]

To the best knowledge, there have been no studies on the influence of elasticity on the sedimentation dynamics of finite size cylinders with small aspect ratios ($l/r < 10$) and small Reynolds numbers $Re_P \lessapprox O(1)$ to date.

Salez and Mahadevan (2015) determined an asymptotic theory for the sedimentation, sliding and spinning motions of a cylinder near a soft wall. The cylinder falls perpendicularly to its axis towards a soft, inclined wall. Despite the low-Reynolds-number feature of the flow, the particle oscillated spontaneously when sliding, generated lift via a Magnus-like effect, was able to undergo a spin-induced reversal effect and they also showed an unusual sedimentation singularity. [126] Rallabandi *et al.* used the Lorentz reciprocal theorem to show analytically that for small deformations of an elastic layer, the angular velocity of the cylinder translating parallel to a soft wall scales with the cube of the sliding speed. The infinitely long cylinders translate perpendicularly to the cylinder axis within the lubrication limit in a viscous fluid parallel to a soft wall. They showed that, at constant speed and separation distance, the cylinder must also rotate in order to remain free of torque. Furthermore, they showed that a softer elastic layer results in a greater angular speed of the cylinder. With their calculations, they confirmed the corresponding experiments by Saintyves *et al.*

(2015). [127],[128] With their experiment, they showed that there were robust steady-state sliding regimes of cylinders translating due to gravity down an inclined soft wall (*e.g.* a PDMS wall). The effective friction of the cylinders was significantly reduced relative to that of rigid fluid-lubricated contacts. To date, no experimental or theoretical investigation are available, were a finite size cylinder sediments axially aligned near a soft wall.

There is an increasing sparsity of literature on unsteady axial motion of cylindrical particles. Although there are rudimentary theories on the transient dynamics of non-spherical bodies (including general mathematical formulations for arbitrary axisymmetric bodies), the equations are only solved for particles that deviate only slightly from a sphere. [2] For example, Lawrence and Weinbaum showed, that the total hydrodynamic force on a slightly eccentric spheroid (prolate or oblate) in oscillatory motion contains four terms: three of which correspond to the classical solutions for the Stokes drag, added mass and Basset force on the perturbed sphere; the fourth term is only present when the body is non-spherical, *i.e.* an additional memory force. [86],[87] However, an analytically formula including an integrodifferential term accounting for a history force of a cylinder does nor exist to date due to the mathematical complexity. Recently, J.-L. Pierson (2023) dealt with the problem of inertial settling of an obliquely sedimenting cylinder in an unbounded fluid and presented an analytical equation for the sedimentation during transient mass acceleration (short-time limit) with the help of an additional added mass term. However, the system of equations of motion must be solved numerically, as there is no closed-form solution. Furthermore, he checked the validity of the quasi-stationary assumption (equilibrium of forces) for calculating the sedimentation velocity. He came to the conclusion that the quasi-stationary assumption for calculating the velocity is valid for small Reynolds numbers and that additional inertial forces such as the added mass had no effect on the long-term dynamics. [129]

The modeling of sedimentation of finite size cylindrical particles remains a challenging and active area of research in fluid dynamics and applied physics. The current scientific understanding is incomplete, particularly in the area of short, elastic cylinders, and significant research is still required. Gaining a better understanding of the dynamics of finite size, elastic cylinders near walls is especially important due to potential applications- such as serving as a simplified model for bacteria prior to surface adhesion. To address this, experiments involving rigid and elastic cylinders sedimenting in a rectangular duct filled with high viscosity silicone oil, analogous to the sphere experiments discussed in Chapter 3, were conducted.The cylinders started sedimentation axially aligned from rest in an otherwise quiescent fluid. Both elastic and rigid cylinders started in the center of the duct and at various distances from elastic and from rigid walls in the duct. The experiments were performed in a scaled experimental design in the cm-range resulting in translational particle Reynolds numbers $Re_{\mathrm{P}} = |\vec{U}|l\rho\eta^{-1} \lessapprox 0.1$. The chapter is structured as follows: Section 5.3 presents the basic equations that can be used to approximate the drag force and translational velocity

on a axially sedimenting cylinder. In Section 5.4, the methods such as the experimental setup, the optical measurement technique for tracking the kinematics of cylindrical objects and the fabrication of polymer cylinders and the soft wall are explained. In the first part of Section 5.5, kinematics of experiments with rigid and elastic cylinders sedimenting at different particle Reynolds numbers in the duct center and at various distances to rigid walls are presented. The results of the experiments with the rigid rods ($l/r \approx 5.3 - 6$ and $Re_\mathrm{P} \approx O(10^{-1})$) are compared with theoretical values. For experiments with decreasing Young´s elastic modulus and decreasing density ($Re_\mathrm{P} \approx O(10^{-2})$, a purely qualitative evaluation of the (unstable) kinematics is carried out. In the second part of section 5.5, results of experiments with rigid rods sedimenting along an elastic wall are presented and discussed.

5.3 Theory

A rigid rod with circular cross section, *i.e.* radius r, length $2l$, volume $V_\mathrm{P} = 2\pi r^2 l$, and density ρ_P sediments due to gravitational acceleration with velocity $|\vec{U}|$ in an unbounded fluid. The fluid density is ρ and the fluid dynamic viscosity η. The density ratio is $\gamma = \rho_\mathrm{P}/\rho \rightarrow 1^+$, *i.e.* the difference in density is small. The aspect ratio of the cylinder is defined as l/r. Furthermore, the particle starts from rest at $t = 0$ s and, initially, the fluid velocity field around the particle is $|\vec{U}_\mathbf{f}| = 0$ m·s^{-1}. In the stationary state, the particle sediments with constant inclination angle θ in the Stokes regime with the translational particle Reynolds number $Re_\mathrm{P} = |\vec{U}| l \rho \eta^{-1} \rightarrow 0$, *cf.* definitions of spatial and angular dimensions in Fig. 5.2. If the particle falls axially aligned ($\theta = 0°$), the steady axial drag is balanced by the gravitational force and the buoyancy of the cylinder. The force balance around the cylinder reads

$$(\rho_\mathrm{P} - \rho)\, V_\mathrm{P} g = F_{\mathrm{D,\,ub}}^{\theta=0°,\, Re_\mathrm{P}\approx 0}. \tag{5.1}$$

Accordingly, the steady force equilibrium of a cylinder falling perpendicularly to its cylinder axis (transverse fall) is

$$(\rho_\mathrm{P} - \rho)\, V_\mathrm{P} g = F_{\mathrm{D,\,ub}}^{\theta=90°,\, Re_\mathrm{P}\approx 0}. \tag{5.2}$$

Kharrouba *et al.* (2021) derived a semiempirical model for the drag force on a cylinder for aspect ratios in the range $2 \leqslant l/r \leqslant 10$. [110] Their model based on the slender body approximation by Batchelor (1970), Cox (1970) and Keller & Rubinow (1976). [130],[131],[103] They incorporated a fourth order correction term and an empirical term extracted from numerical simulations to account for the finite-length effects which

become significant as soon as $l/r \lessapprox 10$. The axial drag in an unbounded fluid is approximated with

$$F_{\mathrm{D,\,ub}}^{\theta=0^\circ,Re_\mathrm{P}\approx 0} = 4\pi\eta l U \left(\frac{a_\mathrm{x}^{(1)}}{\ln\left(\frac{2l}{r}\right)} + \frac{a_\mathrm{x}^{(2)}}{\left[\ln\left(\frac{2l}{r}\right)\right]^2} + \frac{a_\mathrm{x}^{(3)}}{\left[\ln\left(\frac{2l}{r}\right)\right]^3} + \frac{a_\mathrm{x}^{(4)}}{\left[\ln\left(\frac{2l}{r}\right)\right]^4} - \frac{2.4}{\left(\frac{l}{r}\right)^{2/3}\left(\left(\frac{l}{r}\right)-\frac{1}{2}\right)^{1.75}} \right) \tag{5.3}$$

with $a_\mathrm{x}^{(1)} = 1$, $a_\mathrm{x}^{(2)} \approx 0.80685$, $a_\mathrm{x}^{(3)} \approx 0.82854$ and $a_\mathrm{x}^{(4)} \approx 1.45243$.

The transverse drag in an unbounded fluid is approximated with

$$F_{\mathrm{D,\,ub}}^{\theta=90^\circ,Re_\mathrm{P}\approx 0} = 8\pi\eta l U \left[\frac{a_\mathrm{y}^{(1)}}{\ln\left(\frac{2l}{r}\right)} + \frac{a_\mathrm{y}^{(2)}}{\left[\ln\left(\frac{2l}{r}\right)\right]^2} + \left(1 - e^{-c_1 (l/r)^{c_2}}\right)\left(\frac{a_\mathrm{y}^{(3)}}{\left[\ln\left(\frac{2l}{r}\right)\right]^3} + \frac{a_\mathrm{y}^{(4)}}{\left[\ln\left(\frac{2l}{r}\right)\right]^4} \right) \right] \tag{5.4}$$

with $a_\mathrm{y}^{(1)} = 1$, $a_\mathrm{y}^{(2)} \approx -0.19315$, $a_\mathrm{y}^{(3)} \approx 0.21484$, $a^{(4)} \approx 0.38735$, $c_1 = 0.01$ and $c_2 = 2.5$.

Based on the theory of Khayat and Cox (1989), Kharrouba *et al.* also derived a semiempirical equation that takes into account the effects of small inertial contributions (analogous to the Oseen´s corrections for a sphere, see Eq. 3.8). [123] In the limit of $2Re_\mathrm{P} = O(1)$, the axial drag on a cylinder with inertial corrections reads

$$F_{\mathrm{D,\,ub}}^{\theta=0^\circ,2Re_\mathrm{P}=O(1)} = 4\pi\eta l U \left(\frac{a_\mathrm{x}^{(1)}}{\ln\left(\frac{2l}{r}\right)} + \frac{a_\mathrm{x}^{(2)} + f_\parallel}{\left[\ln\left(\frac{2l}{r}\right)\right]^2} + \frac{a_\mathrm{x}^{(3)} + f_3 f_\parallel}{\left[\ln\left(\frac{2l}{r}\right)\right]^3} + \frac{a_\mathrm{x}^{(4)} + f_4 f_\parallel}{\left[\ln\left(\frac{2l}{r}\right)\right]^4} - \frac{2.4}{\left(\frac{l}{r}\right)^{2/3}\left(\left(\frac{l}{r}\right)-\frac{1}{2}\right)^{1.75}} \right) \tag{5.5}$$

with $f_\parallel \approx \frac{2}{8} Re_\mathrm{P}$, $f_3 = (2Re_\mathrm{P})^{0.07(l/r)^{0.5}}$ and $f_4 = (2Re_\mathrm{P})^{0.03(l/r)^{0.9}}$.

In the case of transverse motion, only the second order term was corrected, which results in

$$F_{\mathrm{D,\,ub}}^{\theta=90^\circ,2Re_\mathrm{P}=O(1)} = 8\pi\eta l U \left[\frac{a_\mathrm{y}^{(1)}}{\ln\left(\frac{2l}{r}\right)} + \frac{a_\mathrm{y}^{(2)} + f_\perp}{\left[\ln\left(\frac{2l}{r}\right)\right]^2} + \left(1 - e^{-c_1 (l/r)^{c_2}}\right)\left(\frac{a_\mathrm{y}^{(3)}}{\left[\ln\left(\frac{2l}{r}\right)\right]^3} + \frac{a_\mathrm{y}^{(4)}}{\left[\ln\left(\frac{2l}{r}\right)\right]^4} \right) \right] \tag{5.6}$$

with $f_\perp \to \frac{1}{2} Re_\mathrm{P}$ when $2Re_\mathrm{P} \to 0$. For larger Reynolds numbers, *cf.* the exact correlation for $f_\perp$ in Eq. (C3) in [110].

The drag force of a moderately inclined cylinder in the Stokes regime $Re_\mathrm{P} = 0$ can be calculated using trigonometric relationships. This results in Eq. 5.7 and Eq. 5.8 for an moderately inclined cylinder falling obliquely without torque in an unbounded fluid. [110]

$$F_{\mathrm{D,\,ub}}^{Re_\mathrm{P}=0}(\phi) = F_{\mathrm{D,\,ub}}^{\theta=0^\circ,Re_\mathrm{P}\approx 0} \cos\phi \tag{5.7}$$

$$F_{\mathrm{D,\,ub}}^{Re_\mathrm{P}=0}(\phi) = F_{\mathrm{D,\,ub}}^{\theta=90^\circ,Re_\mathrm{P}\approx 0} \sin\phi \tag{5.8}$$

In Eqs. 5.7 and 5.8, ϕ denotes the angle of attack, *i.e.*, the angle between the velocity vector $\vec{U}$ and the cylinder axis (see Fig. 5.9). If the cylinder sediments obliquely without lateral motion- *i.e.,* if the velocity vector is defined solely by the axial component, $\vec{U} = \begin{pmatrix} 0 & 0 & U_{\mathrm{P,\,x}}(\theta) \end{pmatrix}^T$, and lift due to fluid inertia is absent- then the angle ϕ coincides with the inclination angle relative to the vertical, θ (see Fig. 5.2). In the presence of lateral motion, ϕ is given by $\phi = \arctan U_{\mathrm{P,\,y}}/U_{\mathrm{P,\,x}}$. Nevertheless, as emphasized previously, fluid inertia is inherently finite, and its effects invariably induce a torque and also lead to lateral motion, especially near walls due to lift forces. Consequently, a rod would not fall at a constant inclination angle without rotation. Equations 5.7 and 5.8 would thus lose their validity. However, Kharrouba *et al.* found that in the limit of small Reynolds numbers and moderate inclination angles ($\theta \leqslant 30°$), the relationships from Eq. 5.7 and Eq. 5.8 are still valid if the inertia-corrected drag from Eq. 5.6, $F_{\mathrm{D,\,ub}}^{\theta=0°,2Re_{\mathrm{P}}=O(1)}$, is used instead of $F_{\mathrm{D,\,ub}}^{\theta=0°,Re_{\mathrm{P}}\approx 0}$.

Howard Brenner (1962) put forward a theory which states that the wall-effect correction on a particle with arbitrary cross section falling along a principal axis of resistance, *i.e.* an axis of symmetry, can be calculated entirely from knowledge of the force experienced by the particle in an unbounded fluid, providing that the wall correction is already known for a spherical particle and that the particle is small in comparison to its distance from the boundary. [119] According to Brenner, the wall effect on the drag of an arbitrary shaped particle with characteristic length l^* moving at a characteristic distance d^* from a boundary, or within a bounded fluid, respectively, can be expressed with Eq. 5.9.

$$\frac{F_{\mathrm{D,\,wb}}^*}{F_{\mathrm{D,\,ub}}^*} = \frac{1}{1 - C_1 F_{\mathrm{D,\,ub}}^* \left(\frac{l^*}{d^*}\right) + O\left(\frac{l^*}{d^*}\right)^3} \tag{5.9}$$

$F_{\mathrm{D,\,wb}}^*$ is the dimensionless drag in the wall-bounded fluid ($F_{\mathrm{D,\,wb}}/2\pi\eta l^* U_{\mathrm{th,\,wb}}$) and $F_{\mathrm{D,\,ub}}^*$ is the dimensionless drag in the unbounded fluid ($F_{\mathrm{D,\,ub}}/2\pi\eta l^* U_{\mathrm{th,\,ub}}$), therefore sometimes referred to as the Stokes drag of the arbitrarily shaped particle. For example, the dimensionless drag in the unbounded fluid of an axially falling cylinder ($l^* = 2l$) at $Re_{\mathrm{P}} \approx 0$ is derived from Eq. 5.3 and reads

$$F_{\mathrm{D,\,ub}}^{*(\theta=0°,Re_{\mathrm{P}}\approx 0)} = \frac{a_{\mathrm{x}}^{(1)}}{\ln\left(\frac{2l}{r}\right)} + \frac{a_{\mathrm{x}}^{(2)}}{\left[\ln\left(\frac{2l}{r}\right)\right]^2} + \frac{a_{\mathrm{x}}^{(3)}}{\left[\ln\left(\frac{2l}{r}\right)\right]^3} + \frac{a_{\mathrm{x}}^{(4)}}{\left[\ln\left(\frac{2l}{r}\right)\right]^4} - \frac{2.4}{\left(\frac{l}{r}\right)^{2/3}\left(\left(\frac{l}{r}\right) - \frac{1}{2}\right)^{1.75}}. \tag{5.10}$$

The dimensionless drag with inertia correction, $F_{\mathrm{D,\,ub}}^{*(\theta=0°,2Re_{\mathrm{P}}\approx O(1))}$, is obtained accordingly from Eq. 5.5 (term in the large bracket).

Ui *et al.* investigated rods with various aspect ratios that fell in the center of tubes with a cylindrical cross-section (tube diameter D). They varied the tube cross-section, measured the stationary sedimentation velocity and determined the dimensionless drag from the force equilibrium. By plotting the measured di-

mensionless drag against $l^*/d^* = l/(D/2)$, the dimensionless unbounded drag could be read off by means of linear extrapolation at the point $l/(D/2) = 0$, *i.e.* the intersection point on the ordinate. They found that in the case of a rod falling in a cylindrical tube, the relationship in Eq. 5.11 gives a more appropriate linear relationship than Brenner's theory. [118]

$$\frac{F^*_{\mathrm{D,\,wb}}}{F^*_{\mathrm{D,\,ub}}} = 1 + \left(C_1 F^*_{\mathrm{D,\,ub}} \left(\frac{l^*}{d^*} \right) + O\left(\frac{l^*}{d^*} \right)^3 \right) \tag{5.11}$$

In the original work by Ui *et al.*, the third-order correction term is neglected, as their extrapolation was limited to linear order. For large wall distances - such as at the center of a duct - the first-order approximation remains sufficiently accurate, as will be demonstrated below. However, when the distance between the sphere and the wall becomes small, as in the axial case near the wall, the third-order term becomes increasingly significant and must be taken into account.

Happel and Bart (1974) derived the wall wall-bounded drag for a sphere falling in the center of a channel with a square cross-section. [132] According to their drag formula, the wall correction factor for a square duct *i.e.* a rectangular duct with square cross-section, is $C_1 = 1.903266$. In this geometry, the characteristic distance is the half-width of the duct, $W/2$. Therefore, the wall-bounded steady-state velocity of a a cylinder falling axially in the center of a square duct at $Re_\mathrm{P} \approx 0$ can be approximated using Brenner´s first order correction from 5.9 (in the following indexed as *(Br)*) and is given by

$$U^{(\theta=0^\circ, Re_\mathrm{P}\approx 0)}_{\mathrm{th,\,wb}}\Big|^{(Br)}_{\square} \approx \frac{(\rho_\mathrm{P} - \rho)\, r^2 g \left(1 - 1.903266 F^{*(\theta=0^\circ, Re_\mathrm{P}\approx 0)}_{\mathrm{D,\,ub}} \left(\frac{2l}{W} \right) \right)}{2\eta F^{*(\theta=0^\circ, Re_\mathrm{P}\approx 0)}_{\mathrm{D,\,ub}}}. \tag{5.12}$$

Using the first order correction of Ui *et al.* from Eq. 5.11 (denoted with *(Ui)* in the following), the wall-bounded steady velocity of an axially falling cylinder in the center of a square duct at $Re_\mathrm{P} \approx 0$ is

$$U^{(\theta=0^\circ, Re_\mathrm{P}\approx 0)}_{\mathrm{th,\,wb}}\Big|^{(Ui)}_{\square} \approx \frac{(\rho_\mathrm{P} - \rho)\, r^2 g}{2\eta F^{*(\theta=0^\circ, Re_\mathrm{P}\approx 0)}_{\mathrm{D,\,ub}} \left(1 + 1.903266 F^{*(\theta=0^\circ, Re_\mathrm{P}\approx 0)}_{\mathrm{D,\,ub}} \left(\frac{2l}{W} \right) \right)}. \tag{5.13}$$

In Chapter 3, it was demonstrated that when a rigid sphere sediments at $Re_\mathrm{P} \approx O(10^{-1})$ near a wall in a rectangular duct (asymmetric sedimentation), the drag force is primarily governed by the nearest plane wall, while the influence of the remaining walls is comparatively minor. The velocity of a rigid sphere in the near-wall region at $d/R \approx 2$ could be accurately approximated using Eq. 3.5, which is based on Faxén's formulation of the drag force. [29] Following Brenner's theory, the wall-induced effects on the drag of an axially sedimenting cylinder near a plane wall can similarly be described using Faxén's wall correction term. In the near-wall region, higher-order terms are essential for a precise and comprehensive representation of wall-bounded drag. Accordingly, the following equation is proposed to describe the theoretical, wall-

bounded velocity of a cylinder falling axially aligned at a distance of d from a plane wall:

$$U_{\text{th, wb}}^{(\theta=0^\circ, Re_\text{P}\approx 0)}\big|_{|}^{(Br)} \approx \frac{(\rho_\text{P}-\rho)\, r^2 g \left[1-\left(\frac{9}{16}F_{\text{D, ub}}^{*(\theta=0^\circ, Re_\text{P}\approx 0)}\left(\frac{l}{d}\right)-\frac{1}{8}F_{\text{D, ub}}^{*(\theta=0^\circ, Re_\text{P}\approx 0)}\left(\frac{l}{d}\right)^3\right)\right]}{2\eta F_{\text{D, ub}}^{*(\theta=0^\circ, Re_\text{P}\approx 0)}}. \tag{5.14}$$

Eq. 5.14 is based on Brenner's relation (Eq. 5.9). Accordingly, the theoretical velocity based on the relation of Ui *et al.* (Eq. 5.11) is

$$U_{\text{th, wb}}^{(\theta=0^\circ, Re_\text{P}\approx 0)}\big|_{|}^{(Ui)} \approx \frac{(\rho_\text{P}-\rho)\, r^2 g}{2\eta F_{\text{D, ub}}^{*(\theta=0^\circ, Re_\text{P}\approx 0)}\left[1+\left(\frac{9}{16}F_{\text{D, ub}}^{*(\theta=0^\circ, Re_\text{P}\approx 0)}\left(\frac{l}{d}\right)-\frac{1}{8}F_{\text{D, ub}}^{*(\theta=0^\circ, Re_\text{P}\approx 0)}\left(\frac{l}{d}\right)^3\right)\right]}. \tag{5.15}$$

For Reynolds numbers $Re = 2Re_\text{P}\left(\frac{l}{r}\right)^{-1} \leq 1$, the wall correction term must also account for the influence of inertia. This inertia correction is applied analogously to equations 3.13 and 3.14, *cf.* Chapter 3. Even at very low Reynolds numbers, inertia continues to play a significant role in the near-wall region due to the reflection of disturbance flows from the wall. As a result, a torque is induced on the cylinder, causing it to rotate. The following general equation, Eq. 5.16, is derived for cylinders translating with moderate inclination angles θ at a distance d in the region close to a plane wall and under conditions of small but finite inertia ($Re \leq 1$). This expression is based on the approach of Ui *et al.*, incorporating wall corrections along with inertial effects.

$$U_{\text{th, wb}}^{(Re\leq 1)}(\phi)\big|_{|}^{(Ui)} \approx \frac{(\rho_\text{P}-\rho)\, r^2 g}{2\eta F_{\text{D, ub}}^{*(\theta=0^\circ, 2Re_\text{P}\approx O(1))}\cos(\phi)\left[1+\left(\begin{array}{c}\frac{3}{8}Re_{\text{P,th}}(\phi)+\frac{9}{16}F_{\text{D, ub}}^{*(\theta=0^\circ, 2Re_\text{P}\approx O(1))}\cos(\phi)\left(\frac{l}{d}\right)\chi(\phi)\\ -\frac{1}{8}F_{\text{D, ub}}^{*(\theta=0^\circ, 2Re_\text{P}\approx O(1))}\cos(\phi)\left(\frac{l}{d}\right)^3\end{array}\right)\right]} \tag{5.16}$$

with

$$Re_{\text{P,th}}(\phi) = \frac{(\rho_\text{P}-\rho)\,\rho l r^2 g}{2\eta^2 F_{\text{D, ub}}^{*(\theta=0^\circ, 2Re_\text{P}\approx O(1))}\cos(\phi)} \tag{5.17}$$

and

$$\chi(\phi) = 1-\frac{4}{3}\left(\frac{Re_{\text{P,th}}(\phi)}{2\left(\frac{l}{d}\right)}\right)+\frac{23}{16}\left(\frac{Re_{\text{P,th}}(\phi)}{2\left(\frac{l}{d}\right)}\right)^3. \tag{5.18}$$

The theoretical angular velocity $\dot{\theta}$ of a rotating cylinder results from the torque equilibrium with respect to the rotation axis of the cylinder which is directed perpendicularly through the center of mass at the half-length (*i.e.* rotation around the z-axis without tilting out of plane $\phi = 0^\circ$, see Fig. 5.2). The torque balance reads

$$I_\text{P}\ddot{\theta} = T_\text{H} + T_\text{I}. \tag{5.19}$$

In Eq. 5.19, I_P is the moment of inertia of the cylinder, T_H is the hydrodynamic torque (sometimes also referred to as Stokes torque) and T_I is the inertial torque contribution due to an impressed force. The hydrodynamic torque T_H can be considered, analogous to the drag force in the force equilibrium, as resistance against the rotation with angular velocity $\dot{\theta}$ and can be described with $T_H = -C_H\dot{\theta}$, where C_H is the torque resistance coefficient. The negative sign indicates the resistance against the angular motion. The inertial torque T_I stems from impressed forces, *e.g.* the hydrodynamic drag force or impressed advective inertial forces such as fluid reflections from walls. In the stationary state ($\ddot{\theta} = 0\ s^{-1}$), the angular velocity is derived by

$$\dot{\theta} = \frac{T_I}{C_H} \tag{5.20}$$

The first order slender rod approximation for the resistance coefficient of an infinitely long cylinder rotating in an unbounded fluid at small Reynolds numbers was derived by Batchelor (1970) and reads:[130]

$$C_H^{(\frac{r}{l})\to 0} \approx \frac{8\pi}{3}\frac{\eta l^3}{\ln\left(\frac{l}{r}\right)} \tag{5.21}$$

Higher order expansions which take into account the end effects and the effects of finite fluid inertia on the rotation of cylinders with smaller aspect ratio were recently derived by Pierson *et. al* (2021). [133] [1]

An expression for the inertial torque T_I acting on a slender rod due to the translational motion drag force at low Reynolds numbers was obtained by Khayat and Cox (1989). [123] Substituting their first-order slender-body approximation, together with Eq. 5.20, in Eq. 5.19 yields the theoretical angular velocity of a long, slender rod in an unbounded fluid under low Reynolds number conditions, $2Re_P \ll 1$.

$$\dot{\theta}_{\text{th, ub}}^{(\frac{r}{l})\to 0} \approx \frac{\frac{-5\pi}{3\left[\ln\left(\frac{l}{r}\right)\right]^2}\frac{\rho l^3}{2}|\vec{U}|^2\sin^2\phi}{C_H^{(\frac{r}{l})\to 0}} = \frac{-5}{16\left[\ln\left(\frac{l}{r}\right)\right]}\frac{\rho|\vec{U}|^2}{\eta}\sin 2\phi \tag{5.22}$$

Higher-order expansions, analogous to those for the drag force on a rod with moderate aspect ratio and including inertial effects, were presented by Kharrouba *et al.* (*cf.* equation 18 in their paper [110]). However, for comparison with the measured values in Section 5.5, only the slender-body approximation from Eq. 5.22 is employed. As will be shown, fluid reflected from the walls induces a significantly large torque. To account for this torque, an additional term must be included in Eq. 5.19, representing either the velocity associated with the reflected flow disturbances or the lateral velocity component of the cylinder $U_{P,\,y}$. Such a term was incorporated in the derivation of angular velocity using slender-body theory by Russel *et al.* (1977). [115] The resulting analytical expression is highly complex and lengthy. Owing to its algebraic complexity, the

[1] In [133], certain notations and mathematical expressions are either unclear or inconsistent (*e.g.*, the term $\ln^3(2)$). As a result, the corresponding formula is not employed in this thesis, as it does not yield meaningful results within the context of this study. Nevertheless, given the relevance of the term and the lack of alternative contributions for short rods in the existing literature, explicit reference is still made to Eq. (1) of that paper.

equation was only evaluated for two limiting cases: an axially falling cylinder near the wall ($\theta = 0^\circ$) and a vertically falling cylinder ($\theta = 90^\circ$). [2]

5.4 Methods

5.4.1 Experimental setup and definitions

Sedimentation experiments of cylindrical model particles were performed in a rectangular duct, which was also used for the experiments with the spherical model particles, *cf.* Chapter 3 and Chapter 5. Figure 5.1 shows a photograph of the experimental setup and a schematic with the corresponding dimensions of the setup.

A glass container of 140 mm x 140 mm x 500 mm (W x D x H) was used as a vessel for the experiments. The container was filled up to a height of approximately 450 mm with silicone oil. The silicone oil had a nominal viscosity of 1000 cSt (measured value of $\eta = 0.9797 \pm 0.012$ Pa·s using a rotational viscometer IKA® Rotavisc lo-vi). The liquid density at room temperature was measured using a hydrostatic balance (analytical balance Sartorius® ENTRIS BCE 224i-1s equipped with a density determination kit (Sartorius® YDK03) for determination of solid and liquid densities). The liquid density at room temperature was $\rho = 971.28 \pm 0.134$ kg·m^{-3}. The choice of the liquid properties allowed to investigate sedimentation in the creeping flow regime ($Re_P \lessapprox 0.1$), *i.e.*, cm-sized particles with small density difference to the liquid experienced the same flow conditions as small, µm-sized particles sedimenting in aqueous liquids. The rods were hold with a pipette under weak vacuum and then immersed in the liquid. The initial inclination angle of the rods with respect to the xy-plane was approximately $\theta = 0^\circ$, *i.e.*, the rods accelerated from rest axially aligned to the center-line of the duct. The rod was positioned at the mid-plane between two opposing walls, having a distance d to the nearest wall, *cf.* Fig. 5.1. After immersion, the vacuum was released. The cylindrical model particle began to fall due to gravity. This ensured that the the cylinder began to sediment with an initial velocity of $U_{P,\,t=0s} = 0$ m·s^{-1} (starting from rest) and that the fluid is initially quiescent $\vec{U}_{f,\,t=0\,s} = \begin{pmatrix} 0 & 0 & 0 \end{pmatrix}^T$. There were rest periods between the experiments so that the fluid could come to rest completely before the new experiment was started. There was also a pause after the immersion of the pipette before the vacuum was removed and the particle began to fall.

The sedimentation experiments were recorded by a DSLR camera (Nikon® D7200 with Sigma® 50 mm f1.4 objective lens). The DSLR camera recorded videos with a resolution of 1.920 px ($W_{px,\,vid}$) x 1.080 px

[2] Unfortunately, the results of the integrals in Eq. (8) of [115] were not explicitly presented for these limiting cases, making it difficult to directly compare values or validate the theoretical predictions.

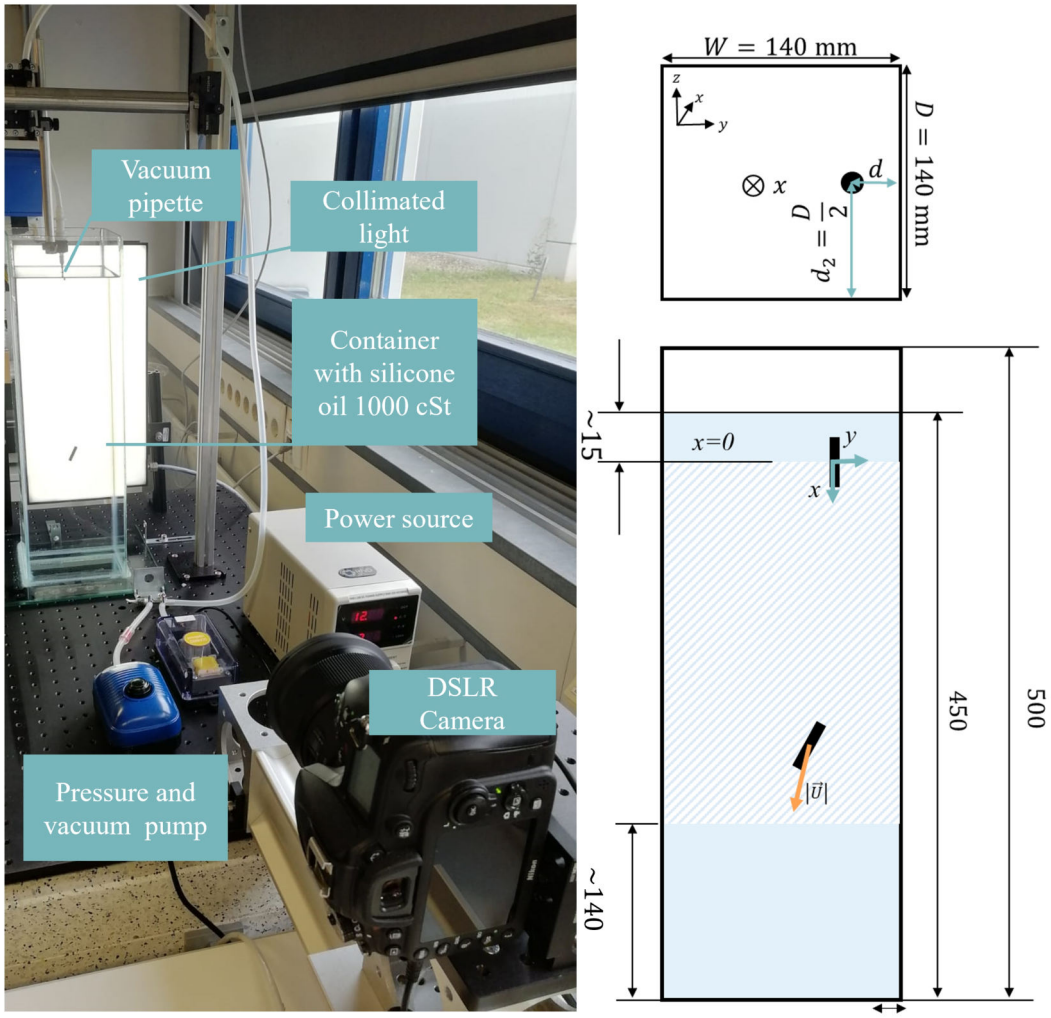


Figure 5.1: Left: photograph of the experimental setup. The setup consists of a glass container filled with 1000 cSt silicone oil, a collimated light panel with power source, a vacuum pipette connected to a vacuum and a pressure pump and a DSLR camera. Right: schematic of the setup and dimensions of the setup (top view and side view (imaging plane/ xy-plane)); Dashed area: measurement range

($H_{\text{px, vid}}$) in the .mov file format. The videos were recorded with the maximum frame rate of 25 frames per second (fps). During the experiments, the container with silicone oil was illuminated from the opposite side of the camera by a collimated light panel. This ensured a sharp contour of the model particle recorded by the camera sensor. To avoid blur effects or artifacts at the edges of the image (*e.g.*, due to spherical aberration), the camera must be aligned so that the object moves in the center of the image. Before starting the experiment, a high-resolution image with a resolution of 3.368 px ($W_{\text{px, start}}$) x 6.000 px ($H_{\text{px, start}}$) was captured and saved in the same directory, or folder respectively, as the video file. Fig. 5.2 shows the definitions of the spatial and angular dimensions during the experiment.

The focal plane of the camera corresponds to the xy-plane of the experimental setup. If the cylinders fall with the cylinder axis along the focal plane (xy- plane) and rotate with angle θ (orientation angle) around

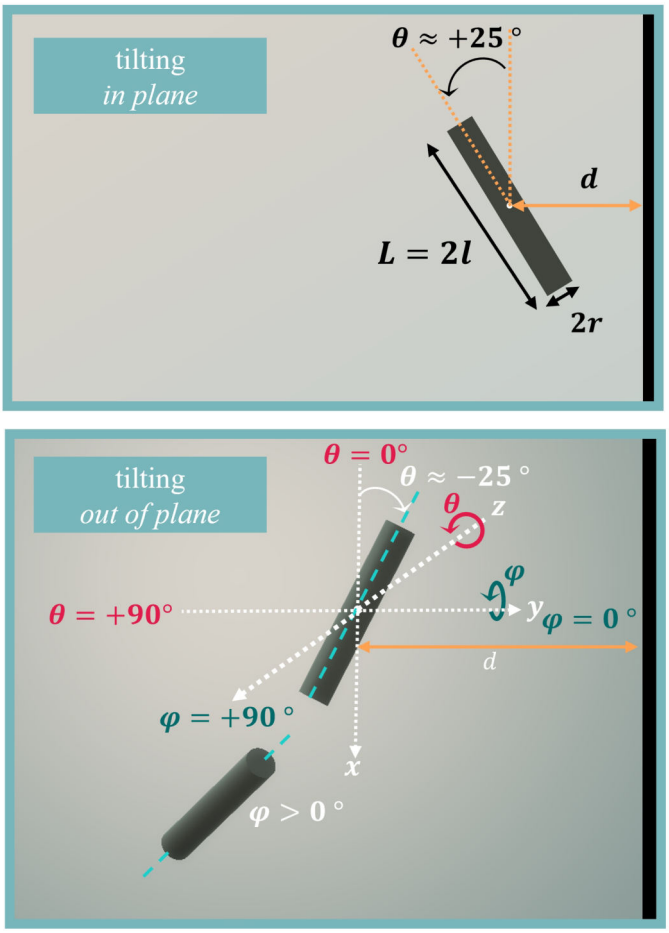


Figure 5.2: Definitions of spatial and angular dimensions during sedimentation of a rod near a wall. The (soft) wall on the right is aligned parallel to the xz-plane and the rod rotates with angle θ around the z-axis in the xy-plane and with angle φ around the y-axis in the xz-plane.

the z-axis (axis perpendicularly to the xy-plane), the center of gravity corresponds to the centroid of the projection area (A_{px}). The centroid is located at the half-length l of the cylinder and at the half-diameter, or radius, respectively, r. In the following, the configuration during sedimentation within the focal plane ($A_{\mathrm{px}} = const.$ and $\theta \neq 0°$) is named the *"in plane"* configuration, *e.g.,* tilting *in plane* means, that the cylinder inclines with respect to the wall with angle θ (*cf.* the upper panel in Fig. 5.2). If the cylinder also rotates around the y-axis ($\varphi \neq 0°$), this is referred to as the *"out of plane"* configuration (*cf.* the lower panel in Fig. 5.2). With the single-camera system used in these experiments, a quantitative evaluation of the kinematics in this configuration is not possible. For a correct evaluation and scaling of the image data from pixels to real lengths, a second camera with a focal plane in the xz-plane would be required. The results of experiments in the "*out of plane*" configuration can therefore only be evaluated qualitatively and phenomenologically with the the recorded videos.

5.4.2 Data acquisition - Particle tracking velocimetry of cylindrical particles

The trajectories and velocities were evaluated with a self-programmed image processing tool in MATLAB®. The code for programming the app in the MATLAB App Designer can be found in the dissertation appendix A.2.

Fig. 5.3 shows a flow chart which illustrates the basic principles and relevant functions in the algorithm of the app.

The object tracking app starts by importing the video saved in the .mov file format. Individual video frames are loaded at specific sampling rates (*"Load every XXX. frame")*, *i.e.*, the measuring points and the time step size $\Delta t = t_{i+1} - t_i$ are chosen. For example, by loading every 25. frame, the app extracts an image from the recorded video every second. Accordingly, the smallest selectable time step size is $\Delta t = 0.04$ s (extracting every frame of the video). The choice of the time step size depends in particular on the total length of the video. If the time step is selected too large, this will result in a loss of velocity data due to mean value smoothing. If the time step is selected too small (*e.g.*, if the object is moving very slowly and the video consists of a huge amount of images), this results in a strong scattering of the measured velocity values. To map the complete kinematics in a measurement range of 300 mm in sufficient detail (*cf.*, dashed area in Fig. 5.1 on the right) a total number of 150 to 200 images have proven to be an adequate number.

The selected images are cropped and binarized in the next step. The BW-sensitivity (black and white sensitivity), which controls whether a pixel receives a black or a white binary attribute (0 or 1) depending on the gray value, can be set in the app with a slider. The value should be set as small as possible. For example, blurring around the object can lead to a loss of pixels around the object if the sensitivity value is set too large. Consequently the projection area A_{px} is not determined correctly.

In the next step, the `regionprops()` function is applied to the resulting binarized images. Among other things, this function detects in each frame the pixel position of the centroid of the object´s projection area, *cf.* the panel with purple frame in Fig. 5.3.

One of the key challenges is to automatically recognize and detect the characteristic lengths and sizes of the object to be tracked in the individual images of the video. If the app loads a video of a sphere (which must be clearly identified in the file name, *cf.* A.2.1.1), the `imfindcircles()` function is used. This function determines the best-fit circle around a disc-shaped object with a given pixel area A_{px} and outputs the diameter $2R_{\mathrm{px}}$. In the case of a cylinder, the diameter of the cylinder is determined by applying the `regionprops()` function and outputting the value 'MinFeretProperties'. This output corresponds to the minimum Feret diameter. The minimum Feret diameter is defined as the smallest measurable distance between two tangents in a specific measuring direction on an object (*cf.*, the measuring principle of a caliper). In the case of a cylindrical object, the minimum Feret diameter corresponds to the diameter of the cylinder, $2r_{\mathrm{px}}$. The length

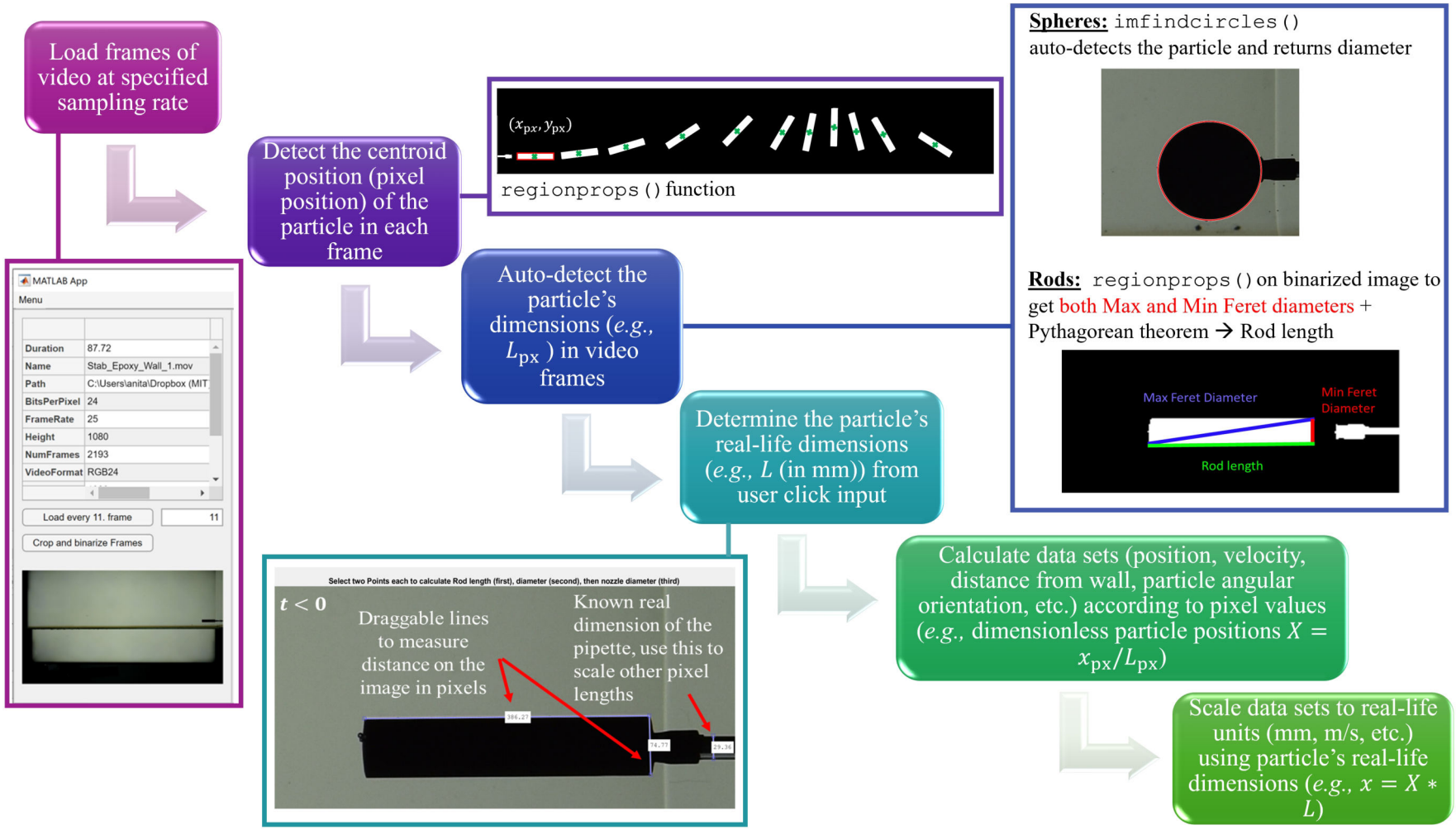


Figure 5.3: Particle tracking velocimetry process and relevant functions applied in the algorithm

of the cylinder in the video, $2L_{\mathrm{px}}$, is not determined directly, but via the Pythagorean theorem using the value 'MinFeretProperties' and the output value 'MaxFeretProperties'. Analogous to the minimum Feret diameter, the maximum Feret diameter corresponds to the largest measurable distance between two tangents on an object. In the case of a cylinder, the maximum Feret diameter is the diagonal of the projection surface.

In an intermediate step, the real-life (metric) dimensions of the cylinder L and $2r$, or the real radius of the sphere R respectively, are determined by scaling over a known length in a high-resolution image. For this purpose, the start image captured before starting the experiment is imported by the object tracking app. Within this start image, the diameter of the pipette in pixels ($D_{\mathrm{Pipette,\,[px]}}$) is determined using a draggable line. The real-life diameter, or metric diameter respectively, $D_{\mathrm{Pipette,\,[m]}}$, must be determined externally using a suitable measurement method that is independent of the experiment (*e.g.*, measurement with a caliper once in advance to the experiments). The two measured values are used to determine the corresponding scaling factor $\kappa = D_{\mathrm{Pipette,[m]}}/D_{\mathrm{Pipette,[px]}}$ with the unit m/px. In the case of a sphere, the pixel radius in the start image $R_{\mathrm{px,\,start}}$ is determined using the `imfindcircles()` function. The real-life radius R of the sphere used in the experiment is then given by the relation $R = \kappa \cdot R_{\mathrm{px,\,start}}$. In the case of a cylinder, the cylinder diameter in the start image, $2r_{\mathrm{px,\,start}}$, and the cylinder length, $L_{\mathrm{px,\,start}}$, must be measured manually with draggable lines, *cf.* the panel with blue-green frame in Fig. 5.3. The scaling with κ is analogous to that of a sphere.

All output values of the video, *i.e.*, output values of the experiment at $t > 0$s, that are generated up to this point (*e.g.*, the position of the pixel centroid at the image coordinate $(x_{\mathrm{px}}|y_{\mathrm{px}})$) are now related to the radius R_{px}, or length L_{px} respectively, measured automatically in the single video images. This results in dimensionless quantities, *e.g.*, the dimensionless sedimentation distance of a cylinder with respect to the half-length $X = x_{\mathrm{px}}/l_{\mathrm{px}} \equiv x/l \Leftrightarrow x = X \cdot l$. Accordingly, the dimensionless data can then be scaled to real dimensions using the real dimensions R and L measured in the intermediate step previously described.

In addition to the spatial coordinates like the centroid and the resulting lengths and translational velocities (*e.g.*, the velocity in x-direction $U_{\mathrm{P}} = (x_{i+1} - x_i)/\Delta t$), the angular trajectories can also be output and saved. For example, the output of the value 'Orientation' of the `regionprops()` function gives the orientation/tilting angle θ of the cylinder, *cf.* Fig. 5.2.

5.4.3 Model particle fabrication and soft wall fabrication

The experiments were performed with cylindrical model particles made of two types of polymers. On the one hand, an epoxy resin blend (casting resin MS 1000 by Weicon®) was prepared according to the manufacturer´s specifications and coloured black 1 w-% iron oxide powder. On the other hand, cylinders were

made of polydimethylsiloxane (PDMS). To vary the solid density ρ_s and the Young´s elastic modulus E of the PDMS cylinders, three different PDMS types or mixtures, respectively, were produced. Firstly, base blends of two commercially available PDMS elastomers by Dow Corning® were prepared according to the manufacturer's specifications (Sylgard™ 184 silicone oil: curing agent in a 10:1 ratio and Sylgard™ 527 part A: part B in a 1:1 ratio). Each base blend was then colored black with 1 w-% iron oxide powder and degassed. Secondly, the base blends were mixed with each other in a 1:0 ratio (*i.e.*, pure Sylgard™ 184), a 1:1 ratio and a 1:5 ratio (*i.e.*, 1 part Sylgard™ 184 and 5 parts Sylgard™ 527). All liquid blends were properly degassed before casting.

The following casting and curing process was carieed out to fabricate cylinders from the liquid blends. Liquid epoxy resin blend, or the liquid PDMS mixtures, respectively, were drawn into a 1 ml syringe (Ominfix®-F LuerSolo (0.01 ml - 1 ml)). The barrel of the syringe was completely filled with the polymer. The syringe was then set upright so that the needle adapter was pointing upwards and so that the syringe could stand on the extended plunger. This allowed air inside the barrel or air bubbles inside the blends still remained from mixing, respectively, to rise upwards and to degas via the needle adapter. The plunger was fixed in a suitable holder, *e.g.* a hard foam plate with slots. The syringes filled with the epoxy resin were cured in an oven according to the manufacturer´s specifications. The syringes filled with the PDMS mixtures were hardened for 12 h at 60 °C. For at least another 36 h, they were cured at room temperature.

After curing, the syringe adapter was cut off with a tube cutter to achieve a fully opened syringe barrel. The plunger was removed and the resulting space between the cured polymer and the flange was filled with distilled water. Hereafter, the plunger was pushed back into the syringe. As a result, the water pressed past the hardened polymer cylinder and the cylinder detached from the inner wall of the syringe. The polymer cylinder could be pressed out of the syringe via the previously cut barrel opening. The long cylinders produced in this way had a diameter of $2r \approx 4.7$ mm. The long cylinders were finally cut into shorter rods with a length of $2l \approx 24.6$ mm using a tube cutter.

The cured epoxy resin cylinders had a higher solid density ($\rho_{s,Epoxy} = 1159.8 \pm 1.9$ kg· m^{-3}) and were rigid (according to the manufacturer´s specifications having a Young´s elastic modulus of $E = 2.9$ GPa). The cylinders made of PDMS had lower densities ($\rho_{s,SYL184} = 1037.6 \pm 0.3$ kg· m^{-3}, $\rho_{s,MIX11} = 1007.2 \pm 2.2$ kg· m^{-3} and $\rho_{s,MIX15} = 988.0 \pm 1.4$ kg· m^{-3}) and the Young´s elastic moduli were measured to be of $E_{Epoxy} \approx 1712$ kPa, $E_{MIX11} \approx 936$ kPa and $E_{MIX15} \approx 135$ kPa (softest cylinder), *cf.* measurement of Young´s moduli in Chapter 3.4.2. The solid density of the cured epoxy resin and the cured PDMS was determined using a hydrostatic balance (Sartorius® ENTRIS BCE 224i-1s analytical balance + density determination kit YDK03 for determination of solid densities). The balance had a readability of 0.1 mg. Density measurements were performed in distilled water.

To add a soft layer to the rectangular duct, a PDMS plate of approximately 13 mm thickness ($h_{sl} \approx$

13 mm) was produced via casting. The base blends, Sylgard™ 184 and Sylgard™ 527 from Dow Corning®, were prepared according to the manufacturer's instructions and mixed with 1-w% iron oxide powder to achieve a black color. The materials were combined in a 1:5 ratio, similar to the method used for fabricating the softest cylinder. After degassing, the PDMS mixture was poured into a shallow rectangular dish and cured for 12 hours at 60 °C. This layer had similar properties to the softest cylinder, with a Young's elastic modulus in the dry state of approximately 135 kPa ($E_{\text{layer},0}$) and a solid density of around 987 kg/m^3 ($\rho_{\text{s, layer},0}$). A thin layer of epoxy resin was used to bond the soft layer onto a stainless-steel sheet, which was then placed in a container filled with silicone oil and attached to one of the container walls (one of the walls parallel to the xz-plane, *cf.* Fig. 5.2). Since the soft layer's properties may change due to oil diffusion, particularly in terms of solid density, this effect was assessed by immersing samples of the material in silicone oil for various durations and measuring density. The findings indicated that density stabilized after 14 days, with no further changes observed afterward. All experiments involving the soft layer were performed after this stabilization period to ensure consistency in material properties.

5

5.5 Results and Disucssion

The first part of this chapter deals with the sedimentation of cylindrical rods with circular cross-section and cylinder aspect ratios of $l/r \approx 5-6$. The cylinders started axially aligned from rest at various positions to a rigid wall in a rectangular glass duct. The Youngs´s elastic modulus E of the rods was varied by employing various polymers and polymer mixtures. The change of polymer composition led to small variations in the solid density and consequently to variation of the translational particle Reynolds number $Re_{\text{P}} \approx \frac{|\vec{U}|l\rho_{\text{s}}}{\eta}$. Re_{P} ranged from $Re_{\text{P}} \approx O(10^{-1})$ for the rigid rods down to $Re_{\text{P}} \approx O(10^{-2})$ for the softest rods.

In the second part of the chapter in Section 5.5.2, results of sedimentation experiments of cylindrical rods falling at various positions in the container equipped with an additional soft layer are presented. The experiments near the soft layer were performed with rigid rods sedimenting at larger Reynolds number $Re_{\text{P}} \approx O(10^{-1})$ and with quasi non-deformable PDMS rods sedimenting at $Re_{\text{P}} \approx O(10^{-2})$.

5.5.1 Kinematics of short, cylindrical rods falling near rigid, plane walls

In the following, both the spatial kinematics - *i.e.*, the dimensionless wall distance d/l and translational velocity $|\vec{U}|$ - and the angular kinematics - specifically, the orientation angle θ - are presented for all exper-

iments performed with a given material (characterized by constant density ρ_s and Young´s elastic modulus E) and cylinder aspect ratio l/r. These quantities are plotted together in a single diagram as functions of the dimensionless sedimentation distance xl^{-1}. The diagrams include variations in the initial wall distance d_{ini} as well as repeated measurements within each experimental series. Each experiment was repeated at least four times per wall distance for the respective material. The experiment number (*i.e.,* the time sequence within a measurement series) is indicated by the symbol used: ▲ (1), ■ (2), ★ (3), and ● (4). These comprehensive "All-in-One" kinematics diagrams provide a holistic view of the sedimentation behavior for a given material and aspect ratio across various wall distances.

Following the All-in-One kinematics diagrams, more detailed plots of individual measurement series - either at specific initial wall distances or selected based on distinct kinematic characteristics - are presented to facilitate a more precise analysis and interpretation of specific effects.

5.5.1.1 Kinematics of rigid, short rods sedimenting at $Re_P \approx O(10^{-1})$ near a rigid, plane wall

Fig. 5.4 shows the kinematics diagram of cylindrical rods with aspect ratio $\frac{\overline{l}}{r} \approx 5.2$ made of epoxy resin ($E \approx 2900$ MPa; $\rho_P \approx 1159.8$ kg·m^{-3}). The rods were released ($xl^{-1} = 0$) with an initial orientation angle of $\theta_{ini} \approx 0°$ in the center of the duct ($d/l \approx 5.8$; spatial trajectories with light gray, filled symbols), in the intermediate region between center and a plane wall ($d/l \approx 2$; spatial trajectories with gray, filled symbols) and in the near-wall region ($d/l \approx 1$; spatial trajectories with black, filled symbols). For the remaining color coding, see the individual diagrams in Fig. 5.5 and Fig. 5.7.

In Fig. 5.5, only the experiments of short rods in the center are shown. The upper diagram displays the measured values starting at the center position, identical to those shown in the All-in-One diagram, with all other data points hidden while retaining the original axis scaling. By contrast, the lower diagram uses a different axis scaling and presents the actual wall distance d instead of the dimensionless value.

The spatial trajectory shown in the lower diagram highlights the usefulness of a dimensional representation in the center of the duct. While the plot of d/l versus x/l reveals no clear trend, the lower (dimensional) trajectories show that three of the cylinder centroids converge at a common point around $d \approx 70$ mm, indicating that they align at the center. This phenomenon, known as channel focusing, has also been observed during the sedimentation of spheres in the center of the duct. The angular trajectories demonstrate that the rods sediment in an almost straight, axially aligned manner. Initial orientation angles range from 1 °to 2.5 °, and the angles increase approximately linearly. However, the change in orientation angle over the full sedimentation distance - and thus the angular velocity $\dot{\theta}$ - is negligible. The velocity curves show a short initial acceleration due to acceleration of mass and then show a stationary velocity. Overall, the experiments are reproducible, showing only small deviations in the measured values between individual experiments.

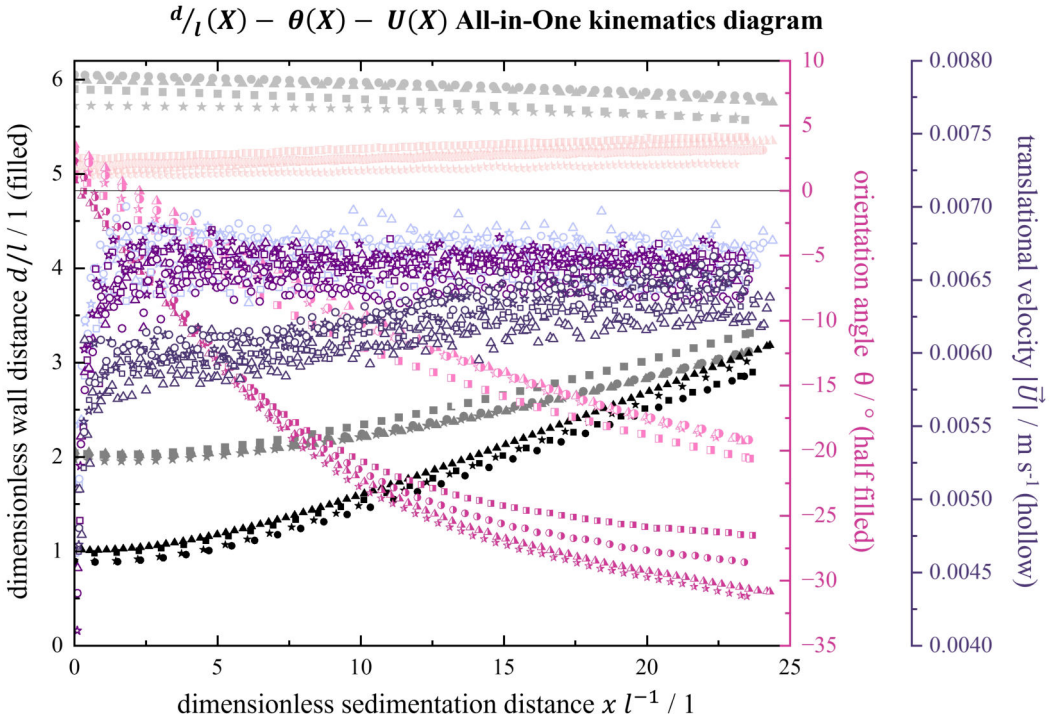


Figure 5.4: All-in-one kinematics diagram of rigid rods ($E \approx 2900$ MPa; $\rho_P \approx 1159.8$ kg·m^{-3}) sedimenting at $Re_P \approx O(10^{-1})$ at various distances from the plane walls in a rectangular duct. The dimensionless wall distance d/l (filled), orientation angle θ (half-filled) and translational velocity $|\vec{U}|$ (hollow) are plotted against the dimensionless sedimentation distance xl^{-1} for short, cylindrical rods with aspect ratio $\frac{l}{r} \approx 5.2$ sedimenting axially aligned from rest ($\theta_{ini} \approx 0°$) in the center of the duct ($d/l \approx 5.8$), in the intermediate region ($d/l \approx 2$) and in the near-wall region ($d/l \approx 1$) of a rigid, plane wall.

Experiment 3 (★ in Fig. 5.5) had both the smallest initial orientation angle and the initial wall distance closest to the center. The measured steady-state translational velocity was $|\vec{U}|_{\bigstar} \approx 6.7 \pm 0.1$ mm · s^{-1}. This result agrees well with the theoretical value predicted by Eq. 5.13, which uses the approach of Ui *et al.* and Happel's wall correction factor for a square duct. Applying Eq. 5.13 with the parameters of experiment 3 yields $U_{\text{th, wb}}^{(\theta=0°, Re_P \approx 0)}|_{\boxdot}^{(Ui)} \approx 6.6$ mm s^{-1}. By contrast, predictions based on Brenner's approach (Eq. 5.12) or including inertial corrections resulted in larger deviations from the measured velocity. However, as the Reynolds number increases, even slightly, incorporating inertial corrections into the theoretical model becomes necessary.

Fig 5.6 shows the velocity curve of an epoxy resin rod ($E \approx 2900$ MPa; $\rho_P \approx 1159.8$ kg·m^{-3}) with length $2l \approx 28$ mm ($l/r \approx 6$) which sedimented at $Re_P \approx 0.1$ in the center of the duct.

For measurements involving longer rods sedimenting in the center, which exhibited slightly higher particle Reynolds numbers compared to the shorter rods (0.1 *vs.* 0.08), the theoretical velocity calculated using

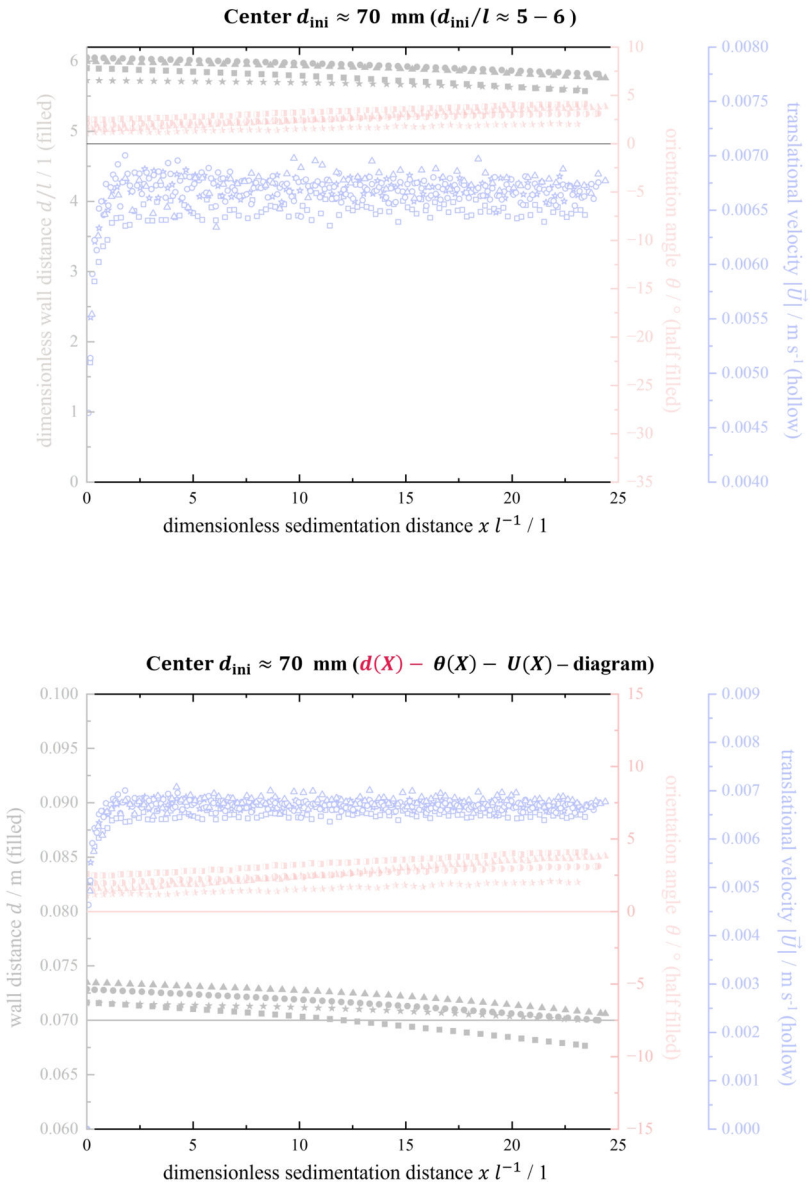


Figure 5.5: Top: dimensionless wall distance d/l (filled), orientation angle θ (half-filled) and translational velocity $|\vec{U}|$ (hollow) plotted against the dimensionless sedimentation distance xl^{-1} for short, cylindrical rods ($E \approx 2900$ MPa; $\rho_P \approx 1159.8$ kg·m^{-3}) with aspect ratio $\frac{l}{r} \approx 5.2$ sedimenting axially aligned from rest ($\theta_{ini} \approx 0°$) at $Re_P \approx 0.08$) in the center of the duct ($d/l \approx 5.8$); Bottom: rescaled plot with dimensional values of the wall distance d in the center.

the inertia-corrected drag force by substituting $F^{*(\theta=0°, 2Re_P \approx O(1))}_{D,\,ub}$ into Eq. 5.13 yielded more accurate predictions. This clearly indicates that the kinematics in this Reynolds number range fall within a transitional regime between creeping flow and moderate inertial regime on the order of $Re_P = O(1)$. Interestingly, the longer rods in the center tended to straighten their orientation rather than increase the inclination angle during sedimentation, as seen in the angular trajectory (■) in Fig. 5.6.

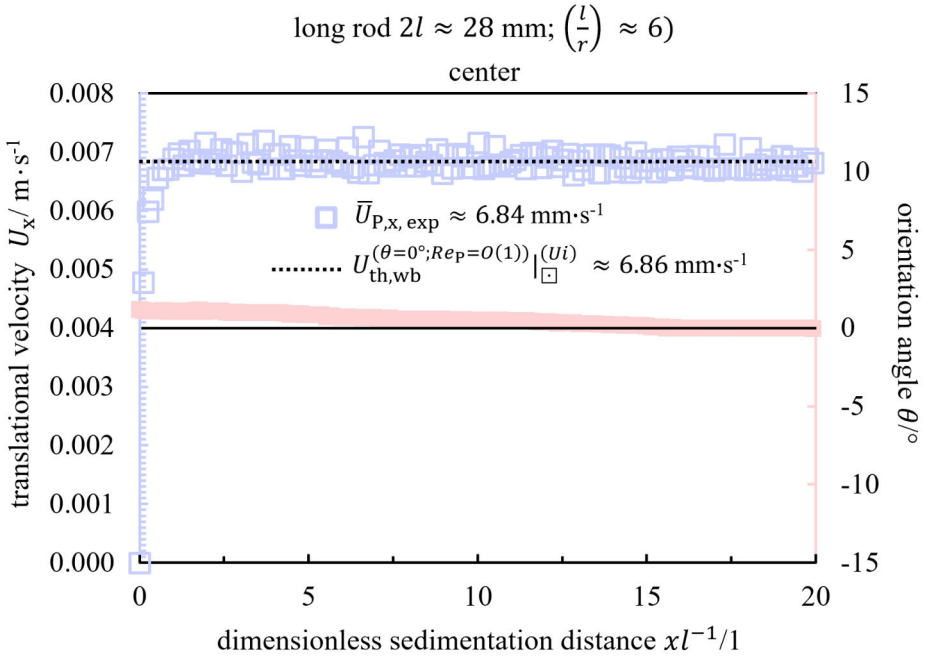


Figure 5.6: Translational velocity $U_x \approx |\vec{U}|$ (□) and orientation angle θ (■) plotted against the dimensionless sedimentation distance xl^{-1} for a cylindrical rod ($E \approx 2900$ MPa; $\rho_P \approx 1159.8$ kg·m^{-3}) with larger aspect ratio $l/r \approx 6$ sedimenting axially aligned from rest ($\theta_{ini} \approx 0°$) at $Re_P \approx 0.1$ in the center of the duct ($d/l \approx 5.8$).

Fig. 5.7 shows the individual diagrams of the sedimentation of epoxy resin rods ($E \approx 2900$ MPa; $\rho_P \approx 1159.8$ kg·m^{-3}) starting of axially aligned from rest in the intermediate region ($d/l \approx 2$) (top) and in the near wall region ($d/l \approx 1$) (bottom).

The measured kinematics in the intermediate region at $d/l = 2$ are highly reproducible. Both the spatial and angular trajectories (except for experiment 2 (■)) converge toward a common point or an equilibrium trajectory, respectively. However, the theoretical velocity predictions based on Faxén's wall correction factor (*cf.* Eq. 5.14 to Eq. 5.16) do not yield accurate results in this intermediate region. This discrepancy is expected, as the distance to the nearest wall is relatively large, and the influence of the remaining three walls contributes significantly to the velocity, making a single-wall approximation insufficient.

In contrast, in the near-wall region ($d/l = 1$), the angular trajectories diverge significantly at the end, *i.e.* the rods inclined to completely different orientation angles at the end. Within the approximately linear portion of the angular trajectories (in the range $0 < xl^{-1} \lessapprox 5$), the individual curves exhibit similar slopes, indicating an identical angular velocity $\dot{\theta}$ across the experiments. Beyond this point, however, the trajectories diverge, suggesting a deviation in the underlying torque dynamics.

Interestingly, the spatial trajectory behaves in the opposite manner: it transitions from an initially nonlinear trend (possibly quadratic or sinusoidal) to a linear trajectory. This indicates that the rod's centroid

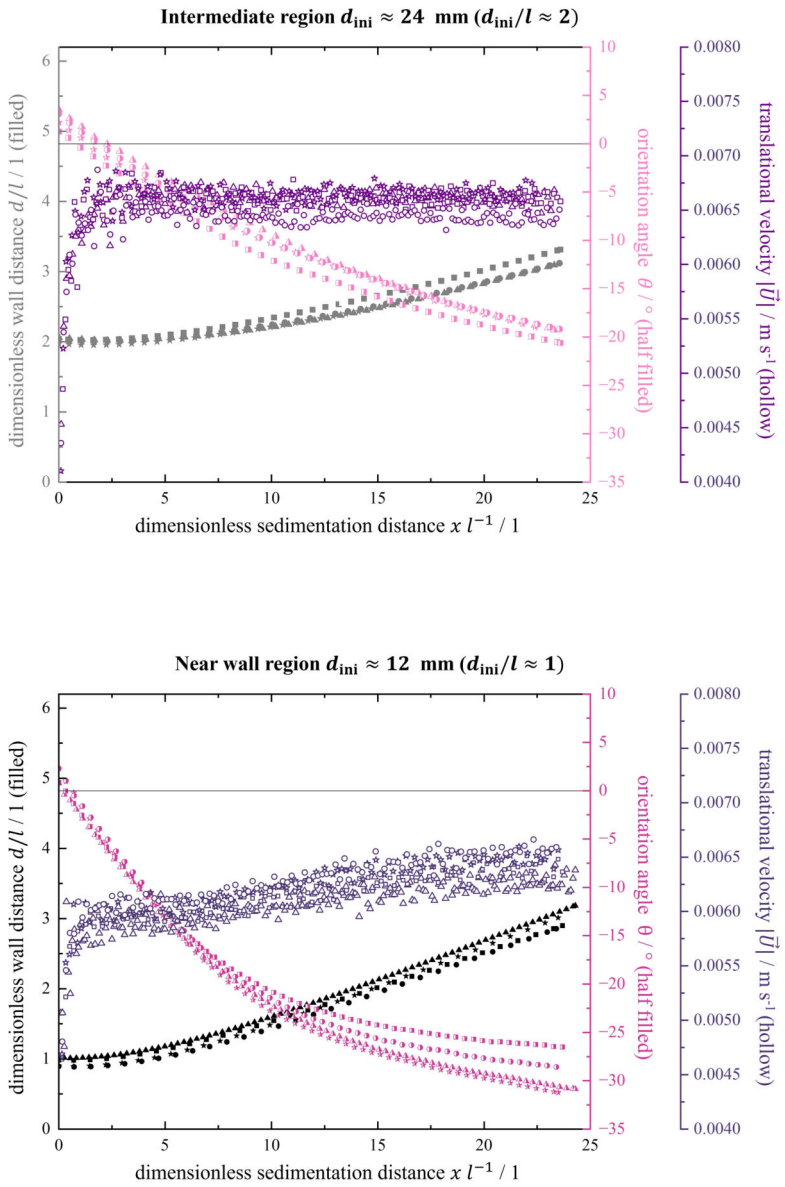


Figure 5.7: Dimensionless wall distance d/l (filled), orientation angle θ (half-filled) and translational velocity $|\vec{U}|$ (hollow) plotted against the dimensionless sedimentation distance xl^{-1} for short, cylindrical rods with aspect ratio $\frac{l}{r} \approx 5.2$ sedimenting axially aligned from rest ($\theta_{ini} \approx 0°$) at $Re_P \approx 0.08$ in the intermediate region ($d/l \approx 2$) (top) and at $Re_P \approx 0.07$ in the near wall region ($d/l \approx 1$) (bottom).

translates linearly away from the wall - similar to the linear migration away from the wall observed in the sedimentation of spheres. The velocity curves in this near-wall region exhibit strongly transient behavior, which is expected given the substantial changes in orientation angle during sedimentation.

Fig. 5.8 shows the translational velocity $|\vec{U}|$ of experiments 1 (△) and 2 (○) from Fig. 5.7 plotted against the magnitude of the orientation angle $|\theta|$. The measured values are compared with the theoretical velocities

$U_{\text{th, wb}}^{(Re\leq 1)}(\phi)|_{|}^{(Ui)}$ (orange lines) of the corresponding rods calculated with Eq. 5.18.

The measured values align well with Eq. 5.18 up to an orientation angle of $|\theta| \approx 15^\circ$, indicating that the

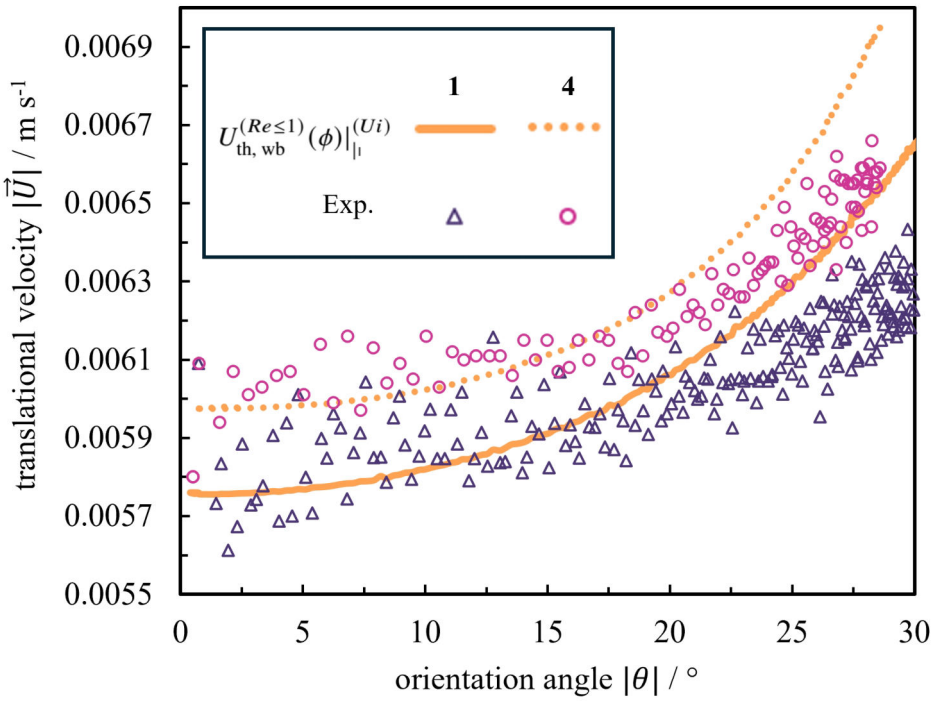


Figure 5.8: Measured translational velocity $|\vec{U}|$ plotted against the measured orientation angle $|\theta|$ of short, cylindrical rods with aspect ratio $l/r \approx 5.1$ sedimenting axially aligned from rest ($\theta_{\text{ini}} \approx 0°$) at $Re_{\text{P}} \approx 0.07$ in the near wall region ($d/l \approx 1$). Experimental values of experiment 1 (△) and 4 (○) from Fig. 5.7. Orange (dotted) line: theoretical translational velocity calculated with Eq. 5.18.

experimental data follow a sinusoidal trend within this range. For orientation angles $|\theta| \gtrsim 15^\circ$, however, the theoretical predictions begin to overestimate the measured values. This deviation is expected, as the influence of the additional walls becomes increasingly significant in the intermediate region, thereby increasing the hydrodynamic drag. Nevertheless, it is noteworthy that Eq. 5.18 captures the experimental behavior so accurately over a considerable range, despite being derived from a simple combination of slender-body theory and wall correction factors for a single plane wall. It is also important to emphasize that $U_{\text{th, wb}}^{(Re\leq 1)}|_{|}^{(Ui)}$ is not a pure function of $|\theta|$ in this case - except at the very beginning. A lateral velocity component $U_{\text{P,y}}$ is present in the measurements. Consequently, the angle of attack ϕ must be computed from the measured components $U_{\text{P,x}}$ and $U_{\text{P,y}}$. A schematic of the rod and the angle of attack during sedimentation and its range in the measurement of experiment 4 (○) from Fig. 5.7 is illustrated in Fig. 5.9. In Fig. 5.9, the measured angular velocity $\dot{\theta}$ is plotted against the angle of attack ϕ. The dotted line represents the theoretical prediction of $\dot{\theta}$ derived from the first order slender-body approximation for this rod in an unbounded fluid (Eq. 5.22).

For orientation angles $|\theta| < 15^\circ$ (corresponding to the range of approximately constant angular velocity

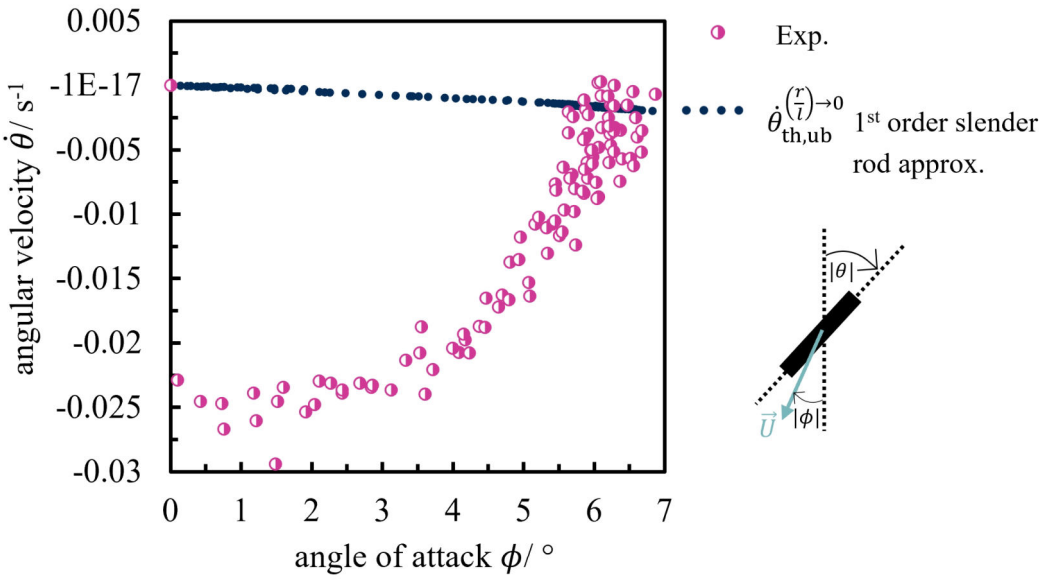


Figure 5.9: Measured angular velocity $\dot{\theta}$ plotted against the angle of attack ϕ of a short, cylindrical rod with aspect ratio $l/r \approx 5.1$ sedimenting axially aligned from rest ($\theta_{\text{ini}} \approx 0°$) at $Re_{\text{P}} \approx 0.07$ in the near wall region ($d/l \approx 1$). Experimental values of experiment 4 (○) from Fig. 5.7. Dotted: theoretical values Eq. 5.22.

in Fig. 5.9 and to the linear portion of the trajectory in trajectory in Fig. 5.7), the orientation angle and the angle of attack are linearly related: $\phi \approx 0.27\theta$. The mean angular velocity within this range ($\phi < 4°$) is $\dot{\theta}_{\circ} \approx -0.0246 \pm 0.0057$ s^{-1}. Beyond this range, the angular velocity decreases rapidly and approaches 0. For the non-constant range, the following approximate relation holds: $\dot{\theta}_{\circ}(\phi > 4°) \approx 0.0075\phi - 0.0503$. It is evident that a comparison with the theoretical value derived from slender-body theory in an unbounded fluid does not yield comparable results. The angular velocity calculated using Eq.5.22, $\dot{\bar{\theta}}^{(\frac{r}{l})\to 0}_{\text{th, ub, }\circ} \approx -0.00127$ s^{-1}, is negligibly small. However, this highlights the large torque induced by the nearby wall and underscores the substantial influence of the rod's end effects.

5.5.1.2 Kinematics of soft, short rods sedimenting at $Re_{\text{P}} \approx O(10^{-2})$ near a rigid, plane wall

Up to this point, the focus has been on rigid, short rods sedimenting at $Re_{\text{P}} \approx 0.07$–$0.1$ (*i.e.* $Re_{\text{P}} \approx O(10^{-1})$). This section presents experiments with soft rods made from PDMS mixtures, which have lower densities than epoxy resin and therefore sediment at lower Reynolds numbers, around $Re_{\text{P}} \approx O(10^{-2})$. The first set of experiments involves rods made of pure PDMS (Sylgard™ 184). This material has a comparatively large Young's elastic modulus ($E \approx 1712$ kPa), and as such, no significant deformation or bending is expected, *i.e.*, these rods were the stiffest among the soft rods studied. These experiments serve as a benchmark for

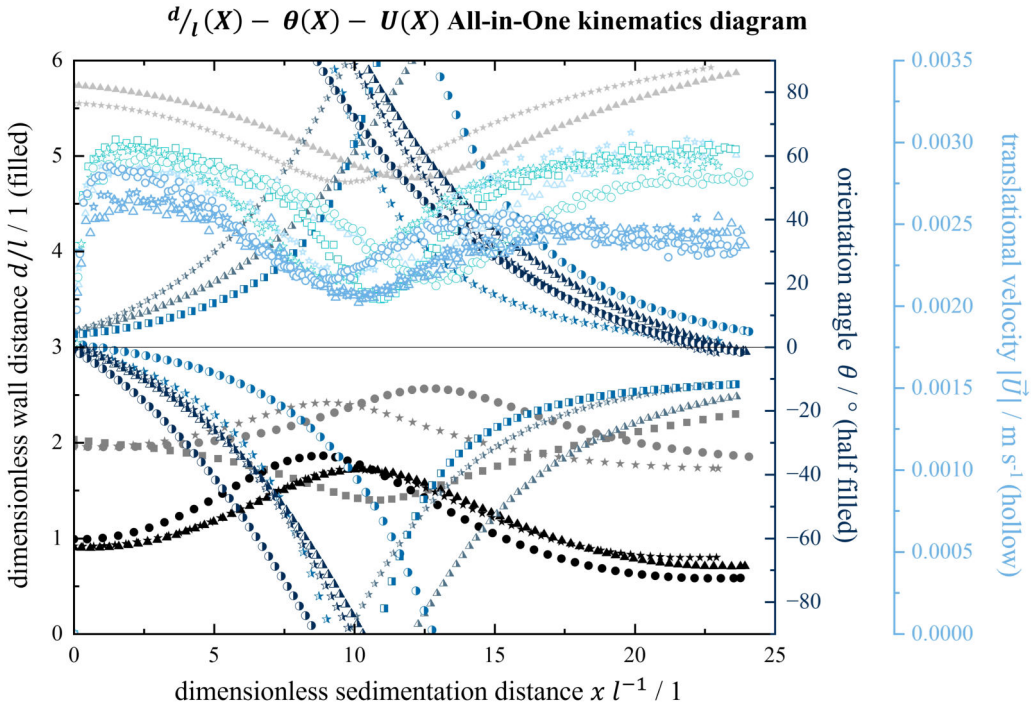


Figure 5.10: All-in-one kinematics diagram of the least soft rods ($E \approx 1712$ kPa; $\rho_P \approx 1037.6$ kg·m^{-3}) sedimenting at $Re_P \approx O(10^{-2})$ at various distances from the plane walls in a rectangular duct. Dimensionless wall distance d/l (filled), orientation angle θ (half-filled) and translational velocity $|\vec{U}|$ (hollow) are plotted against the dimensionless sedimentation distance xl^{-1} for short, cylindrical rods with aspect ratio $\frac{\overline{l}}{r} \approx 5.2$ sedimenting axially aligned from rest ($\theta_{ini} \approx 0°$) in the center of the duct ($d/l \approx 5.8$), in the intermediate region ($d/l \approx 2$) and in the near-wall region ($d/l \approx 1$) of a rigid, plane wall.

rods sedimenting at $Re_P \approx O(10^{-2})$, where elastic effects are still negligible.

Analogous to Fig. 5.4, Fig. 5.10 presents the "All-in-One" kinematics diagram for these least soft cylindrical rods with an aspect ratio of $\frac{\overline{l}}{r} \approx 5.2$. The rods were released ($xl^{-1} = 0$) with an initial orientation angle of $\theta_{ini} \approx 0°$ at three different positions: (1) in the center of the duct ($d/l \approx 5.8$; spatial trajectories with light gray, filled symbols), (2) in the intermediate region between the center and a wall ($d/l \approx 2$; gray, filled symbols), and (3) near the wall ($d/l \approx 1$; black, filled symbols). For additional color coding and further details, see the individual diagrams in Fig. 5.11.

Fig. 5.11 shows individual diagrams of the sedimentation of the least soft rods ($E \approx 1712$ kPa; $\rho_P \approx 1037.6$ kg·m^{-3}) starting axially aligned from rest in the center of the duct ($d/l \approx 5.8$) (top), the intermediate region ($d/l \approx 2$) (middle) and in the near wall region ($d/l \approx 1$) (bottom).

In contrast to the experiments conducted at higher Reynolds numbers of $O(10^{-1})$, the present experiments show a lack of reproducibility. As with the experiments in the previous Section 5.5.1.1, at least four

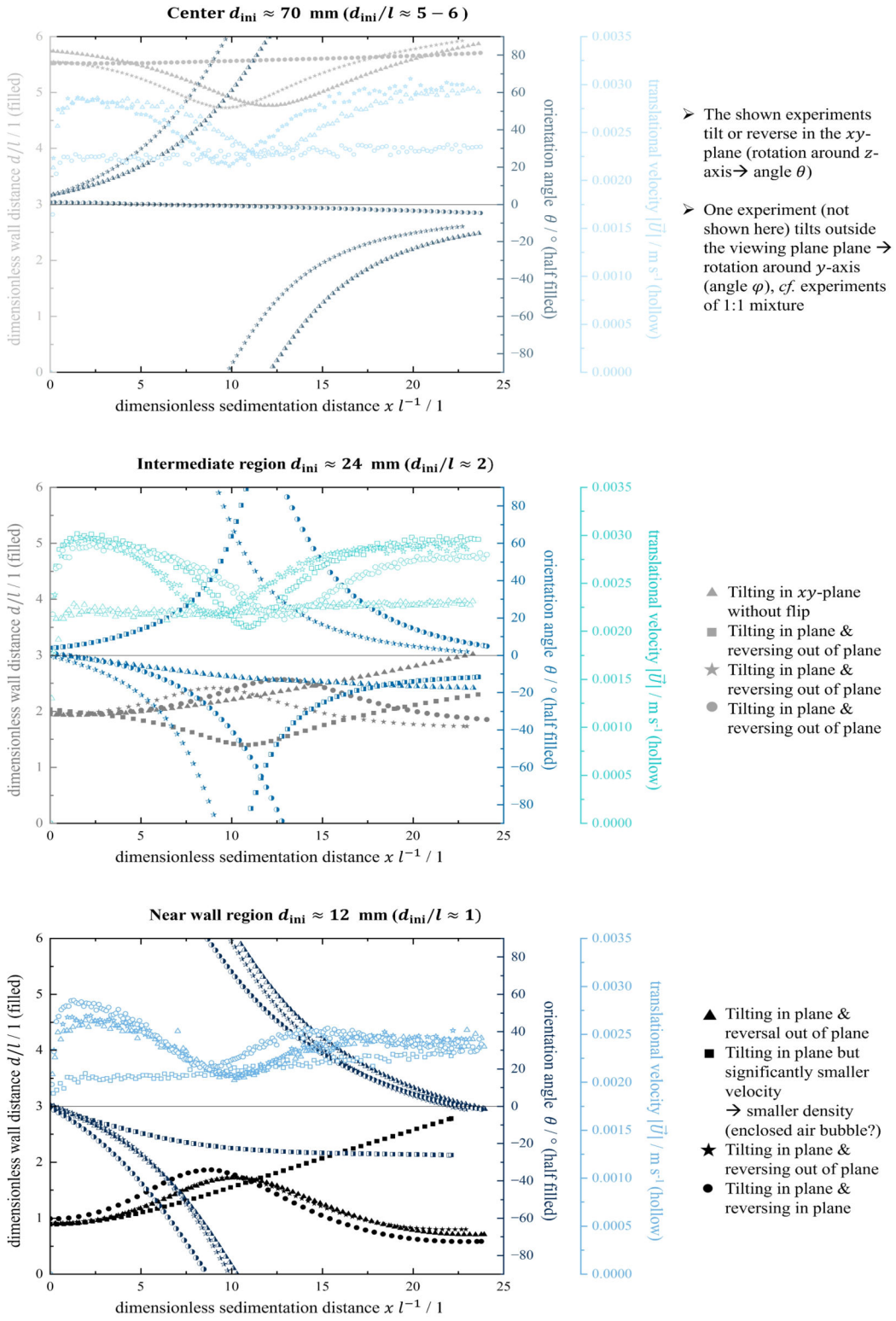


Figure 5.11: Dimensionless wall distance d/l (filled), orientation angle θ (half-filled) and translational velocity $|\vec{U}|$ (hollow) plotted against the dimensionless sedimentation distance xl^{-1} for short, cylindrical soft rods ($E \approx 1712$ kPa; $\rho_P \approx 1037.6$ kg·m^{-3}) with aspect ratio $\frac{l}{r} \approx 5.2$ sedimenting axially aligned from rest ($\theta_{ini} \approx 0°$) at $Re_P \approx 0.03$ in the center of a rectangular duct ($d/l \approx 5.8$) (top); in the intermediate region (($d/l \approx 2$) (middle) and in the near wall region ($d/l \approx 1$) (bottom).

sedimentation experiments were performed for each wall distance with initial axial alignment. However, each trial resulted in markedly different kinematic behavior, *i.e.* the kinematics do not differ only between different wall distances, but even among trials within a measurement series of the same initial wall distance, *cf.* Fig. 5.11. The characteristics of the individual kinematics are explained in the legends next to the diagrams of Fig. 5.11.

While a quantitative evaluation and comparison with theoretical predictions were still feasible at higher Reynolds numbers due to the high reproducibility - despite having only four trials per wall distance - this is no longer the case in the current experiments of the least soft rods and subsequent experiments involving softer rods. From a statistical standpoint, the number of trials conducted is insufficient to support a robust quantitative analysis. However, as will be shown, even an increased number of repetitions does not necessarily yield a consistent pattern, *cf.* the All-in-One kinematic diagrams Fig. 5.17 of the experiments with the softest rods. Therefore, the following analysis is limited to a qualitative assessment based on the available experimental data after four trials per wall distance.

The most striking difference in the kinematics, compared to the previous experiments at higher Reynolds numbers, is already evident in the All-in-One diagram: the rods exhibit flipping behavior - that is, the orientation angle reverses direction after tilting completely to the horizontal, either from negative to positive (*i.e.*, θ^- to θ^+) or *vice versa*. Remarkably, this flipping occurs even for rods sedimenting in the center of the duct, where the denser rods fell almost straight.

What significantly increases the complexity and limits the evaluability of these and subsequent experiments is the observation that some rods initially tilt within the imaging plane and then rotate out of it during the flipping process, *cf.* the kinematic descriptions accompanying the diagrams in Fig. 5.11. This introduces an additional orientation angle, φ, as illustrated in Fig. 5.2. As a result, quantitative evaluation of these experiments is not feasible, since accurately capturing the full 3D orientation would require a second camera to measure the kinematics in the plane perpendicular to the current imaging plane.

One of the curves in each diagram of Fig. 5.11 shows a significantly smaller translational velocity and deviates from the others in its trajectory. The reduced velocity suggests a lower density, possibly due to an enclosed air bubble inside the rod. This experiment is therefore considered invalid and will not be included in further analysis.

Since flipping appears to be a characteristic feature of the kinematics for rods of this density, all rods - regardless of their initial wall distance - are now grouped based on this behavior. Fig. 5.12 shows the All-in-One kinematics diagram of the least soft rods ($E \approx 1712$ kPa; $\rho_P \approx 1037.6$ kg·m^{-3}) sedimenting at $Re_P \approx O(10^{-2})$ sorted by the direction of the flip, *i.e.*, whether the orientation angle reverses from positive (θ^+) to negative orientation angle (θ^-) (top) or from negative to positive (bottom).

Sorting according to this criterion already introduces a certain degree of order within the diagrams.

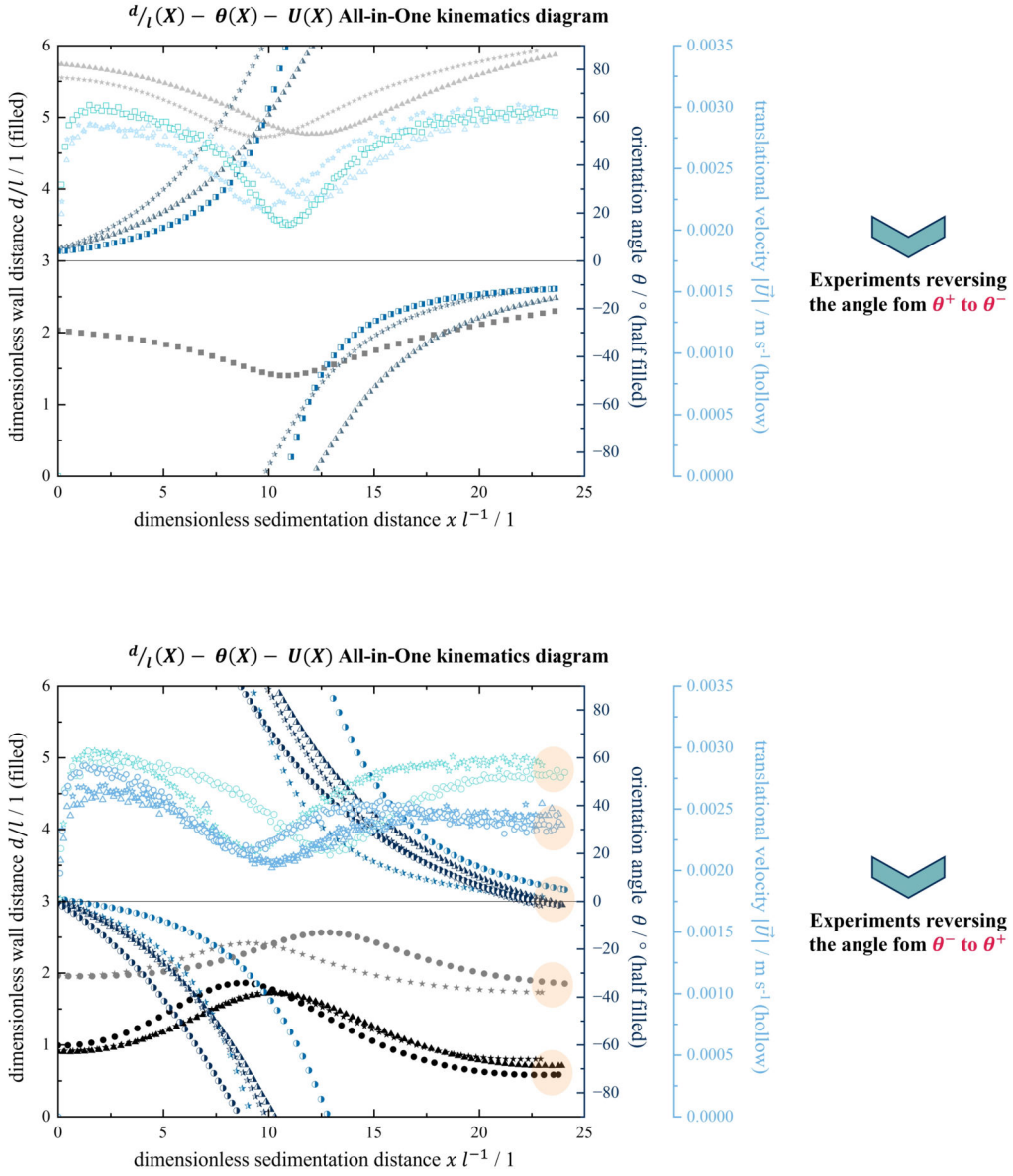


Figure 5.12: All-in-One kinematics diagram of the least soft rods ($E \approx 1712$ kPa; $\rho_P \approx 1037.6$ kg·m^{-3}) sedimenting at $Re_P \approx O(10^{-2})$ at various distances from the plane walls in a rectangular duct (*cf.* Fig. 5.10) sorted by the direction of orientation angle reversal: from θ^+ to θ^- (top) and from θ^- to θ^+ (bottom).

The individual trajectories exhibit qualitatively similar behavior, such as comparable translational velocities during the flip, similar flip locations or that the rods in the near-wall region only flip from θ^- to θ^+ (to mention only a few). Notably, despite considerable variations in kinematic behavior, the curves tend to converge toward common points at the end (highlighted in orange in the bottom diagram of Fig. 5.12).

In summary, the rod experiments at this density exhibit limited reproducibility. The rods predominantly undergo flipping in various directions. The direction of the flip - or more precisely, the reversal of the orientation angle - serves as a useful criterion for categorizing the overarching kinematic behavior. The rods show long-term transient kinematics, yet the sorted velocity curves and the trajectories ultimately converge. The exact cause of the variability in the observed kinematics cannot be clearly identified. It appears that even minimal variations in the initial conditions can lead to significant differences in the dynamic behavior, indicating an underlying instability. Moreover, additional torques (variations in the angle φ) which are undetectable with the measurement technique used, contribute to complex three-dimensional force and torque dynamics.

By adjusting the PDMS mixing ratio - through the addition of Sylgard™ 527 - the Young's elastic modulus can be progressively reduced. Fig. 5.13 presents the "All-in-One" kinematics diagram of the intermediately soft cylindrical rods ($E \approx 936$ kPa; $\rho_P \approx 1007.2$ kg·m^{-3}) with an aspect ratio of $\overline{\frac{l}{r}} \approx 5.2$. The rods were released ($xl^{-1} = 0$) with an initial orientation angle of $\theta_{ini} \approx 0°$ in the center of the duct ($d/l \approx 5.8$; spatial trajectories with light gray, filled symbols), in the intermediate region between the center and a wall ($d/l \approx 2$; gray, filled symbols), and in the near-wall region ($d/l \approx 1$; black, filled symbols). For additional color coding and further details, see the individual diagrams in Fig. 5.14.

Fig. 5.14 shows individual diagrams of the sedimentation kinematics of the intermediately soft rods ($E \approx 936$kPa; $\rho_P \approx 1007.2$kg·m^{-3}), sorted by wall distance.

In this series of experiments, there was again an increased occurrence of tilting rods without flips. Many of the flipping rods exhibited a flip only toward the end of the trajectory, after having tilted for almost the complete sedimentation distance, *i.e.*, they showed late reversals of θ at $xl^{-1} > 15$. As in the previous experiments, several trials could not be evaluated reliably and must be interpreted with caution, as the rods rotated out of the image plane - even during simple tilting motions. This was particularly common in the center of the container, *cf.* experiments 3 (★) and 4 (●) in the upper diagram off Fig.5.14.

Fig.5.15 presents the All-in-One kinematics diagram (originally shown in Fig. 5.13), now sorted by the flipping behavior of the rods. The upper diagram includes all experiments with flipping rods (both within and outside the image plane). The center diagram shows only those with orientation reversals occurring within the image plane. The remaining cases, where flips occurred outside the image plane, are shown in the bottom diagram of Fig.5.15.

Particularly noteworthy is the middle diagram in Fig. 5.15, which shows the experiments with in-

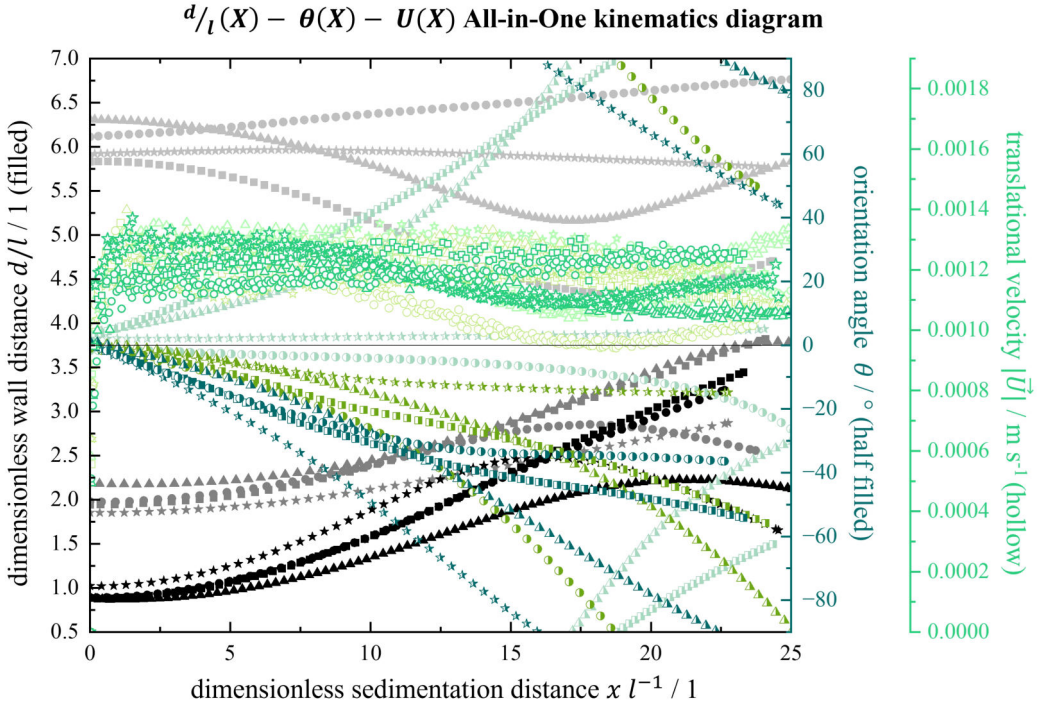


Figure 5.13: All-in-one kinematics diagram of the intermediately soft rods ($E \approx 936$ kPa; $\rho_P \approx 1007.2$ kg·m^{-3}) sedimenting at $Re_P \approx O(10^{-2})$ at various distances from the plane walls in a rectangular duct. Dimensionless wall distance d/l (filled), orientation angle θ (half-filled) and translational velocity $|\vec{U}|$ (hollow) are plotted against the dimensionless sedimentation distance xl^{-1} for short, cylindrical rods with aspect ratio $\frac{l}{r} \approx 5.2$ sedimenting axially aligned from rest ($\theta_{ini} \approx 0°$) in the center of the duct ($d/l \approx 5.8$), in the intermediate region ($d/l \approx 2$) and in the near-wall region ($d/l \approx 1$) of a rigid, plane wall.

plane flipping rods ($\varphi = 0°$). The two experiments show flips in opposite directions at two distinct wall distances: one in the center (■) and one in the near-wall region (★). Despite these markedly different initial conditions and differences in angular dynamics, both the local and the angular trajectories appear quasi mirror-symmetrical. The velocity curves are also remarkable: despite the significant difference in wall distance and the associated impact on drag, the velocity curves are nearly identical.

The kinematics of the intermediately soft rods reveal an additional characteristic behavior in this Reynolds number regime under the influence of elasticity: drift modes. During drifting, the rate of change of the orientation angles tends to vanish although the rods continue to increase the wall distance, *i.e.*, $\dot{\theta} \to 0$ and/or $\varphi \to 0$. Fig. 5.16 shows the All-in-One kinematics diagram, sorted according to the presence of these drift modes. The upper diagram includes all experiments in which the rods initially tilt and subsequently develop a drift mode, regardless of whether this occurs within or outside the image plane. The bottom diagram of Fig. 5.16 presents only the evaluable tests in which the rods first tilt and then transition into a drifting motion, both occurring within the image plane.

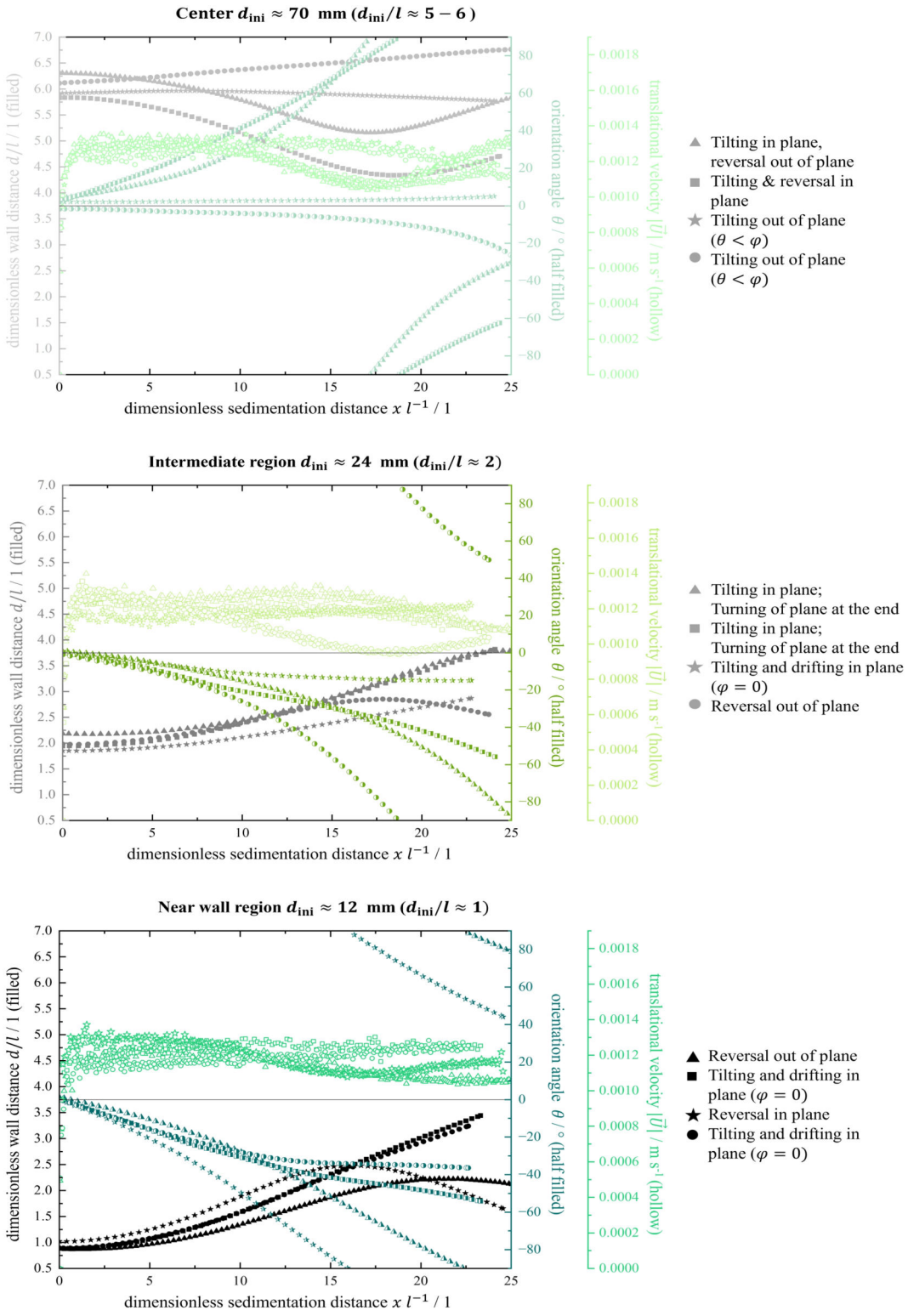


Figure 5.14: Dimensionless wall distance d/l (filled), orientation angle θ (half-filled) and translational velocity $|\vec{U}|$ (hollow) plotted against the dimensionless sedimentation distance xl^{-1} for short, cylindrical soft rods ($E \approx 936$ kPa; $\rho_P \approx 1007.2$ kg·m^{-3}) with aspect ratio $\frac{l}{r} \approx 5.2$ sedimenting axially aligned from rest ($\theta_{ini} \approx 0°$) at $Re_P \approx 0.015$ in the center of a rectangular duct ($d/l \approx 5.8$) (top); in the intermediate region (($d/l \approx 2$) (middle) and in the near wall region ($d/l \approx 1$) (bottom).

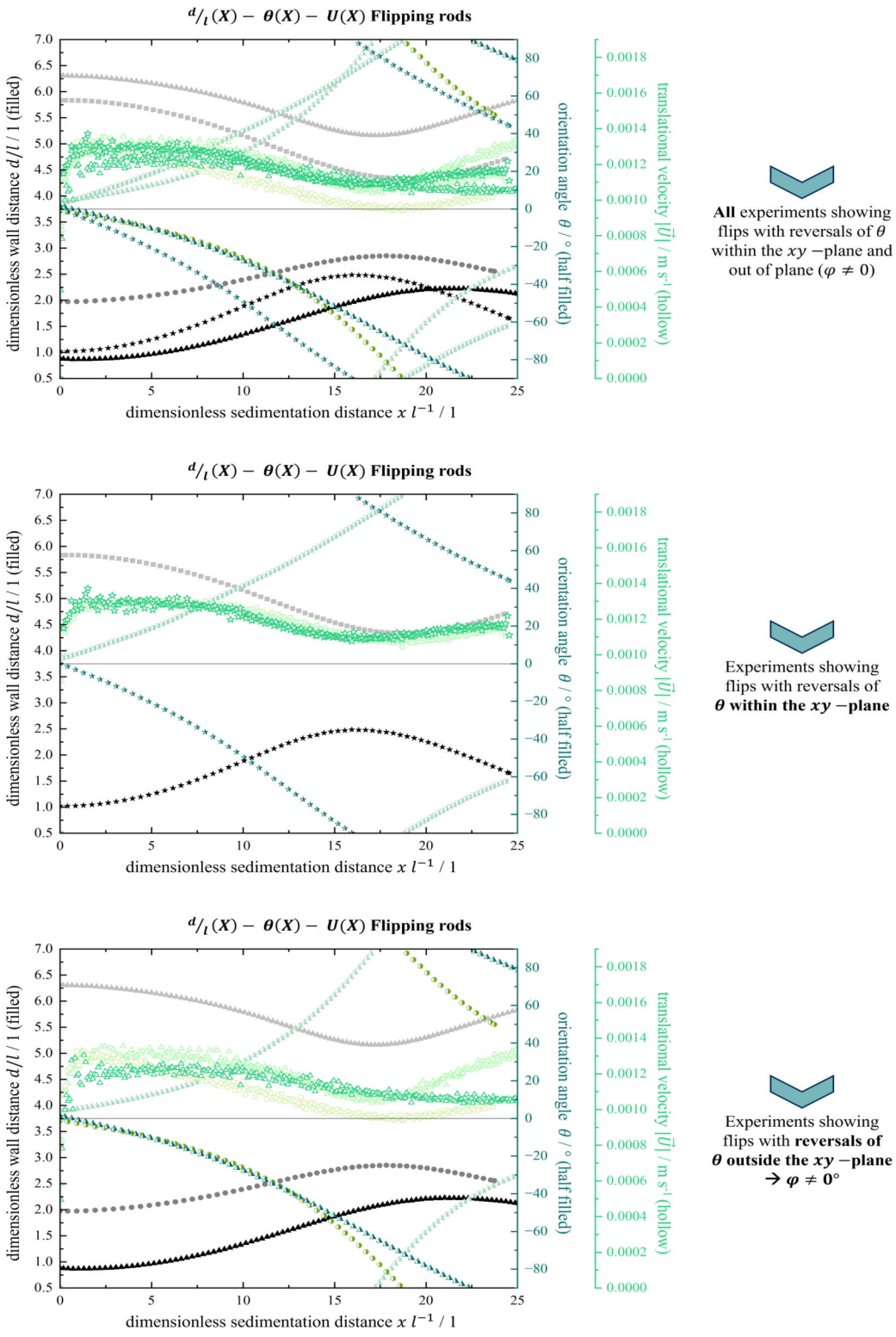


Figure 5.15: All-in-One kinematics diagram of the intermediately soft rods ($E \approx 936$ kPa; $\rho_P \approx 1007.2$ kg·m^{-3}) sedimenting at $Re_P \approx O(10^{-2})$ at various distances from the plane walls in a rectangular duct (*cf.* Fig. 5.13) sorted by their flipping behavior: all rods reversing θ within the image plane and outside (top); reversal of θ within the image plane (middle) and reversal out of the plane (bottom).

The drift mode phenomenon became more pronounced as the Reynolds number decreased further and the elasticity increased. It is therefore revisited and discussed in more detail below, see Fig. 5.22.

Fig. 5.17 presents the "All-in-One" kinematics diagram of the softest cylindrical rods ($E \approx 135$ kPa; $\rho_P \approx 988.0$ kg·m^{-3}) with an aspect ratio of $\frac{\overline{l}}{r} \approx 5.2$. The rods were released ($xl^{-1} = 0$) with an initial orientation angle of $\theta_{ini} \approx 0°$ in the center of the duct ($d/l \approx 5.8$; spatial trajectories with light gray, filled symbols), in the intermediate region between the center and a wall ($d/l \approx 2$; gray, filled symbols), and in the near-wall region ($d/l \approx 1$; black, filled symbols). For additional color coding and further details, see the individual diagrams and short descriptions of the kinematics in Fig. 5.18.

As previously mentioned, increasing the number of experiments per wall distance does not necessarily lead to a clearer understanding of the kinematic instabilities. As shown in Figs. 5.17 and 5.18, more than the four experiments per wall distance considered so far are plotted here. This extended dataset allows for testing whether the previously applied sorting criteria (flipping, in-plane/out-of-plane motion, tilting and drifting) help to identify reproducible patterns within a single wall distance. In the chapter appendix 5.7, the corresponding sorting algorithms are applied to the experiments with sedimenting rods in the center (*i.e.*, sorting the upper diagram in 5.18). As seen there, even the sorted trials within the image plane (see, for example, Fig. 5.26, bottom diagram) exhibit different kinematics. A more reliable analysis would require a significantly larger number of experiments, along with the introduction of additional sorting criteria - for example, introducing the behavior at or following specific dynamic inflection points as a criterion, *e.g.*, the behavior after the transient mass acceleration.

Figure 5.19 shows the All-in-One kinematics diagram of the softest rods at different wall distances, sorted according to their flipping behavior. The upper diagram presents the evaluable experiments in which flipping occurs within the image plane ($\varphi = 0°$), while the lower diagram shows the experiments whose kinematics are influenced by an additional out-of-plane angle ($\varphi \neq 0°$).

As seen in the diagram on top, sorting by flipping behavior does not result in improved order or reproducibility, even when considering only the trials that flip within the image plane. Only vague observations can be made, *e.g.*, a reversal of the orientation angle from negative to positive (θ^- to θ^+) tends to occur earlier (*i.e.*, at smaller xl^{-1}) than a reversal from positive to negative.

Figure 5.20 shows the All-in-One kinematics diagram of the softest rods at different wall distances (originally Fig. 5.17), sorted according to their tilting and drifting behavior. The upper diagram presents all experiments that exhibit tilting motion, with or without temporary drift modes, regardless of whether this occurs within or outside the image plane. The lower diagram includes only the experiments in which the softest rods either tilt only or tilt with a temporary drift mode entirely within the image plane. The image below the diagram shows experiment 2 (■) from the near-wall region, which exhibits a temporary drift mode ($\dot{\theta} \rightarrow 0$ s^{-1}).

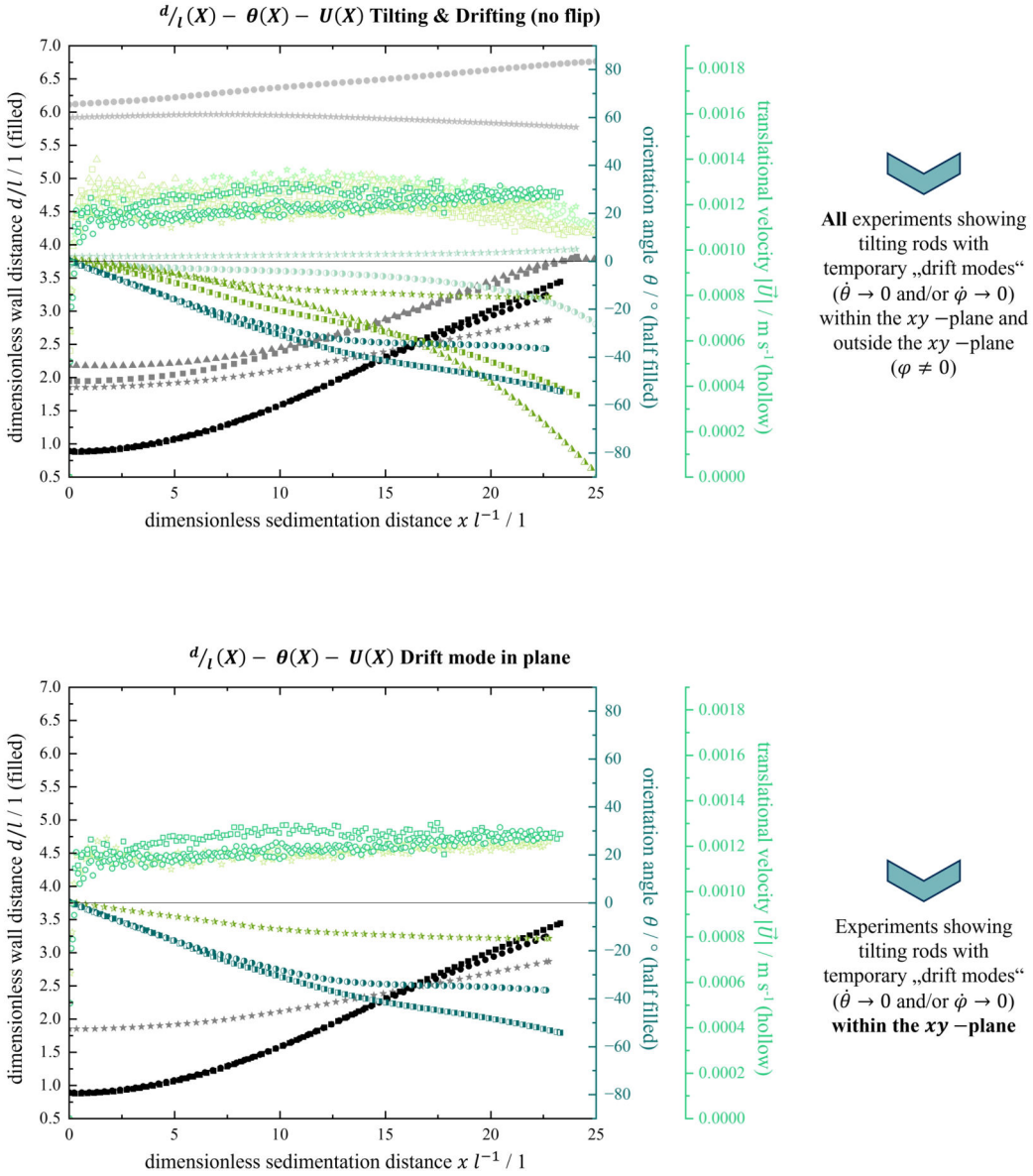


Figure 5.16: All-in-One kinematics diagram of the intermediately soft rods ($E \approx 936$ kPa; $\rho_P \approx 1007.2$ kg·m^{-3}) sedimenting at $Re_P \approx O(10^{-2})$ at various distances from the plane walls in a rectangular duct (*cf.* Fig. 5.13) sorted according to their tilting and drifting behavior: all rods exhibiting tilting and drifting within and out of the image plane (top), and rods showing only in-plane drift modes (bottom).

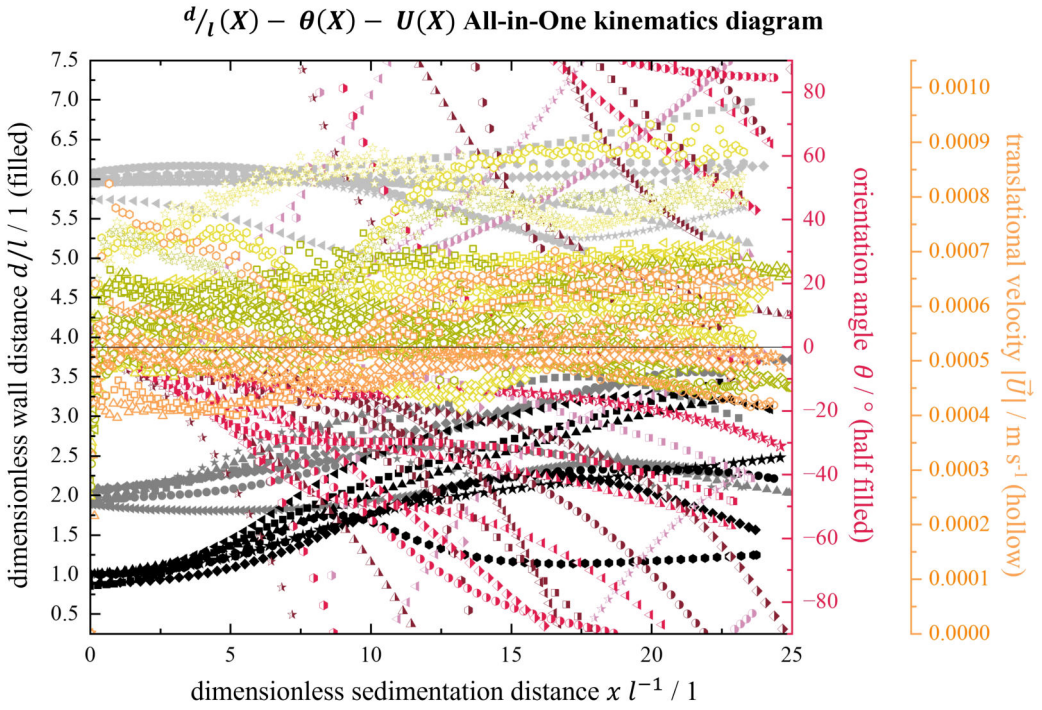


Figure 5.17: All-in-one kinematics diagram of the softest rods ($E \approx 135$ kPa; $\rho_P \approx 988.0$ kg·m^{-3}) sedimenting at $Re_P \approx O(10^{-2})$ at various distances from the plane walls in a rectangular duct: dimensionless wall distance d/l (filled), orientation angle θ (half-filled) and translational velocity $|\vec{U}|$ (hollow) plotted against the dimensionless sedimentation distance xl^{-1} for short, cylindrical rods with aspect ratio $\frac{l}{r} \approx 5.2$ sedimenting axially aligned from rest ($\theta_{ini} \approx 0°$) in the center of the duct ($d/l \approx 5.8$), in the intermediate region ($d/l \approx 2$) and in the near-wall region ($d/l \approx 1$) of a rigid, plane wall.

Fig. 5.20 shows that the drift mode observed in the experiments with the softest rods is typically only temporary. The rods initially tilt and then enter a temporary drift phase (highlighted in red in the lower diagram), during which the orientation angle remains approximately constant. In this phase, the rods do not rotate (*i.e.*, $\dot{\theta} = 0$ s^{-1}) but sediment at a fixed angle while gradually increasing their wall distance. Toward the end of this phase, the rods resume tilting. The curvature of the angular trajectory changes before and after the drift: it is degressive before the drift mode and becomes progressive afterward. This behavior suggests the presence of a dynamic switching point. During the drift phase, the induced torques appear to be in equilibrium for a period of time. That means, in addition to the hydrodynamic (Stokes) torque, another torque must be present to counterbalance the substantial inertial torque induced by fluid reflections from the wall (see previous Section 5.5.1.1 and discussion of Fig. 5.9).

It remains to be clarified whether drifting is a purely hydrodynamic phenomenon or to what extent it is influenced by the rod's elasticity. A phenomenon from nature may offer insight into this question. It is well established that red blood cells (RBCs), when flowing near a surface at low shear rates, exhibit different

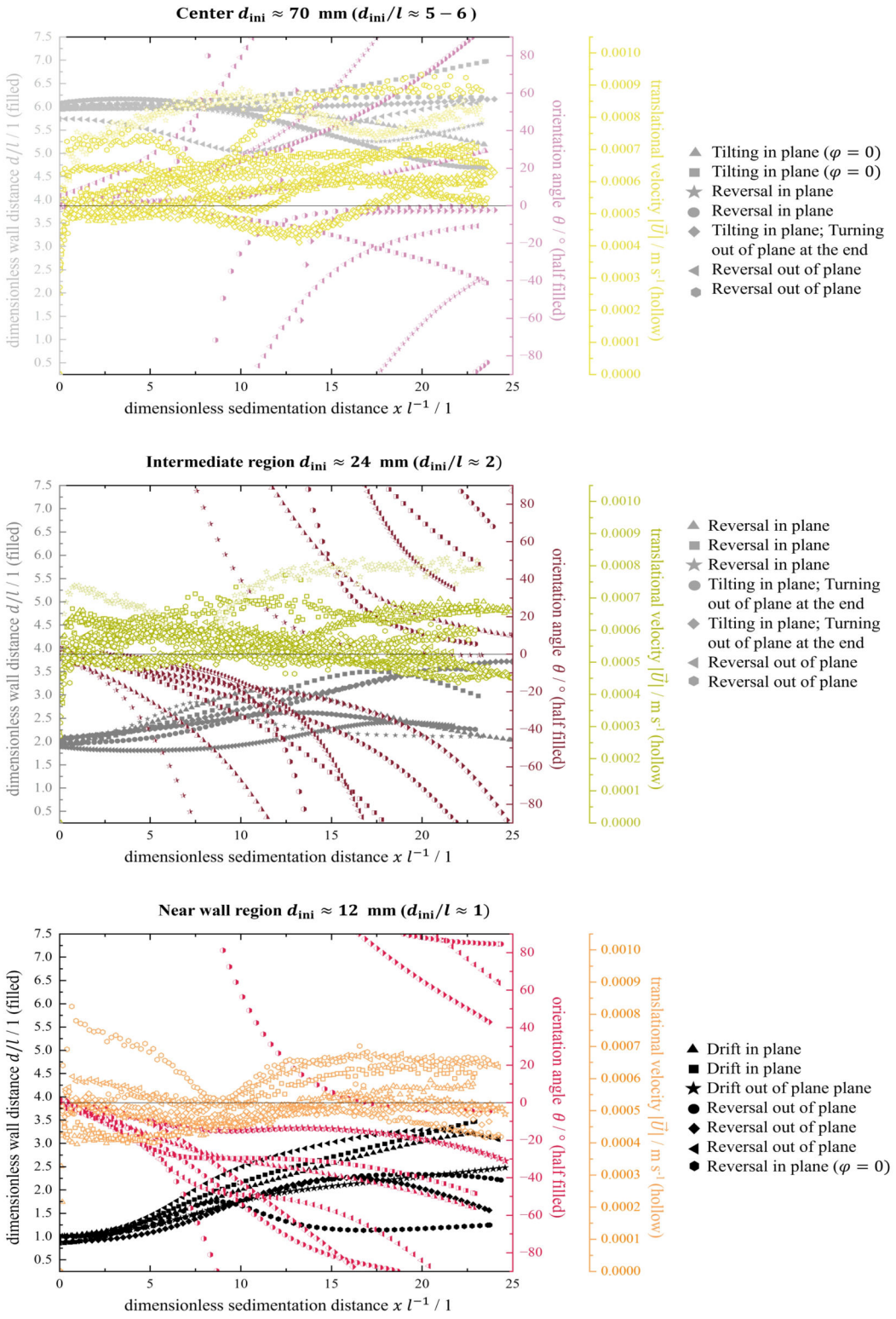


Figure 5.18: Dimensionless wall distance d/l (filled), orientation angle θ (half-filled) and translational velocity $|\vec{U}|$ (hollow) plotted against the dimensionless sedimentation distance xl^{-1} for short, cylindrical soft rods ($E \approx 135$ kPa; $\rho_P \approx 988.0$ kg·m^{-3}) with aspect ratio $\frac{l}{r} \approx 5.2$ sedimenting axially aligned from rest ($\theta_{ini} \approx 0°$) at $Re_P \approx 0.007$ in the center of a rectangular duct ($d/l \approx 5.8$) (top) and in the intermediate region ($d/l \approx 2$) (middle) and at $Re_P \approx 0.006$ in the near wall region ($d/l \approx 1$) (bottom).

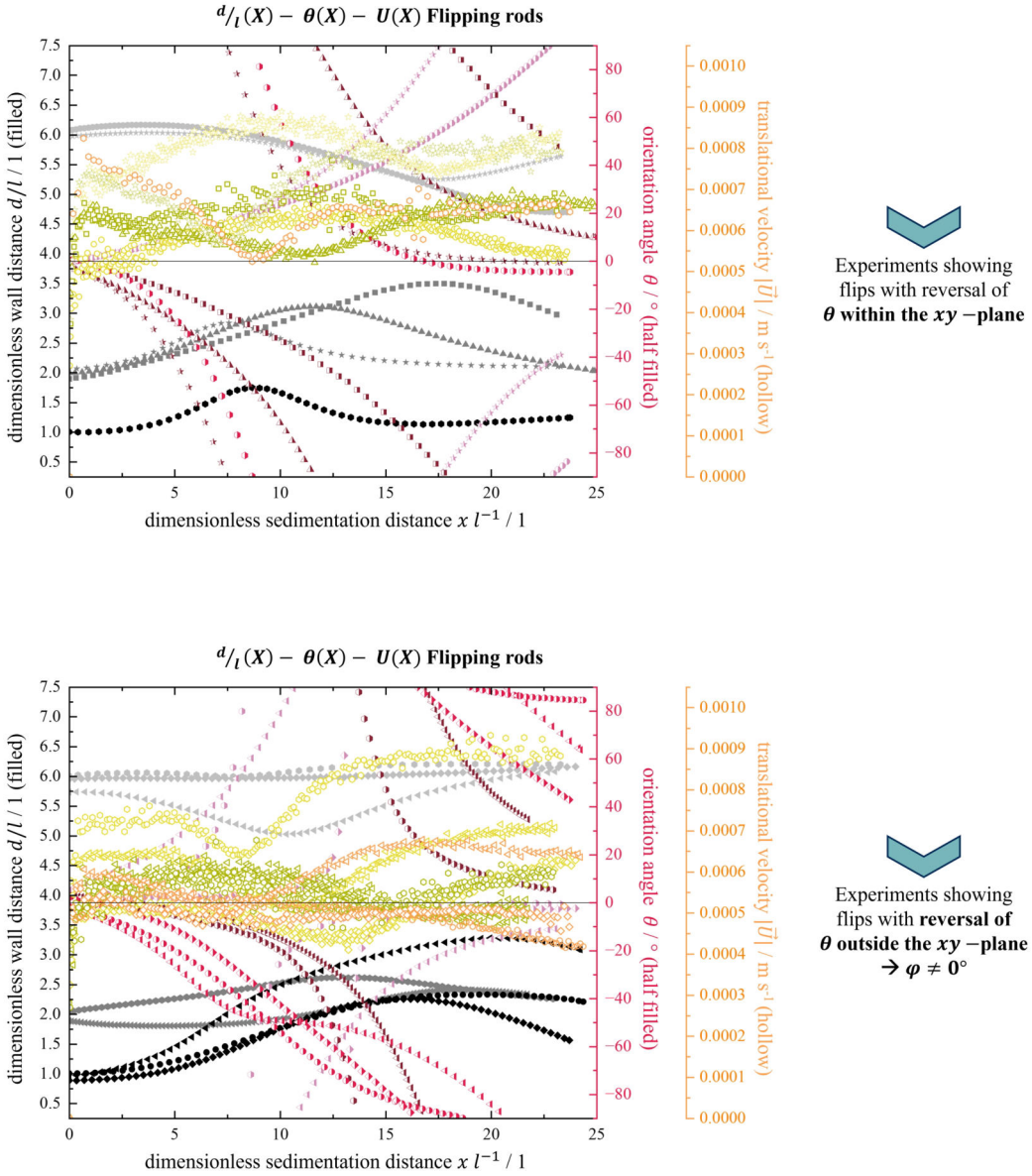


Figure 5.19: All-in-One kinematics diagram of the softest rods ($E \approx 135$ kPa; $\rho_P \approx 988.0$ kg·m^{-3}) sedimenting at $Re_P \approx O(10^{-2})$ at various distances from the plane walls in a rectangular duct (*cf.* Fig. 5.17) sorted by their flipping behavior: rods reversing θ inside the image plane ($\varphi = 0°$) (top) and reversal of θ outside the image plane ($\varphi \neq 0°$) (bottom).

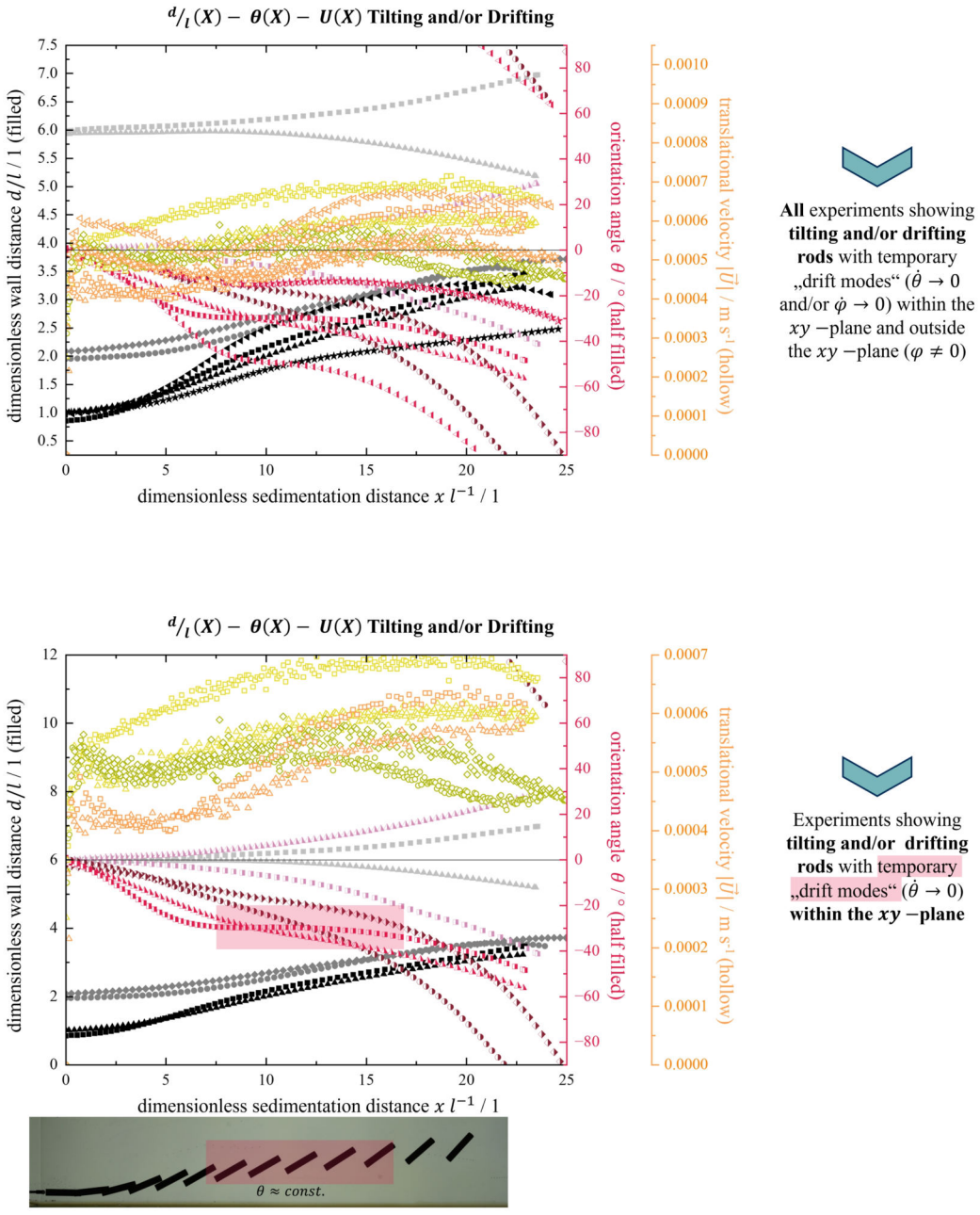


Figure 5.20: All-in-One kinematics diagram of the softest rods ($E \approx 936$ kPa; $\rho_P \approx 1007.2$ kg·m^{-3}) sedimenting at $Re_P \approx O(10^{-2})$ at various distances from the plane walls in a rectangular duct (*cf.* Fig. 5.17) sorted according to their tilting and drifting behavior: all rods exhibiting tilting and drifting within and out of the image plane (top diagram), and rods showing tilting and/or drifting with temporary drift modes only in the image plane (bottom diagram). Figure below: merged photograph of the rod from experiment 2 starting at $d/l = 1$ (■) showing a temporary drift mode.

motion behaviors depending on their deformability. Healthy RBCs are highly elastic and capable of significant deformation in fluid flows. In contrast, diseases or infections can reduce their deformability, altering their mechanical properties. For example, it has been observed that less deformable, diseased RBCs tend to exhibit increased tumbling near surfaces, *i.e.*, an effect analogous to the flipping behavior of the rods. [134],[135] Recall that the least soft rods at $Re_P = O(10^{-2})$ only exhibited flipping. Conversely, above a critical shear rate, *i.e.*, depending on the shear flow Reynolds number, healthy, highly deformable RBCs undergo a transition to a stationary, droplet-like "tank-treading" motion. In this state of motion, the cell maintains a constant orientation relative to the flow direction, while the membrane rotates around the cell body like a tank tread. [136] This tank-treading motion, in which the cell drifts with a fixed orientation angle, is directly comparable to the observed drifting behavior of the softest rods, despite the difference in shape between RBCs and cylindrical rods. Numerous studies have shown that the key factor governing the transition to tank-treading (and thus to drifting behavior) is the cell's deformability. In fact, such motion characteristics are utilized in cell cytometry, a promising tool in diagnostics, to assess the mechanical health of cells and, by extension, the health status of patients. [45],[136]

It can therefore be assumed that the drifting observed in the experiments with rods with medium and the lowest Young's elastic modulus ($E = 936$ kPa and $E = 135$ kPa) is an elastohydrodynamic effect. Finally, attention should again be drawn to the translational velocity ($\vec{U}$) curves in Fig. 5.20. With one exception, all curves exhibit a significant reduction in velocity after the transient mass acceleration phase. A similar deceleration after reaching a peak in velocity was also observed for spheres made of the same material in both the near-wall and intermediate region (see Figs. 3.2 and 3.3 in Chapter 3.5.1.1). Based on comparisons with rigid spheres at a comparable Reynolds number (*cf.* Fig. 3.4), it was concluded that this deceleration is caused by purely hydrodynamic effects, so-called memory effects. Since the translational kinematics show similar behavior, it is therefore likely that memory effects also play a crucial role in the rod dynamics and contribute to observed phenomena such as drifting. Another similarity to the experiments with elastic spheres near the rigid wall can be found in the spatial trajectories. While the rigid rods sedimenting at higher Re_P show a linear increase in wall distance, the spatial trajectories become increasingly curved as the rods become more elastic. In the sphere experiments, these superimposed nonlinearities could be attributed with high confidence to the elasticity of the spheres. It is therefore reasonable to attribute the curvature in the trajectories of the intermediate and softest rods to the influence of elasticity as well.

5.5.2 Kinematics of short, cylindrical rods falling near a soft, plane wall

Analogous to the experiments with spheres sedimenting near an elastic layer (*cf.*, 3.5.2, this section presents sedimentation experiments of rods made of epoxy resin ($E \approx 2900$ MPa; $\rho_P \approx 1159.8$ kg·m^{-3}) sedimenting at $Re_P \approx O(10^{-1})$ and PDMS ($E \approx 1712$ kPa; $\rho_P \approx 1037.6$ kg·m^{-3}) sedimenting at $Re_P \approx O(10^{-2})$ near a plane, elastic wall with a thickness of approximately 13 mm and a Young's elastic modulus of $E \leq 135$ kPa. As in the previous section on elastic rods, only a qualitative description of the kinematics is provided here.

5.5.2.1 Kinematics of rigid, short rods sedimenting at $Re_P \approx O(10^{-1})$ near a soft wall

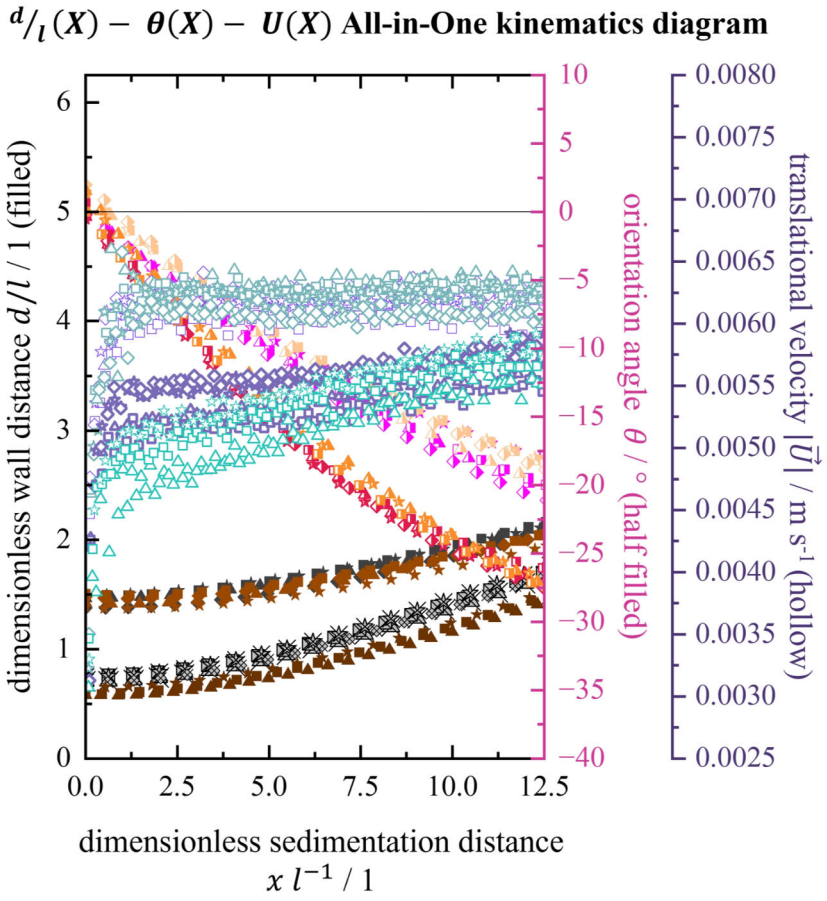
Fig. 5.21 presents the "All-in-One" kinematics diagram of rigid, cylindrical rods ($E \approx 2900$ MPa; $\rho_P \approx 1159.82$ kg·m^{-3}) with an aspect ratio of $\frac{\overline{l}}{r} \approx 5.2$. The rods were released ($xl^{-1} = 0$) with an initial orientation angle of $\theta_{ini} \approx 0°$ in the the near-wall region at $d/l \approx 1.33$ ($d = 16$ mm) and at $d/l \approx 0.66$ ($d = 8$ mm) near a rigid wall and near a soft wall, *cf.* legend table below the diagram in Fig. 5.21.

Even at a wall distance of $d/l \approx 1.33$, there is no noticeable difference between sedimentation near a rigid wall and near an elastic wall. The spatial and angular trajectories, as well as the velocities, are nearly identical. This suggests that the wall's elasticity has no significant influence on the dynamics at this distance - that is, the rod senses the presence of the wall but moves away too quickly for any wall deformation to affect its kinematics.

However, at a very small wall distance ($d/l \approx 0.66$), the spatial trajectories begin to diverge from those near the rigid wall as sedimentation progresses.[3] The clearest difference is seen in the translational velocity: the curve exhibits a significantly shorter phase of transient mass acceleration. This behavior closely resembles that of a sphere made of the same material starting from a similar initial distance ($d \approx 8$ mm), as shown in Fig.3.7 in Chapter3.5.2. Throughout this work, the term *damped velocity curves* has been used to characterize this behavior. Due to the increased wall-induced drag, rods at $d/l \approx 0.66$ experienced a lower particle Reynolds number of only $Re_P \approx 0.04$. To confirm that the rigid rods still behave consistently with others at $d/l > 1$(where $Re_P \gtrapprox 0.07$), the All-in-One kinematics diagram showing all wall distances studied in this chapter is provided in one diagram in the chapter appendix 5.7 (see Fig.5.24).

The angular trajectories differ only slightly in the range $xl^{-1} < 12.5$. However, there are indications that the curves begin to flatten earlier - that is, the orientation angle remains nearly constant sooner than is the case for rigid rods near the rigid wall. Although the range $xl^{-1} > 12.5$ is excluded from the evaluation

[3] Measurements beyond $xl^{-1} > 12.5$ were not reliable in the case of the soft wall, as the elastic layer in the lower region detached and tilted slightly (see Fig.5.27 in the chapter appendix 5.7). To avoid superimposed effects from this inclined wall, the measurement range was limited accordingly.



		Rigid wall			Soft wall		
	Exp. N°	d/l	θ	$\lvert\vec{U}\rvert$	d/l	θ	$\lvert\vec{U}\rvert$
$d_{ini}/l \approx 1.33$	1	▲	◭	△	▲	◭	△
	2	■	◨	□	■	◨	□
	3	★	☆	☆	★	☆	☆
	4	◆	◈	◇	◆	◈	◇
$d_{ini}/l \approx 0.66$	1	▲	◭	△	▲	◭	△
	2	■	◨	□	■	◨	□
	3	★	☆	☆	★	☆	☆
	4	◆	◈	◇			

Figure 5.21: All-in-one kinematics diagram of rigid rods ($E \approx 2900$ MPa; $\rho_P \approx 1159.8$ kg·m^{-3}) sedimenting at $Re_P \approx O(10^{-1})$ at various distances from a plane wall in a rectangular duct. The dimensionless wall distance d/l (filled), orientation angle θ (half-filled) and translational velocity $|\vec{U}|$ (hollow) are plotted against the dimensionless sedimentation distance xl^{-1} for short, cylindrical rods with aspect ratio $\frac{l}{r} \approx 5.2$ sedimenting axially aligned from rest ($\theta_{ini} \approx 0°$) in the near-wall region ($d/l \approx 1.33$ and $d/l \approx 0.66$) near both a rigid and an elastic, plane wall.

due to the inclined elastic layer, a composite image of the rod starting at $d/l \approx 0.66$ is shown in the chapter appendix 5.7, *cf.* rust-colored rods on the right side of Fig. 5.27. The lower, inclined area of the elastic layer is also depicted there. From the superimposed images, it becomes apparent that the rod's orientation angle in the lower region remains nearly constant, indicating that the rod is drifting. The rod is positioned far from the inclined wall in this region, so its influence should be negligible (it is also clearly visible that the inclination is small). It would be highly interesting to determine whether the elastic wall indeed triggers this drifting behavior - *i.e.,* whether it is an elastohydrodynamic phenomenon - by repeating the experiments with a straight elastic wall in future studies.

5.5.2.2 Kinematics of rigid, short rods sedimenting at $Re_{\mathrm{P}} \approx O(10^{-2})$ near a soft wall

Experiments close to the elastic wall at small wall distances ($d/l \approx 1.33$ and $d/l \approx 0.66$) were also performed using PDMS rods with an aspect ratio of $\frac{\overline{l}}{r} \approx 5.2$($E \approx 1712$ kPa; $\rho_{\mathrm{P}} \approx 1037.6$ kg·m^{-3}) sedimenting axially aligned from rest at $Re_{\mathrm{P}} \approx O(10^{-2})$. Since these rods can be considered non-deformable, any differences between the kinematics near the rigid wall and near to the elastic wall - a significantly smaller Young´s elastic modulus - can be attributed to the wall´s elasticity. Fig. 5.22 shows the corresponding All-in-One kinematics diagram.

At a wall distance of $d/\approx 1.33$, only one experiment was evaluable. In almost all other cases, the rods rotated out of the image plane early on, preventing further analysis using particle tracking velocimetry. The single evaluable experiment, however, shows a rod tilting within the image plane without flipping. Its trajectory closely resembles that of the single rod near the rigid wall, which also only tilted and likely had a lower density (see bottom diagram in Fig. 5.11). It can therefore be assumed that this is the same rod. Nevertheless, this experiment suggests that, at a wall distance of $d/\approx 1.33$, there is still no significant difference between sedimentation near a rigid wall and near an elastic wall, even at lower Reynolds numbers. The stronger rotation out of the plane observed in some experiments might hint at an elastic influence (additional nonlinearities), though given the small number of usable experiments, such speculation remains inconclusive.

More definitive conclusions about the influence of wall elasticity can only be drawn at very small wall distances, such as $d/\approx 0.66$. Some experiments at this distance show the same acceleration behavior as near the rigid wall - typically the ones with early flips. Others exhibit damped acceleration, and depending on the extent of this damping, either flip later or remain in the tilting state. The angular trajectory of experiment 4 (♦), for example, suggests the onset of drifting, as the change in angle becomes very small. This is likely again the rod with the lower density. Interestingly, at $d/\approx 0.66$, all experiments remained entirely within

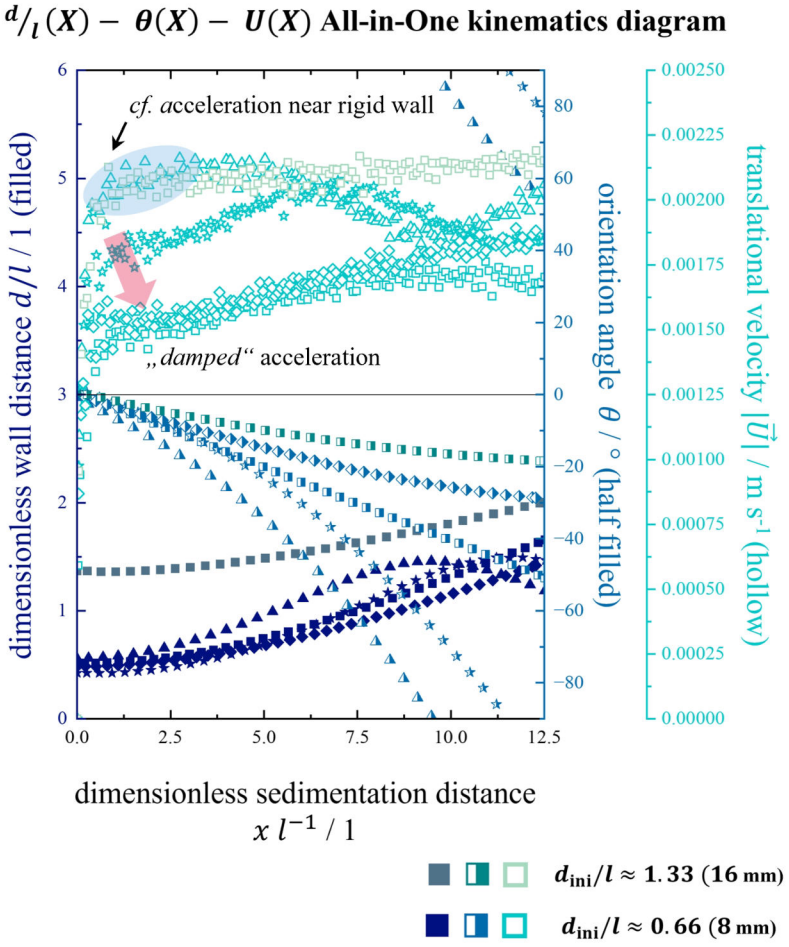


Figure 5.22: All-in-one kinematics diagram of PDMS rods ($E \approx 1712$ kPa; $\rho_P \approx 1037.6$ kg·m^{-3}) sedimenting at $Re_P \approx O(10^{-2})$ at various distances from a plane, elastic wall in a rectangular duct. The dimensionless wall distance d/l (filled), orientation angle θ (half-filled) and translational velocity $|\vec{U}|$ (hollow) are plotted against the dimensionless sedimentation distance xl^{-1} for short, cylindrical rods with aspect ratio $\frac{l}{r} \approx 5.2$ sedimenting axially aligned from rest ($\theta_{ini} \approx 0^{\circ}$) in the near-wall region ($d/l \approx 1.33$ and $d/l \approx 0.66$) near an elastic, plane wall.

the image plane, even when flipping - unlike at the larger wall distance, where out-of-plane motion was more common. This suggests that proximity to the (elastic) wall may have a stabilizing effect on the rod's kinematics.

A direct comparison of rods with different Reynolds numbers in the near-wall region is provided in the chapter appendix 5.7, see Fig. 5.27. The composite image on the right highlights the overall behavior near the elastic wall: at higher Reynolds numbers, rods tend to tilt (and may exhibit drift later), while at lower Reynolds numbers, they show stable in-plane flips.

5.6 Conclusions and outlook

In this chapter, the sedimentation behavior of short, cylindrical rods with aspect ratios of $l/r \approx 5-6$ at particle Reynolds numbers $Re_P = \rho \vec{U} l \eta^{-1} \lessapprox 0.1$ was experimentally investigated in a rectangular container filled with a highly viscous Newtonian fluid. The rods were initially aligned with their cylindrical axis (orientation angle $\theta \approx 0°$) and released from rest, either in the center of the container or at varying distances from the plane walls. Their kinematics - both translational and rotational - were recorded using a camera system and analyzed with a self-programmed particle-tracking velocimetry (PTV) tool designed to automatically evaluate the motion of finite-sized rods. By using high-viscosity silicone oil, macroscopic rods with a length of approximately $2l \approx 24.6$ mm and diameter $2r \approx 4.7$ mm sedimented in a hydrodynamic regime comparable to that of micron-scale particles in aqueous fluids. Elastohydrodynamic interactions were introduced either by using rods with various Young's moduli or by equipping the experimental setup with a thick, soft wall layer. Rigid epoxy rods, which had the highest density and elastic modulus $E \approx 2900$ MPa; $\rho_P \approx 1159.8$ kg·m^{-3}), sedimented at $Re_P \approx O(10^{-1})$. PDMS rods, fabricated with varying mixing ratios, had lower elastic moduli ($E \approx 1712; 936; 135$ kPa) and lower densities, leading to sedimentation at $Re_P \approx O(10^{-2})$.

The results for the rigid rods at $Re_P \approx O(10^{-1})$ were highly reproducible and aligned well with expected behavior. In the duct center, the rods sedimented nearly vertically, while in the near-wall region, inertial torques induced by fluid reflections at the wall caused the rods to rotate and drift away from the wall. A quantitative comparison was made between the measured translational velocities and theoretical predictions obtained by combining a translational velocity estimate for axial sedimentation in unbounded fluids (based on semi-empirical slender-body theory predictions with inertial corrections by Kharrouba *et al.* (2021)) with wall correction factors derived from experiments on spheres in rectangular ducts. [110] The theoretical velocities of rods in the duct center were well predicted by Eq. 5.13, and in the near-wall

region - depending on the angle of attack ϕ - by Eq. 5.16. Good agreement between experiment and theory was observed for moderate orientation angles up to $\theta \approx 15°$. The angular velocity of the rigid rods near the wall was also measured. Compared to theoretical predictions based on slender body theory in an unbounded fluid, *i.e.*, neglecting both inertial corrections and wall effects - the measured angular velocities were significantly larger. These markedly higher values underscore the importance of considering angular dynamics in near-wall regions. However, the absence of suitable theoretical models that account for wall influences currently limits the ability to quantitatively predict the torques acting on the particles.

Rods sedimenting at $Re_P \approx O(10^{-2})$ exhibited in general limited reproducibility, with their kinematic behavior characterized by significant variability. The non-deformable PDMS rods ($E \approx 1712$ kPa; $\rho_P \approx 1037.6$ kg·m^{-3}) frequently undergo flipping motions in different directions, even in the center of the duct. While the direction of flipping - or, more specifically, the reversal of the orientation angle - proves useful for categorizing general kinematic trends, the underlying cause of the variability remains unclear. The experiments show that small deviations in initial conditions can lead to pronounced differences in particle kinematics, suggesting an inherent instability in the system. Additionally, undetectable torques acting outside the image plane (*e.g.,* due to variations in the angle φ) likely contribute to complex, three-dimensional force and torque interactions that are not captured by the current measurement techniques. Despite these transient behaviors, sorted velocity curves and trajectories eventually converge over time.

By adjusting the PDMS mixing ratios, both the Young´s elastic modulus and density of the rods were systematically reduced. As the rods became softer, the system exhibited increasing instability and more pronounced three-dimensional force and torque interactions - evident in the rods' chaotic rotations out of the image plane. At intermediate Young's moduli, an additional mode of motion emerged: drifting along the wall. In this mode, the rods moved along the wall while gradually increasing their distance from it, maintaining a constant orientation angle (*i.e.*, angular velocity $\theta = 0°$). This behavior implies that an additional torque must be generated to counteract the inertial torques primarily caused by fluid reflections at the wall.

Drifting is a well-known motion pattern in the kinematics of red blood cells (RBCs) in shear flows. Numerous studies have shown that only soft, healthy cells exhibit drifting, while stiffer or diseased cells tend to undergo tumbling - a motion similar to the flipping observed in the non-deformable PDMS rods. Accordingly, the drifting observed in the softest rods can be attributed to elastohydrodynamic effects. Moreover, the velocity curves of the softest rods showed a markedly deceleration following the initial mass acceleration. This pronounced velocity reduction resembles a damping effect, with the curve appearing to be "pushed down." In addition, the local trajectories of soft rods become increasingly curved (*i.e.*, nonlinear), particularly in regions where the trajectories of rigid rods remained linear - at both $Re_P \approx O(10^{-1})$ and $Re_P \approx O(10^{-2})$. These superimposed nonlinearities and the damping-like behavior are kinematic signatures also observed in the soft sphere experiments presented in Chapter 3. It is therefore reasonable to

attribute the damping to memory effects and the nonlinearities to elasticity - suggesting the presence of *elastohydrodynamic memory* in the sedimentation dynamics of soft rods as well.

Furthermore, experiments were conducted with rigid rods that initially started in axial alignment near a thick elastic layer ($E < 135$kPa). At wall distances of $d/l \approx 1.3$, no significant differences were observed between the kinematics near a rigid wall and those near an elastic wall, neither at $Re_P \approx O(10^{-1})$ nor at $Re_P \approx O(10^{-2})$. Noticeable differences in kinematics only emerged at much smaller initial wall distances ($d/l \approx 0.6$). The rigid epoxy resin rods sedimenting at $Re_P \approx O(10^{-1})$ exhibited the same flattened, damped acceleration behavior as the spheres of comparable density near the elastic wall (see Fig. 3.7 in Section 3.5.2.1).

The non-deformable PDMS rods sedimenting at $Re_P \approx O(10^{-2})$ revealed another striking feature: while their kinematics were highly unstable at larger wall distances or near the rigid wall - especially with respect to chaotic out-of-plane rotations - the same rods near the elastic wall exhibited a much more stable behavior. In this case, the dynamics depended only on the orientation angle within the image plane. This suggests that the elastic wall exerted a stabilizing effect, enabling the rods to flip stably in a plane perpendicular to the wall.

Unfortunately, the experiments could not be evaluated in the lower part of the container. In this region, the elastic layer had slightly detached from the container wall, resulting in a slight inclination of the elastic layer. Since such an inclination is expected to influence kinematics, the corresponding results were excluded from the analysis. Nevertheless, it is worth noting that both the rigid rods at $Re_P \approx O(10^{-1})$ and some rods at $Re_P \approx O(10^{-2})$ exhibited drifting behavior in this area. Repeating the experiments with a truly vertical, flat elastic wall would be highly informative. If similar drifting behavior of the rigid rods were observed under those conditions, it would provide further compelling evidence that the drifting is indeed an elastohydrodynamic effect.

Further experiments that should definitely be repeated or explored in greater depth include the investigation of rod kinematics starting from an initial orientation angle $\theta \neq 0°$. Additional influences - such as history forces during transient mass acceleration or proximity to the liquid–air interface - were already discussed in Chapters 3 and 4 in the context of the sphere experiments and simulations. Although the rods did not exhibit notable kinematic phenomena like *inertial wall attraction* (see Chapter 3), it would still be valuable to examine how elasticity affects their kinematics after the transient acceleration phase, once the rods are moving at a higher or constant velocity. In particular, it would be of interest to study how the kinematics evolve when the rods approach the wall while already rotating - analogous to the experimental configurations used by Russel *et al.* (1977). [115]

These were, in fact, the experiments conducted at the very beginning of this project. For example, tests were performed with initial orientation angles of $\theta = 20°$, $45°$, and $65°$. However, as might be expected,

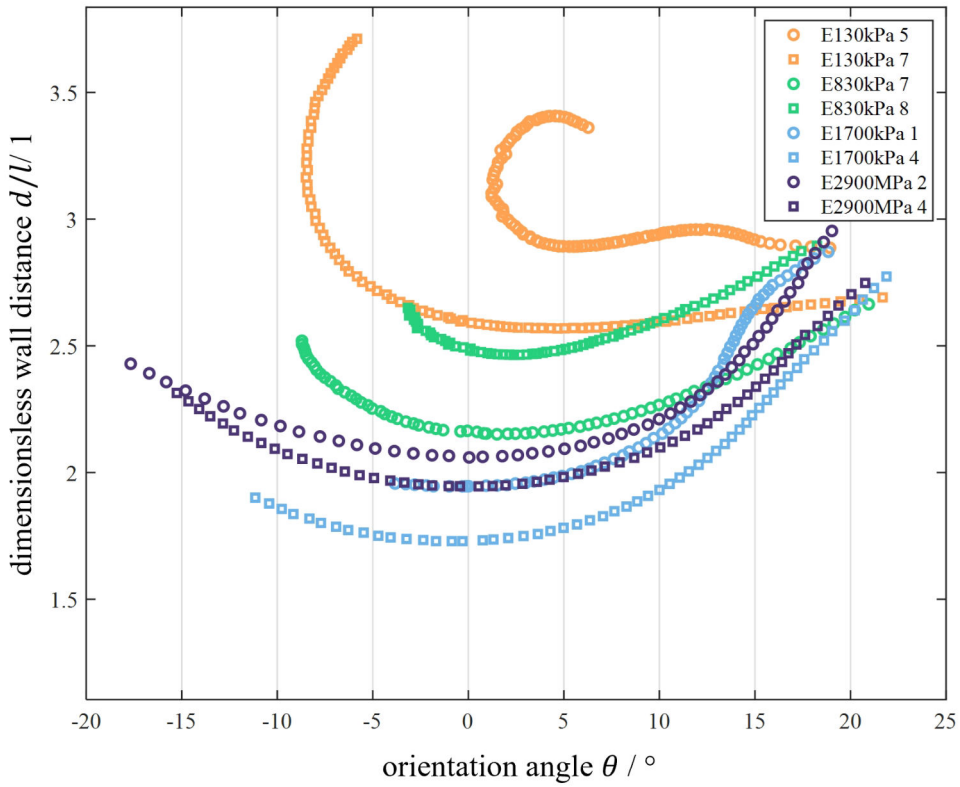


Figure 5.23: Dimensionless wall distance d/l plotted against the orientation angle θ of short rods with various Young´s elastic modulus and density (orange: $E \approx 135$ kPa; $\rho_P \approx 988.0$ kg·m^{-3}); green: $E \approx 936$ kPa; $\rho_P \approx 1007.2$ kg·m^{-3}); light blue: $E \approx 1712$ kPa; $\rho_P \approx 1037.6$ kg·m^{-3}); purple: $E \approx 2900$ MPa; $\rho_P \approx 1159.8$ kg·m^{-3}). The rods of small aspect ratio $\frac{l}{r} \approx 4$ started with an initial orientation angle of $\theta_{ini} \approx 20°$ at a wall distances of $d/l \approx 2.7; 2.9$ from a rigid, plane wall in a rectangular duct.

these experiments were even less reproducible and more unstable than the previously discussed experiments. Due to limited experience at the time, no consistent trends could be identified in the measurement results. Consequently, the decision was made to begin with the supposedly simpler experiments using spheres, followed by experiments with rods initially aligned axially.

With the insights gained since then, and based on the sorting criteria established for axial sedimentation, the "old data" were reanalyzed. Fig. 5.23 presents a specialized visualization of the spatial trajectories of shorter rods ($l/r \approx 4$) with varying Young's modulus, shown here as dimensionless wall distance d/l versus orientation angle θ. In these experiments, an additional sorting criterion was applied: only data sets with comparable pairings of initial orientation angle and wall distance (d/l–θ pairs) across all tested Young's moduli were included.

Fig. 5.23 shows that the rigid rods (purple and blue curves) approach the wall and exhibit symmetric *glancing* behavior. In contrast, the elastic rods display clear asymmetries, with the softest rods (orange curves) exhibiting pronounced drifting. However, the experiments shown in Fig. 5.23 should be considered

preliminary. For this limited set of experiments, sorting based on the criteria of ”glancing or drifting only” and ”similar initial wall distance–orientation angle pairings” proved effective. Nonetheless, a significantly larger number of experiments would be required to generate statistically robust data.

The data presented in this chapter is ideally suited for further analysis using data science methods such as machine learning. However, additional experiments are required to generate more data, particularly from unstable systems. This chapter has already introduced essential tools—such as sorting criteria - that would facilitate the application of appropriate data science techniques to these datasets. By now, it should be evident that there is only one viable path toward “solving the problem” of the dynamics of elastic, nonheavy particles: first, take a deliberate step back to classical experimental physics and robust data generation. Only then should modern data science methods be applied.

After all, a step backward can also be a step forward.

5.7 Chapter Appendix

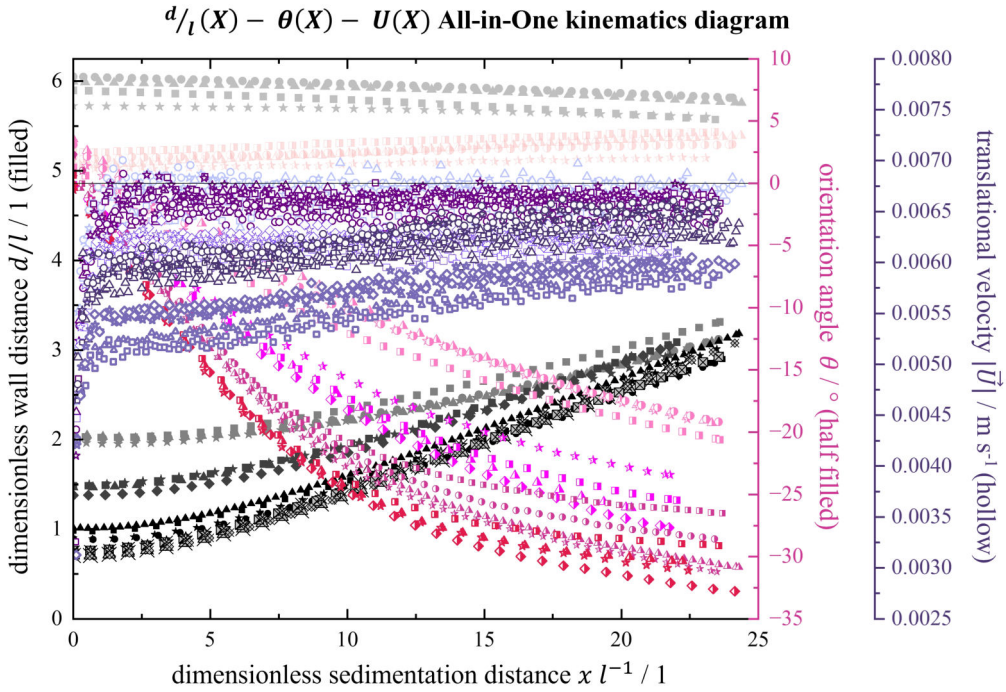


Figure 5.24: All-in-one kinematics diagram of rigid rods ($E \approx 2900$ MPa; $\rho_P \approx 1159.8$ kg·m^{-3}) sedimenting at $Re_P \approx O(10^{-1})$ at various distances from the plane walls in a rectangular duct. The dimensionless wall distance d/l (filled), orientation angle θ (half-filled) and translational velocity $|\vec{U}|$ (hollow) are plotted against the dimensionless sedimentation distance xl^{-1} for short, cylindrical rods with aspect ratio $\frac{l}{r} \approx 5.2$ sedimenting axially aligned from rest ($\theta_{ini} \approx 0°$) in the center of the duct ($d/l \approx 5.8$), in the intermediate region ($d/l \approx 2$) and in the near-wall region ($d/l \approx 1.33$; $d/l \approx 1$ and $d/l \approx 0.66$) of a rigid, plane wall.

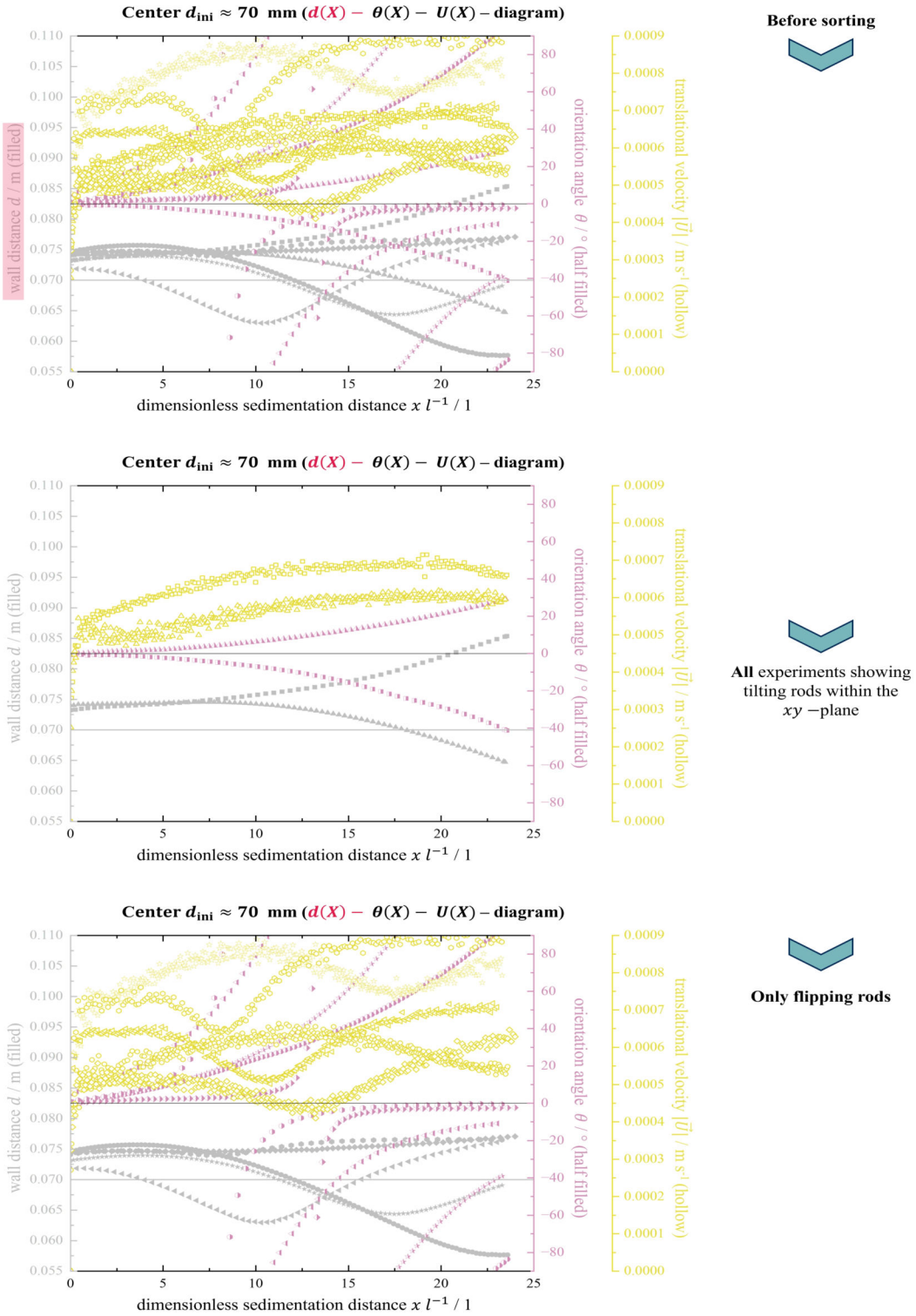


Figure 5.25: Wall distance d (filled), orientation angle θ (half-filled) and translational velocity $|\vec{U}|$ (hollow) plotted against the dimensionless sedimentation distance xl^{-1} of short, cylindrical soft rods ($E \approx 135$ kPa; $\rho_P \approx 988.0\,\mathrm{kg{\cdot}m^{-3}}$) with aspect ratio $\frac{l}{r} \approx 5.2$ sedimenting axially aligned from rest ($\theta_{ini} \approx 0°$) at $Re_P \approx 0.007$ in the center of a rectangular duct ($d/l \approx 5.8$). All experiments before sorting (top); All rods tilting within the image plane (middle); All flipping rods (in-plane and out-plane flips).

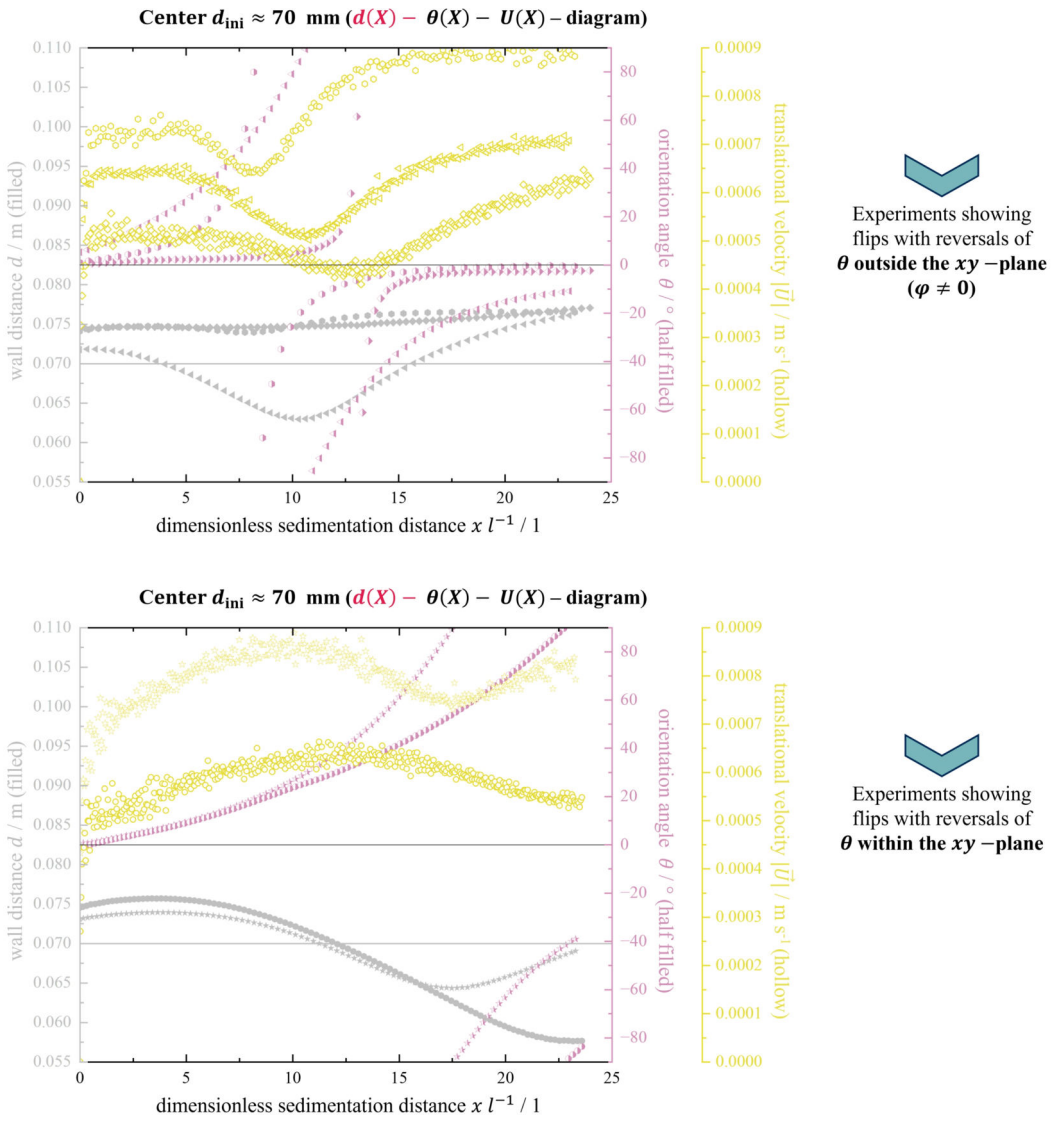


Figure 5.26: Wall distance d (filled), orientation angle θ (half-filled) and translational velocity $|\vec{U}|$ (hollow) plotted against the dimensionless sedimentation distance xl^{-1} of short, cylindrical soft rods ($E \approx 135$ kPa; $\rho_P \approx 988.0\,\mathrm{kg{\cdot}m^{-3}}$) with aspect ratio $\frac{l}{r} \approx 5.2$ sedimenting axially aligned from rest ($\theta_{ini} \approx 0^\circ$) at $Re_P \approx 0.007$ in the center of a rectangular duct ($d/l \approx 5.8$). Flipping rods with reversal of θ outside the image plane ($\varphi \neq 0^\circ$) (top) and rods with in-plane reversal of θ ($\varphi \neq 0^\circ$) (bottom).

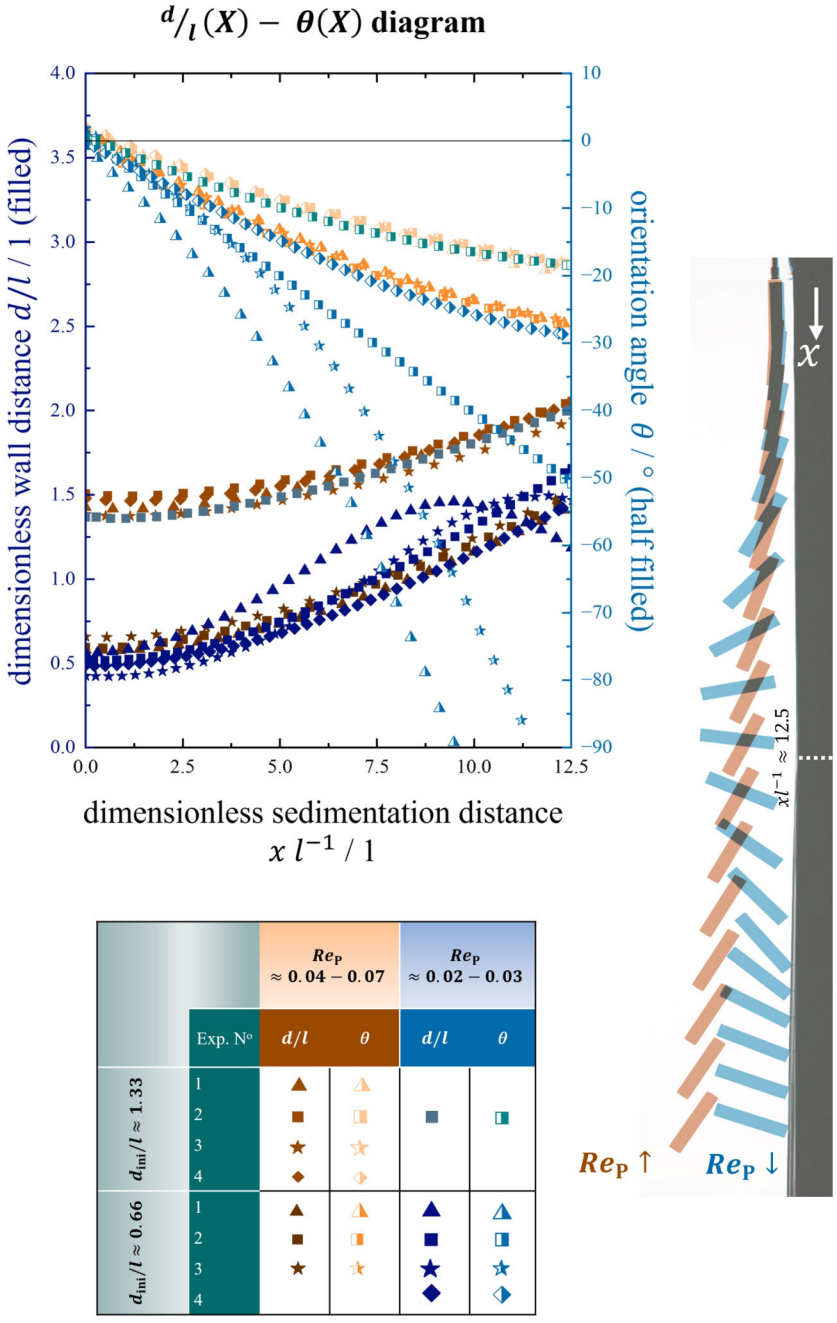


Figure 5.27: Direct comparison between rigid rods sedimenting with various Re_P: Dimensionless wall distance d/l and orientation angle θ plotted against the dimensionless sedimentation distance xl^{-1} for cylindrical rods with aspect ratio $l/r \approx 5.2$ sedimenting axially aligned from rest ($\theta_{ini} \approx 0°$) at $Re_P \approx 0.04 - 0.07$ ($E \approx 2900$ MPa; $\rho_P \approx 1159.8$ kg·m^{-3}) and at $Re_P \approx 0.02 - 0.03$ ($E \approx 1712$ kPa; $\rho_P \approx 1037.6$ kg·m^{-3}) in the near-wall region ($d/l \approx 1.33$ and $d/l \approx 0.66$). Right: merged video images of experiments at $d/l \approx 0.66$ at two different Reynolds numbers.

Conclusions

This dissertation examined the influence of elasticity on the dynamics of nonheavy particles moving near surfaces in the creeping flow regime. The flow properties and particle characteristics investigated are highly relevant to applications such as filtration or the sedimentation of soft microparticles - *e.g.*, biological particles or soft microplastics. To isolate elastic effects from other factors that could dominate in microscopic systems, such as electrostatics or diffusion, scaled model experiments were conducted at the centimeter scale. For this purpose, a large rectangular tank was filled with a highly viscous Newtonian fluid, and sedimentation experiments were performed with macroscopic rigid and elastic model particles.

In the first part of the study, model experiments involving rigid and deformable, nonheavy spheres were conducted in the center of the rectangular tank. Although particle deformations were small, the dynamics of elastic spheres differed fundamentally from those of rigid spheres. Initially, elastic spheres sedimented similarly to rigid ones. However, beyond a characteristic onset position of approximately $10R$, a second acceleration phase appeared. The softer the spheres (in terms of Young's elastic modulus), the higher their terminal velocities - up to 9 % larger than that of comparable rigid spheres. At the time, this additional acceleration was attributed to elastic deformation effects.

In the next phase, the complete kinematics of both elastic and rigid spheres sedimenting from rest at varying distances from either a rigid or elastic plane wall were recorded. Several specific phenomena and peculiarities in the kinematics of both particle types - sedimenting at $Re_\mathrm{P} \approx O(10^{-2})$ - were observed, which could not be attributed to elasticity alone but instead to the influence of fluid inertia. One such phenomenon was *inertial wall attraction*, *i.e.*, particles approaching the wall while being accelerated from rest. This initial attraction was found to be a purely hydrodynamic effect, occurring in all experiments at $Re_\mathrm{P} \lessapprox 0.1$.

Following the initial stage, rigid spheres sedimenting at $Re_\mathrm{P} \approx O(10^{-1})$ near a wall displayed classic behavior, such as linear migration due to hydrodynamic lift. In contrast, for both rigid and soft spheres at $Re_\mathrm{P} \approx O(10^{-2})$, the evolution of velocity with wall distance was non-classical. Sedimentation remained unsteady, with particles decelerating even as wall distance increased. For very soft spheres, these instationarities were further superimposed with nonlinearities, attributed to the complex coupling between inertial fluid-particle forces and small elastic deformations. This interplay is assumed to result in an *elastohydrodynamic memory effect*. Instationarities were also observed in rigid spheres sedimenting near elastic walls. In these cases, elastohydrodynamic interactions dampened dynamics during the mass acceleration phase. Instead of experiencing lift away from the wall, spheres showed persistent undulating motion towards the

wall - an effect termed *elastohydrodynamic trapping*.

Complementing the experiments, 3D computational fluid dynamics (CFD) simulations were performed to model a sphere sedimenting in a rectangular fluid domain. These simulations examined transient dynamics near a plane wall ($d/R = 2$) and near an open boundary representing a liquid–air interface, solving the time-dependent creeping flow equations for a Newtonian fluid. The simulations aimed to visualize the flow field within the experimental container. They revealed the development of a large vortex between the particle and the distant wall. During initial acceleration, this vortex was influenced by the open boundary. This interface effect likely existed in the experiments as well and could explain the peculiar initial behavior - namely, inertial wall attraction. The simulations further demonstrated that assuming a quiescent fluid in a confined space, such as a closed container, is unrealistic; fluid disturbances must be accounted for.

In the final part of this study, sedimentation of rods with small aspect ratios ($l/r \approx 5-6$) at Reynolds numbers $Re_P = \rho|\vec{U}|l\eta^{-1} \lessapprox 0.1$ was investigated. The rods were initially aligned axially ($\theta \approx 0^\circ$) and released from rest at various wall distances. Similar to the sphere experiments, both rigid (non-deformable) and soft (deformable) rods were studied near both rigid and elastic plane walls. Rigid rods at $Re_P \approx O(10^{-1})$ exhibited stable, reproducible behavior. Their motion could be compared with theoretical predictions obtained by combining a semi-empirical velocity estimate based on slender-body theory (Kharrouba *et al.* (2021)) with wall correction factors derived from sedimentation of spherical particles with comparable characteristic length. Good agreement was observed for axially falling cylinders in the center of the duct and for inclined cylinders near walls, up to orientation angles of $\theta \approx 15^\circ$. At $Re_P \approx O(10^{-2})$, the kinematics of the rods became unstable, with increasing nonlinear behavior as deformability increased. The results were sensitive to small variations in initial conditions and therefore could not be reproduced consistently; only qualitative analysis was possible. Nonetheless, using sorting and classification techniques, key kinematic features were identified - particularly those suggestive of elastohydrodynamic interactions. Notable among these was the *drifting of soft rods* at a nearly constant orientation angle near a wall. In contrast, non-deformable rods at similar Reynolds numbers primarily exhibited *flipping*. These patterns resemble the behavior of red blood cells (RBCs) in shear flow, where deformable cells show tank-treading (drifting), and stiffened cells exhibit tumbling.

The original objective of the research project underpinning this thesis was to derive an explicit elastohydrodynamic force acting on elastic particles flowing along surfaces at moderate wall distances. However, the model experiments revealed that it is not elasticity alone that governs the dynamics of nonheavy, soft spheres and rods. Instead, inertial effects - somewhat paradoxically - become more significant the slower a particle moves near a wall. Fig.5.28 graphically illustrates this *inertia paradox* for spheres and summarizes the key findings.

Fig. 5.28 illustrates the sedimentation of spheres at slightly different Reynolds numbers: $Re_P \approx O(10^{-1})$

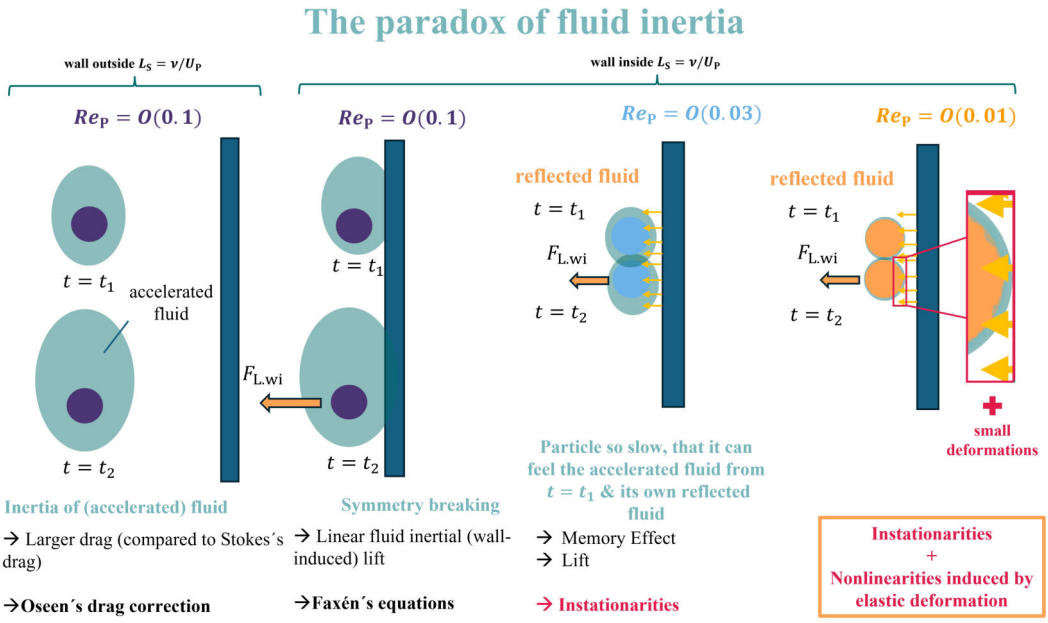


Figure 5.28: The paradox of fluid inertia in the presence of walls.

(purple) and $Re_P \approx O(10^{-2})$ (blue and orange) from the reference frame of an external observer. The surrounding disturbance flows are visualized in blue-green and can be imagined as an expanding "shell" of fluid moving with the sphere. As the Reynolds number increases, this shell grows larger. The influence of this imaginary shell on the drag experienced by the sphere was first approximated by Oseen through a linearization of the Navier–Stokes equations. Hence, the shell represents the dominant, linear part of the disturbance. This fluid shell effectively increases the hydrodynamic resistance.

In the left panel of Fig. 5.28, the spheres are fast enough that their disturbance shells at two consecutive times, t_1 and t_2, do not overlap. Additionally, any nearby wall has negligible influence on the sphere's motion as long as it remains outside the Stokes length $L_S = \nu/U_P$ - a characteristic length scale that defines the extent of the region where linear approximations hold.

In the second panel, the wall lies within the Stokes length. Now, symmetry of the disturbance shell is broken and the linear disturbance region is reflected by the wall, induces a lift force and influences the sphere's drag. The corresponding wall-induced corrections were described by Faxén.

As the Reynolds number decreases further - around $Re_P \approx 0.01$ - a paradoxical effect emerges. The disturbance shell becomes much smaller, as the sphere accelerates less fluid. However, the sphere is now so slow that it begins to "feel" the fluid disturbances it generated at previous time steps. These overlapping disturbance fields result in a hydrodynamic memory effect, which leads to unsteady motion - even in the absence of nearby walls. In the third panel, the wall is again within the Stokes length, but now the linear disturbance region no longer intersects the wall. Nevertheless, the non-linear, inertial part of the disturbance

field, which decays slower than the linear part, still reaches the wall and is reflected. These nonlinear components of the reflections (indicated by orange arrows) act back on the sphere, further complicating its motion.

The fourth panel shows a slow sphere moving at $Re_P \approx 0.01$ within the Stokes length, now exhibiting small elastic deformations. If the sphere were faster or further from the wall, these deformations would likely have negligible influence on the dynamics. However, under these conditions, the nonlinear reflections from the wall can interact with the elastic deformations, producing a complex feedback loop: deformations induce flow disturbances, which reflect off the wall, interact again with the deformable particle, and so on. This scenario likely explains the superimposed nonlinearities observed in the dynamics of soft spheres - and presumably also those of rods.

Ultimately, it should be clear that in the proximity of walls, it makes a significant difference whether an object moves at Reynolds number $Re_P \approx O(10^{-1})$ or $Re_P \approx O(10^{-2})$. The widespread assumption that particle dynamics behave purely linearly for $Re_P \lessapprox 0.1$ is demonstrably invalid in the presence of boundaries. The observed nonlinearities and instabilities - particularly those seen in rod sedimentation - clearly contradict this assumption. To accurately characterize forces such as elastohydrodynamic interactions at low Reynolds numbers in future studies, it is essential to deepen our understanding of overarching influences, especially memory effects, and to incorporate them more prominently into dynamic modeling frameworks.

A Appendix

A.1 Supplementary information

§1 Experimental setup and materials

Fig. A.1 *(a)* shows a photograph of the experimental setup in our laboratory. The container, the collimated light panel and a mounting rail with the DSLR camera were fixed and positioned on an optics breadboard. The camera and the container are aligned against each other and the camera is focused in such a way that the object falls within the optical plane. 3D effects, *i.e.* movement out of the plane, are thus minimized. If these occur for other reasons during the experiment, *e.g.* due to air bubbles detaching from the sphere, this can be determined during the evaluation, see also Fig. A.5 in §2.

Fig. A.1 *(b)* clearly shows that the plane glass wall, against which the wall distance d was measured, had no appreciable inclination. The inclination of the plane wall over the entire container height was less than $\varepsilon \lessapprox 0.2^{\circ}$.

Fig. A.2 shows density measurements of remaining parts of the 1:5 mixture soft layer, which were immersed in silicone oil for several days.

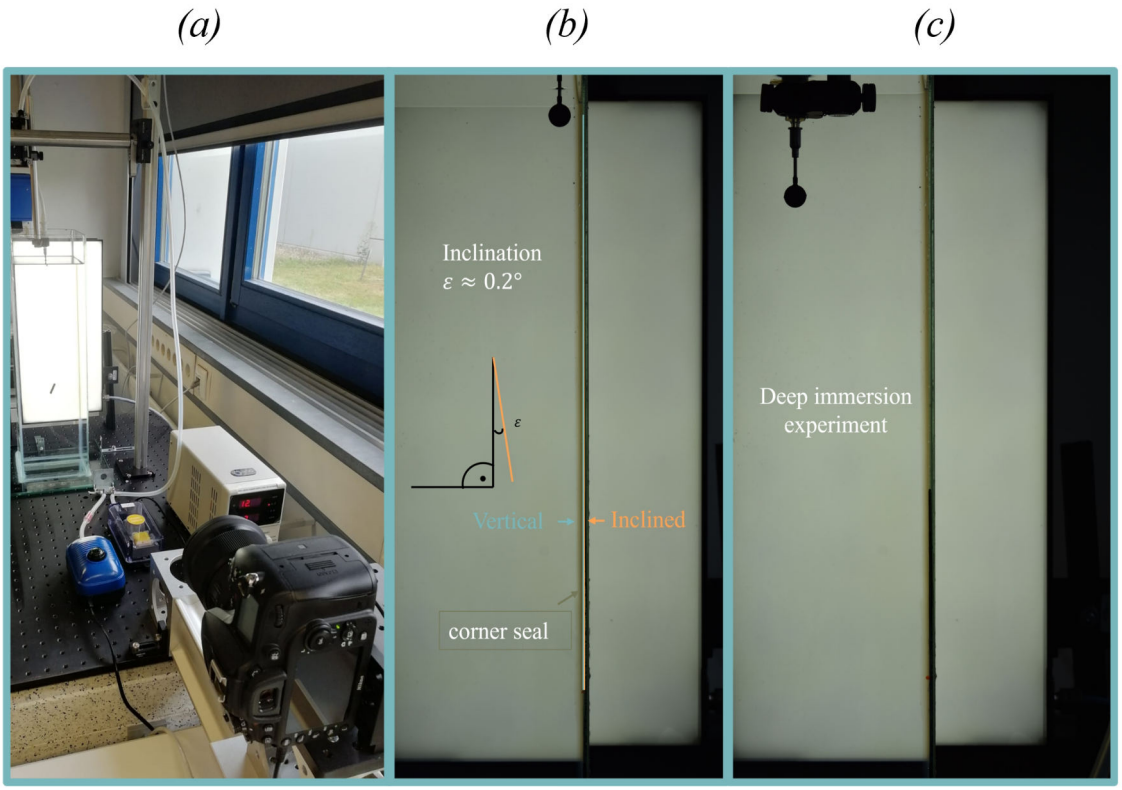


Figure A.1: *(a)* Photograph of the experimental setup; *(b)* Start image of a near-wall experiment; *(c)* Start image of the deep immersion experiment.

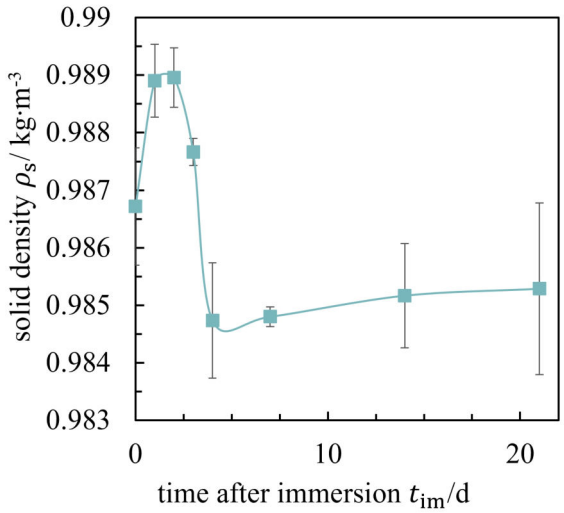


Figure A.2: Measurement data of the solid density of the 1:5 PDMS mixture depending on time after immersion into silicone oil.

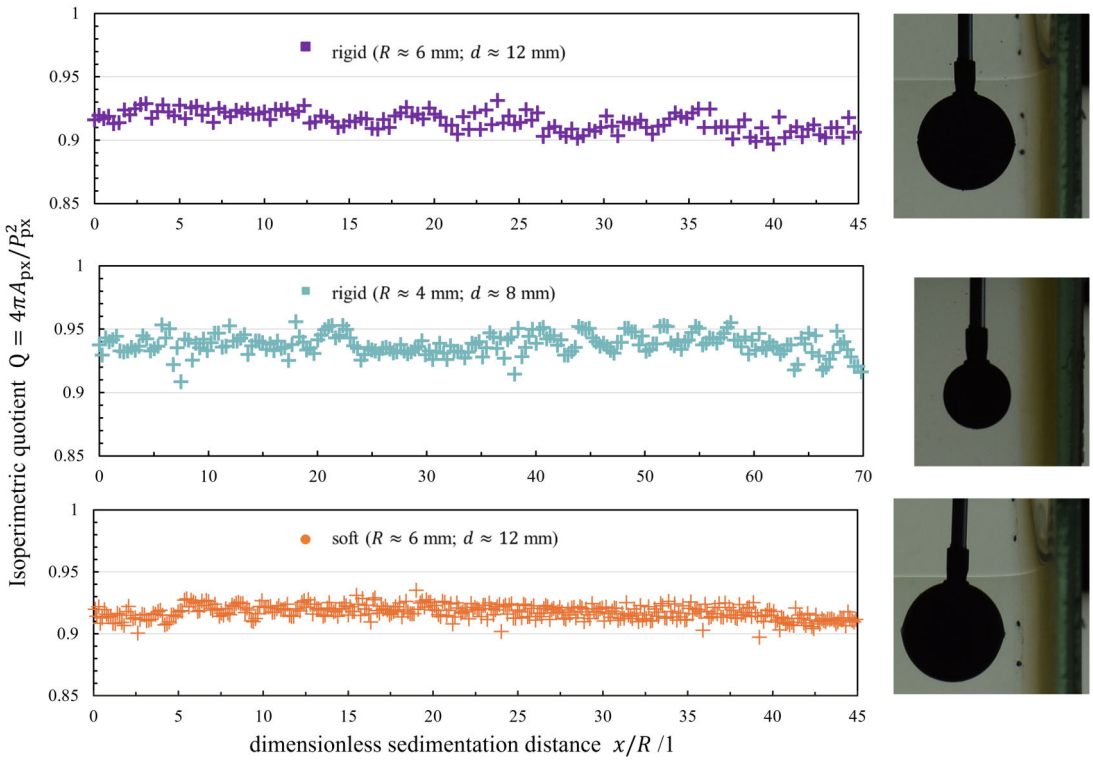


Figure A.3: Isoperimetric quotient Q as a function of the dimensionless sedimentation distance x/R of the experiments corresponding to Fig. 3.4. Top: rigid sphere (epoxy resin) in the near-wall region $d/R \approx 2$; Middle: rigid sphere (polystyrene) in the near-wall region $d/R \approx 2$; Bottom. soft sphere (PDMS 1:5 mixture) in the near-wall region $d/R \approx 2$.

§2 Optical resolution and shape analysis

As a measure for the shape of spherical objects, the parameter of circularity, or the isoperimetric quotient Q, respectively, was employed. Q can be easily computed with MATAB with the functions `bwboundaries(bw,'noholes')` and `regionprops(L,'Area','Centroid')`. The circularity is defined as $Q = 4\pi A_{px}/P_{px}^2$, where A is the area of the projected disc and P is the perimeter of the disc. The Circularity during experiments was always approximately 0.9 for the spheres used in our experiments (a perfect sphere would correspond to a value of 1), see Fig. A.3.

As exemplary shown in the circularity diagrams, the values of the circularity vary within a certain range. No clear correlation between the circularity over time/the sedimentation distance and the observed instationarities in sedimentation velocity could be observed. This implies, that there are no large, measurable deformations or shape deviations, *e.g.* into a prolate spheroid. It is assumed, that deformations (which are assumed to be small, as characterized by the parameter $\alpha = U\eta G^{-1}R^{-1} \ll 1$) only take place on the surface of the object, *i.e.* in the contour area of our video images. However, the recorded contour of the spheres during the experiments is blurry, *cf.* the comparison between the start image and the video image of the pipette in Fig. A.4 or of a sphere in Fig. A.5. As a consequence, small deviations of the perimeter of the disc, *e.g.*

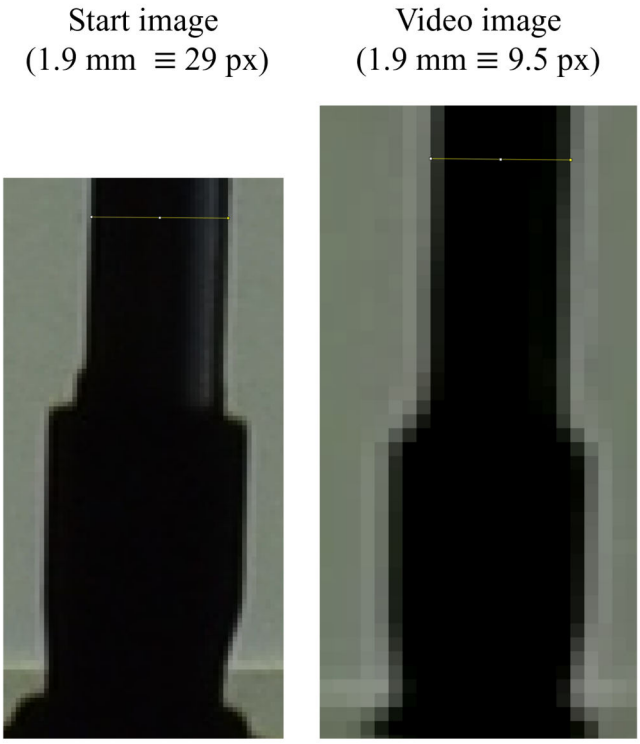


Figure A.4: Optical resolution and scaling parameters from pixel to real length in a start image (left) and an extracted video image (right). Yellow lines: distance lines to measure the thickness of the pipette tube in pixels. The thickness of the tube measured with a caliper was 1.9 mm.

due to deformations, can not be evaluated accurately, *i.e. resolving small deformations* is not possible with our optical resolution.

Nevertheless, MATLAB can determine reliably the centroid and the radius (even if the contour is less sharp). Fitting circles onto the discs to determine the radius of the sphere in the start image and the radius in the video images delivers comparable results. Scaling via the radius is performed by measuring the thickness of the pipette with a draggable distance line in the start image of each experiment and calculating the scaling factor. An exemplary distance measurement (yellow distance lines) for scaling in a start image and in a less sharp video image is shown in Fig. A.4.

The real-length resolution of the kinematical measurements (*i.e.* the accuracy of centroid tracking) was also calculated with the known distance of the pipette tube thickness in the less sharp video image. The displacement of the centroid can be resolved in the range of 3,5% of the sphere´s radius (corresponding also to the size of a pixel in the video images). We checked whether the measurement technique and the scaling works by measuring the radii and lengths of different objects, such as spheres and cylinders, twice. The relevant dimensions were measured with an external measuring method, a measuring caliper and internally with

the optical measuring technique of the evaluation program. A mean deviation of 4.5% for large distances was determined between the optical method and measurements with a caliper. The radii and corresponding lengths were corrected for this error. It should be noted, that this error has no influence on, *e.g.* the dimensionless sedimentation distance shown on the abscissa in the diagrams. The dimensionless distances are the dimensionless values calculated internally from pixel values (coordinate of the centroid (pixel) in relation to the disc radius (pixel)). The values on the abscissa of the respective diagrams therefore do not distort the appearance of the curve. Thus, the kinematic curves, such as the dimensionless trajectories, are qualitatively independent of the scaling method.

Fig. A.5 *(a)* shows the start image and a video image during the experiment of the softest sphere (specimen *A2_1*), which is shown in the results section. Fig. A.5 *(b)* and *(c)* illustrate the principle of contour line plotting at various sedimentation distances.

As discussed before, the optical resolution in the start image (left in Fig. A.5 *(a)*) is higher than in the video image (right). The ridges caused by bonding two hemisphere together should best be assessed in the high resolution image. As the high-resolution image shows, the ridges are small. However, in the lower-resolution image, they are blurred, partly due to the movement, and therefore appear larger.

Lower resolution during video recording and the blurring caused by the movement also affects the detection of the contour line, which has already been discussed in the context of the isoperimetric quotient. The detected contour line shows artifacts and appears wavy or jagged, respectively, *cf.* Fig. A.5 *(c)*. However, the contour lines can be used to assess that no large-scale deformations or overall deformation of the sphere (for example into a prolate spheroid) occur. In addition, a superposition of the contour lines at different sedimentation positions can be used to assess 3D effects, *cf.* Fig.A.5 *(c)*) and Fig. A.6.

In the superposition, rotation of the sphere becomes visible if the ridges change the position. Without ridges, rotation is not visible and cannot be evaluated. In the special case of sphere specimen *A2_1*, it can be seen that the sphere only rotates by approx. 5 ˚ over the entire sedimentation distance. It is assumed, that this low rotation and the resulting small angular velocity have no significant influence on the dynamics. The low rotation is probably induced by presence of the ridges in this specific experiment. It should be emphasized that in most experiments no rotation was observed at all, *i.e.* the bonding line (the equator line of the two hemispheres) was always perpendicular to the direction of fall.

The superposition shown in Fig. A.6 illustrates the difference between a valid experiment and a failed experiment. In a valid experiment (left), the contour lines lay almost perfectly on top of each other. In contrast, if 3D effects or rotation play a role, *e.g.* induced by detaching bubbles, the contour lines scatter and the perimeter varies (contour line plot on the right).

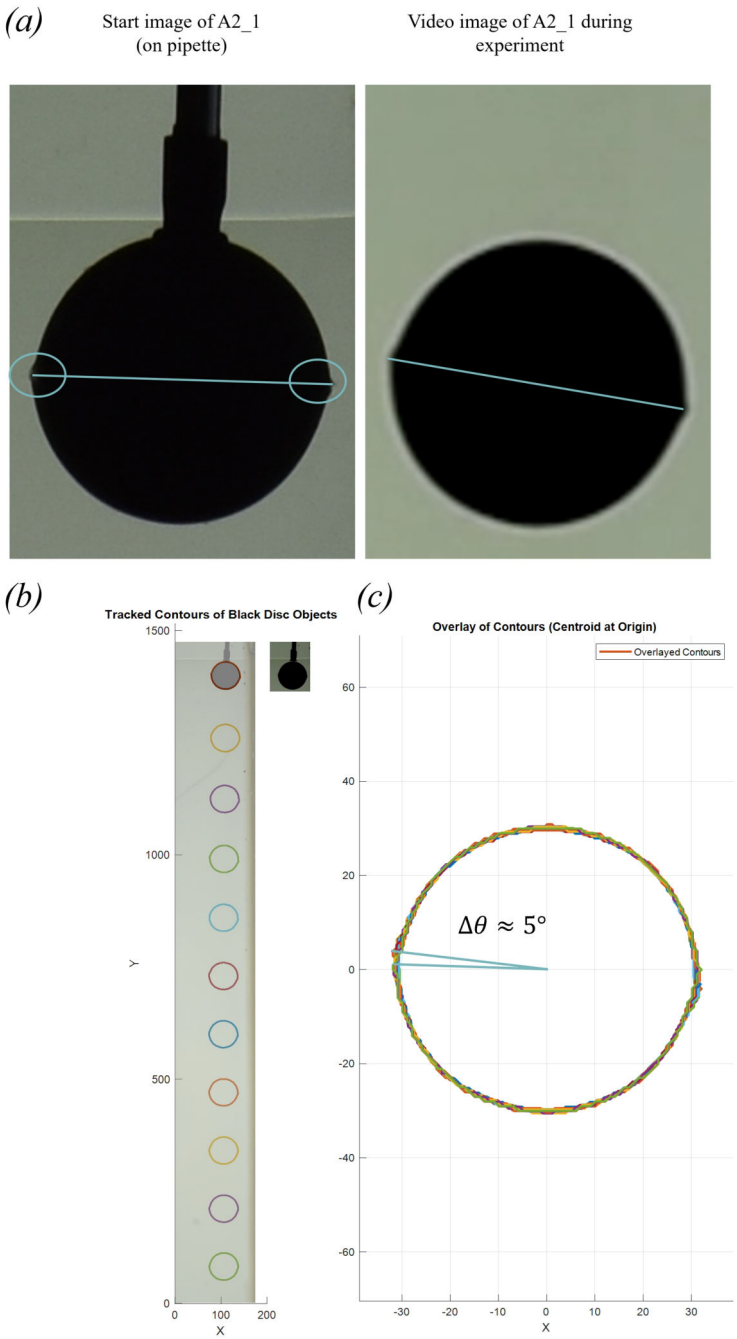


Figure A.5: *(a)* Left: high resolution start image of the sphere (specimen *A2_1*, which is shown in the results section as exemplary sphere specimen); Right: video image with lower optical resolution of specimen *A2_1* during the experiment. Blue lines: illustration of the bonding line; *(b)* perimeter and contour line detection during the experiment at several sedimentation positions; *(c)* contour line plots shown in *(b)* which are superimposed at the pixel centroid position.

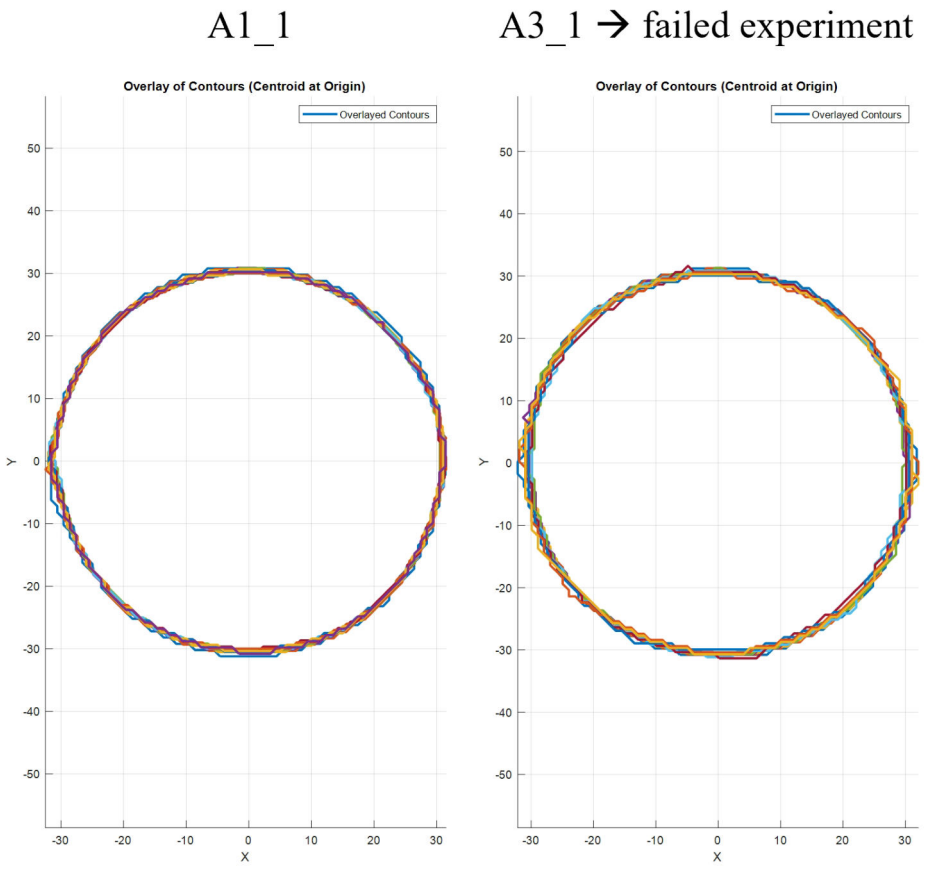


Figure A.6: Evaluation of 3D effects shown on two exemplary specimens. Left: Contour line plot of sphere ”Mix 1:5 *A1_1*” in a valid experiment; Right: Contour line plot of sphere ”Mix 1:5 *A3_1*” in a failed experiment (air bubble detached during the experiment).

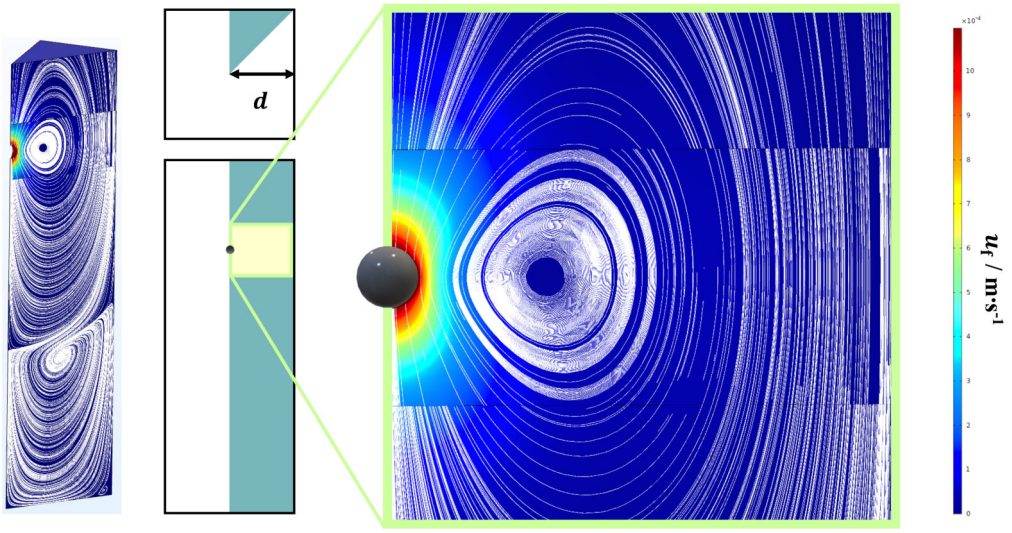


Figure A.7: 3D simulation results of a sedimenting sphere in the center of a rectangular duct (magnitude of fluid velocity as contour plot and streamlines on the diagonal plane between the sphere and the corner of the duct). The distance from sphere center to the wall was set to d = 70 mm.

A sharp detection of the contour and resolution of small deformations during the experiments would be possible for the given sphere diameter of 12 mm only with limitations. The optical settings would have to be changed, *e.g.*, by using a larger camera sensor, by shortening the distance between the camera and the container or by using a macro-lens. However, this would reduce the field of view/the measurement range (or one has to move the camera downwards with the object, which makes the experiment much more challenging). The effort required to control camera displacement and to convert distances of a tracked particle increases enormously. From our point of view, we made the best compromise between field of view and optical resolution for what we want to show - the complete trajectory/dynamics during sedimentation.

§3 CFD Simulations

In the middle of Fig. A.7 the simulated fluid domain (one eighth of the container volume) is shown schematically. A 3D plot of the whole simulated domain is shown on the left and a detail of the post-processed velocity contour plot on a plane through the duct center is shown on the right of Fig. A.7.

§4 Results

Fig, A.8 shows the (normalized) dimensionsless particle velocity plotted against the dimensionless sedimentation distance and the trajectories of spheres with varying Young's elastic modulus sedimenting from rest in the center of the duct, cf. Chapter 2.

Fig. A.9 shows absolute values of a measurement series of the softest spheres with a Young´s elastic

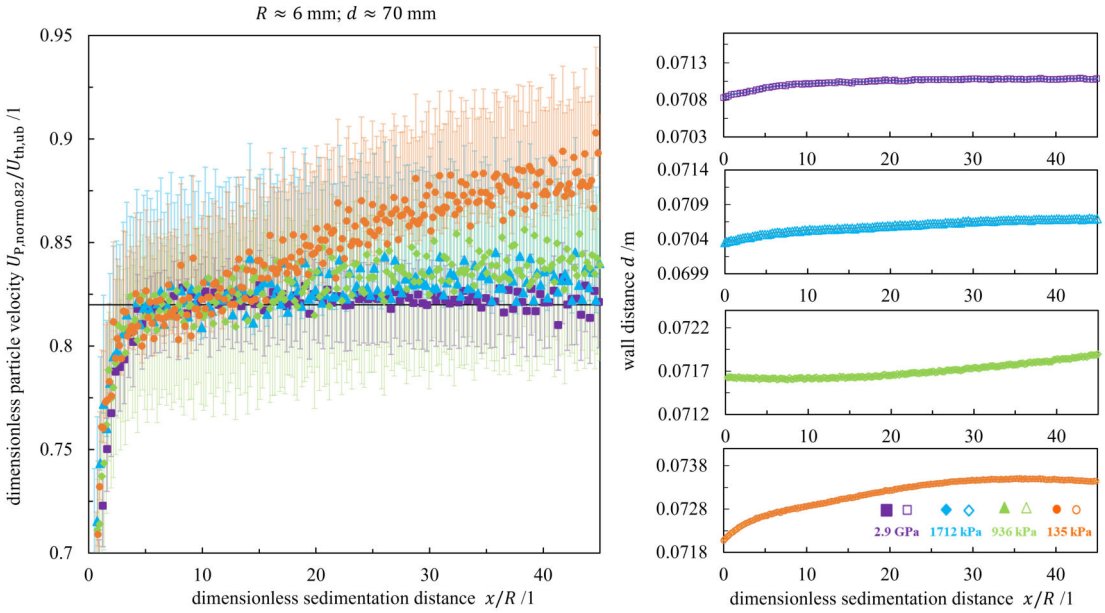


Figure A.8: Left: dimensionless particle velocity $U_P/U_{th,ub}$ plotted over the dimensionless sedimentation distance x/R of sedimenting rigid and soft spheres with a radius of $R \approx 6$ mm in the vicinity of a plane, rigid wall. The spheres start from an initial dimensionless wall distance of $d/R \approx 11.7$; Right: corresponding trajectories as $(x/R) - (d/R)$-plot.

modulus of $E \approx 135$ kPa. Furthermore, absolute values of simulation 2 discussed in Sec. 3.5.1.3 are plotted in the diagram.

In addition to *valid* experiments, the diagram also shows experiments that were classified as *invalid* (*e.g.* experiment *A3_1*, *i.e.* first experiment with specimen *A3*). Here, as already discussed, an air bubble detached during sedimentation, causing the sphere to rotate and move out of the plane. As can be seen in the absolute values, the imposed rotation also increased the sedimentation velocity. In the second, valid experiment performed with this specimen (*A3_2*), the measured velocity was smaller and comparable with others.

The experiment discussed in Sec. 3.5.1.2 is *A2_1*. As can be seen, the results are qualitatively and quantitatively comparable with other experiments.

Fig. A.10 shows the dimensionless particle velocity $U_P/U_{th,ub}$ plotted over the dimensionless sedimentation distance x/R of a large rigid sphere with $R \approx 6$ mm starting from an initial wall distance of $d/R \approx 1.5$ and corresponding trajectory ($(x/R) - (d/R)$-plot).

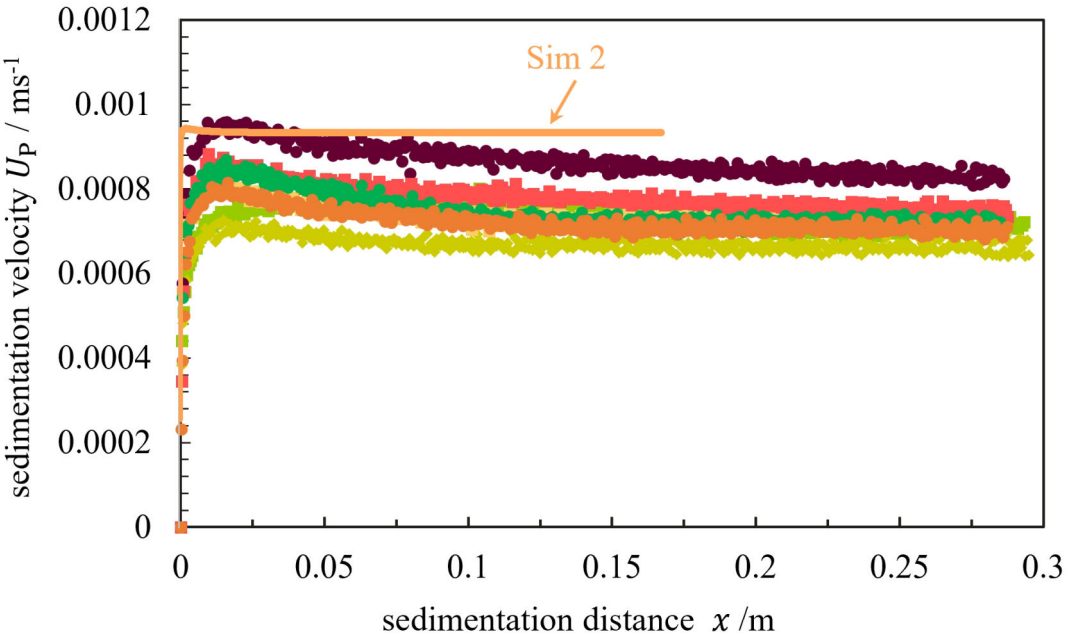


Figure A.9: Experimentally measured absolute particle velocity U_P plotted over the sedimentation distance x of sedimenting soft spheres with a Young´s elastic modulus of $E \approx 135$ kPa and with a radius of $R \approx 6$ mm in the vicinity of a plane, rigid wall. The spheres start from an initial dimensionless wall distance of $d/R \approx 4$. Absolute values of the simulated velocity (simulation 2) is plotted for comparison.

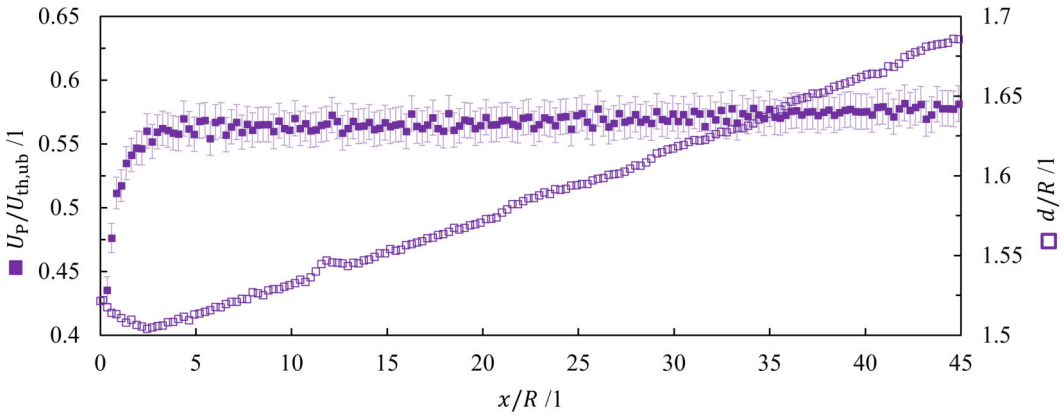


Figure A.10: Dimensionless particle velocity $U_P/U_{th,ub}$ plotted over the dimensionless sedimentation distance x/R of a large rigid sphere with $R \approx 6$ mm starting from an initial wall distance of $d/R \approx 1.5$ and corresponding trajectory ($(x/R) - (d/R)$-plot).

A.2 Programming and Codes

A.2.1 MATLAB object tracking application

A MATLAB® application with graphical user interface (GUI) for particle tracking velocimetry (PTV) was programmed with MATLAB´s internal App designer.

A.2.1.1 App code

The app code was exported to the .m file format, which is shown below.
Notes:

ObjectTrakking_spheres_rods_4 is the file name of the app. The app needs additional external functions in the .m file format, see subsection A.2.1.2.

That application needs video files in the .mov file format. Videos of spheres have to be named ”Kugel_*sample name*.mov” and videos of rods have to be named ”Stab_*sample name.mov*” or ”Zylinder_*sample name*.mov”, respectively. In the same directory where the .mov video file is saved, an additional high resolution image in the .jpg format captured before starting the experiment has to be saved with the file name ”Start_Kugel_*sample name*.jpg” (”Start_Stab_*sample name*.jpg” or ”Start_Zylinder_*sample name*.jpg”).
The code is shown without spaces. Code that is specific to Matlab app programming has been shortened. The complete code for creating the app is stored centrally.

A

```
classdef ObjectTrakking_spheres_rods_4_exported < matlab.apps.AppBase

    % Properties that correspond to app components
    properties (Access = public)
                UIFigure                        matlab.ui.Figure
                Menu                            matlab.ui.container.
                    Menu
                %...
    end
    % Properties that correspond to apps with auto-reflow
    properties (Access = private)
        onePanelWidth = 576;
        twoPanelWidth = 768;
    end
    properties (Access = private)
        FileName
        Folder
        %...
    end
    methods (Access = private)
        function GetFirstLastFrame(app,FramesBefore,FramesAfter)
            First = FramesBefore*app.EveryFrameEditField.Value;
            Last = FramesAfter*app.EveryFrameEditField.Value;
            img = imcomplement(app.Frames.Cropped_BW.(join(['Frame_',
                string(app.Frames.Count(1))],'')));
            img = bwareaopen(img,00);
            s = regionprops(img,'centroid','area','orientation');
            Area = s.Area;
            count = 0;
            cla(app.UIAxes,"reset")
            app.UIAxes.YLim = [-1 1];
            xlabel(app.UIAxes,"Frame Number / 1");
            ylabel(app.UIAxes,"Change of Area / %");
            hold(app.UIAxes,"on")
            for i = app.Frames.Count(2):app.Frames.Count(3)-app.Frames.
                Count(2):app.Frames.Count(end)
                s = regionprops(imcomplement(app.Frames.Cropped_BW.(
                    join(['Frame_',string(i)],''))),'centroid','area','
                    orientation');
                Area2 = s.Area;
                perc = abs(Area2 - Area)/Area;
                if abs(perc)>app.VidCutSensitivity
                    count = count + 1;
                    if count <= 2
                        plot(app.UIAxes,[i, i],[-1, 1],'LineWidth',4,"
                            Color",'r')
                        if count == 1
                            Im_BW_3D = Cropped_BW_3D(app,(i+First));
                            app.Image_FirstFrame.ImageSource =
                                insertText(double(Im_BW_3D),[0 size(
                                Im_BW_3D,1)/2],...
                                join(['First Frame = ',string(i+First)
                                    ],''),...
                                "FontSize",100,'BoxColor','white');
                            app.FirstFrame = i+First;
```

```
                else
                    Im_BW_3D = Cropped_BW_3D(app,(i+Last));
                    app.Image_LastFrame.ImageSource =
                        insertText(double(Im_BW_3D),[0 size(
                        Im_BW_3D,1)/2],...
                         join(['Last Frame = ',string(i+Last)],'
                             '),...
                         "FontSize",100,'BoxColor','white');
                    app.LastFrame = i+Last;
                end
            end
        end
        Area = Area2;
        numframes = (app.LastFrame - app.FirstFrame)/app.
            EveryFrameEditField.Value + 1;
        app.SaveButton.Text = join(["Save ",string(numframes),
            " frames from ",string(app.FirstFrame)," to ",
            string(app.LastFrame)],'');
        plot(app.UIAxes,i,perc,'LineStyle',"none",'Marker'
            ,"*","MarkerEdgeColor",'k')
    end
end
function Im_BW_3D = Cropped_BW_3D(app,FrameNumber)
    Im_BW_3D(:,:,1) = app.Frames.Cropped_BW.(join(['Frame_',
        string(FrameNumber)],''));
    Im_BW_3D(:,:,2) = app.Frames.Cropped_BW.(join(['Frame_',
        string(FrameNumber)],''));
    Im_BW_3D(:,:,3) = app.Frames.Cropped_BW.(join(['Frame_',
        string(FrameNumber)],''));
    Im_BW_3D = double(Im_BW_3D);
end
function BW_Binarize(app)
    for i = app.Frames.Count
        app.Frames.Cropped_BW.(join(['Frame_',string(i)],'')) =
            ...
            im2bw(app.Frames.Cropped.(join(['Frame_',string(i)
                ],'')),app.BW_Level);
    end
    Im_BW_3D = Cropped_BW_3D(app,app.Frames.Count(1));
    app.Image_Copped_BW.ImageSource = Im_BW_3D;
end
function RegionPropFunc(app)
    if contains(app.Video.Name,'Kugel') == 1
        app.TerminalStokesVelocity = (2 * app.Result.
            SphereRadiusReal.^2 * 9.81 * (app.
            soliddensitykgm3EditField.Value - app.
            fluiddensitykgm3EditField.Value))/(9 * app.
            fluidviscosityPasEditField.Value);
        app.DimlessTimeFaktor_B = 9 * app.
            fluidviscosityPasEditField.Value / (app.Result.
            SphereRadiusReal.^2 * (2 * app.
            soliddensitykgm3EditField.Value + app.
            fluiddensitykgm3EditField.Value));
        j = 0;
        app.Result.RegionProperties = table;
```

```
for i = app.FirstFrame:app.EveryFrameEditField.Value:
    app.LastFrame
    j = j +1;
    Im = imcomplement(app.Frames.Cropped_BW.(join(['
        Frame_',string(i)],'')));
    stats = regionprops("table",Im,"Area","Centroid","
        Orientation");
    Idx = find(max(stats.Area)==stats.Area);
    Cent(j,:) = stats.Centroid(Idx,:);
    Ori(j,:) = stats.Orientation(Idx,:);
    WallDist(j,:) = size(app.Frames.Cropped_BW.(join(['
        Frame_',string(app.FirstFrame)],'')),1)-Cent(j
        ,2);
    app.Result.RegionProperties.Frame(j) = i;
    app.Result.RegionProperties.Time(j) = (app.Result.
        RegionProperties.Frame(j)-app.FirstFrame)/app.
        Video.FrameRate;
    app.Result.RegionProperties.DimlessTime_B(j) = app.
        Result.RegionProperties.Time(j) * app.
        DimlessTimeFaktor_B;
    app.Result.RegionProperties.Metric(j) =
        MeasureCircularity(app,app.Frames.Cropped_BW.(
        join(['Frame_',string(i)],'')));
end
[~,radii] = imfindcircles((app.Frames.Cropped.(join(['
    Frame_',string(app.FirstFrame)],''))),[10 100],'
    ObjectPolarity','dark','Sensitivity',0.85);
XVelo(1,:) = 0;
YVelo(1,:) = 0;
TimeStep = app.Result.RegionProperties.Time(2);
for i = 2:length(app.Result.RegionProperties.Frame)
    XVelo(i,:) = abs(Cent(i,1) - Cent(i-1,1))/(radii*
        TimeStep);
    YVelo(i,:) = abs(Cent(i,2) - Cent(i-1,2))/(radii*
        TimeStep);
end
app.Result.SphereRadiusPixel = radii;
app.Result.RegionProperties.XPositionPixel = (Cent(1,1)
    -Cent(:,1))/radii;
app.Result.RegionProperties.YPositionPixel = (Cent(1,2)
    -Cent(:,2))/radii;
app.Result.RegionProperties.XVelocityPixel = XVelo;
app.Result.RegionProperties.YVelocityPixel = YVelo;
app.Result.RegionProperties.VelocityMagnitudePixel =
    sqrt(app.Result.RegionProperties.XVelocityPixel.^2+
    app.Result.RegionProperties.YVelocityPixel.^2);
app.Result.RegionProperties.WallDistance = WallDist/
    radii;
app.Result.RegionProperties.Orientation = Ori;
app.Result.RegionProperties.XPositionReal = app.Result.
    RegionProperties.XPositionPixel * app.Result.
    SphereRadiusReal;
app.Result.RegionProperties.YPositionReal = app.Result.
    RegionProperties.YPositionPixel * app.Result.
    SphereRadiusReal;
```

```
        app.Result.RegionProperties.WallDistanceReal = app.
            Result.RegionProperties.WallDistance * app.Result.
            SphereRadiusReal;
        app.Result.RegionProperties.XVelocityReal = app.Result.
            RegionProperties.XVelocityPixel * app.Result.
            SphereRadiusReal;
        app.Result.RegionProperties.YVelocityReal = app.Result.
            RegionProperties.YVelocityPixel * app.Result.
            SphereRadiusReal;
        app.Result.RegionProperties.VelocityMagnitudeReal =
            sqrt(app.Result.RegionProperties.XVelocityReal.^2+
            app.Result.RegionProperties.YVelocityReal.^2);
        app.Result.RegionProperties.DimlessVelocity = app.
            Result.RegionProperties.XVelocityReal / app.
            TerminalStokesVelocity;
        Items = string(fieldnames(app.Result.RegionProperties))
            ;
        app.XAxisDropDown.Items = Items(1:end-3);
        app.YAxisDropDown.Items = Items(1:end-3);
        app.XAxisDropDown.Value = app.XAxisDropDown.Items(3);
        app.YAxisDropDown.Value = app.YAxisDropDown.Items(17);
        app.ReynoldsNumber = mean(app.Result.RegionProperties.
            XVelocityReal(end-5:end) * 2 * app.Result.
            SphereRadiusReal * app.fluiddensitykgm3EditField.
            Value / app.fluidviscosityPasEditField.Value);
        app.Result.ReynoldsNumber = app.ReynoldsNumber;
        app.Result.TerminalStokesVelocity = app.
            TerminalStokesVelocity;
        app.Result.FluidViscosity = app.
            fluidviscosityPasEditField.Value;
        app.Result.SolidDensity = app.soliddensitykgm3EditField
            .Value;
        app.Result.FluidDensity = app.fluiddensitykgm3EditField
            .Value;
    elseif contains(app.Video.Name,'Stab') == 1
        j = 0;
        app.Result.RegionProperties = table;
        for i = app.FirstFrame:app.EveryFrameEditField.Value:
            app.LastFrame
            j = j +1;
            Im = imcomplement(app.Frames.Cropped_BW.(join(['
                Frame_',string(i)],'')));
            stats = regionprops("table",Im,"Area","Centroid","
                Orientation");
            Idx = find(max(stats.Area)==stats.Area);
            Cent(j,:) = stats.Centroid(Idx,:);
            Ori(j,:) = stats.Orientation(Idx,:);
            PxArea(j,:) = stats.Area(Idx,:);
            WallDist(j,:) = size(app.Frames.Cropped_BW.(join(['
                Frame_',string(app.FirstFrame)],'')),1)-Cent(j
                ,2);
            app.Result.RegionProperties.Frame(j) = i;
            app.Result.RegionProperties.Time(j) = (app.Result.
                RegionProperties.Frame(j)-app.FirstFrame)/app.
                Video.FrameRate;
        end
```

```
FirstFrameImage = imcomplement(app.Frames.Cropped_BW.(
    join(['Frame_',string(app.FirstFrame)],'')));
AreaStats = regionprops(FirstFrameImage,'Area');
FirstFrameStats = struct2table(regionprops(
    FirstFrameImage,'MaxFeretProperties'));
FirstFrameStats2 = struct2table(regionprops(
    FirstFrameImage,'MinFeretProperties'));
maxferetdiameters = table2array(FirstFrameStats(:,1));
minferetdiameters = table2array(FirstFrameStats2(:,1));
rod_diagonal = max(maxferetdiameters);
rod_diameter = max(minferetdiameters);
rodlength = sqrt(((rod_diagonal^2)-(rod_diameter^2)));
half_rodlength = rodlength/2;
RealHalfRodlength = app.Result.RodLengthReal/2;
XVelo(1,:) = 0;
YVelo(1,:) = 0;
TimeStep = app.Result.RegionProperties.Time(2);
for i = 2:length(app.Result.RegionProperties.Frame)
     XVelo(i,:) = abs(Cent(i,1) - Cent(i-1,1))/(
         half_rodlength*TimeStep);
     YVelo(i,:) = abs(Cent(i,2) - Cent(i-1,2))/(
         half_rodlength*TimeStep);
end
app.Result.RodLengthPixel = rodlength;
app.Result.RegionProperties.XPositionPixel = (Cent(1,1)
    -Cent(:,1))/half_rodlength;
app.Result.RegionProperties.YPositionPixel = (Cent(1,2)
    -Cent(:,2))/half_rodlength;
app.Result.RegionProperties.XVelocityPixel = XVelo;
app.Result.RegionProperties.YVelocityPixel = YVelo;
app.Result.RegionProperties.VelocityMagnitudePixel =
    sqrt(app.Result.RegionProperties.XVelocityPixel.^2+
    app.Result.RegionProperties.YVelocityPixel.^2);
app.Result.RegionProperties.WallDistance = WallDist/
    half_rodlength;
app.Result.RegionProperties.Orientation = Ori;
app.Result.RegionProperties.PixelArea = PxArea;
app.Result.RegionProperties.XPositionReal = app.Result.
    RegionProperties.XPositionPixel * RealHalfRodlength
     ;
app.Result.RegionProperties.YPositionReal = app.Result.
    RegionProperties.YPositionPixel * RealHalfRodlength
    ;
app.Result.RegionProperties.WallDistanceReal = app.
    Result.RegionProperties.WallDistance *
    RealHalfRodlength;
app.Result.RegionProperties.XVelocityReal = app.Result.
    RegionProperties.XVelocityPixel * RealHalfRodlength
    ;
app.Result.RegionProperties.YVelocityReal = app.Result.
    RegionProperties.YVelocityPixel* RealHalfRodlength;
     %
app.Result.RegionProperties.VelocityMagnitudeReal =
    sqrt(app.Result.RegionProperties.XVelocityReal.^2+
    app.Result.RegionProperties.YVelocityReal.^2);
```

```
            Items = string(fieldnames(app.Result.RegionProperties))
                ;
            app.XAxisDropDown.Items = Items(1:end-3);
            app.YAxisDropDown.Items = Items(1:end-3);
            app.XAxisDropDown.Value = app.XAxisDropDown.Items(3);
            app.YAxisDropDown.Value = app.YAxisDropDown.Items(15);
            app.ReynoldsNumber = mean(app.Result.RegionProperties.
                XVelocityReal(end-4:end) * app.Result.RodLengthReal
                 * app.fluiddensitykgm3EditField.Value / app.
                fluidviscosityPasEditField.Value);
            app.Result.ReynoldsNumber = app.ReynoldsNumber;
            app.Result.TerminalStokesVelocity = app.
                TerminalStokesVelocity;
            app.Result.FluidViscosity = app.
                fluidviscosityPasEditField.Value;
            app.Result.SolidDensity = app.soliddensitykgm3EditField
                .Value;
            app.Result.FluidDensity = app.fluiddensitykgm3EditField
                .Value;
        elseif contains(app.Video.Name,'Zylinder') == 1
                    %cf. 'Stab'
        else
        end
    end
    function RadiusMeasurement(app)
        assignin("base","test",app.Video)
        Img = imread(join([app.Video.Path,'\Start_',app.Video.Name
            (1:end-4),'.jpg'],''));
        imshow(Img)
        title('Select corners for the image crop for length
            measurements (click bottom left, then top right corner
            of desired crop)')
        fig = gcf;
        Continue = 0;
        while Continue == 0
            [xkante,ykante] = ginput(2);
            rec = rectangle('Position',[xkante(1) ykante(2) xkante
                (2)-xkante(1) ykante(1)-ykante(2)],...
                'LineStyle',"--","LineWidth",4,"EdgeColor",'r');
            answer = questdlg('Is this the correct crop?','','Yes',
                'No','Yes');
            switch answer
                case 'Yes'
                    Continue = 1;
                    delete(fig)
                case 'No'
                    Continue = 0;
                    delete(rec)
            end
        end
        Img_crop = imcrop(Img,[xkante(1) ykante(2) xkante(2)-xkante
            (1) ykante(1)-ykante(2)]);
        if contains(app.Video.Name,'Kugel') == 1
            sensi = 0.2;
            centers = [];
```

```
        wb = uiprogressdlg(app.UIFigure,'Title','Finding
            circles',"Indeterminate","on");
        while isempty(centers) == 1
            [centers,radii] = imfindcircles(Img_crop,[25 150],'
                ObjectPolarity','dark','Sensitivity',sensi);
            sensi = sensi + 0.01;
        end
        delete(wb)
        fig = figure;
        fig.Name = join(['Start_',app.Video.Name(1:end-4),'.jpg
            '],'');
        hold all
        imshow(Img_crop);
        fig.WindowState = 'maximized';
        viscircles(centers,radii);
        [xkante,ykante] = ginput(2);
        imdistline(gca,[xkante(1) xkante(2)],[ykante(1) ykante
            (2)]);
        set(fig,'CloseRequestFcn',@closeRequest_1)
        waitfor(fig)
        distance = evalin("base",'Noz_Diam'); %1.9 = length of
            nozzle in mm, 0.045 onwards = error correction
        MeasureReal = (radii / distance * 1.9 / 1000)-0.045*(
            radii / distance * 1.9 / 1000);
        MeasureReal_mm = MeasureReal*1000;
        app.RodSpherehasmetersLabel.Text = join(["Sphere has a
            radius of ",string(MeasureReal_mm)," mm"],'');
        app.Result.SphereRadiusReal = MeasureReal;
    elseif contains(app.Video.Name,'Stab') == 1
        fig = figure;
        fig.Name = join(['Start_',app.Video.Name(1:end-4),'.jpg
            '],'');
        imshow(Img_crop);
        hold on
        title('Select two Points each to calculate Rod length (
            first), diameter (second), then nozzle diameter (
            third)')
        fig.WindowState = 'maximized';
        [xkante, ykante] = ginput(6);
        h1 = imdistline(gca,[xkante(5) xkante(6)],[ykante(5)
            ykante(6)]);
        h2 = imdistline(gca,[xkante(3) xkante(4)],[ykante(3)
            ykante(4)]);
        h3 = imdistline(gca,[xkante(1) xkante(2)],[ykante(1)
            ykante(2)]);
        set(fig,'CloseRequestFcn',@closeRequest_2)
        waitfor(fig)
        distance = evalin("base",'Noz_Diam');
        length = evalin("base",'Length');
        diameter = evalin("base",'Diameter');
        DiameterReal = (diameter / distance * 1.9 / 1000)
            -0.045*(diameter / distance * 1.9 / 1000);
        DiameterReal_mm = DiameterReal*1000;
        LengthReal = (length / distance * 1.9 / 1000)-0.045*(
            length / distance * 1.9 / 1000);
        LengthReal_mm = LengthReal*1000;
```

```
            displaytext = join(["Rod diameter is ", string(
                DiameterReal_mm),"mm, length is ", string(
                LengthReal_mm),"mm"]);
            app.Result.RodDiameterReal = DiameterReal;
            app.Result.RodLengthReal = LengthReal;
            app.RodSpherehasmetersLabel.Text = displaytext ;
        elseif contains(app.Video.Name,'Zylinder') == 1
            %cf. 'Stab'
        else
        end
    end
    function PlotResult(app)
        cla(app.UIAxes2,"reset")
        hold(app.UIAxes2,"on")
        grid(app.UIAxes2,"on")
        box(app.UIAxes2,"on")
        pp = plot(app.UIAxes2,app.Result.RegionProperties.(app.
            XAxisDropDown.Value), ...
            app.Result.RegionProperties.(app.YAxisDropDown.Value),'
                LineStyle',"none","Marker","*",'DisplayName','
                Experimental');
        text(max(pp.XData)*0.5,max(pp.YData)*0.5, join(['Reynolds
            number = ',string(app.ReynoldsNumber)],''), 'Parent',
            app.UIAxes2,"FontSize",20);
        xlabel(app.UIAxes2,app.XAxisDropDown.Value)
        ylabel(app.UIAxes2,app.YAxisDropDown.Value)
        legend(app.UIAxes2,'Location',"best");
    end
end
% Callbacks that handle component events
methods (Access = private)
    % Code that executes after component creation
    function startupFcn(app)
        clc
        addpath("HelpingFunctions\")
        app.BW_Level = 0.01;
                %... Matlab App specific
    end
    % Changes arrangement of the app based on UIFigure width
    function updateAppLayout(app, event)
        currentFigureWidth = app.UIFigure.Position(3);
                %... Matlab App specific
        end
    end
    % Menu selected function: GetVideoMenu
    function GetVideoMenuSelected(app, event)
        app.FileName = [];
        app.Folder = [];
        app.Video = [];
        [app.FileName,app.Folder] = uigetfile('*.mov','Select an
            Video-file',' ',"MultiSelect","off");
        if app.FileName==0
            % user pressed cancel
            return
        else
```

```
            app.Video = VideoReader(join([app.Folder,'\',app.
                FileName],''));
            Fields = properties(app.Video);
            app.UITable.RowName = Fields;
            TableData(:,1) = string(zeros(length(Fields),1));
            for i = 1:length(Fields)
                if isempty(string(app.Video.(string(Fields(i)))))
                    == 0
                    TableData(i,1) = string(app.Video.(string(
                        Fields(i))));
                else
                    TableData(i,1) = "";
                end
            end
            app.UITable.Data = TableData;
            app.EveryFrameEditField.Value = app.Video.FrameRate;
            app.LoadVideoButton.Text = join(["Load every ",app.
                EveryFrameEditField.Value,". frame"],'');
            app.LoadVideoButton.Enable = 'on';
            app.EveryFrameEditField.Enable = 'on';
        end
        app.TabGroup.SelectedTab = app.ImagesTab;
        app.CenterPanel.Visible = 'off';
        app.RightPanel.Visible = 'off';
    end
    % Value changed function: EveryFrameEditField
    function EveryFrameEditFieldValueChanged(app, event)
        app.LoadVideoButton.Text = join(["Load every ",app.
            EveryFrameEditField.Value,". frame"],'');
    end
    % Button pushed function: LoadVideoButton
    function LoadVideoButtonPushed(app, event)
        app.Frames = [];
        app.FirstFrame = [];
        app.LastFrame = [];
        app.Result = [];
        app.Result = struct;
        app.TerminalStokesVelocity = [];
        app.ReynoldsNumber = [];
        app.DimlessTimeFaktor_B = [];
        app.Frames.Count = 1:app.EveryFrameEditField.Value:app.
            Video.NumFrames;
        for i = 1:length(app.Frames.Count)
            app.Frames.Count_2(i,1) = join(['Frame_',string(app.
                Frames.Count(i))],'');
        end
        wb = uiprogressdlg(app.UIFigure,'Title',join(['Load every '
            ,string(app.EveryFrameEditField.Value),'. frame from ',
            app.FileName],''),...
            "ShowPercentage","on","Value",0,"Cancelable","on");
        j = 0;
        for i = app.Frames.Count
            j = j + 1;
            app.Frames.Origin.(join(['Frame_',string(i)],'')) =
                read(app.Video,i);
            wb.Value = i/app.Video.NumFrames;
```

```
            if wb.CancelRequested
                delete(wb)
                return
            end
        end
        delete(wb)
        app.Image_Origin.Visible = 'on';
        app.Image_Origin.ImageSource = app.Frames.Origin.(join(['
            Frame_',string(app.Frames.Count(1))],''));
        app.CropandbinarizeFramesButton.Enable = 'on';
        app.LastFrameLabel.Text = join(["Last Frame +/- ",app.
            EveryFrameEditField.Value, " x:"],'');
        app.FirstFrameLabel.Text = join(["First Frame +/- ",app.
            EveryFrameEditField.Value, " x:"],'');
    end
    % Button pushed function: CropandbinarizeFramesButton
    function CropandbinarizeFramesButtonPushed(app, event)
        Continue = 0;
        while Continue == 0
            imshow(app.Frames.Origin.(join(['Frame_',string(app.
                Frames.Count(1))],'')));
            Img = gcf;
            [xkante,ykante] = ginput(2);
            rectangle('Position',[xkante(1) ykante(2) xkante(2)-
                xkante(1) ykante(1)-ykante(2)],'LineStyle',"--","
                LineWidth",4,"EdgeColor",'r')
            answer = questdlg('If this the correct crop?','','Yes',
                'No','Yes');
            switch answer
                case 'Yes'
                    Continue = 1;
                case 'No'
                    Continue = 0;
            end
        end
        for i = app.Frames.Count
            app.Frames.Cropped.(join(['Frame_',string(i)],'')) =
                ...
                imcrop(app.Frames.Origin.(join(['Frame_',string(i)
                    ],'')),[xkante(1) ykante(2) xkante(2)-xkante(1)
                     ykante(1)-ykante(2)]);
        end
        app.Image_Cropped.ImageSource = app.Frames.Cropped.(join(['
            Frame_',string(app.Frames.Count(1))],''));
        BW_Binarize(app)
        GetFirstLastFrame(app,app.FirstFrameSpinner.Value,app.
            LastFrameSpinner.Value)
        app.CenterPanel.Visible = 'on';
        app.RightPanel.Visible = 'on';
        close(Img)
    end
%  $------------Matlab App specific--------------$
                                                          ......
                                                          .....
                                                          .....
    % Button pushed function: SaveButton
```

```
        function SaveButtonPushed(app, event)
            Name = split(replace(string(app.FileName),'.',' '));
            if isfolder(join([app.Folder,'\',string(Name(1)),'_Frames'
                ],'')) == 1
                rmdir(join([app.Folder,'\',string(Name(1)),'_Frames'],'
                    '),"s")
            end
            mkdir(join([app.Folder,'\',string(Name(1)),'_Frames'],''))
            wb = uiprogressdlg(app.UIFigure,'Title','Save cropped
                frames',"ShowPercentage","on","Value",0);
            for i = app.FirstFrame:app.EveryFrameEditField.Value:app.
                LastFrame
                imwrite(app.Frames.Cropped.(join(['Frame_',string(i)],'
                    ')),...
                    join([app.Folder,'\',Name(1),'_Frames\','Frame_',
                        string(i),'.png'],''));
                app.Result.Cropped_BW.(join(['Frame_',string(i)],'')) =
                    app.Frames.Cropped_BW.(join(['Frame_',string(i)],'
                    '));
                wb.Value = i/app.LastFrame;
                app.Result.VideoInformation.FrameRate = app.Video.
                    FrameRate;
                app.Result.VideoInformation.FrameNumber = str2double(
                    erase(string(fieldnames(app.Result.Cropped_BW)),'
                    Frame_'));

            end
            Solution = app.Result;
            save(join([string(app.Folder),'\',string(Name(1)),"_Frames\
                Solution.mat"],''),"Solution")
            delete(wb)
%  $------------Matlab App specific--------------$
                                                                  ......
                                                                  .....
                                                                  .....
end
```

A.2.1.2 Helping functions for the tracking app

The following functions have to be saved as *FunctionName*.m files in a folder named ”HelpingFunctions”, which is saved in the same directory as the MATLAB App (.mlapp file format). Example: ”*closeRequest_1.m*”

```
_ _ _ _ _ _ _ _ _ _ _ _ _ _ _ _ _ _ _ _ _ _ _ _ _ _
```

```
 function closeRequest_1(fig,event)

fig = gcf;
ff = gca;
Name = fig.Name;
Noz_Diam = str2double(ff.Children(1).Children(1).String);

if contains(fig.Name,'Kugel') == 1
```

```
    radii = 0.5 * (max(fig.Children(3).Children(2).Children(1).XData) -
        min(fig.Children(3).Children(2).Children(1).XData));

else
end

ButtonName = questdlg(join(['Nozzle has ',string(Noz_Diam),' Pixels?
    Close window?'],''), ...
    'Close Check', ...
    'Yes', 'No','No');
switch ButtonName
    case 'Yes'
        delete(fig)
    case 'No'
        return
end

assignin('base','Noz_Diam',Noz_Diam);
% assignin('base','MeasureReal',MeasureReal);
end
```

---------- next file ----------

```
function closeRequest_2(fig,event)

fig = gcf;
ff = gca;
Name = fig.Name;
Length = str2double(ff.Children(1).Children(1).String);
Diameter = str2double(ff.Children(2).Children(1).String);
Noz_Diam = str2double(ff.Children(3).Children(1).String);

ButtonName = questdlg(join(['The measured rod length is ',string(Length
    ),...
    ', with rod diameter of ',string(Diameter),...
    ' and nozzle diameter of ',string(Noz_Diam)...
    ,' Pixels. Would you like to close the window?'],''), ...
    'Close Check', ...
    'Yes', 'No','No');
switch ButtonName
    case 'Yes'

        delete(fig)
    case 'No'
        return
end

assignin('base','Length',Length);
assignin('base','Diameter',Diameter);
assignin('base','Noz_Diam',Noz_Diam);

end
```

---------- next file ----------

```
function copyAXES_NewFigure(Source)

relevantProperties = ["Color";"LineStyle";"LineWidth";"Marker";"
    MarkerSize";"MarkerFaceColor";"MarkerEdgeColor"];

figure
Target = gca;

if length(Source.YAxis) == 1
     copyobj(Source.Children,Target);
     for i = 1:length(Source.Children)
          for j = 1:length(relevantProperties)
               if sum(strcmp(string(fieldnames(get(Source.Children(i)))),
                   relevantProperties(j))) == 1
                    Target.Children(i).(relevantProperties(j)) = Source.
                        Children(i).(relevantProperties(j));
               end
          end
     end
     ylabel(Source.YLabel.String)
end
xlabel(Source.XLabel.String)

if length(Source.YAxis) > 1
     axes = ["left";"right"];
     for g = 1:length(axes)
          yyaxis(Source,axes(g))
          yyaxis(axes(g))
          copyobj(Source.Children,Target);
          ylabel(Source.YLabel.String)

          for i = 1:length(Source.Children)
               for j = 1:length(relevantProperties)
                    if sum(strcmp(string(fieldnames(get(Source.Children(i))
                        )),relevantProperties(j))) == 1
                         Target.Children(i).(relevantProperties(j)) = Source
                             .Children(i).(relevantProperties(j));
                    end
               end
          end
     end
end

for i = 1:length(Source.YAxis)
     Target.YAxis(i).Color = Source.YAxis(i).Color;
end

grid on
box on
legend('location','best')
Target.Parent.Color = [1 1 1];
Target.View = Source.View;
end
```

---------- next file ----------

```
function Metric = MeasureCircularity(app,BW_Img)
```

```
bw = bwareaopen(imcomplement(BW_Img),100);
se = strel('disk',2);
bw = imclose(bw,se);
[B,L] = bwboundaries(bw,'noholes');
stats = regionprops(L,'Area','Centroid');
A = struct2table(stats);
A = A.Area;
k = find(max(A)==A);
% obtain (X,Y) boundary coordinates corresponding to label 'k'
boundary = B{k};

% compute a simple estimate of the object's perimeter
delta_sq = diff(boundary).^2;
perimeter = sum(sqrt(sum(delta_sq,2)));

% obtain the area calculation corresponding to label 'k'
area = stats(k).Area;

% compute the roundness metric
Metric = 4*pi*area/perimeter^2;
end
```

A

Bibliography

[1] J. C. Aurich and H. Hasse, Eds., *Component Surfaces: Manufacturing-Morphology-Property Relationships*. Springer Cham, 2023, ISBN: 978-3-031-35574-5. DOI: 10.1007/978-3-031-35575-2.

[2] J. Happel and H. Brenner, *Low Reynolds number hydrodynamics: with special applications to particulate media* (Mechanics of Fluids and Transport Processes). Springer Netherlands, 1983, ISBN: 9789024728770.

[3] A. De, *Sedimentation Process and Design of Settling Systems* (Springer Transactions in Civil and Environmental Engineering). New Delhi: Springer, 2017, ISBN: 978-81-322-3634-4.

[4] G. R. d. S. Araújo, N. B. Viana, F. Gómez, B. Pontes, and S. Frases, "The mechanical properties of microbial surfaces and biofilms", *Cell surface (Amsterdam, Netherlands)*, vol. 5, p. 100 028, 2019. DOI: 10.1016/j.tcsw.2019.100028.

[5] W. E. Dietrich, "Settling velocity of natural particles", *Water Resour. Res.*, no. 18 (6), pp. 1615–1626, 1982.

[6] P. U. Iyare, S. K. Ouki, and T. Bond, "Microplastics removal in wastewater treatment plants: A critical review", *Environmental Science: Water Research & Technology*, vol. 6, no. 10, pp. 2664–2675, 2020, ISSN: 2053-1400. DOI: 10.1039/D0EW00397B.

[7] D. Barthès-Biesel, "Motion and deformation of elastic capsules and vesicles in flow", *Annual Review of Fluid Mechanics*, vol. 48, no. 1, pp. 25–52, 2016, ISSN: 0066-4189. DOI: 10.1146/annurev-fluid-122414-034345.

[8] A. N. Balachandran Nair, S. Pirker, T. Umundum, and M. Saeedipour, "A reduced-order model for deformable particles with application in bio-microfluidics", *Comp. Part. Mech.*, no. 7, pp. 593–601, 2020. DOI: 10.1007/s40571-019-00283-8.

[9] M. M. Villone and P. L. Maffettone, "Dynamics, rheology, and applications of elastic deformable particle suspensions: A review", *Rheologica Acta*, vol. 58, pp. 109–130, 2019, ISSN: 0035-4511. DOI: 10.1007/s00397-019-01134-2.

[10] M. M. Villone, "Lateral migration of deformable particles in microfluidic channel flow of newtonian and viscoelastic media: A computational study", *Microfluidics and Nanofluidics*, vol. 23, no. 3, 2019, ISSN: 1613-4982. DOI: 10.1007/s10404-019-2212-3.

[11] M. de Corato, F. Greco, G. D'Avino, and P. L. Maffettone, "Hydrodynamics and brownian motions of a spheroid near a rigid wall", *The Journal of chemical physics*, vol. 142, no. 19, p. 194 901, 2015. DOI: 10.1063/1.4920981.

[12] T. Tohme, P. Magaud, and L. Baldas, "Transport of non-spherical particles in square microchannel flows: A review", *Micromachines*, vol. 12, no. 3, 2021, ISSN: 2072-666X. DOI: 10.3390/mi12030277.

[13] K. Patel and H. Stark, "A pair of particles in inertial microfluidics: Effect of shape, softness, and position", *Soft Matter*, vol. 17, no. 18, pp. 4804–4817, 2021. DOI: 10.1039/d1sm00276g.

[14] M. Bukowicki, M. Gruca, and M. L. Ekiel-Jeżewska, "Dynamics of elastic dumbbells sedimenting in a viscous fluid: Oscillations and hydrodynamic repulsion", *Journal of Fluid Mechanics*, vol. 767, pp. 95–108, 2015, ISSN: 0022-1120. DOI: 10.1017/jfm.2015.31.

[15] T. Murata, "On the deformation of an elastic particle falling in a viscous fluid", *Journal of the Physical Society of Japan*, no. 48 (5), 1980.

[16] S. Takeuchi, Y. Yuki, A. Ueyama, and T. Kajishima, "A conservative momentum-exchange algorithm for interaction problem between fluid and deformable particles", *International Journal for Numerical Methods in Fluids*, vol. 64, no. 10-12, pp. 1084–1101, 2010, ISSN: 02712091. DOI: 10.1002/fld.2272.

[17] Clift, R., Grace, J., & Weber, M., *Bubbles, Drops, and Particles*. New York: Acad. Press., 1978.

[18] H. A. Stone, "Dynamics of drop deformation and breakup in viscous fluids", *Annu Rev Fluid Mech.*, vol. 26, pp. 65–102, 1994.

[19] J. Tsamopoulos, Y. Dimakopoulos, N. Chatzidai, G. Karapetsas, and M. Pavlidis, "Steady bubble rise and deformation in newtonian and viscoplastic fluids and conditions for bubble entrapment", *Journal of Fluid Mechanics*, vol. 601, pp. 123–164, 2008, ISSN: 0022-1120. DOI: 10.1017/S0022112008000517.

[20] R. Nimmagadda, "Dynamics of rising bubbles in initially quiescent liquids that are later on disturbed by falling drops", *Journal of the Brazilian Society of Mechanical Sciences and Engineering*, vol. 42, no. 10, 2020, ISSN: 1678-5878. DOI: 10.1007/s40430-020-02612-y.

[21] A. Cioncolini and M. Magnini, "Shapes and rise velocities of single bubbles in a confined annular channel: Experiments and numerical simulations", *Fluids*, vol. 6, no. 12, p. 437, 2021. DOI: 10.3390/fluids6120437.

[22] A. R. Wadhwa, V. Magi, and J. Abraham, "Transient deformation and drag of decelerating drops in axisymmetric flows", *Physics of Fluids*, vol. 19, no. 11, p. 113 301, 2007, ISSN: 1070-6631. DOI: 10.1063/1.2800038.

[23] A. B. Basset, *A Treatise on Hydrodynamics*. London: George Bell and Sons, 1888.

[24] J. V. Boussinesq, *Theorie analytique de la chaleur*, 2nd ed. Paris: Gauthier-Villars, 1903.

[25] C. W. Oseen, *Neuere Methoden und Ergebnisse in der Hydrodynamik*. Leipzig: Akademische Verlagsgesellschaft M.B.H., 1927.

[26] T.-J. Chang and B. C. Yen, "Gravitational fall velocity of sphere in viscous fluid", *J. Eng. Mech.*, no. 124(11), pp. 1193–1199, 1998.

[27] G. G. Stokes, "On the effect of the internal friction of fluids on the motion of pendulums", *Trans. Camb. Phil. Soc.*, no. 9, pp. 8–106, 1851.

[28] E. E. Michaelides, "Review—the transient equation of motion for particles, bubbles, and droplets", *Journal of Fluids Engineering*, vol. 119, no. 2, pp. 233–247, 1997, ISSN: 0098-2202. DOI: 10.1115/1.2819127.

[29] H. Faxén, "Der widerstand gegen die bewegung einer starren kugel in einer zähen flüssigkeit, die zwischen zwei parallelen ebenen wänden eingeschlossen ist", *Annalen der Physik*, no. 373, pp. 89–119, 1922.

[30] J. W. Swan and J. F. Brady, "Particle motion between parallel walls: Hydrodynamics and simulation", *Physics of Fluids*, vol. 22, no. 10, p. 103 301, 2010, ISSN: 1070-6631. DOI: 10.1063/1.3487748.

[31] Z. D. Hensley and D. V. Papavassiliou, "Drag coefficient correction for spherical and nonspherical particles suspended in square microducts", *Industrial & Engineering Chemistry Research*, vol. 53, no. 25, pp. 10 465–10 474, 2014, ISSN: 0888-5885. DOI: 10.1021/ie5007646.

[32] R. N. Palchesko, L. Zhang, Y. Sun, and A. W. Feinberg, "Development of polydimethylsiloxane substrates with tunable elastic modulus to study cell mechanobiology in muscle and nerve", *PloS one*, vol. 7, no. 12, e51499, 2012. DOI: 10.1371/journal.pone.0051499.

[33] *DIN ISO 7743:2016-08, Rubber, vulcanized or thermoplastic – Determination of compression stress-strain properties (ISO 7743:2011)*.

[34] M. Tashibana and K. Kitasho, "The motion of a falling sphere in a viscous fluid and the effects of side walls", *Memoirs of the Faculty of Engineering Fukui University*, vol. 24, no. 2, 1976.

[35] R. Moorman, *Motion of a Spherical Particle in the Accelerated Portion of Free Fall: PhD Dissertation*. 1955.

[36] J. Urzay, S. G. Llewellyn Smith, and B. J. Glover, "The elastohydrodynamic force on a sphere near a soft wall", *Physics of Fluids*, vol. 19, no. 10, p. 103 106, 2007, ISSN: 1070-6631. DOI: 10.1063/1.2799148.

[37] A. Kargar-Estahbanati and B. Rallabandi, "Lift forces on three-dimensional elastic and viscoelastic lubricated contacts", *Physical Review Fluids*, vol. 6, no. 3, 2021. DOI: 10.1103/PhysRevFluids.6.034003.

[38] A. Müller, M. C. Wapler, and U. Wallrabe, "A quick and accurate method to determine the poisson's ratio and the coefficient of thermal expansion of pdms", *Soft Matter*, vol. 15, no. 4, pp. 779–784, 2019. DOI: 10.1039/c8sm02105h.

[39] R. Fåhraeus, "The suspension stability of the blood", *Physiological Reviews*, vol. 4, no. 2, pp. 241–274, 1929. DOI: 10.1152/physrev.1929.9.2.241.

[40] M. M. Naderi, L. Barilla, J. Zhou, I. Papautsky, and Z. Peng, "Elasto-inertial focusing mechanisms of particles in shear-thinning viscoelastic fluid in rectangular microchannels", *Micromachines*, vol. 13, no. 12, 2022, ISSN: 2072-666X. DOI: 10.3390/mi13122131.

[41] G. Segré and A. Silberberg, "Radial particle displacements in poiseuille flow of suspensions", *Nature*, vol. 189, no. 4760, pp. 209–210, 1961.

[42] D. Di Carlo, D. Irima, R. G. Tompkins, and M. Toner, "Continuous inertial focusing, ordering, and separation of particles in microchannels", *PNAS*, vol. 104, no. 48, pp. 18 892–18 897, 2007. DOI: 10.1073/pnas.0704958104.

[43] Y. Zhou, Z. Ma, and Y. Ai, "Dynamically tunable elasto-inertial particle focusing and sorting in microfluidics", *Lab on a chip*, vol. 20, no. 3, pp. 568–581, 2020. DOI: 10.1039/c9lc01071h.

[44] G. Choi, R. Nouri, L. Zarzar, and W. Guan, "Microfluidic deformability-activated sorting of single particles", *Microsystems & nanoengineering*, vol. 6, no. 11, 2020. DOI: 10.1038/s41378-019-0107-9.

[45] M. Kubánková et al., "Physical phenotype of blood cells is altered in covid-19", *Biophysical journal*, vol. 120, no. 14, pp. 2838–2847, 2021. DOI: 10.1016/j.bpj.2021.05.025.

[46] A. Mietke et al., "Extracting cell stiffness from real-time deformability cytometry: Theory and experiment", *Biophysical journal*, vol. 109, no. 10, pp. 2023–2036, 2015. DOI: 10.1016/j.bpj.2015.09.006.

[47] P. G. Saffman, "The lift on a small sphere in a slow shear flow", *Journal of Fluid Mechanics*, vol. 22, no. 2, pp. 385–400, 1965, ISSN: 0022-1120. DOI: 10.1017/S0022112065000824.

[48] L. Bureau, G. Coupier, and T. Salez, "Lift at low reynolds number", *The European physical journal. E, Soft matter*, vol. 46, no. 11, p. 111, 2023. DOI: 10.1140/epje/s10189-023-00369-5.

[49] C. W. Oseen, "Ueber die stokes´sche formel und ueber eine verwandte aufgabe in der hydrodynamik", *Arkiv fuer matematik, astronomi o. fysik*, vol. 6, no. 29, 1910.

[50] P. Vasseur and R. G. Cox, "The lateral migration of spherical particles sedimenting in a stagnant bounded fluid", *Journal of Fluid Mechanics*, vol. 80, no. 03, pp. 561–591, 1977, ISSN: 0022-1120. DOI: 10.1017/S0022112077001840.

[51] V. Bertin, Y. Amarouchene, E. Raphaël, and T. Salez, "Soft-lubrication interactions between a rigid sphere and an elastic wall", *Journal of Fluid Mechanics*, vol. 933, no. A23, pp. 1–21, 2022, ISSN: 0022-1120. DOI: 10.1017/jfm.2021.1063.

[52] N. I. Ekanayake, J. D. Berry, and D. J. Harvie, "Lift and drag forces acting on a particle moving in the presence of slip and shear near a wall", *Journal of Fluid Mechanics*, vol. 915, no. A103, p. 40, 2021, ISSN: 0022-1120. DOI: 10.1017/jfm.2021.138.

[53] J. Beaucourt, T. Biben, and C. Misbah, "Optimal lift force on vesicles near a compressible substrate", *Europhysics Letters (EPL)*, vol. 67, no. 4, pp. 676–682, 2004, ISSN: 0295-5075. DOI: 10.1209/epl/i2004-10103-0.

[54] H. S. Davies, D. Débarre, N. El Amri, C. Verdier, R. P. Richter, and L. Bureau, "Elastohydrodynamic lift at a soft wall", *Physical review letters*, vol. 120, no. 19, p. 198 001, 2018, ISSN: 0031-9007. DOI: 10.1103/PhysRevLett.120.198001.

[55] B. Rallabandi et al., "Rotation of an immersed cylinder sliding near a thin elastic coating", *Physical Review Fluids*, vol. 2, no. 7, 2017. DOI: 10.1103/PhysRevFluids.2.074102.

[56] B. Rallabandi, N. Oppenheimer, M. Y. Ben Zion, and H. A. Stone, "Membrane-induced hydroelastic migration of a particle surfing its own wave", *Nature Physics*, vol. 14, no. 12, pp. 1211–1215, 2018, ISSN: 1745-2481. DOI: 10.1038/s41567-018-0272-z.

[57] Z. Zhang, V. Bertin, M. Arshad, E. Raphaël, T. Salez, and A. Maali, "Direct measurement of the elastohydrodynamic lift force at the nanoscale", *Physical review letters*, vol. 124, no. 5, p. 054 502, 2020, ISSN: 0031-9007. DOI: 10.1103/PhysRevLett.124.054502.

[58] M. J. Lighthill, "On the squirming motion of nearly spherical deformable bodies through liquids at very small reynolds numbers", *Communications on Pure and Applied Mathematics*, vol. 5, no. 2, pp. 109–118, 1952, ISSN: 0010-3640. DOI: 10.1002/cpa.3160050201.

[59] J. R. Blake, "A spherical envelope approach to ciliary propulsion", *Journal of Fluid Mechanics*, vol. 46, no. 1, pp. 199–208, 1971, ISSN: 0022-1120. DOI: 10.1017/S002211207100048X. [Online]. Available: https://www.cambridge.org/core/product/577A4CDB372F7DE7C232F0CF613E36F8.

[60] D. Takagi and J. R. Strickler, "Active hydrodynamic imaging of a rigid spherical particle", *Scientific reports*, vol. 10, no. 1, p. 2665, 2020. DOI: 10.1038/s41598-020-58880-0.

[61] J. R. Blake, "A note on the image system for a stokeslet in a no-slip boundary", *Mathematical Proceedings of the Cambridge Philosophical Society*, vol. 70, no. 2, pp. 303–310, 1971, ISSN: 0305-0041. DOI: 10.1017/S0305004100049902. [Online]. Available: https://www.cambridge.org/core/product/369E2BBCEBC791AA02BF9145A5D6208F.

[62] J. R. Blake and A. T. Chwang, "Fundamental singularities of viscous flow", *Journal of Engineering Mathematics*, vol. 8, no. 1, pp. 23–29, 1974, ISSN: 1573-2703. DOI: 10.1007/BF02353701.

[63] S. E. Spagnolie and E. Lauga, "Hydrodynamics of self-propulsion near a boundary: Predictions and accuracy of far-field approximations", *Journal of Fluid Mechanics*, vol. 700, pp. 105–147, 2012, ISSN: 0022-1120. DOI: 10.1017/jfm.2012.101.

[64] J. S. Lintuvuori, A. T. Brown, K. Stratford, and D. Marenduzzo, "Hydrodynamic oscillations and variable swimming speed in squirmers close to repulsive walls", *Soft Matter*, vol. 12, no. 38, pp. 7959–7968, 2016. DOI: 10.1039/C6SM01353H.

[65] F. Rühle, J. Blaschke, J.-T. Kuhr, and H. Stark, "Gravity-induced dynamics of a squirmer microswimmer in wall proximity", *New Journal of Physics*, vol. 20, no. 2, p. 025 003, 2018. DOI: 10.1088/1367-2630/aa9ed3.

[66] Q. Tingting, L. Jianzhong, O. Zhenyu, and Z. Jue, "Settling mode of a bottom-heavy squirmer in a narrow vessel", *Soft Matter*, vol. 19, no. 4, pp. 652–669, 2023. DOI: 10.1039/d2sm01442d.

[67] A. Théry, C. C. Maaß, and E. Lauga, "Hydrodynamic interactions between squirmers near walls: Far-field dynamics and near-field cluster stability", *Royal Society open science*, vol. 10, no. 6, p. 230 223, 2023, ISSN: 2054-5703. DOI: 10.1098/rsos.230223.

[68] P. M. Lovalenti and J. F. Brady, "The hydrodynamic force on a rigid particle undergoing arbitrary time-dependent motion at small reynolds number", *Journal of Fluid Mechanics*, vol. 256, pp. 561–605, 1993, ISSN: 0022-1120.

[69] T. Redaelli, F. Candelier, R. Mehaddi, and B. Mehlig, "Unsteady and inertial dynamics of a small active particle in a fluid", *Physical Review Fluids*, vol. 7, no. 4, 2022. DOI: 10.1103/PhysRevFluids.7.044304.

[70] I. Noichl and C. Schönecker, "Dynamics of elastic, nonheavy spheres sedimenting in a rectangular duct", *Soft Matter*, vol. 18, no. 12, pp. 2462–2472, 2022. DOI: 10.1039/D1SM01789F.

[71] J. Feng and D. D. Joseph, "The unsteady motion of solid bodies in creeping flows", *Journal of Fluid Mechanics*, vol. 303, pp. 83–102, 1995, ISSN: 0022-1120.

[72] F. Takemura, S. Takagi, J. Magnaudet, and Y. Matsumoto, "Drag and lift forces on a bubble rising near a vertical wall in a viscous liquid", *Journal of Fluid Mechanics*, vol. 461, pp. 277–300, 2002, ISSN: 0022-1120.

[73] L. E. Becker, G. H. McKinley, H. K. Rasmussen, and O. Hassager, "The unsteady motion of a sphere in a viscoelastic fluid", *Journal of Rheology*, vol. 38, no. 2, pp. 377–403, 1994, ISSN: 0148-6055. DOI: 10.1122/1.550519.

[74] J. Magnaudet, S. Takagi, and D. Legendre, "Drag, deformation and lateral migration of a buoyant drop moving near a wall", *Journal of Fluid Mechanics*, vol. 476, pp. 115–157, 2003, ISSN: 0022-1120. DOI: 10.1017/S0022112002002902.

[75] M. R. Maxey, "Equation of motion for a small rigid sphere in a nonuniform flow", *Physics of Fluids*, vol. 26, no. 4, p. 883, 1983, ISSN: 00319171. DOI: 10.1063/1.864230.

[76] B. Rallabandi, "Inertial forces in the maxey–riley equation in nonuniform flows", *Physical Review Fluids*, vol. 6, no. 1, 2021. DOI: 10.1103/PhysRevFluids.6.L012302.

[77] H. Haddadi and D. Di Carlo, "Inertial flow of a dilute suspension over cavities in a microchannel", *Journal of Fluid Mechanics*, vol. 811, pp. 436–467, 2017, ISSN: 0022-1120. DOI: 10.1017/jfm.2016.709.

[78] P. Shi and R. Rzehak, "Lift forces on solid spherical particles in wall-bounded flows", *Chemical Engineering Science*, vol. 211, p. 115 264, 2020, ISSN: 00092509. DOI: 10.1016/j.ces.2019.115264.

[79] F. Takemura, "Migration velocities of spherical solid particles near a vertical wall for reynolds number from 0.1 to 5", *Physics of Fluids*, vol. 16, no. 1, pp. 204–207, 2004, ISSN: 1070-6631. DOI: 10.1063/1.1629129.

[80] S. Wakiya, "Effect of a plane wall on the impulsive motion of a sphere in a viscous fluid", *Journal of the Physical Society of Japan*, vol. 19, no. 8, pp. 1401–1408, 1964.

[81] S. J. Weekley, S. L. Waters, and O. E. Jensen, "Transient elastohydrodynamic drag on a particle moving near a deformable wall", *The Quarterly Journal of Mechanics and Applied Mathematics*, vol. 59, no. 2, pp. 277–300, 2006, ISSN: 0033-5614. DOI: 10.1093/qjmam/hbl002.

[82] A. Daddi-Moussa-Ider, B. Rallabandi, S. Gekle, and H. A. Stone, "Reciprocal theorem for the prediction of the normal force induced on a particle translating parallel to an elastic membrane", *Physical Review Fluids*, vol. 3, no. 8, 2018. DOI: 10.1103/PhysRevFluids.3.084101.

[83] S. Ghosh and J. M. Stockie, "Numerical simulations of particle sedimentation using the immersed boundary method", *Communications in Computational Physics*, vol. 18, no. 2, pp. 380–416, 2015, ISSN: 1815-2406. DOI: 10.4208/cicp.061113.050115a.

[84] F. Toschi and M. Sega, Eds., *Flowing matter* (Springer eBook Collection). Cham, Switzerland: Springer Open, 2019, ISBN: 9783030233709. DOI: 10.1007/978-3-030-23370-9.

[85] M. V. Díaz, "On the long-time persistence of hydrodynamic memory", *The European physical journal. E, Soft matter*, vol. 44, no. 11, p. 141, 2021. DOI: 10.1140/epje/s10189-021-00151-5.

[86] C. J. Lawrence and S. Weinbaum, "The force on an axisymmetric body in linearized, time-dependent motion: A new memory term", *Journal of Fluid Mechanics*, vol. 171, pp. 209–218, 1986, ISSN: 0022-1120. DOI: 10.1017/S0022112086001428.

[87] C. J. Lawrence and S. Weinbaum, "The unsteady force on a body at low reynolds number; the axisymmetric motion of a spheroid", *Journal of Fluid Mechanics*, vol. 189, pp. 463–489, 1988, ISSN: 0022-1120. DOI: 10.1017/S0022112088001107.

[88] S. L. Seyler and S. Pressé, "Long-time persistence of hydrodynamic memory boosts microparticle transport", *Physical Review Research*, vol. 1, no. 3, 2019. DOI: 10.1103/PhysRevResearch.1.032003.

[89] J. Urzay, "Asymptotic theory of the elastohydrodynamic adhesion and gliding motion of a solid particle over soft and sticky substrates at low reynolds numbers", *Journal of Fluid Mechanics*, vol. 653, pp. 391–429, 2010, ISSN: 0022-1120. DOI: 10.1017/S0022112010000364.

[90] M. A. Biot, "Surface instability of rubber in compression", *Appl.sci. Res.*, vol. 12, no. A, pp. 168–182, 1962.

[91] S. Mora, M. Abkarian, H. Tabuteau, and Y. Pomeau, "Surface instability of soft solids under strain", *Soft Matter*, vol. 7, no. 22, p. 10 612, 2011. DOI: 10.1039/c1sm06051a.

[92] Z. Li, Z. Zhou, Y. Li, and S. Tang, "Effect of cyclic loading on surface instability of silicone rubber under compression", *Polymers*, vol. 9, no. 4, p. 148, 2017. DOI: 10.3390/polym9040148.

[93] N. I. K. Ekanayake et al., "Lift and drag forces acting on a particle moving with zero slip in a linear shear flow near a wall", *Journal of Fluid Mechanics*, vol. 904, 2020, ISSN: 0022-1120. DOI: 10.1017/jfm.2020.662.

[94] N. Goyal and J. J. Derksen, "Direct simulations of spherical particles sedimenting in viscoelastic fluids", *Journal of Non-Newtonian Fluid Mechanics*, vol. 183-184, pp. 1–13, 2012, ISSN: 03770257. DOI: 10.1016/j.jnnfm.2012.07.006.

[95] T.-W. Pan and R. Glowinski, "Numerical study of spheres settling in oldroyd-b fluids", *Physics of Fluids*, vol. 30, no. 11, p. 113 102, 2018, ISSN: 1070-6631. DOI: 10.1063/1.5032324.

[96] A. Heydari-Beni, R. J. Shor, and G. Natale, "Sedimentation behavior of a spherical particle in a giesekus fluid: A cfd–dem solution", *Journal of Non-Newtonian Fluid Mechanics*, vol. 291, p. 104 465, 2021, ISSN: 03770257. DOI: 10.1016/j.jnnfm.2020.104465.

[97] M. M. Villone and P. L. Maffettone, "Numerical simulations of the sedimentation of soft particles in confined newtonian liquids", *Physics of Fluids*, vol. 36, no. 3, 2024, ISSN: 1070-6631. DOI: 10.1063/5.0189169.

[98] I. COMSOL, *Comsol multiphysics reference manual, version 5.5*. [Online]. Available: https://doc.comsol.com.

[99] R. Courant, K. Friedrichs, and H. Lewy, "Über die partiellen differenzengleichungen der mathematischen physik", *Mathematische Annalen*, vol. 100, no. 1, pp. 32–74, 1928, ISSN: 1432-1807. DOI: 10.1007/BF01448839.

[100] A.-K. Dahlberg, A. Apler, L. Vogel, K. Wiberg, and S. Josefsson, "Persistent organic pollutants in wood fiber–contaminated sediments from the baltic sea", *Journal of Soils and Sediments*, vol. 20, no. 5, pp. 2471–2483, 2020, ISSN: 1439-0108. DOI: 10.1007/s11368-020-02610-6.

[101] T. H. Nguyen, T.-C. Kieu-Le, F. H. M. Tang, and F. Maggi, "Controlling factors of microplastic fibre settling through a water column", *The Science of the total environment*, vol. 838, no. Pt 1, p. 156 011, 2022. DOI: 10.1016/j.scitotenv.2022.156011.

[102] S. Broersma, "Viscous force constant of a closed cylinder", *The Journal of chemical physics*, vol. 32, no. 6, pp. 1632–1635, 1960. [Online]. Available: https://doi.org/10.1063/1.1730995.

[103] Joseph B. Keller and Sol I. Rubinow, "Slender-body theory for slow viscous flow", *Journal of Fluid Mechanics*, vol. 75, no. 4, pp. 705–714, 1976, ISSN: 0022-1120. DOI: 10.1017/S0022112076000475.

[104] G. K. Youngren and A. Acrivos, "Stokes flow past a particle of arbitrary shape: A numerical method of solution", *Journal of Fluid Mechanics*, vol. 69, no. 2, pp. 377–403, 1975, ISSN: 0022-1120.

[105] J. Feng, H. H. Hu, and D. D. Joseph, "Direct simulation of initial value problems for the motion of solid bodies in a newtonian fluid part 1. sedimentation", *Journal of Fluid Mechanics*, vol. 261, pp. 95–134, 1994, ISSN: 0022-1120. DOI: 10.1017/S0022112094000285.

[106] J. Strnadel, B. Šiška, and I. Machač, "Dynamic shape and wall correction factors of cylindrical particles falling vertically in a newtonian liquid", *Chemical Papers*, vol. 67, no. 9, 2013. DOI: 10.2478/s11696-012-0285-5.

[107] W. H. Mitchell and S. E. Spagnolie, "Sedimentation of spheroidal bodies near walls in viscous fluids: Glancing, reversing, tumbling and sliding", *Journal of Fluid Mechanics*, vol. 772, pp. 600–629, 2015, ISSN: 0022-1120. DOI: 10.1017/jfm.2015.222.

[108] V. Dabade, N. K. Marath, and G. Subramanian, "Effects of inertia and viscoelasticity on sedimenting anisotropic particles", *Journal of Fluid Mechanics*, vol. 778, pp. 133–188, 2015, ISSN: 0022-1120. DOI: 10.1017/jfm.2015.360.

[109] K. Fröhlich, M. Meinke, and W. Schröder, "Correlations for inclined prolates based on highly resolved simulations", *Journal of Fluid Mechanics*, vol. 901, 2020, ISSN: 0022-1120. DOI: 10.1017/jfm.2020.482.

[110] M. Kharrouba, J.-L. Pierson, and J. Magnaudet, "Flow structure and loads over inclined cylindrical rodlike particles and fibers", *Physical Review Fluids*, vol. 6, no. 4, 2021. DOI: 10.1103/PhysRevFluids.6.044308.

[111] N. Fintzi, L. Gamet, and J.-L. Pierson, "Inertial loads on a finite-length cylinder embedded in a steady uniform flow", *Physical Review Fluids*, vol. 8, no. 4, 2023. DOI: 10.1103/PhysRevFluids.8.044302.

[112] V. Chéron, F. Evrard, and B. van Wachem, "Drag, lift and torque correlations for axi-symmetric rodlike non-spherical particles in locally linear shear flows", *International Journal of Multiphase Flow*, vol. 171, p. 104 692, 2024, ISSN: 03019322. DOI: 10.1016/j.ijmultiphaseflow.2023.104692.

[113] H. J. Keh and L. R. Wang, "Slow motions of a circular cylinder experiencing slip near a plane wall", *Journal of Fluids and Structures*, vol. 24, no. 5, pp. 651–663, 2008, ISSN: 08899746. DOI: 10.1016/j.jfluidstructs.2007.11.002.

[114] N. J. de Mestre and W. B. Russel, "Low-reynolds-number translation of a slender cylinder near a plane wall", *J Eng Math*, vol. 9, pp. 81–91, 1975. DOI: 10.1007/BF01535390.

[115] W. B. Russel, Hinch E.J., and Leal L.G. and Tieffenbruck G., "Rods falling near a vertical wall", *Journal of Fluid Mechanics*, vol. 83, pp. 273–287, 1977, ISSN: 0022-1120. DOI: 10.1017/S0022112077001190.

[116] L. Koens and T. D. Montenegro-Johnson, "Local drag of a slender rod parallel to a plane wall in a viscous fluid", *Physical Review Fluids*, vol. 6, no. 6, 2021. DOI: 10.1103/PhysRevFluids.6.064101.

[117] J. Teng, B. Rallabandi, H. A. Stone, and J. T. Ault, "Coupling of translation and rotation in the motion of finite-length rods near solid boundaries", *Journal of Fluid Mechanics*, vol. 938, 2022, ISSN: 0022-1120. DOI: 10.1017/jfm.2022.177.

[118] T. J. Ui, R. G. Hussey, and R. P. Roger, "Stokes drag on a cylinder in axial motion", *The Physics of Fluids*, vol. 27, no. 4, pp. 787–795, 1984, ISSN: 0031-9171. DOI: 10.1063/1.864706.

[119] H. Brenner, "Effect of finite boundaries on the stokes resistance of an arbitrary particle", *Journal of Fluid Mechanics*, vol. 12, no. 1, pp. 35–48, 1962, ISSN: 0022-1120. DOI: 10.1017/S0022112062000026.

[120] D. Lopez and E. Guazzelli, "Inertial effects on fibers settling in a vortical flow", *Physical Review Fluids*, vol. 2, no. 2, 2017. DOI: 10.1103/PhysRevFluids.2.024306.

[121] A. Roy, R. J. Hamati, L. Tierney, D. L. Koch, and G. A. Voth, "Inertial torques and a symmetry breaking orientational transition in the sedimentation of slender fibres", *Journal of Fluid Mechanics*, vol. 875, pp. 576–596, 2019, ISSN: 0022-1120. DOI: 10.1017/jfm.2019.492.

[122] F. Cabrera et al., "Experimental validation of fluid inertia models for a cylinder settling in a quiescent flow", *Physical Review Fluids*, vol. 7, no. 2, 2022. DOI: 10.1103/PhysRevFluids.7.024301.

[123] R. E. Khayat and R. G. Cox, "Inertia effects on the motion of long slender bodies", *Journal of Fluid Mechanics*, vol. 209, pp. 435–462, 1989, ISSN: 0022-1120. DOI: 10.1017/S0022112089003174.

[124] X. Xu and A. Nadim, "Deformation and orientation of an elastic slender body sedimenting in a viscous liquid", *Physics of Fluids*, vol. 6, no. 9, pp. 2889–2893, 1994, ISSN: 1070-6631. DOI: 10.1063/1.868116.

[125] B. Marchetti et al., "Deformation of a flexible fiber settling in a quiescent viscous fluid", *Physical Review Fluids*, vol. 3, no. 10, 2018. DOI: 10.1103/PhysRevFluids.3.104102.

[126] T. Salez and L. Mahadevan, "Elastohydrodynamics of a sliding, spinning and sedimenting cylinder near a soft wall", *Journal of Fluid Mechanics*, vol. 779, pp. 181–196, 2015, ISSN: 0022-1120. DOI: 10.1017/jfm.2015.425.

[127] B. Rallabandi et al., "Rotation of an immersed cylinder sliding near a thin elastic coating", *Physical Review Fluids*, vol. 2, no. 7, 2017. DOI: 10.1103/PhysRevFluids.2.074102.

[128] B. Saintyves, T. Jules, T. Salez, and L. Mahadevan, "Self-sustained lift and low friction via soft lubrication", *Proceedings of the National Academy of Sciences of the United States of America*, vol. 113, no. 21, pp. 5847–5849, 2016. DOI: 10.1073/pnas.1525462113.

[129] J.-L. Pierson, "Inertial settling of an arbitrarily oriented cylinder in a quiescent flow: From short-time to quasisteady motion", *Physical Review Fluids*, vol. 8, no. 10, 2023. DOI: 10.1103/PhysRevFluids.8.104301.

[130] G. K. Batchelor, "Slender-body theory for particles of arbitrary cross-section in stokes flow", *Journal of Fluid Mechanics*, vol. 44, no. 3, pp. 419–440, 1970, ISSN: 0022-1120. DOI: 10.1017/S002211207000191X.

[131] R. G. Cox, "The motion of long slender bodies in a viscous fluid part 1. general theory", *Journal of Fluid Mechanics*, vol. 44, no. 4, pp. 791–810, 1970, ISSN: 0022-1120. DOI: 10.1017/S002211207000215X.

[132] J. Happel and E. Bart, "The settling of a sphere along the axis of a long square duct at low reynolds' number", *Appl. Sci. Res.*, no. 29, pp. 241–258, 1974.

[133] J.-L. Pierson, M. Kharrouba, and J. Magnaudet, "Hydrodynamic torque on a slender cylinder rotating perpendicularly to its symmetry axis", *Physical Review Fluids*, vol. 6, no. 9, 2021. DOI: 10.1103/PhysRevFluids.6.094303.

[134] T. M. Fischer, M. Stöhr-Lissen, and H. Schmid-Schönbein, "The red cell as a fluid droplet: Tank tread-like motion of the human erythrocyte membrane in shear flow", *Science (New York, N.Y.)*, vol. 202, no. 4370, pp. 894–896, 1978, ISSN: 0036-8075. DOI: 10.1126/science.715448.

[135] J. Dupire, M. Socol, and A. Viallat, "Full dynamics of a red blood cell in shear flow", *Proceedings of the National Academy of Sciences of the United States of America*, vol. 109, no. 51, pp. 20 808–20 813, 2012. DOI: 10.1073/pnas.1210236109.

[136] M. Darrin et al., "Classification of red cell dynamics with convolutional and recurrent neural networks: A sickle cell disease case study", *Scientific reports*, vol. 13, no. 1, p. 745, 2023. DOI: 10.1038/s41598-023-27718-w.

Declaration of authorship

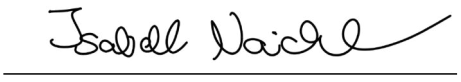
I, Isabell Noichl, declare that this thesis titled 'Elastohydrodynamic interaction of flowing particles with surfaces' and the work presented in it are my own and that I have not used any sources, resources or technical tools other than those specified. All statements that were taken from other publications, either literally or analogously, are marked accordingly. This work has not been submitted as a dissertation or other scientific examination to any other department or university.

In the preparation of this thesis, I made use of generative artificial intelligence systems, specifically ChatGPT, developed by OpenAI. These tools were not employed for the generation of substantive content but were used primarily for linguistic refinement (*i.e.*, copyediting) to improve clarity and style. Additionally, the system was used as a supportive resource for programming-related queries, such as assistance with MATLAB syntax and LaTeX formatting.

Notice that the present dissertation includes previously published or (prepared to be) submitted material, which is listed below:

- I. Noichl and C. Schönecker. Dynamics of elastic, nonheavy spheres sedimenting in a rectangular duct. *Soft Matter*, 2022,18, 2462-2472 ; DOI: 10.1039/d1sm01789f
- Chapter "Interaction of Elastic Particles with Surfaces" in: Aurich, Jan C.; Hasse, Hans (eds). Component Surfaces. Manufacturing-Morphology-Property Relationships. *Springer Cham.* 2023. ISBN 978-3-031-35574-5
- I. Noichl and C. Schönecker. Inertial forces and elastohydrodynamic interaction of spherical particles in wall-bounded sedimentation experiments at low Re_P number. *Manuscript currently in preparation for submission to Journal of Fluid Mechanics.*

Kaiserslautern, den 01.08.2025



List of supervised theses

The following theses were supervised by the author and are related to this dissertation.

- S. Zimmermann. Numerical investigation of particle-loaded fluid flow over microstructured surfaces. Master thesis. 2019.
- X. Wu. 3D computational fluid dynamics (CFD) simulation of the sedimentation of spheres and rods in a rectangular duct. 2021.

Curriculum vitae

Personal Information

Name	Isabell Noichl
Birth name	Behrendt

Education

2012 - 2017	Diploma course Mechanical and Process Engineering at TU Kaiserslautern Specialization: Process Engineering Diploma thesis: 'Simulation of a fluidized bed reactor by coupling computational fluid dynamics (CFD) and discrete element method (DEM)'. Institute of Particle Process Engineering, Prof. Antonyuk Degree: Dipl.-Ing.
2003 - 2012	Sickingen-Gymnasium in Landstuhl Degree: Allgemeine Hochschulreife
1999 - 2003	Elementary school in Waldfischbach-Burgalben

Professional

2018 -	Research associate at the Chair of Micro Fluid Mechanics, Prof. Dr.-Ing. Clarissa Schönecker, RPTU, Kaiserslautern